
# Growth, Morphology and Solid State Miscibility of Alkali Nitrates

Raúl Benages Vilau

UNIVERSITAT DE BARCELONA

Departartament de Cristal·lografia, Mineralogia i Dipòsits Minerals.
Grup de Aliatges Moleculars

# GROWTH, MORPHOLOGY AND SOLID STATE MISCIBILITY OF ALKALI NITRATES

-2013-

Programa de Doctorat: Ciències de la Terra

El doctorand,

Raúl Benages Vilau
Dpt. Cristal·lografia, Mineralogia
i Dipòsits Minerals.
Universitat de Barcelona

Els directors:

Dr. M A. Cuevas-Diarte.
Dpt. Cristal·lografia, Mineralogia
i Dipòsits Minerals.
Universitat de Barcelona

La tutora:

Dra. Mª T. Calvet i Pallàs
Dpt. Cristal·lografia, Mineralogia
i Dipòsits Minerals.
Universitat de Barcelona

**ACKNOWLEDGEMENTS**

This PhD thesis must be addressed to my mother's memory. She was always proud of me and let me study what I want. She supported me until the end of her days. Although you can not read this THANK YOU →GRACIAS!!

To my family for their support.

Thanks to Miquel Àngel and Teresa for trust me and support me in this thesis and in all other researches performed. They give me the opportunity to work with many techniques and many people in order to achieve satisfactory results in several fields.

I should recollect here all the important people that conduct me to here.

My first contact with crystallography was early, when I had 16-17 years old. My teacher explains us the seven crystal systems and the 320 point groups. I was amazed about symmetry. But, not only that, he also introduced us, in a certain way, the Kossel crystal and the kink sites for the preffered sites for a crystal growth. In that time, if I had thought about working on this subject I would not have believed it. Thus, my high-school teacher was the first who introduce me in the crystallography. Thank you, wherever you are.

Next person was Laura Bayes. In the second year of chemistry degree we decided to assist to crystallography course. During the course she motivated me to study hard this subject. It was a fruitfull course because she and me begun to work in the crystallography department. I think that without her, probably I never started to make research here. For this reason I may say thank you to you.

Obviously, our crystallography teacher was Miquel Àngel Cuevas-Diarte. So, a first thanks for him and for Teresa Calvet to let me start my career here while I was studying the chemistry and the material science degrees. About 6 years after that beginning I started this PhD.

Thanks to all the 'aliatges moleculars' group people who has helped me at some time: Laura, Raquel, Mercedes, Evelyn, Xabier… and also for the rest of the department people: Thomas, Cristina, Montgarri…

Big thanks for the people from Turin who make me understand the crystal morphology and the crystal growth. Thank you: Dino, Marco, Marco and Emmanuelle. Thank you for make me so easy and fruitfull my residencies there. Many thanks to Dino for his passion in this project and his hospitality. Than you to his wife Renata for ther lovely meals.

Thank you to Carlos Pina for the fruitful experiments of epitaxy in the AFM. To Sander, for the nice pictures taken in the confocal microscopy on a growing surface of nitratine.

During the PhD I learnt lots of things from the academic point of view. Apart from all the knowledge in this manuscript I performed some research work about solar thermal energy storage. Thanks to the people of Quality Chemicals to have done with us that

research. We have organized two crystal growth competitions to present high school students this beautiful subject.

Next, I have to give a big thank YOU to Heura. We shared a flat during 1 year and a half. They were very pleasant and wonderful days. THANK YOU Heura to be with me in my hardest and sad days after my mother's dead.

Thank you to beer!!! It seems strange but I have lernt to brew in the past 4-5 years. I enjoy a lot to brew and to share the final product. Many people loved every beer I brew: a pleasure for me!

Thank you to David and Dani to be friends and to create my outstanding logo!


Thank you to Maria to take me out for a beer whenever I need it. To Pilar because she is always there

Lastly, I want to give a large THANK YOU to Layita for all the wonderfull days you are with me: love forever! Thank you for the peace I feel at your side. Thank you to make me feel special… thank you to be with me!

I hope you enjoy this reading with a good beer.

Content

Content

# GENERAL INTRODUCTION

The work presented in this memory has been performed in 'Aliatges Moleculars' group in the department of 'Cristal·lografia, Mineralogia i Dipòsits Minerals' of the 'Facultat de Geologia' under the co-supervision of Dr Miquel Àngel Cuevas-Diarte and Dra Teresa Calvet Pallàs. This group boasts extensive experience in polymorphism and phase diagram determination in aliphatic compounds and our publications show the importance of using complementary techniques to effectively establish the stability regions within a binary system. Thus, we can begin a study of inorganic polymorphism and phase diagram determination.

This PhD thesis was funded by a CENIT - CONSOLIDA industrial development grant for solar thermal energy storage. Therefore, it has been developed in parallel with industrial development. It is well known that the efficiency of electric production through the Carnot (or similar) cycles is limited by the difference in the hot and cold point. Consequently, industry is being searching for new compositions to act as a heat transfer fluid. Nitrate base compositions are, nowadays, the most promising fluid to enhance the electric production because some liquid alkali nitrates mixtures can hold 400 K of difference between the liquid solidification and its decomposition.

While studying these compounds we have noticed that alkali nitrates polymorphism and crystal growth was not studied in depth. Therefore, we thought that a research at fundamental level would be interesting to be performed.

The crystal growth and morphological aspects were performed in close collaboration with Prof. Dino Aquilano, Prof. Marco Rubbo and Dr Marco Bruno of *Scienze Minealogiche e Petrologiche* department of *Univesitá degli Studi di Torino* in Italy. Long time residencies have been done in order to learn the PBC theory, to acquire crystallization and crystal growth skills; and to discuss the results obtained in crystal growth measurements. With their advices we were able to build a device to measure the specific face growth of highly soluble substances. These experiments were executed in the microscope light. But we wanted to go further, in order to look at the dislocation movement on crystal surfaces we used a laser confocal differential interference contrast microscopy (LCM-DIM) installed in *Laboratorio de Estudios Cristalográficos* of *Instituto Andaluz de Ciencias de la Tierra* (LEC-IACT) belonging to the *Centro*

*Superior de Investigaciones Científicas* (CSIC). With this technique we can observe elementary steps (up to 3 nm height), and at the same time, a large area of the growing crystal surface. These measurements were performed with the aid of Dr A. E. S. van Driessche during a residency in Granada. Furthermore, we made epitaxial growth in the *Centro Nacional de Microscopia Electrónica* (CNME-ICTS) at the *Universidad Complutense de Madrid* during two shorts residencies under the supervision of Dr Carlos M. Pina.

As can be appreciated this PhD implements a high mobility because we looked for the expertise at international level, so that new and fruitful collaborations have begun in the course of these last four years.

This PhD thesis is focused in structural aspects of alkali nitrates. In the first chapter, we recollected the most important advancement in this field in alkali nitrates compounds published since 1970. Along this lines, crystal structure, polymorphism and phase transition is discussed first; second, crystal growth, and third, the morphology. And, finally a section concerning solid state miscibility and binary phase diagrams between these compounds is presented.

The following chapters present a deeper study of growth morphology and how the impurities affect to the morphology and growth rate. These two topics are closely related because the growth morphology is a consequence of the growth rate ratio of different faces. Evidently, we chose only one compound of all the alkali nitrate family. It turned to be sodium nitrate, nitratine or $NaNO_3$. First, in chapter 2, we calculate the morphology of nitratine by applying the two most common approaches to determine the theoretic morphology of crystals: the Bravais-Friedel-Donnay-Harker (BFDH) methodology and the periodic bond chains (PBCs) procedure proposed by Hartman and Perdok (HP). Then we compare the obtained morphology with the experimental growth shape. This compound is interesting from the morphological and structural point of view because it is isostructural with calcite, a calcium carbonate ($CaCO_3$) polymorph. This fact will permit us to discuss how the charges affect the final crystal morphology; an introduction to this question is in chapter 2.

In chapter 3 we sought to determination of the normal growth rates ($R_{104}$) of {104} faces of sodium nitrate single crystals under isothermal conditions in the temperature interval 288 K – 297.5 K and hence find the most probable growth mechanisms.

Chapter 4 is devoted to the morphology change in $NaNO_3$ crystals by the effect of impurities. It is followed by an atomic force microscopy (AFM) investigation of

heterogeneous nucleation of nitratine on calcite in chapter 5. Finally, the $NaNO_3$ – $KNO_3$ phase diagram has been studied from both experimental and theoretical aspects in chapter 6. In this case, we collaborated with Professor Harry Oonk of Utrech University in order to model the phase diagram. Some X Ray diffraction measurements and checkings were performed with the help of Dra Denise Mondieig and Dr Philippe Negrier of 'Centre de Physique Moléculaire Optique et Hertzienne' of 'Université Bordeaux 1'.

We can see here that we have looked over some aspects with the same background: crystallization, crystal growth and polymorphism.

# CHAPTER 1

## ALKALI NITRATES REVIEW

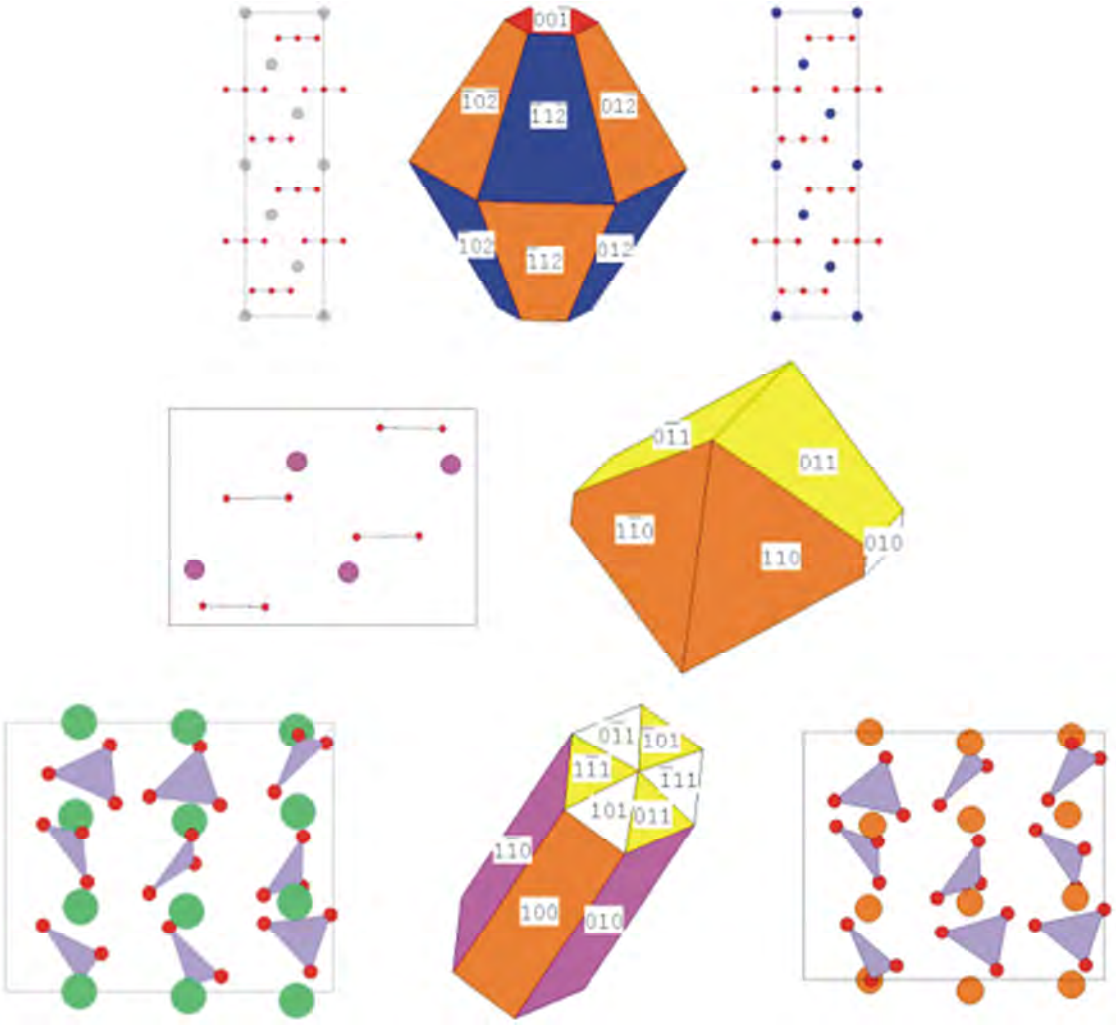

## 1.1. INTRODUCTION

The general formula for alkali nitrates is $XNO_3$ with X = Li, Na, K, Rb or Cs. They are formed only by a triangular nitrate group and a spherical alkali atom. These compounds are interesting to study because they have, in principle, a simple structure. Despite this they can crystallize into a variety of crystalline forms. Some of them would be interesting from the technological point of view. For example, $NaNO_3$ has an extended second order polymorphic transition,[1] and can be considered a model for the isostructural calcite mineral; γ-$KNO_3$ is a ferroelectric phase;[2] rubidium nitrate has a rich polymorphism with four phases at ambient pressure.[3] On the other hand, $LiNO_3$ and $CsNO_3$ have not been widely studied, but they are important in order to obtain a unified vision of the alkali nitrate family.

Polymorphism of alkali nitrates has been extensively reviewed by Rao et al.[4] The authors recollected all the information available up to 1975 and organized it in tables highlighting the most important conclusions extracted in each technique used to characterize alkali nitrates. Our aim is first to complete the Rao et al. summary with more recent information about polymorphism and phase transition. Second, to make a recollection of crystal growth data because we noticed that some interesting work has been published, but there is not a complete review that puts results in this field all together, in fact only $NaNO_3$ and $KNO_3$ are widely studied because they have several important industrial applications such as fertilizer. Chernov and Sipyagin[5] recollected kinetic parameters of nitrates and sulphates, so that is our starting point. Third, morphological studies are interesting because we can compare how the final crystal shape varies by only changing the alkali metal. Finally, it is also motivating to include solid solution and phase diagrams in this review, so that we can have a complete vision of structural facts in the alkali nitrates family. Alkali nitrate phase diagrams have been recently calculated by the FACTsage software developed for over 20 years.[6]

In the last 40 years, many papers about crystal structure, polymorphism, phase transition, crystal growth, morphology and solid state miscibility including phase diagram determination of the alkali nitrate family have appeared. Unfortunately, the publications are scattered; therefore we think that it is essential to have all the information about structural aspects in a single chapter.

This review is divided into compounds, where crystal structure, polymorphism and phase transition is discussed first; second, crystal growth, and third, the morphology.

And, finally a section concerning solid state miscibility and binary phase diagrams between these compounds is presented.

## 1.2. LITHIUM NITRATE

### 1.2.1. Crystal structure, polymorphism and phase transitions.

As Rao et al. exposed,[4] lithium nitrate crystallizes in rhombohedral (calcite type), $R\bar{3}c$ group with Z = 6, **a** = 4.692 Å and **b** = 15.22 Å at 298 K. There is no evidence for a phase transition in the thermodynamic properties from 298 K to the melting point.[7] However, discontinuities in the absorption coefficient[8] and changes in electric properties[9] may indicate an orientational transition just like $NaNO_3$ or $NH_4NO_3$.

After Rao et al., only Wu et al.[10] determined $LiNO_3$ crystal structure gives a significant variation in the **c** parameter as can be seen in Table 1. The unit cell determined by Wu et al.[10] is presented in figure 1, where blue spheres are lithium ions and red spheres are oxygen atoms. These authors grew the crystal from the melt and despite not having a good single crystal they were able to determine its structure. According to them, $LiNO_3$ is isostructural to both calcite and $NaNO_3$. No evidences have been found for a high temperature phase. Moreover, Stromme[11] modelled a positional ordered equilibrium structure of $LiNO_3$ at all temperatures.

Accordingly, $LiNO_3$ has only one structure as a function of temperature as is recollected in Table 1.

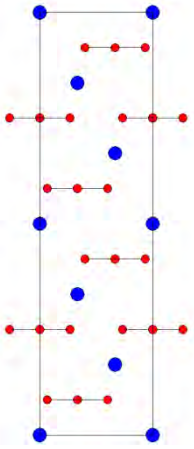

**Figure 1.** Structure of $LiNO_3$.[10]

### 1.2.2. Crystal growth.

We have not found any paper related to anhydrous lithium nitrate growth because it is deliquescent. Nonetheless, Chernov and Sipyagin[5] give some kinetic data for $LiNO_3 \cdot 3H_2O$ compound, which is not of interest for this review.

### 1.2.3. Morphology.

As far as we know, neither theoretical nor experimental morphology is reported for lithium nitrate crystals. However, we expect that the theoretical morphology determined by the Bravais-Friedel-Donnay-Harker (BFDH) method will be equal to calcite[12] and nitratine[13] because they are isostructural crystals. Therefore, {012}, {01$\bar{2}$} and {001} forms appears in the morphology.

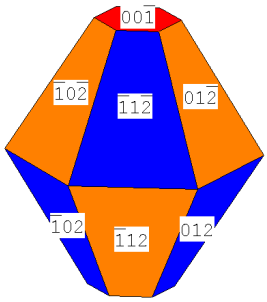


**Figure 2.** Morphology of $LiNO_3$ calculated by the BFDH method.

## 1.3. SODIUM NITRATE

### 1.3.1. Crystal structure, polymorphism and phase transitions.

Sodium nitrate crystallizes in rhombohedral (calcite type), $R\bar{3}c$ group with Z = 6; **a** = 5.0396 Å and **b** = 16.829 Å at 298 K.[4] A phase transition from II-$NaNO_3$ ($R\bar{3}c$) to a disordered phase I-$NaNO_3$ ($R\bar{3}m$) around 548.5 K was observed.[14] The $R\bar{3}m$ polymorph has Z = 3 with **a** = 5.0889 Å and **b** = 8.868 Å at 563 K.[15] In figure 3 we show the 2 structures, grey spheres are sodium atoms.

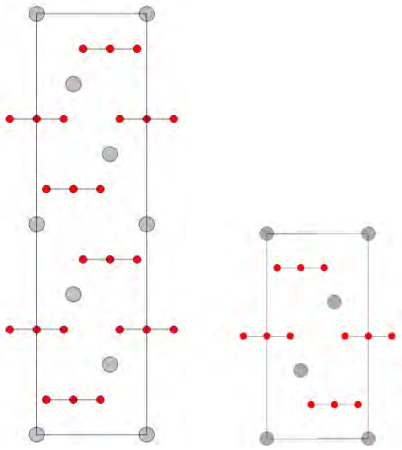

**Figure 3.** Left: II-$NaNO_3$ crystal structure.[15]
Right: I-$NaNO_3$ crystal structure.[15]

II-$NaNO_3$ ($R\bar{3}c$) structure consists in alternating layers of sodium ions and nitrate groups, nitrate layers being rotated each other by 60º around the triad axis,[16] each sodium ion has an octahedral coordination with oxygen atoms. II-$NaNO_3$ has a known stability temperature range between 100 K and 550 K.

The high temperature form (phase I-$NaNO_3$) crystallizes in the $R\bar{3}m$ space group with 3 formula units per cell. Its structure is also formed by alternating layers of nitrate groups and sodium ions, but in this case nitrate ions display rotational disorder. I-$NaNO_3$ is stable until melting point (581 K). Gonschorek et al.[15] determined the crystal structure of $NaNO_3$ at three temperatures by synchrotron or neutron diffraction from 100 K to 563 K. Effectively, results agree well with those reviewed by Rao et al. (see Table 1). Teo[17] reported a new phase above 14 kbar which is similar to the II-$NaNO_3$ phase because the volume change in the phase transition is small.

The transition between low and high temperature form of $NaNO_3$ is a second order (order-disorder) transition and some authors propose an extension of more or less 100 K.[15] According to several authors, it is the $NO_3$ anion that changes from a static position to a rotational disorder through the transition, hence all nitrate planes become equivalent and the cell loses the **c** glide plane. Fermor and Kjekshus[18] wrote a detailed report on the electric properties of $NaNO_3$ and proposed that the second order transition begins at a temperature of 433 K because the apparent energy gap changes at this temperature. All the data gathered by Rao et al.[4] suggest that this order - disorder transition is due to the activation of the rotation of the nitrate group around its trigonal axis although spectroscopic studies seemed to show that $NO_3$ does not have a free rotation above the transition temperature.

Since sodium nitrate is a compound obtainable in a state of high purity, which has an extended gradual transition, it has been regarded as a particularly suitable system for testing certain theories and relations proposed for higher order transitions.[19] Therefore this phase transition has been studied by many techniques such as thermal expansion, DTA, heat capacity, DC electrical conductivity.[4] However, these are unable to provide any structural information. X-Ray diffraction is the best technique to examine this gradual transition. For a comprehensive discussion of this matter see the papers of Antao et al.,[20, 21] Ballirano,[22] and Harris[23] and references therein.

As Antao et al.[20] described, and also according to Harris,[23] there is a lot of work devoted to the phase transition of calcite and the related mineral $NaNO_3$. More than 80 works have been published in this field (see reference therein). Transitions are of interest because $CaCO_3$ and $NaNO_3$ are both chemically and structurally very simple materials, but attempts to assign the transitions to standard models have been unsuccessful.[23] Across the transition, a reduction of the c axis occurs such that **c** ($R\bar{3}m$) = 1/2**c** ($R\bar{3}c$). In the high-temperature phases, both $CO_3$ and $NO_3$ groups are orientationally disordered around their threefold axis parallel to the **c** axis.

In an interesting paper, Harris[23] sums up the two possible models for this second order transition: the 'free rotation' model first proposed by Kracek[24] and the 'two-position disorder' first proposed by Ketalaar[25]. Harris assimilated the free rotation model to the XY model, where a magnetic dipole can take any orientation in the x-y plane perpendicular to the z axis; on the other hand, the author adapted the two position disorder model to the standard Ising model. The author combined the data of Schmahl and Salje[26] and Payne et al.[27] to increase the precision of the results. According to

Harris the two dimensional XY model is consistent with the birefringence studies carried out by Poon and Salje[28] and with the spontaneous strain data published by Reeder.[29] Thus, he arrived to the conclusion that all the experimental data is consistent with the two dimensional XY model. Conversely, Ballirano[22] recollected high quality T-XRD data for $NaNO_3$ and made an excellent discussion for all the structural models that had been proposed so far. He concluded that no univocal indication on the transition mechanism can be extracted from the analysis of the spontaneous strain alone. Molecular dynamics of the phase transition have been performed by Liu et al.[30] and Lynden-Bell et al.[31] Both works agree that the phase transition starts out with $NO_3$ ions rotation around the 3 – fold axis in the **ab** plane. Therefore, XY transition model gained force.

Rysiakiewicz-Pasek et al.[32] studied the order disorder transition in a nanocomposite materials based on porous glasses with average pore diameters of 320, 46 and 7 nm. The authors found that decreasing the crystal size results in decreasing de transition and melting temperature.

### 1.3.2. Crystal growth.

$NaNO_3$ crystal growth has not been widely studied over the years. The earliest research found was made by Sipyagin and Chernov[33] who measured the crystal growth as a function of temperature (273 K – 323 K) at a constant supercooling of $T\text{-}T_{eq} = 0.3$ K. They found that the growth rate (R) of a single crystal face was always below 12 µm/min. They highlighted a succession of hills and valleys in the T - R rplot. Following these experiments, Kiryanova[34] explained them by a determination of a non-monotonic solubility curve in sodium nitrate. The author also found that $C_{16}H_{33}NC_5H_5Br$ has a great effect on equilibrium temperature, in contrast, a trace impurity of polyvinyl alcohol hardly affects this temperature.[35] In the same way Franke et al.[36] found that $NaNO_3$ solubility decreases exponentially when $HNO_3$ is added and that $NaNO_3$ growth rate increases considerably. Kirkova and Nikolaeva[37] measured the growth rate of faces of nitratine as a function of the flow rate at different supersaturations. Their results were essentially in agreement with those of Sipyagin and Chernov.[33] Two drawbacks affected these measurements: firstly, the indexes of the growing faces were ambiguous in both cases and, secondly, neither of these two researchers measured an isothermal growth rate that is necessary to discriminate the

$NaNO_3$ crystal growth mechanism. However, Treivus[38] pointed out that the $NaNO_3$ solution growth proceeds according to the dislocation mechanism in a free convection regime.

Jones and Larson[39] characterized statistically the growth rate dispersion of secondary nuclei. They used a 5 ml isothermal chamber for growing experiments under a microscope. The initial growth rate they measured was about 20 µm/min. Jones et al.[40] studied the strain in $NaNO_3$ secondary nuclei as a function of supersaturation. These authors report that the strain effect in the growth rate is more pronounced at high than at low supersaturation. The authors determined the growth rate with laser interferometer equipment and proposed the Burton Cabrera and Frank (BCF) model even though they did not work in isothermal conditions. The face growth rate results were between 0.6 and 6 µm/min depending on the relative supersaturation. Furthermore, Jones and Larson[41] developed a model which predicts the dependence between growth rate and dislocation density and strain. Ristic et al.[42] used Michelson interferometry to investigate the growth rate of strained crystal by means of synchrotron radiation. They exposed that sodium nitrate is a ductile material so that the growth of 150 µm of new crystalline matter is enough to recover its normal growth rate, i.e. equivalent to a non-irradiated crystal. Ristic et al.[43] also studied the influence of tensile strain on the growth behaviour. In this case they used a special cell where tensile strain can be applied during the growth. According to these authors the application of tensile strain led to a decrease in the growth rate. The growth rate published was about 5 µm/min at a supersaturation $\sigma = 0.004$.

As can be read in chapter 3, we constructed a device in order to study isothermal $NaNO_3$ crystal growth. We have worked at $\sigma < 0.005$ to avoid unwanted nucleation; the growth rate we measured on {104} form was always below $R_{104} < 2.5$ µm/min. Growth rate results are in the same order of magnitude as those of Ristic et al.,[42] however calculated supersaturations differed indicating that a crossover holds. Finally, we concluded that the growth mechanism depends on the relative position of a (equivalent) face in respect to the flow direction. This is the subject of a paper[44] Furthermore in chapter 4 we demonstrate how the growth rate of {104} decreases abruptly by the addition of $LiNO_3$ or $KNO_3$ impurities. This will be the subject of a forthcoming paper.[45]

Graber et al. studied the mass transfer and growth in industrial crystallization[46] and found a diffusion controlled growth in a perfect stirred industrial tank. And, finally,

Oosterhof et al.[47] experimented with isopropoxyethanol-water mixtures to find that the same morphology appears using this solvent.

The crystal growth of $NaNO_3$ efflorescence has been studied by Zehner and Arnold[48] and by Lu et al.[49] They described the four phases of sodium nitrate crystallization from water solution. First, perfect crystals were formed immersed in solution. Second, a granular crust of small isometric crystals appeared at the solution border and spread outwards (efflorescence). Third, if the substrate is porous, a fibrous crust was formed. And, finally, some thin, straight whiskers occasionally grew on almost dry crust.

Concerning the growth from the melt, Komnik and Startsev[50] and references therein, grew $NaNO_3$ single crystals. More recently, Gopalakrishnan et al.[51] were able to grow 40 x 10 mm cylindrical $NaNO_3$ single crystals from the melt with a specially designed strip heater by a travelling zone method with a dislocation density of about $10^3$ - $10^4$ $cm^{-2}$. Anilkumar et al.[52] suppressed the thermocapillary oscillations by using high-frequency end-wall vibrations in floating half-zones. They observed that by generating a sufficiently strong streaming flow the thermocapillary oscillations could be quenched everywhere in the melt zone. Lan et al.[53] used a horizontal Bridgman furnace to grow large sodium nitrate crystals. They also simulated the crystal growth of sodium nitrate with a multigrid finite volume calculations. The authors observed that both the buoyancy and the Marangoni flows were dominant in the melt causing a highly concave interface. As a result, $NaNO_3$ single-crystal growth is very difficult. Sawada and Shichiri[54] found that $NaNO_3$ crystals growing from the melt developed a non-faceted morphology at low subcooling and dendritic behaviour at higher subcoolings.

### 1.3.3. Morphology.

In chapter 3 we study the crystal morphology obtained from pure aqueous solution. We found that single {104} rhombohedral crystals systematically grows in this condition, while {001} truncated rhombohedra were obtained in the presence of K and Li ions in the mother solution, a preliminary study has been published.[55] Following with impurities Punin and Fanke[56] reported that the addition of $(NH_4)_2Mo_2O_7$ results in the development of curved {001} pinacoid faces on $NaNO_3$ crystals. The authors also noticed that some impurities ($KH_2PO_4$, $KHSO_4$, KF, LiCl, and $KIO_8$) give rise to the formation of the pinacoid.

The athermal equilibrium morphology taking into account the surface energy calculated in chapter 2 is a simple cleavage rhombohedra. It is reproduced here (Figure 4)

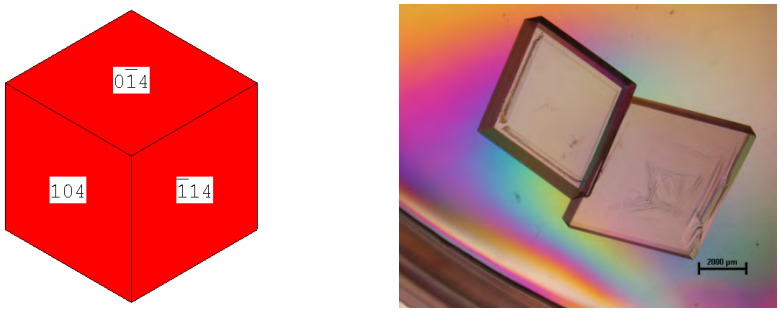


**Figure 4.** Theoretical[13, 55] and experimental morphology[44] of $NaNO_3$.

## 1.4. POTASSIUM NITRATE

### 1.4.1. Crystal structure, polymorphism and phase transition.

According to Rao et al. review[4] potassium nitrate exists in three polymorphic forms at atmospheric pressure. Form II (α-$KNO_3$, orthorhombic Pmcn, aragonite type with **a** = 5.414 Å, **b** = 9.164 Å and **c** = 6.431 Å) is stable at 299 K. On heating, phase II transforms to phase I (β-$KNO_3$, rhombohedral $R\bar{3}m$, calcite type with **a** = 5.42 Å and **c** = 19.41 Å at 425 K) stable at 403 K. In contrast, on cooling, phase II transforms to a ferroelectric phase III at 397 K (γ-$KNO_3$, rhombohedral, R3m with **a** = 5.43 Å and **c** = 9.112 Å at 388 K). The cycle is closed when phase III transforms to phase II at 383 K.

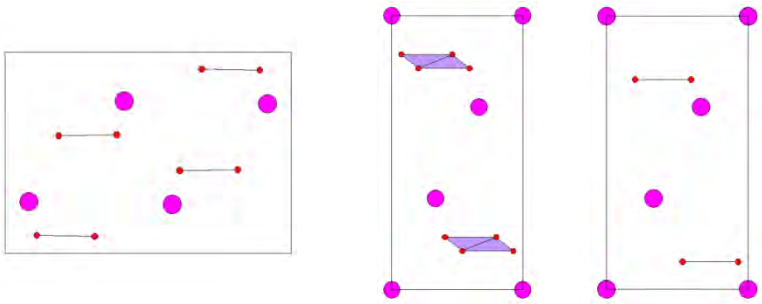

**Figure 5.** Left: α-$KNO_3$ crystal structure.[57] Middle: β-$KNO_3$ crystal structure.[58] Right: γ-$KNO_3$ crystal structure.[58]

In α-$KNO_3$, the stacking sequence is ABCABC…, where A is a K layer and B and C are $NO_3$ layers. Obviously, in order to maintain the electrical neutrality, the number of $NO_3$ groups in each layer is half that of K ions in each layer. Adiwidjaja and Pohl[59] recently reported that α-$KNO_3$ is better described as a superstructure with the $Cmc2_1$ space group (which is a subgroup of the Pmcn space group generally accepted in literature). In contrast, for β-$KNO_3$ the stacking of $NO_3$ and K layers is similar to that of I-$NaNO_3$.[57] In β-phase a vibrational disorder of $NO_3$ is a more plausible form of disorder than the rotation in the plane about the nitrogen atoms,[4] this group is not coplanar i.e. the four atoms in $NO_3^-$ group do not lie in the same plane.[58] Finally, in the γ-$KNO_3$ phase the stacking is similar to that of the β-$KNO_3$ phase, but in this case the $NO_3$ groups are not located half way between the K layers. All these facts can be observed in figure 5. The permanent dipole in γ-$KNO_3$ phase is believed to be due to the

displacement of the nitrate ion from the centre of the unit cell. Then, ferroelectricity in $KNO_3$ is due to the ordering of permanent dipoles.[4] Finally, Fermor and Kjekshus[60] claimed to have found another phase at temperatures below 213 K but unfortunately could not determinate the space group.

Nimmo and Lucas studied in detail the three forms that can be obtained at normal pressure by synchrotron or neutron radiation.[57, 58] They give comparable values to those reported in the Rao et al. report,[4] except for **c** parameter in β-$KNO_3$ which is practically halved. These authors[57, 58] reported that γ-$KNO_3$ could be only achieved upon cooling. However, Freney et al.[61] recently claimed to have obtained γ-$KNO_3$ phase at room temperature and pressure by an atomizing process, in this method the crystals obtained were oriented and stable unless mechanically disturbed. Viedma et al.[62] were able to crystallize β-$KNO_3$ at 20ºC when using more than 2.45 % (w/w) of $NaClO_3$. Finally, Tuech and Combet[63] studied the crystallization of $KNO_3$ by thermal analysis and arrived at the conclusion that a simultaneous crystallization of α-$KNO_3$ and γ-$KNO_3$ phases existed for concentrations higher than 5.52 m. Then the metastable solid phase γ-$KNO_3$ transformed into the stable one α-$KNO_3$ with time. A more recent work performed by Laval et al.[64-66] with a newly developed microfluidic device gave essentially the same results. Even more, the authors were able to determine the solubility curves for both polymorphs.

As a function of pressure, potassium nitrate has seven polymorphic forms.[67] Only pressure IV-$KNO_3$ structure was determined by Worlton et al.[68] Aquino-Olivos et al.[69] determined a P-T phase diagram from 250 K to 650 K and up to 100 MPa with a scanning transiometre. It was similar to that depicted in Adam et al.[67] The authors proposed $KNO_3$ as a reference substance for high pressure and high temperature studies by scanning transitiometry. Potassium nitrate has also been proposed as a temperature standard in differential scanning calorimetry.[70]

$KNO_3$ phase transitions have been studied by many techniques such as, IR spectroscopy,[71-73] thermo-Raman spectroscopy,[74] magic angle spinning NMR spectroscopy,[75] dielectric and dilatometric measurements,[76] calorimetric techniques,[77-80] thermobarometric measurements,[81] acoustic techniques,[79, 82, 83] and X-Ray diffraction.[84] Additionally, theoretical works have also been published.

Some more comments should be made about the relationship of $KNO_3$ phases. As the high temperature form has been described to have an $NO_3$ rotational disorder,[4]

α-$KNO_3$ → β-$KNO_3$ transition can also be considered as an order-disorder transition, in contrast to $NaNO_3$ described above, $KNO_3$ transition is a first order transition.[85] α-$KNO_3$ → β-$KNO_3$ transition seems to be the less problematic and references appear to point at a single temperature transition. Nonetheless, Asadov et al.[86] claimed that the α-$KNO_3$ → β-$KNO_3$ transition is reversible when working at the temperature range between 400 K and 397 K. Kawashima et al.[87] reported an anomalous temperature dependence of ultraviolet absorption spectra near the transition point. They linked this result to anomalies in the dielectric constant and lattice constant of $KNO_3$. Moreover, Nagase et al.[88] discovered a change in Brillouin shift, line width, and mode number on heating during α-$KNO_3$ → β-$KNO_3$ transition. Consequently, the authors appealed to have found an "intermediate phase". Additionally, Cornelison et al.[89] established that $KNO_3$ shows significant reflection losses as the temperature is raised toward the order/disorder transition temperature of 401 K. They proposed that the "induced" dipole moments become increasingly disordered.

In this system the most studied form was γ-$KNO_3$ because it is ferroelectric, though it is metastable. Therefore, many efforts have been put forward to stabilize γ-$KNO_3$ phase at room temperature and to understand γ-$KNO_3$ → α-$KNO_3$ transition behaviour in pure systems,[90] as well as into porous glasses,[76, 91] molecular sieves,[92] nonporous alumina,[93] and different polymer-$KNO_3$ films.[94-97] Fermor and Kjekshus[98] highlighted that when $KNO_3$ is heated above 473 K it recrystallizes, increasing the complexity of the subsequent γ-$KNO_3$ → α-$KNO_3$ transition on cooling. This result is supported by the work of Muntasell et al.[81] They realized that upon cooling, the β-$KNO_3$ phase transforms into γ-$KNO_3$ somewhere between 397 K and 373 K. Rao et al.[4] reported that this temperature is different when a dried or moist sample is analysed. However, Muntasell[77] concluded that the apparition of γ-$KNO_3$ was independent of humidity. When crystals are cooled from temperatures above 453 K, γ-$KNO_3$ always appears, but it does not appear when crystals are heated from the α-phase.[2] Nimmo and Lucas[58] found that the γ-$KNO_3$ phase could be cooled at room temperature and remain stable for approximately 30 minutes. Indeed, the stability of the γ-$KNO_3$ phase depends on the preparation, particle size, thermal history, impurities in the sample,[99] and the cooling rate.[84] According to Westphal[100] and references therein the temperature of γ-$KNO_3$ → α-$KNO_3$ transition may be affected by sample geometry, temperature scan

rate, impurities, stress effects, defects or thermal history of the sample. Additionally, hydrostatic stress may be responsible for the extended γ-$KNO_3$ phase stability in small particles.[90]

From the theoretical point of view, Swaminathan and Srinivasan[101] described the three polymorphic transitions as martensitic like transformations and twinning of the parent phase. Lu and Hardy[102] performed molecular dynamics that closely simulated the α-$KNO_3$ → β-$KNO_3$ and the γ-$KNO_3$ → β-$KNO_3$ phase transitions. They reported that both transitions are initiated by the rotation of the nitrate ions about their triad axes. Erdinc and Akkus[103] performed ab-initio calculations using DFT theory of the electronic band structure and optical properties of the ferroelectric γ-$KNO_3$ phase. Dieguez and Vanderbilt,[104] and references therein, presented a theoretical study of the structural behaviour of γ-$KNO_3$ phase. They concluded that the polarisation reversal mechanism is accompanied by a 60º rotation of nitrate group. Aidynol et al.[105] performed ab inito calculation to find that interactions within the $NO_3$ groups are covalent while the ionic interactions occurred between the negatively charged nitrate group and potassium cations. They compared the structures with that of calcite. Rao et al.[4] summed up that paraelectric to ferroelectric transition (β-$KNO_3$ → γ-$KNO_3$) was interpreted as being due to the electrostriction effect. As was determined by Raman scattering[74] the α-$KNO_3$ → β-$KNO_3$ transition is of sudden nature, but the limits between γ-$KNO_3$ and β-$KNO_3$ phases may be less precise than those in the α-$KNO_3$ → β-$KNO_3$ transition. Finally, γ-$KNO_3$ → α-$KNO_3$ phase transition probably occurs more gradually than the other two transitions.

### 1.4.2. Crystal growth.

Chernov and Sipyagin[5] determined the growth rate of (111) and (110) faces of $KNO_3$ at growth temperature between 296 K – 298 K. The authors found a decrease in the growth rate for the same faces in a ternary system $KNO_3$-$NaNO_3$-$H_2O$. Franke and Treivus[36] found that the solubility curve passes through a minimum with the addition of nitric acid. Kipp and Lacmann[106] measured the growth rate of (110) face by SFM with DOW FAX 3B2 additive, they investigated the influence of the concentration of the additive and of the supercooling. Rolfs et al.[107] were able to study the face specific crystal growth of up to 6 faces. The growth rate published by these authors have a

maximum deviation of about two orders of magnitude in respect to other researchers[108, 109] mainly because of different experimental conditions but also due to the crystal quality. Kipp et al.[110] investigated further the influence of some additives in the growth rate and habit of $KNO_3$. They demonstrated that a minimum concentration of additive is necessary to lower the growth rate of some faces and, thus, change the growth habit. Pradell[111] in his master thesis studied the isothermal crystal growth and dissolution of potassium nitrate single crystals in pure solutions and in the presence of calcium nitrate. He varied both the supersaturation and the flow rate of the solution and established that calcium nitrate decreases the growth rate of potassium nitrate. The author pointed out a high dispersion in crystal growth from different experiments. This is also in accordance with a previous work by Tanneberger et al.[112] who found that $KNO_3$ crystal growth in an industrial crystallization can be described by a random fluctuation model. Herden and Lacmann[108, 113] went further and investigated the effect of different treatments on face-specific growth rate of $KNO_3$ crystals, they concluded that mechanical stress may be a possible reason for the growth rate dispersion. Even more, they pointed out that a random fluctuation model can describe the system for supersaturations $\sigma > 0.001$. Rolf et al.[107] also arrived to the conclusion that $KNO_3$ crystal growth may be described by the random fluctuation model. However, in some experiments they found that $KNO_3$ follows the constant crystal growth model. This is in accordance with a paper by Wang and Mersmann[114] who concluded that each crystallite have its own constant crystal growth rate. Similarly, Huang et al.[115] found a linear growth rate model. On the contrary, Graber et al.[46] described a diffusion controlled growth in a perfect stirred industrial tank. Herden and Lacmann[113] studied the perfection of crystals, obtained by an evaporation method, by etch pit densities and microhardness measurements. Finally, Zarkadas and Zircar[116] established that the best procedure to have a narrow and reproducible crystal size distribution was by operating schemes that included feed recycling, once through, and solid hollow fibre crystallizer-completely stirred tank (SHFC - CST) in-series operation mode. With this setup a mean size between 100 µm and 150 µm could be achieved, this means 3 - 4 times lower than those of MSMPR (mixed suspension mixed product removal) crystallizers.

Soltzberg et al.[117] investigated the formation of dendrites of $KNO_3$ by growing crystals in a thin layer of saturated solution. They found, as expected, that dendrites are formed at high subcooling and that <031>, <041> and <051> are the preferred crystallographic directions for dendritic growth.

Fujiwara et al.[118] have grown an oriented crystal (along **a** parameter) under an 80 kOe magnetic field with a temperature decrease method.

### 1.4.3. Morphology.

$KNO_3$ crystal morphology has been investigated from both experimental[119] and theoretical[120] points of view by Van der Voort. Experimentally, the author found that the growth habit changes as the crystallization temperature is risen, maintaining the same subcooling of $T_{eq} - T_{growth} = 0.15$ K. The most important forms in $KNO_3$ crystals grown below 32 ºC are {110}, {111}, {010} and the {021} forms. Conversely, at higher temperatures the author experimentally found up to 6 faces. Van der Voort assumed that this difference is due to the water adsorption. Soltzberg et al.[121] calculated the late-growth morphology using only coulombic interactions. They described a good agreement between the calculated and the experimental morphology of $KNO_3$. Rolf et al.[107] also calculated the surface tension of up to 10 different faces of $KNO_3$ using only coulombic potential and three different negative charges on the oxygen atom. Results are reproduced here in figure 6.

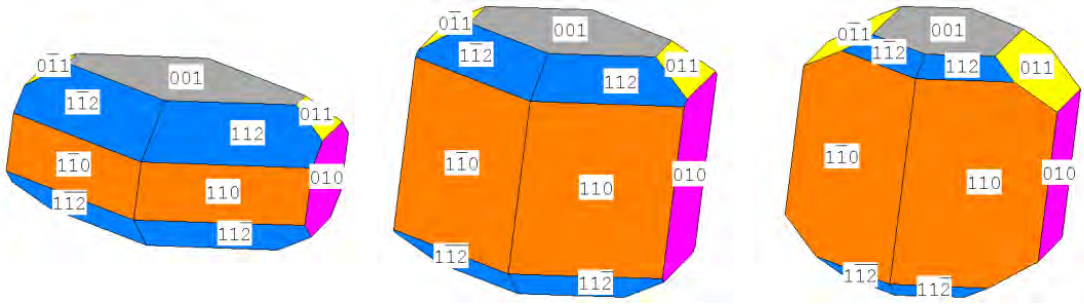


**Figure 6.** Morphology of the $KNO_3$ crystal for a different negative charge onto oxygen atoms: left: $-0.\bar{3}$; middle:$-0.8\bar{3}$; and right:$-1.\ \bar{3}$. According to Rolf et al.[107]

Lovvik et al.[122] calculated the surface stability of different $KNO_3$ faces by *ab initio* DFT procedure arriving to the result that {001} form has the lowest surface energy. When drawing the shape, with unrelaxed values of surface energy, a simple parallelogram {100}, {010} and {001} is obtained. If we use relaxed values, the {110} form also appears. The equilibrium shape is quite different from that proposed by Rolf et al. It is depicted in figure 7 for relaxed values. Conversely, when we simulate the

growth shape by the BFDH method we find a completely different shape where only the {110}, {011} and {010} forms appear (figure 8).

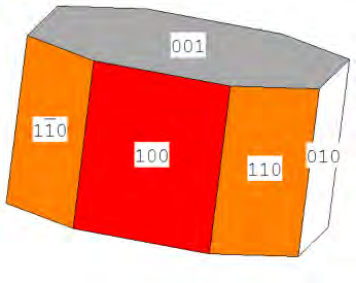


**Figure 7.** Equilibrium form of the $KNO_3$ crystal according to Lovvik.[122]

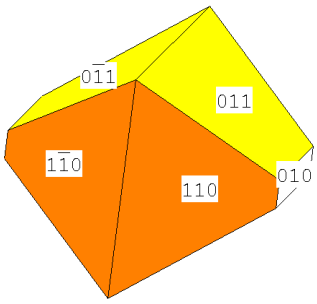


**Figure 8.** Growth morphology according to the BFDH approach.

## 1.5. RUBIDIUM NITRATE

### 1.5.1. Crystal structure, polymorphism and phase transition.

As Rao et al.[4] reviewed, it was established by X-Ray diffraction, DTA, dilatometric, calorimetric, electrical conductivity and optical measurements that $RbNO_3$ undergoes the following phase transformations:

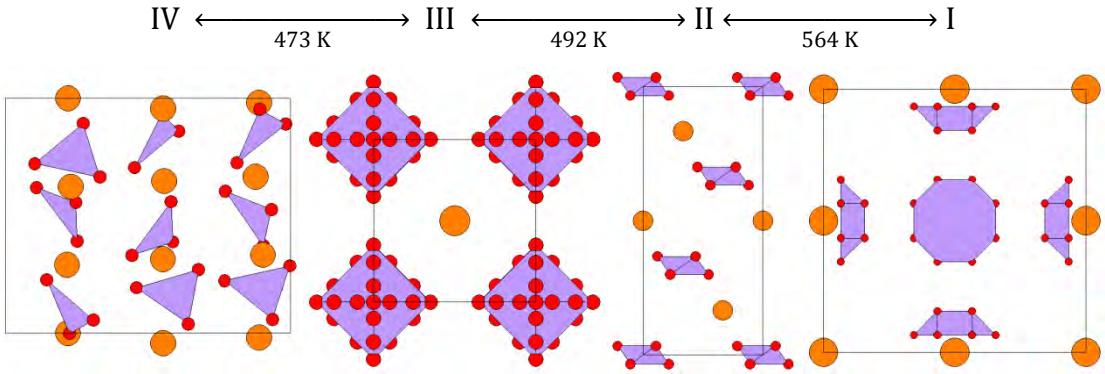


**Figure 9.** $RbNO_3$ phases and its transition temperatures according to Rao at al.[4] IV-$RbNO_3$ after Pohl et al.[124] and III-$RbNO_3$, II-$RbNO_3$, and I-$RbNO_3$ after Ahtee et al.[123] and Unit cells are not at the same scale.

Phase IV, the low temperature form, is trigonal $P3_1m$, with Z = 9, **a** = 10.479 Å and **c** = 7.452 Å, at 298 K.[4] Shamsuzzoha and Lucas[125] pointed out that IV-$RbNO_3$ is isostructural with II-$CsNO_3$. The authors describe the structure as having nine Rb based pseudocubes inside the cell with the $NO_3$ groups enclosed. The nitrate groups are closely planar and there is no evidence of rotational disorder. Zhou et al.[126] using magic angle NMR experiments arrived at the conclusion that only one independent nitrate is in the IV-$RbNO_3$ phase unit cell. They obtained and adjusted the cell by DFT calculations.

It was reported by Rao et al.[4] that III-$RbNO_3$ phase is cubic (CsCl type) with **a**= 4.36 Å and Z = 1 or with a double cell **a** = 8.72 Å and Z = 2, furthermore in this phase $NO_3$ ion has a free rotation. On the contrary, Shamsuzzoha and Lucas[127] reviewed that the III-$RbNO_3$ phase is better described by nitrate eight fold orientational disorder. This means that each cell has a simple nitrate orientation because in this structure the entropy is not high enough to have a free rotation of the nitrate group. Additionally, Ahtee and Hewat[123] studied phase III-$RbNO_3$ by powder neutron diffraction and concluded that III-$RbNO_3$ phase (from 437 K to 492 K) has a cubic CsCl-structure, $Pm\bar{3}m$, with one

molecule per unit cell (Z = 1); the authors had a preference for the 12 fold orientational disorder for the nitrate group (see figure 9). Thus, three models are proposed for the description of III-$RbNO_3$ structure. Moreover, the work performed by Shinnaka and Yamamoto[128] suggests that the orientational disorder of $NO_3$ ions did not show an anomaly associated with the dielectric constant in the vicinity of the transition to the higher temperature phase (II-$RbNO_3$), but showed a pre-transformation effect towards the lower temperature phase (IV-$RbNO_3$).

According to Rao et al.[4] phase II-$RbNO_3$ is rhombohedral with **a** = 4.8 Å and $\gamma = 70^{\circ}\ 28'$ around 520 K, with Z = 1. However, Ahtee and Hewat[123] and Stromme[129] determined that the II-$RbNO_3$ phase has a rhombohedral unit cell with space group $R\bar{3}m$. Ahtee and Hewat[123] and Yamamoto et al.[130] agreed with this space group choice and proposed an aragonite-type disorder, as is depicted in figure 9. On the contrary, Shamsuzzoha and Lucas[131] preferred a body centred cubic structure (**a** = 8.84 Å, Z = 8 at 517 K).

Phase I is cubic, (NaCl type) with a = 7.32 Å at ~ 573 K with Z = 1 according to Rao et al.[4] Ahtee and Hewat[123] published similar results: I-$RbNO_3$ phase is stable in the region 557 K - 583 K, it has a cubic NaCl-type unit cell, $Fm\bar{3}m$, with Z = 4.

Pohl et al.[124] asserted to have found another phase that is stable at least from 346 K (DTA measurement) to 437 K. Although Fermor and Kjesus[132] report a phase transition at 228 K detected by electric conductivity measurements, Owen and Kenard[133] argued that the anomalous electrical behaviour may be only due to thermal history and that there is not another phase at low temperatures.

Finally, Shamsuzzoha and Lucas[127] explain the difficulties of obtaining good single crystals of phase II and I. Therefore, their structures remain unresolved by single crystal diffraction.

Regarding phase transitions, Rao et al.[4] pointed out that observing with light microscopy on heating from phase IV-$RbNO_3$ to III-$RbNO_3$, the crystals become isotropic, then passing III-$RbNO_3$ → II-$RbNO_3$ transition results in cracking of crystals and become anisotropic again. Around 563 K, crystals become isotropic without further distortion. Using X-ray diffraction studies it can be explained that IV-$RbNO_3$, III-$RbNO_3$ and II-$RbNO_3$ phases are related and the transition between them appears to involve changes in positional randomization of Rb. However, Ahtee and Hewat[123] pointed out that these transformations seemed to be associated with change in

orientational disorder of the nitrate group. The free rotation disorder had been definitively excluded in any phase. In contrast, I-$RbNO_3$ phase is not related with the others, and the transition II-$RbNO_3$ → I-$RbNO_3$ does not imply this randomization.

Kawashima et al.[134] studied the temperature and frequency dependence of AC conductivity of IV-$RbNO_3$, III-$RbNO_3$ and II-$RbNO_3$ phases along **b**-axis[135] and **c**-axis,[136] they found anomalies near the transition points for all three transitions. They also studied the optical properties near the transition.[137]

Shamsuzzoha and Lucas[127] proposed that IV-$RbNO_3$ → III-$RbNO_3$ and III-$RbNO_3$ → II-$RbNO_3$ phase transitions were accomplished by very small changes of the Rb atom sublattices from pseudocubic to cubic. The $NO_3$ groups in these structures change from being orientationally ordered to disordered and have a similar 8-fold anion-cation coordination. This was consistent with the molecular dynamics simulation of IV-$RbNO_3$ → III-$RbNO_3$ phase transition performed by Liu et al.[138] who found that the transition is initiated by an in-plane rotation of $NO_3$ ions: nitrate groups remained planar; there is not a free rotation.

According to Shamsuzzoha and Lucas[127] II-$RbNO_3$ → I-$RbNO_3$ phase transition did not have a simple unit cell relationship. However, Yamamoto et al.[130] proposed that the coupling between the orientation of anions and shear strain played an important role in this phase transition, both structures having an 8-fold orientational disorder.

Additionally, Chary and Reddy[139] and references therein studied the ionic conductivity versus the temperature. They noticed an increase in conductivity in IV-$RbNO_3$ → III-$RbNO_3$ and II-$RbNO_3$ → I-$RbNO_3$ phase transitions while for III-$RbNO_3$ → II-$RbNO_3$ phase transitions there was a decrease. These changes correspond to an increase and decrease in symmetry, correspondingly. Furthermore, Charsley et al.[3] made a careful calorimetric investigation gathering all thermal data about transitions. They also determined the 3 equilibrium temperatures for the transitions, being 438.0 ± 0.1 K (IV-$RbNO_3$ →III-$RbNO_3$ phase transition), 495.3 ± 0.5 K (III-$RbNO_3$ → II-$RbNO_3$ phase transition) and 557.1 ± 0.1 K (II-$RbNO_3$ → I-$RbNO_3$ phase transition) together with the transition enthalpies.

Finally, Dean et al.[140] and references therein give the high pressure polymorphism of $RbNO_3$.

### 1.5.2. Crystal growth.

Chernov and Sipyagin[5] give the kinetic coefficients, exchange fluxes, and other parameters for the growth of (110) and (100) faces of $RbNO_3$. As far as we know, only Treivus and Franke[141] have studied rubidium nitrate kinetics. They found a linear dependence $V = (8.76 \pm 0.75) \cdot 10^{-7} \cdot \Delta m$ in a temperature range of 301.2 K to 297.6 K for the forms {110} and {100} where $\Delta m$ is the supersaturation expressed in mol/Kg $H_2O$.

### 1.5.3. Morphology.

As far as we know neither experimental nor theoretical morphological studies have been published over the years. Only brief descriptions of experimental habit like that proposed by Franke et al.[36] where a pseudohexagonal habit is described. This habit is in accordance with the BFDH morphology calculated and shown in figure 10.

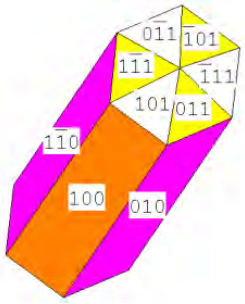


**Figure 10.** $RbNO_3$ morphology calculated by the BFDH procedure.

## 1.6. CAESIUM NITRATE

### 1.6.1. Crystal structure, polymorphism and phase transition.

As Rao et al.[4] described caesium nitrate exists in two polymorphic phases. The low temperature form (phase II, pyroelectric) is hexagonal $P3_1m$, with Z = 9, **a** = 10.87 Å and **c** = 7.76 Å. Lucas[142] pointed out that II-$CsNO_3$ is isostructural with IV-$RbNO_3$. It has $P3_1$ space group with **a** = 10.95(2) Å and **c** = 7.80(2) Å, Z = 9. In this sense, Cs atoms form nine pseudocubes within the unit cell. The $NO_3$ groups are closely planar and enclosed by a Cs atoms pseudocube. There is not any evidence that this phase has a rotational disorder. Pohl and Gross[143] re-determined the II-$CsNO_3$ phase at 296 K by single crystal diffraction. The cell parameters were a little bit different from those reported in the paper by Rao et al. [4] and the space group reported is $P3_1$ (or the enanthiomorph $P3_2$). Pohl and Gross described IV-$RbNO_3$ and II-$CsNO_3$ as isomorphous. As is described later, a complete solid solution between these two compounds is known.[144] In contrast, Zhou et al.[126] using magic angle NMR experiments arrived at the conclusion that only one independent nitrate is in the cell, obtaining an adjusted cell by DFT calculations.

II-$CsNO_3$ phase undergoes a phase transition to I-$CsNO_3$ phase at around 434 K. It is cubic ($Pm\bar{3}m$) with **a** = 4.499 Å with Z = 1 at near 400 K.[4] However, I-$CsNO_3$ phase has also been described with a double cell with Z = 8 and **a** = 8.98 Å belonging to $Pa\bar{3}$ space group.[4] Following the review by Rao et al.,[4] phase I is a slightly distorted version of phase II structure. The structural difference between them is only due to $NO_3$ orientation, Cs ion position being practically the same in both structures. Stromme[129] cited I-$CsNO_3$ as cubic primitive (isostructural with III-$RbNO_3$) containing one molecule of metal nitrate per unit cell. The author discusses two possible structures introducing entropic terms in the same manner as he did with all other alkali nitrates.[11, 145, 146] He concluded that some configurational entropy may exist in this phase.

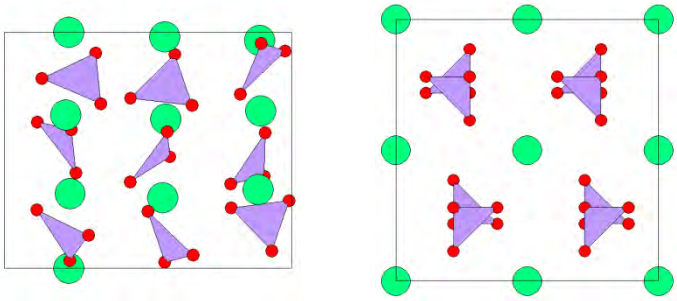

**Figure 11.** $CsNO_3$ unit cell. Left: phase II.[140] And right phase I.[147]

Charrier et al.[148] made a careful calorimetric gathering of thermal data about the transition and also determined the equilibrium temperature for the transition, being 427.1 ± 10.1 K together with the transition enthalpy. These authors[149] found an anomaly in the electric constant near the phase transition. Similarly, Kawashima et al.[150, 151] performed conductivity measurements from room temperature to the melt; they found a discontinuity in the phase transition. Moreover, Tagaki et al.[152] studied the phase transition by Brillouin scattering and concluded that II-$CsNO_3$ is a real ferroelectric phase. Along these lines, Nautiyal et al.[153] prepared polyvinyl alcohol cesium nitrate composite films in order to study its ferroelectric properties. Liu et al. [138] performed molecular dynamics through the phase transition and found that it is initiated by out of plane rotation of the nitrate group, thus, the transition mechanism is slightly different from IV-$RbNO_3$ → III-$RbNO_3$ phase transition even if both the low temperature (IV-$RbNO_3$ and II-$CsNO_3$) and the higher temperature (III-$RbNO_3$ and I-$CsNO_3$) forms of these nitrates are isomorphous.

Finally, Dean et al.[140] and references therein studied the high pressure polymorphism of $CsNO_3$. We highlight the three high pressure polymorphs of $CsNO_3$ found by Kalliomäki and Meisalo.[154] These are III, IV and V-$CsNO_3$ phases, all three phases presented the same Pmmn space group but with different axial ratios.

### 1.6.2. Crystal growth.

Chernov and Sipyagin[5] studied the kinetic coefficients, exchange fluxes and other parameters for the growth of (110) and (100) faces of $CsNO_3$. As far as we know, only Treivus and Franke[141] have studied rubidium nitrate kinetics. They found a linear

dependence $V = (17.97 \pm 1.45)\cdot 10^{-7}\cdot \Delta m$ in a temperature range of 299.3 K to 297 K for the forms {110} and {100} where $\Delta m$ is the supersaturation expressed in mol/Kg $H_2O$.

### 1.6.3. Morphology.

As far as we know neither experimental nor theoretical morphological studies have been published over the years. There are only brief descriptions of experimental habit like that proposed by Pohl[143] that describe the crystal as hexagonal shaped **c**-axis needles. The BFDH calculated morphology is exactly the same as $RbNO_3$ because they are isostructural (isomorphs) materials.

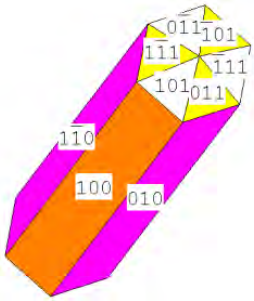


**Figure 12.** BFDH calculated shape for $CsNO_3$.

From this review we can, thus, construct table 1 for the alkali nitrates polymorphism. We summarize here the more relevant data published after the review by Rao et al.[4] which is also included.

Table 1. Crystal data for alkali nitrates polymorphic forms.

| Compound | Form | Space group | a / Å | b / Å | c / Å | Z | T / K | Year | reference |
|---|---|---|---|---|---|---|---|---|---|
| $LiNO_3$ | | $R\bar{3}c$ | 4.692 | | 12.22 | 2 | 298 | 1975 | [4] |
| $LiNO_3$ | | $R\bar{3}c$ | 4.6920 | | 15.2149 | 6 | 298 | 1994 | [10] |
| $NaNO_3$ | II | $R\bar{3}c$ | 5.0696 | | 16.829 | 6 | 298 | 1975 | [4] |
| $NaNO_3$ | II | $R\bar{3}c$ | 5.0655(5) | | 16.577(3) | 6 | 100 | 2000 | [15] |
| $NaNO_3$ | II | $R\bar{3}c$ | 5.0660(5) | | 16.593(3) | 6 | 120 | 2000 | [15] |
| $NaNO_3$ | II | $R\bar{3}c$ | 5.070 | | 16.82 | | 293 | 1972 | [16] |
| $NaNO_3$ | II | $R\bar{3}c$ | 5.07 | | 16.82 | | | 1978 | [155] |
| $NaNO_3$ | I | $R\bar{3}m$ | 5.0889(5) | | 8.868(3) | 3 | 563 | 2000 | [15] |
| $KNO_3$ | II | Pmcn | 5.414 | 9.164 | 6.431 | 4 | 299 | 1975 | [4] |
| $KNO_3$ | α | Pmcn | 5.4119 | 9.1567 | 6.4213 | 4 | 298 | | [57] |
| $KNO_3$ | α | Pmcn | 5.4283 | 9.1849 | 6.5034 | 4 | 373 | | [57] |
| $KNO_3$ | α | $Cmc2_1$ | 10.825 | 18.351 | 6.435 | 16 | 293 | 2003 | [59] |
| $KNO_3$ | α | Pnma | 6.436(1) | 5.430(1) | 9.192(2) | 4 | | | [156] |
| $KNO_3$ | I | $R\bar{3}m$ | 5.43 | | 9.112 | | 388 | 1975 | [4] |
| $KNO_3$ | β | $R\bar{3}m$ | 5.425(1) | | 9.836(4) | 3 | 424 | | [58] |
| $KNO_3$ | III | R3m | 5.42 | | 19.41 | 12 | 425 | 1975 | [4] |
| $KNO_3$ | γ | R3m | 5.487(1) | | 9.156(3) | 3 | 364 | | [58] |
| $RbNO_3$ | | $P3_1m$ | 10.479 | | 7.452 | 9 | 298 | 1975 | [4] |
| $RbNO_3$ | IV | $P3_1$ | 10.067 | | 7.053 | 9 | RT | 2001 | [138] |
| $RbNO_3$ | IV | $P3_1$ | 10.474 | | 7.443 | 9 | RT | 1992 | [124] |
| $RbNO_3$ | IV | $P3_1$ | 10.55 | | 7.47 | 9 | 298 | 1982 | [125] |
| $RbNO_3$ | IV | $P3_1$ | 10.61 | | 7.55 | 9 | 403 | 1982 | [125] |
| $RbNO_3$ | III | $Pm\bar{3}m$ | 4.39(1) | | | 1 | | 1988 | [127] |
| $RbNO_3$ | III | $Pm\bar{3}m$ | 7.32 | | | 1 | | 1971 | [157] |
| $RbNO_3$ | III | $Pm\bar{3}m$ | 4.3718(2) | | | 1 | 1980 | 563 | [123] |
| $RbNO_3$ | | $P3_1$ | 10.474(1) | | 7.443(1) | 9 | 296 | 1992 | [124] |
| $RbNO_3$ | | | 10.506(3) | | 7.469(3) | 9 | 372 | 1992 | [124] |
| $RbNO_3$ | II | | 8.84(3) | | | 9 | | | [131] |
| $RbNO_3$ | II | $R\bar{3}m$ | | | | | 503 | 1980 | [123] |
| $RbNO_3$ | I | $Fm\bar{3}m$ | 7.32 | | | 1 | 573 | 1975 | [4] |

| | | | | | | | | | |
|---|---|---|---|---|---|---|---|---|---|
| $RbNO_3$ | I | $Fm\bar{3}m$ | 7.3150(22) | | | 4 | 568 | 1980 | (123) |
| $CsNO_3$ | II | $P3_1m$ | 10.87 | | 7.76 | 9 | <434 | 1993 | (4) |
| $CsNO_3$ | II | $P3_1/P3_2$ | 10.902(2) | | 7.740(2) | 9 | 296 | 1993 | (126, 143) |
| $CsNO_3$ | II | $P3_1$ | 10.931(2) | | 7.763(3) | 9 | RT | 1984 | (140) |
| $CsNO_3$ | II | $P3_1$ | 10.95(2) | | 7.80(2) | 9 | RT | 1983 | (142) |
| $CsNO_3$ | I | | 4.499 | | | 1 | 400 | 1975 | (4) |
| $CsNO_3$ | I | $Pa\bar{3}$ | 8.98 | | | 4 | 400 | 1975 | (4) |
| $CsNO_3$ | I | $Pa\bar{3}$ | 8.98 | | | 8 | | 1953 | (147) |

## 1.7. SOLID STATE MISCIBILITY AND BINARY PHASE DIAGRAMS

All the phase diagrams between alkali nitrates except $NaNO_3$-$CsNO_3$ have been compiled by Voskresenkaya in 1970.[158] From this compilation we can extract that they were determined by a variety of experimental methods, mainly visual and visual polythermal. Even more, the $NaNO_3$-$KNO_3$ phase diagram is by large the most studied among them with twenty related publications. After this compilation it is worth mentioning the work made by Dessureault et al.[159] in 1990 who made a critical evaluation of the thermodynamic data published up to that moment and extracted a new model to simulate inorganic binary systems. In the paper quoted above we could only find $LiNO_3$-$NaNO_3$, $LiNO_3$-$KNO_3$ and $NaNO_3$-$KNO_3$ but a complete set of the computed phase diagrams can be obtained from the FACTsage web.[6] Figure 13 shows all phase diagrams in a systematic way.

Based on Dessureault's paper[159] we first systematically describe the alkali nitrate binary phase diagrams and solid solutions research done after the quoted paper. And then we try to make a classification.

- $LiNO_3$-$NaNO_3$

Dessurreault et al.[159] proposed that this phase diagram presents a eutectic without a solid solution. Effectively, research by Bélaïd-Drira et al.[160] agreed very well with these results. However, Maeso and Largo[161] questioned whether a flat solidus measured by thermal analysis necessarily indicates a eutectic behaviour.

- $LiNO_3$-$KNO_3$

Dessurreault et al.[159] proposed that this phase diagram presents a eutectic invariant, also without a solid solution. However, Maeso and Largo,[161] as before, questioned whether a flat solidus necessarily indicates a eutectic behaviour. More recent investigations proposed that an equimolar composition $LiK(NO_3)_2$ exists. In actual fact, Xu et al.[162] and Zhang et al.,[163] working with Raman spectroscopy, confirmed a congruent melting point in the system $LiNO_3$-$KNO_3$. Therefore, they proposed two eutectics separated by this congruent melting point. The authors explained that equimolar composition $LiK(NO_3)_2$ only appears in fast cooling conditions without any disturbance. It is a metastable phase at room temperature and decomposes to the

terminal compounds $LiNO_3$ and α-$KNO_3$. The solid solution was only formed by a mixture of $LiNO_3$ and γ-$KNO_3$. These compounds have $R\bar{3}c$ and R3c space groups respectively; therefore the solid solution is more plausible than when α-phase (Pmcn space group) is considered. It appears that this intermediate phase can be stable at high temperature. Unfortunately, we do not have enough information to confirm this hypothesis.

- $NaNO_3$-$KNO_3$

Dessurreault et al.[159] proposed a eutectoid and a minimum of melting point with a complete series of solid solution. Below the eutectoid point a solid solution is formed only for high concentrations of $KNO_3$ (above 90 %). It is by far the most studied nitrate phase diagram within 150 years of history. A thorough study of the $NaNO_3$-$KNO_3$ system can be found in chapter 6 of this PhD thesis. We have demonstrated both experimentally and theoretically a minimum of melting point, an immiscibility gap in the solid state and terminal solid solutions for both components.

- $LiNO_3$-$RbNO_3$

In the FACTsage web page[6] it is depicted with an equimolar congruent melting point, two eutectic invariants, and, finally, no miscibility in the solid state.
Xu[164] presented the congruent melting compound $LiRb(NO_3)_2$. According to Xu, all these three congruent melting compounds ($LiK(NO_3)_2$, $LiRb(NO_3)_2$, $LiCs(NO_3)_2$ have the same crystal structure and the same coordination and nitrate ions environment.

- $NaNO_3$-$RbNO_3$

The FACTsage web page[6] depicted this phase diagram with one eutectic invariant, one peritectic invariant, an incongruent melting point and, finally, no miscibility in the solid state. No more data have been found for this system.

- $KNO_3$-$RbNO_3$

This is the most complex phase diagram for this family of compounds. In the FACTsage web page[6] it is shown that at low temperature there is no miscibility in solid state. Above the first eutectoid there exists a non-stoichiometric compound with a minimum of melting point. For the rubidium rich part there is another eutectoid. Xu[165] reported

that for compositions above 96 % IV-$RbNO_3$ a solid solution exists at room temperature, thus, the phase diagram presented in figure 7 must be changed. The author worked with Raman spectroscopy and assigned the structure of the principal regions of this phase diagram. Unfortunately, he was not able to detect the non-stoichiometric compound. The phase diagram presented in this paper is incomplete.

- $LiNO_3$-$CsNO_3$

The FACTsage web page[6] presented a high temperature equimolar composition congruent melting compound and two eutectic invariants. According to the webpage there is not miscibility in solid state. Drira et al.[166] studied the system by thermal analysis, they found a similar phase diagram. Xu[164] presented the congruent melting compound $LiCs(NO_3)_2$ detected by Raman spectroscopy.

- $NaNO_3$-$CsNO_3$

In the FACTsage web page[6] a simple eutectic without miscibility in the solid state is reported. This phase diagram presents two regions of solid state immiscibility due to $CsNO_3$ phase transition. Jriri et al.[167] reported a similar $NaNO_3$-$CsNO_3$ phase diagram. Finally, they questioned a fundamental aspect: what is the effect of other nitrates in the second order transition of $NaNO_3$? When we take a look in binary systems containing $NaNO_3$ presented here we observe that they are described as a eutectic behaviour except for the $NaNO_3$-$KNO_3$ system. In this last system, phase transition is $KNO_3(\beta)$ + $NaNO_3$ (II) → $NaNO_3$ (I). Then a high temperature solid solution is formed. For the others, the proposed reaction is $XNO_{3(l)}$ + $NaNO_3$ (II) → $XNO_{3(l)}$ + $NaNO_3$ (I).

- $KNO_3$-$CsNO_3$

In the FACTsage web page[6] an eutectic invariant with solid state miscibility in the terminal compositions is stated. Therefore, two eutectoid invariants are also depicted. In contrast, Zamali and Jemal[168] experimentally found a similar phase diagram but only confirmed the eutectoid at high caesium composition. The other was not detected.

- $RbNO_3$-$CsNO_3$

In the FACTsage web page[6] a eutectoid invariant with a total miscibility at high temperature, then a minimum of melting point is proposed.

Secco and Secco[169] demonstated that a terminal solid solution exists at least until 10% of the other component by XRD at room temperature. Moreover, they proposed a somewhat different phase diagram. Unfortunately, they were not able to completely define all transitions by using thermal analysis. Additionally, Wacharine et al.,[144] also working with thermal analysis, gave a detailed description of this phase diagram. According to them it is characterised by a eutectic, two eutectoid, and an azeotropic-like invariants, three limited solid solutions, and a continuous solid solution at high temperature. Therefore, its phase diagram proposition is quite different from that proposed in the factSage web page.[6]

Nasirov et al.[170, 171] and Asadov et al.[171] determined the equilibrium temperature of the transitions IV-III, III-II and in $Rb_{0.975}Cs_{0.025}NO_3$ being 393 ± 0.5 K and 421 ± 0.5 K respectively. They also demonstrated that these transitions are not destructive; they are single crystal to single crystal transitions. These authors[172] continued their work studying $Rb_{0.9}Cs_{0.1}NO_3$ composition. They started with a rhombohedral $RbNO_3$ based solid solution ($P3_1$) which undergoes a transition to a cubic phase ($Fm\bar{3}m$) at 500 K. This, in turn, transforms into a new tetragonal phase at 550 K (I4) which has a transition to a cubic phase ($Fm\bar{3}m$) at 590 K. Therefore, a new phase domain may be introduced in the system.

Nasirov and Asadov[173] studied the formation rate (solid-solid transformations) of α-β-$Rb_xK_{1-x}NO_3$ with x up to 0,1 with perfect faceted single crystals as a function of supercooling. They conclude that the growth of transformation is independent from the composition, but obviously depends on the supercooling.

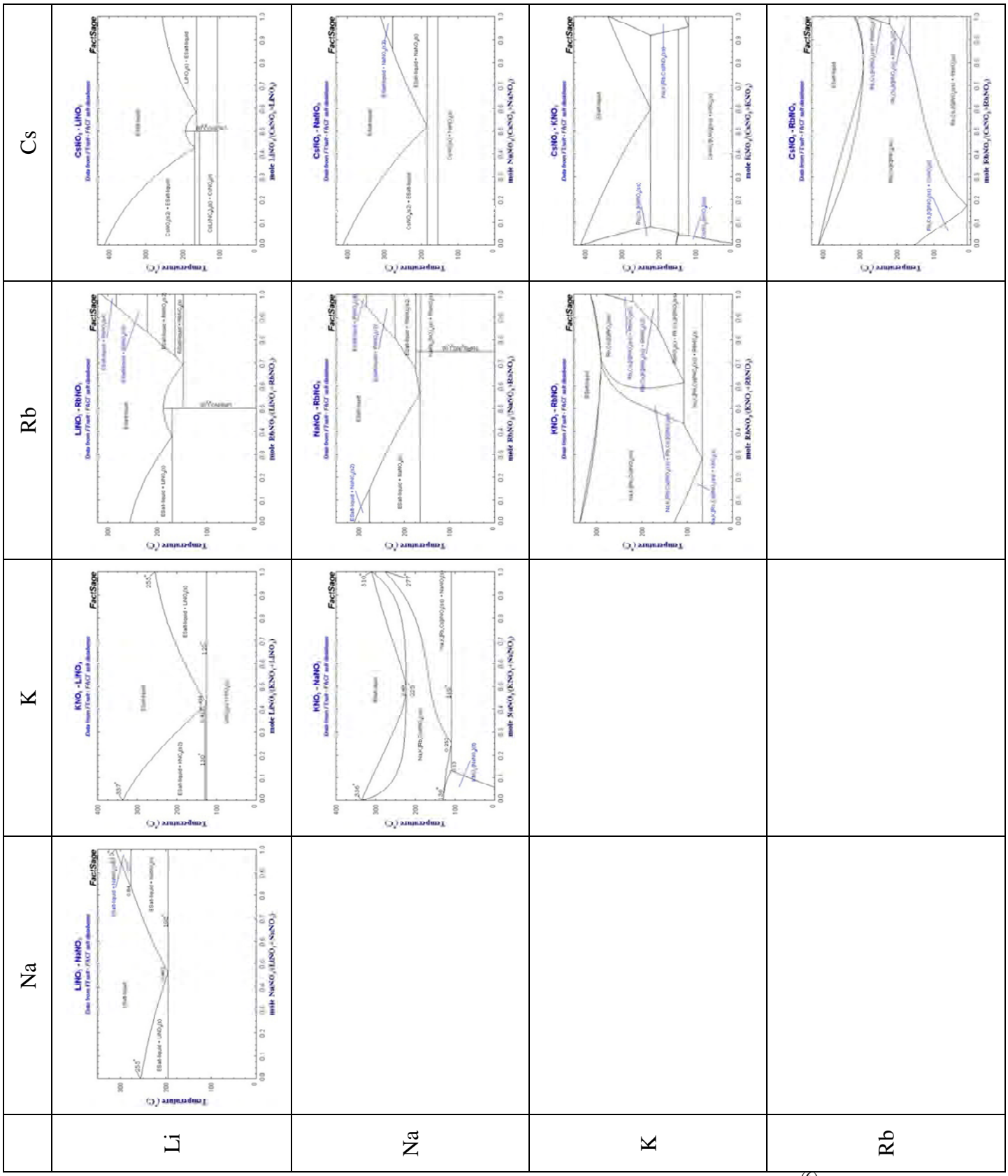


**Figure 13.** Binary phase diagrams of alkali nitrates taken from the FACTsage web page.[6]

## 1.8. DISCUSSION

The polymorphism in alkali nitrates is rich. We find eight different phases at ambient pressure, $RbNO_3$ being the richest with 4 different polymorphs. Evidently, the larger the cation the higher the probability of the nitrate group to be disordered. Notwithstanding, only four out of the twelve phases have been definitively described as being disordered. III-$CsNO_3$ and I-$CsNO_3$ are described as having 12-fold and 8-fold disorder, respectively. Furthermore, many authors have tried to assign to the high temperature polymorphs of $NaNO_3$ and $KNO_3$ either rotational or positional (two-position) disorder. At high temperature (more entropic energy) the disorder in the nitrate group is easier. In this sense, $R\bar{3}c$ phases of $LiNO_3$ and $NaNO_3$ (the two phases) can have some disorder at the highest temperature range of their existence. Additionally, Stromme described all the high temperature forms as being disordered between calcite and aragonite structure type.[11, 129, 145, 146] Therefore, it seems probable that all phases present some disorder. The nitrate group is considered planar in all structures reviewed except for β-$KNO_3$ and II-$RbNO_3$ which are high temperature phases. It is worth noting how $NO_3$ group local symmetry ($D_{3h}$) imposes all phase space groups to have a ternary axis except for α-$KNO_3$. In this phase, we have two non-equivalent oxygen atoms in the asymmetric unit. For $P3_1$ phases of $RbNO_3$ and $CsNO_3$ at room temperature, there are 9 non-equivalent oxygen atoms, in these cases the ternary axes do not pass through any atom, so that equivalent oxygen atoms belong to different nitrate groups (this statement is evident because the nitrate group is planar and the screw axes $3_1$ have a translation of 1/3 **c**). In the rest of the phases, oxygen atoms within a nitrate group become equivalent.
This polymorphic behaviour has repercussions in the phase diagram boundaries. In figure 13 we notice a high dispersion in the behaviour of binary phase diagrams of alkali nitrate. Therefore, we may ask what the reason is. Can we make a systematic classification to predict the binary behaviour? Oonk[174] made a systematic classification of alkali halide series of phase diagram and proposed a rule. He found that the larger the radius difference is the lesser the solubility in the solid state. In this sense, we go from a eutectic invariant with a solid solubility below 1 ppb (at room temperature), through complete miscibility just below the solidus line, to a complete solubility at room temperature. In contrast to alkali halide, where all compounds analysed crystallize in the cubic system at room temperature, seventeen of them have the NaCl structure type ($Fm\bar{3}m$); we have to manage here with different space groups for the components of the

family. We can divide the family of binary phase diagram into three categories depending on the crystalline system at high temperature: both structures are hexagonal, both structures are cubic, and one hexagonal mixed with one cubic structure. We recall *m* as the mismatch parameter defined by:

$$m = \frac{\Delta V}{V_s}$$

where ΔV is the absolute difference between the molar volumes (calculated from crystallographic data) of a complete $XNO_3$ formula and $V_s$ is the smaller of the two volumes. In this case we calculate the molar volume of the high temperature forms from selected crystallographic data given in table 1. Then, the misfit parameters for the binary systems (at different temperatures) are given in table 2.

**Table 2.** Misfit values for alkali nitrate systems.

| m | Na | K | Rb | Cs |
|---|---|---|---|---|
| Li | 0.37 | 0.73 | 1.02 | 0.87 |
| Na | | 0.26 | 0.48 | 0.87 |
| K | | | 0.17 | 0.08 |
| Rb | | | | 0.08 |

In table 2 we have separated the alkali series system according to the high temperature components polymorphs (brown: hexagonal phases; purple: cubic phases; and blue: hexagonal-cubic phases). It is worth remembering that in order to have a complete solid solution, components must have the space group. However, we have experimentally and theoretically demonstrated that $NaNO_3$-$KNO_3$ form a continuous solid solution just below the solidus line (see chapter 6). This situation is also proposed by FactSAGE[6] and depicted in figure 13.

For the hexagonal system compounds we can make a cut-off at m = 0.30. For m < 0.30 we have a complete solid solution. On the contrary, with m > 0.30 we obtain eutectic invariants without appreciable terminal solid solution. Finally, for m > 0.40 an intermediate compound is formed. We have to remember here that $LiNO_3$-$KNO_3$ presents an intermediate compound $LiK(NO_3)_2$[162-164] that probably has an hexagonal symmetry. Therefore, this phase diagram is described by two eutectic invariants.

In the cubic phases of the $CsNO_3$-$RbNO_3$ phase diagram we observe a complete solid solution even though the components do not have the same space group.

For the hexagonal-cubic symmetry phase diagrams we can also impose the same cut-off m = 0.30. In this case, different crystal systems play an important role; we do not expect a total miscibility. However, we propose first, that for m < 0.30 we observe a eutectic with terminal solid solutions. And second, for m > 0.30 we observe a eutectic invariant without a significant solid solution. Finally, when m > 0.40 an intermediate compound exists. It is curious that for larger mismatches an intermediate compound forms. But, taking into account different compounds symmetry, it is possible that an intermediate compound relaxes the system total energy.

We have to make some considerations here about the $KNO_3$-$RbNO_3$ system. In the FACTsage webpage[6] it is described as a minimum of melting point. In this webpage the $CsNO_3$-$RbNO_3$ phase diagram is also simulated as a minimum of melting point. However, Wacharine et al.[144] experimentally demonstrated that the $CsNO_3$-$RbNO_3$ phase diagram has, in reality, a eutectic invariant (among other transitions that we are not interested in). By similarity, we think that the $KNO_3$-$RbNO_3$ phase diagram is not being simulated correctly by FACTsage software. In our opinion, it must be described with a eutectic invariant. Thus, experimental evidences are required to prove this statement.

In summary we can extract the following common conclusions for this whole phase diagram family taking into account the mismatch parameter m:

- m < 0.30 → a complete solid solution if the crystal system is the same, or eutectic invariants with terminal solid solutions when the crystal system is different.
- m > 0.30 → eutectic invariant without solid solution.
- m > 0.40 → eutectic invariant without solid solution and intermediate stoichiometric compound.

At room temperature we obtain 3 kinds of morphologies calculated by the BFDH approach depending on the isostructurallity of nitrates. $LiNO_3$ and $NaNO_3$ compounds have the same growth morphology as calcite (calculated by the same approach).[12] It consist in the {012}, {01$\bar{2}$} and {001} forms. Similarly, $RbNO_3$ and $CsNO_3$ also have the same calculated morphology that is built by {100}, {$\bar{1}$00}, (101} and {011}. $KNO_3$

separates these two morphologies with the {010}, {110} and {011} forms. Only for $NaNO_3$ and $KNO_3$ there are available data for surface energy calculations. The morphology derived from these values differs from that calculated by the BFDH approach. In $KNO_3$, Lovvik et al.[122] showed that the most important form is {001} and for $NaNO_3$ the equilibrium morphology is composed only by {104} form (see chapter 2). Neither of these two forms appeared in the BFDH derivation for their respective compounds.

## 1.9. CONCLUSIONS

In this chapter we have reviewed the most important information about crystal structure, polymorphism, and phase transition; crystal growth and morphology; solid state miscibility and binary phase diagrams between alkali nitrates. Sodium nitrate and potassium nitrate were studied in a deeper way, but more work is needed for a complete and univocally description in the fields treated in this chapter.

It is curious that surrounding such simple compounds there was so much discussion and controversy for the high temperature polymorph crystal structures. It is clear that some disorder exists there, but the different models proposed from X-ray diffraction data fit practically with the same confidence for each phase. Consequently, it is not easy to describe the phases properly.

Authors have agreed with the diverse phase stability domains, only γ-$KNO_3$ phase domain is not well described. It is a metastable phase that appears upon cooling β-$KNO_3$ phase, but its temporal stability depends on many factors as has been reviewed here. Nonetheless, this phase introduces some difficulties in the phase diagram determinations because solid solutions with $LiNO_3$ and II-$NaNO_3$ have been described.

A lot of papers devoted to alkali nitrate phase diagram determination have been published but complete experimental determination has not been carried out. Nonetheless, the FactSage webpage have simulations that seem to be quite correct. From this and morphological data at high temperature we propose a general boundary for the mismatch (m) parameter in order to group the different behaviours by taking into account only geometrical data.

- $m < 0.30$ → a complete solid solution if the crystal system is the same, or eutectic invariants with terminal solid solutions when the crystal system is different.
- $m > 0.30$ → eutectic invariant without solid solution.
- $m > 0.40$ → eutectic invariant without solid solution and intermediate stoichiometric compound.

Morphological studies are not extensive, in fact only $NaNO_3$ and $KNO_3$ have some published papers about them. For the former, a complete PBC analysis is made in

chapter 2. In contrast, for the latter, some theoretical morphologies have been proposed on the ground of the electric field chosen.

$NaNO_3$ and $KNO_3$ are important in the industrial field, so that industrial crystallization is the most studied part. In contrast, the isothermal growth mechanisms were not studied. Because of this, thermodynamic evaluation was not investigated. In chapter 3 we determine the isothermal growth mechanism of $NaNO_3$ and calculate some thermodynamic parameters.

## 1.10. BIBLIOGRAPHY

1. Harris, M. J. *Diffuse X-Ray Scattering and the Anomalous Soft Mode in $NaNO_3$.* J. Phys. Cond. Mat., **(1993)**, 5, 5773-5782.

2. Chen, A.; and Chernow, F. *Nature of Ferroelectricity in $KNO_3$.* Phys. Rev., **(1967)**, 154, 2, 493-505.

3. Charsley, E. L.; Laye, P. G.; Markham, H. M.; Hill, J. O.; Berger, B. and Griffiths, T. T. *Determination of the Equilibrium Temperatures and Enthalpies of the Solid-Solid Transition of Rubidium Nitrate by Differential Scanning Calorimetry.* Thermochim. Acta, **(2008)**, 469, 65-70.

4. Rao, C. N. R.; Prakash, B. and Natarajan, M. *Crystal Structure Transformations in Inorganic Nitrites, Nitrates, and Carbonates***,** National Standard Reference Data System - National Bureau of Standards, **(1975)**.

5. Chernov, A. A.; and Sipyagin, V. V. :*Peculiarities in Crystal Growth from Aqueous Solutions Connected with their Structures, in* Current topics in materials science. Kaldis, E .ed., Amsterdam: North-Holland publishing company, **(1980).**, 279-334.

6. *FACT Salt Phase Diagram: http://www.Crct.Polymtl.ca/fact/documentation/FTsalt/FTsalt_Figs.Htm.*, **2012**.

7. Gordon, S.; and Campbell, C. *Differential Thermal Analysis of Inorganic Compounds. Nitrates and Perchlorates of the Alkali and Alkaline Earth Groups and their Subgroups.* Anal. Chem., **(1955)**, 22, 7, 1102-1109.

8. Rhodes, E.; and Ubbelohde, A. R. *Melting and Crystal Structure - Effects of Thermal Transformations of Ionic Crystals on their Ultra-Violet Absorption.* Proc. Royal Soc. A., **(1959)**, 251, 1265, 156-171.

9. Fermor, J. H.; and Kjekshus, A. *On Electrical Properties of $LiNO_3$.* Acta Chem. Scand., **(1969)**, 23, 5, 1581-1587.

10. Wu, X.; Fronczek, F. and Butler, L. *Structure of $LiNO_3$ - Point-Charge Model and Sign of the $Li^{-7}$ Quadrupole Coupling-Constant.* Inorg. Chem., **(1994)**, 33, 7, 1363-1365.

11. Stromme, K. *On Crystal Structure of Lithium Nitrate Above Room Temperature.* Acta Chem. Scand., **(1970)**, 24, 4, 1479-1481.

12. Aquilano, D.; Benages-Vilau, R.; Bruno, M.; Rubbo, M. and Massaro, F. R. *Positive and Negative Form of Calcite Crystal ($CaCO_3$) in the Light of Bravais-Friedel-Donnay-Harker and Hartman-Perdok Approach. in Press.*

13. Benages-Vilau, R.; Calvet, T.; Cuevas-Diarte, M. A. and Aquilano, D. *The Theoretical Morphology of Nitratine ($NaNO_3$).*(in preparation).

14. McLaren, A. C. *Thermal Transformations in Nitrates of Univalent Ions.* Rev. P. App. Chem., **(1962)**, 12, 54-68.

15. Gonschorek, G.; Weitzel, H.; Miehe, G. and Schmahl, W. *the Crystal Structure of $NaNO_3$ at 100K, 120K, and 563K.* Zeits. Krist., **(2000)**, 215, 752-756.

16. Paul, G. L.; and Pryor, A. W. *Study of Sodium-Nitrate by Neutron Diffraction.* Acta Cryst. B., **(1972)**, 28, 15, 2700-2702.

17. Teo, K. L.; Shen, Z. X.; Kuok, M. H. and Tang, S. H. *High Pressure Phase Transition Study of $NaNO_3$ by Raman Spectroscopy.* J. Mol. Struc., **(1993)**, 294, 163-166.

18. Fermor, J. H.; and Kjekshus, A. *On the Electrical Properties of $NaNO_3$.* Acta Chem. Scand., **(1968)**, 22, 5, 1628-1636.

19. Parsonage, N. G.; and Staveley, L. A. K.:. *Disorder in Crystals,* Oxford: Calerendon Press, **(1978)**.

20. Antao, S. M.; Hassan, I.; Mulder, W. H.;and Lee, P. L., *The R-3c -> R-3m Transition in Nitratine, $NaNO_3$, and Implications for Calcite, $CaCO_3$.* Physics and Chem. Min., **(2008)**, 35, 10, 545-557.

21. Antao, S. M.; Hassan, I.; Mulder, W. H.; Lee, P. L. and Toby, B. H. *In Situ of the R-3c -->R-3m Orientational Disorder in Calcite.* Phys. Chem. Min., **(2009)**, 36, 159-169.

22. Ballirano, P. *Laboratory Parallel-Beam Transmission X-Ray Powder Diffraction Investigation of the Thermal Behavior of Nitratine $NaNO_3$: Spontaneous Strain and Structure Evolution.* Phys. Chem. Min., **(2011)**, 38, 7, 531-541.

23. Harris, M. J. *A New Explanation for the Unusual Critical Behaviour of Calcite and Sodium Nitrate, $NaNO_3$.* Am. Miner., **(1999)**, 84, 1632-1640.

24. Kracek, F. C. *Gradual Transition in Crystalline Sodium Nitrate. II. The Structure at various Temperatures and its Bearing on Molecular Rotation.* J. Am. Chem. Soc., **(1931)**, 53, 3339-3348.

25. Ketelaar, J. A. A.; and Strijk, B. *The Atomic Arrangement in Solid Sodium Nitrate at High Temperatures.* R. Trav. Chim. Pays-Bas, **(1945)**, 64, 6, 174-182.

26. Schmahl, W. W.; and Salje, E. *X-Ray Diffraction Study of the Orientational Order-Disorder Transition in $NaNO_3$ - Evidence for Order Parameter Coupling..* Phys. Chem. Min., **(1989)**, 16, 8. 790-798.

27. Paynet, S. J.; Harris, M. J.; Hagen, M. E. and Dove, M. T. *A Neutron Diffraction Study of Order-Disorder Phase Transition in Sodium Nitrate.* J. Phys. Cond. Mat., **(1997)**, 9, 2423-2432.

28. Poon, W. C. K.; and Salje, E. *The Excess Optical Birrefringence and Phase Transition in Sodium Nitrate.* J. Phys.C., **(1988)**, 21, 4, 715-729.

29. Reeder, R. J.; Redfern S. A. T. and Salje, E. S*pontaneous Strain at the Structural Phase Transition in $NaNO_3$.* Phys. Chem. Min., **(1988)**, 15, 6. 605-611..

30. Liu, J.; Duan, C.; Ossowski, M.; Mei, W. N.; Smith, R. W. and Hardy, J. R. *Simulation of Structural Phase Transition in $NaNO_3$ and $CaNO_3$.* Phys. Chem. Min., **(2001)**, 28, 586-590.

31. Lyndell-bell R. M.; Ferrairo, M.; McDonnald, I. R.; and Salje E. A *Molecular Dynamics Study of Orientational Disordering in Crystalline Sodium Nitrate.* J. Phys. Cond. Mat., **(1989),** 1, 37. 6523-6542.

32. Rysiakiewicz-Pasek, E.; Naberezhnov, A.; Seregin, M.; Koroleva, E.; Glavatskyy, I.; Tovar, M.; Sysoeva, A. and Berman, E. *Phase Transitions and Macroscopic Properties of $NaNO_3$ Embedded into Porous Glasses.* J. Non Cryst. Solids, **(2011)**, 357, 14-20.

33. Sipyagin, V. V.; and Chernov, A. A. *Anomalies of Temperature Dependence of Growth-Rates of Faces of Crystals $KNO_3$, $NaNO_2$, $NaNO_3$, $NaClO_3$ and Rochelle Salt from Aqueous-Solutions.* Kristallografiya, **(1972)**, 17, 5, 1003-1009.

34. Kiryanova, E. V. *New Effects of crystal–solution Phase Equilibria in a Model System NaNO3–H2O.* J. Cryst. Growth, **(2003)**, 253, 1-4, 452-459.

35. Kiryanova, E. V. *Temperature-Concentration Oscillations of Crystal-Solution Phase Equilibria in the Presence of Trace Impurities of Surface-Active Agents.* Cryst. Res. Tech., **(2011)**, 46, 4.

36. Franke, V. D.; Treivus, E. B.; Filippov, V. K. and Antonova, V. A. *Crystallization of Nitrates in the Presence of $HNO_3$ and its Relation to Physical and Chemical Properties of the Systems.* J. Cryst .Growth, **(1981)**, 52, Part 2, 795-800.

37. Kirkova, E.; and Nikolaeva, R. *Influence of the Flow Velocity, Supersaturation and Temperature on the Crystal-Growth from Solutions.* Cryst. Res. Tech., **(1983)**, 18, 6, 743-754.

38. Treivus, E. B. *The Oscillations of Crystal Growth Rates at their Formation in the Regime of Free Convection of a Solution; Statistical Investigation.* Cryst. Res. Tech., **(1997)**, 32, 7, 963-972.

39. Jones, C. M.; and Larson, M. A. *Characterizing Growth-Rate Dispersion of $NaNO_3$ Secondary Nuclei.* AIChE J., **(1999)**, 45, 10, 2128-2135.

40. Jones, C. M., Larson, M. A.; Ristic, R. I.; and Sherwood, J. N. *The Role of Dislocations, Integral Strain, and Supersaturation on the Growth Rates of Sodium Nitrate.* J. Cryst. Growth, **(2000)**, 208, 1-4. 520-524.

41. Jones, C. M.; and Larson, M. A. *Using Dislocations and Integral Strain to Model the Growth Rates of Secondary Nuclei.* Chem. Eng. Sci., **(2000)**, 55, 14, 2563-2570.

42. Ristic, R. I.; Shekunov B. Yu. and Sherwood, J. N. *The Influence of Synchrotron Radiation-Induced Strain on the Growth and Dissolution of Brittle and Ductile Materials.* J. Cryst .Growth, **(1997)**, 179, 205-212.

43. Ristic, R. I.; Sherwood, J. N. and Shripathi, T. *The Influence of Tensile Strain on the Growth of Crystals of Potash Alum and Sodium Nitrate.* J. Cryst. Growth, **(1997)**, 179, 1-2, 194-204.

44. Benages-Vilau, R.; Calvet, T.; Cuevas-Diarte, M. A.; Rubbo, M. and Aquilano, D. *Crystal Growth of $NaNO_3$ from Pure Aqueous Solutions,* **(in preparation)**.

45. Benages-Vilau, R.; Calvet, T.; Cuevas-Diarte, M. A.; Rubbo, M. and Aquilano, D. *Effect of Impurities in the Morphology and Growth Rate of $NaNO_3$*, **(in preparation)**.

46. Graber, T. A.; Taboada, M. E.; Alvarez, M. N. and Schmidt, E. H. *Determination of Mass Transfer Coefficients for Crystal Growth of Nitrate Salts.* Cryst. Res. Tech., **(1999)**, 34, 10, 1269-1277.

47. Oosterhof, H.; Geertman, R. M..; Witkamp, G. J.; and van Rosmalen G. M. *The Growth of Sodium Nitrate from Mixtures of Water and Isopropoxyethanol.* J. Cryst. Growth, **(1999)**, 198, 1. 754-759.

48. Zehnder, K.; and Arnold, A. *Crystal Growth in Salt Efflorescence.* J. Cryst. Growth, **(1989)**, 97, 513-521.

49. Lu, P.; Wang, F.; Zhao, L.; Li, W.; Li, X.; Dong, J.; Zhang, Y. and Lu, G. *Molecular Events in Deliquescence and Efflorescence Phase Transitions of Sodium Nitrate Particles Studied by Fourier Transform Infrared Attenuated Total Reflection Spectroscopy.* J. Chem. Phys., **(2008)**, 129, 10, 104509.

50. Komnik, S. N.; and Startsev, V. I. *On the Growth of Large Perfect Crystals of Sodium Nitrate.* J. Cryst. Growth, **(1969)**, 5, 207-209.

51. Gopalakrishnan, R.; Arivuoli, D. and Ramasamy, P. *Growth and Characterization of $NaNO_3$ Single-Crystals.* Cryst. Res. Tech., **(1991)**, 26, 6, K141-K146.

52. Anilkumar, A. V.; Grugel, R. N.; Bhowmick, J. and Wang, T. G. *Suppression of Thermocapillary Oscillations in Sodium Nitrate Floating Half-Zones by High-Frequency End-Wall Vibrations.* J. Cryst. Growth, **(2005)**, 276, 1–2, 194-203.

53. Lan, C. W.; Su, M. C. and Liang, M. C. *A Visualization and Computational Study of Horizontal Bridgman Crystal Growth.* J. Cryst. Growth, **(2000)**, 208, 1–4, 717-725.

54. Sawada, T.; and Shichiri, T. *Morphology and Kinetics in Ionic Crystals Growing from their Melts.* J. Cryst. Growth, 1984, 67, 2, 233-240.

55. Benages, R.; Costa, E.; Bruno, M.; Cuevas.Diarte, M. A.; Calvet, T. and Aquilano, D. *Experimental and Theoretical Aspects of the Growth and Equilibrium Morphology of $NaNO_3$.* Cryst. Res. Tech., **(2011)**, 1-6.

56. Punin, Y. O.; and Franke, V. D. *Curved-Face Growth of $NaNO_3$ Crystals.* Cryst. Rep., **(2001)**, 49, 2, 256-260.

57. Nimmo, J. K.; and Lucas, B. W. *A Neutron Diffraction Determination of the Crystal Structure of a-Phase Potassium Nitrate at 25ºC and 100ºC.* J. Phys. C., **(1973)**, 6, 201-211.

58. Nimmo, J. K.; and Lucas, B. W. *the Crystal Structures of γ- and β-$KNO_3$ and the α->γ->β Phase Transformations.* Acta Cryst. B., **(1976)**, B-32, 1968-1971.

59. Adiwidjaja, G.; and Pohl, D. *Superstructure of a-Phase Potassium Nitrate.* Acta Cryst. C., **(2003)**, C59, i139-i140.

60. Fermor, J. H.; and Kjekshus, A. *A Phase Transition in $KNO_3$ at Low Temperatures.* Acta Chem. Scand., **(1968)**, 22, 836-842.

61. Freney, E. J.; Garvie, L. A. J.; Groy, T. L. and Buseck, P. R. *Growth and Single-Crystal Refinement of Phase-III Potassium Nitrate, $KNO_3$.* Acta Cryst. B., **(2009)**, B65, 659-663.

62. Viedma, C.; Prieto, M.; Garcia Ruiz, J. M. and Amorós, J. L. *Cristalización Polimórfica del $KNO_3$ (Nitro) a Partir de Soluciones.* I Congreso Español De Geología, **(1984)**, II, 305-316.

63. Tuech, J.; and Combet, S. *Étude Thermodynamique Des Solutions Aqueuses De Nitrate De Potassium Jusq'Au dela Saturation. III.- Cas De Cristallisation En Deux Étapes En Solution Sursaturée.* J. Chim. Phys., **(1977)**, 74, 2, 137-142.

64. Laval, P.; Giroux, C.; Leng, J.; Salmon. J.-B. *Microfluidic Screening of Potassium Nitrate Polymorphism.* J. Cryst. Growth, **(2008)**, 310, 12. 3121-3124.

65. Laval, P. and Salmon. J.-B. *Microfluidic Droplet Method for Nucleation Kinetics Measurement.* Langmuir, **(2009)**, 25, 3, 1836-1841.

66. Salmon, J. and Leng, J. *Microfluidics for Kinetic Inspection of Phase Diagrams.* Comptes Rendus Chimie, **(2009)**, 12, 258-269.

67. Adams, D. M.; Hatton, P. D.; Heath, A. E.; Rusell, D. R., *X.-Ray Diffration Measurements on Potassium Nitrate Under High Pressure using Synchrotron Radiation.* J. Phys. C., **(1988)**, 21, 3, 505-515.

68. Worlton, T. G.; Decker, D. L.; Jorgensen, J. D. and Kleb, R. *Structure of High Pressure $KNO_3$-IV.* Physica, **(1986)**, 136B, 503-506.

69. Aquino-Olivos, M. A.; Grolier, J. E.; Randzio, S. L.; Aguirre-Gutierrez, A. J. and Garcia-Sanchez, F. *Transitiometric Determination of the Phase Diagram of $KNO_3$*

*between (350 and 650) K and at Pressures up to 100 MPa.* J. Chem. Eng. Data, **(2010)**, 55, 12.

70. Kostyrko, K.; and Skoczylas, M. *Temperature Standard Reference Materials for Thermal-Analysis.* J Therm. Anal., **(1992)**, 38, 9.

71. Shultins, A. A.; and Karpov, S. V. *Intermolecular Interactions and Infra-Red Spectra of Three Crystallines Phases of Potassium Nitrate-II. Internal-Lattice Combination Band Region.* J. Phys. Chem. S., **(1969)**, 30, 1981-1988.

72. Khana, R. K.; Lingscheid, J. and Decius, J. C. *Infra.Red Absorption Spectra of Potassium Nitrate in Phases I, II and III.* Spectrochim. Acta, **(1964)**, 20, 1109-1116.

73. Chakraborty, T.; Bajpai, P. K. and Verma, A. L. *Room Temperature Spectroscopic Investigations of $K^{14}NO_3$, $K^{15}NO_3$, $K^{14}N^{16}O_{3-X}{}^{18}O_X$ and a 1:1 Mixture of $K^{14}NO_3$ and $K^{15}NO_3$: Intermolecular Coupling Revealed in the Vibrational Spectra.* J. Raman Spectros., **(1999)**, 30, 189-194.

74. Murugan, R.; Huang, P. J.; Ghule, A. and Chang, H. *Studies on Thermal Hysteresis of $KNO_3$ by Thermo-Raman Spectroscopy.* Thermochim. Acta, **(2000)**, 83-90.

75. Schonwandt, B.; and Jakobsen, H. J. *Phase Transition in $KNO_3$ Studied by Variable-Temperature $^{15}N$ Magic-Angle Spinning NMR Spectroscopy.* J. Sol. State Chem., **(1999)**, 145, 10-14.

76. Poprawski, R.; Rysiakiewicz-Pasek, E.; Sieradzki, A.; Ciżman, A. and Polańska, J. *Ferroelectric Phase Transitions in $KNO_3$ Embedded into Porous Glasses.* J. Non Cryst. Solids, **(2007)**, 353, 47-51, 4457-4461.

77. Muntasell, J.; Navarro, J. and Cesari, E. *A Study of the Polymorphism of Potassium Nitrate Starting from Room Temperature and at Atmospheric Pressure.* Thermochim. Acta, **(1985)**, 83, 2, 173-179.

78. Garn, P. D.; Diamondste, D. I. and Menis, O. *Variations in the Cooling Transitions of Potassium Nitrate.* J. Therm. Anal., **(1974)**, 6, 623-630.

79. Westphal, M. J.; wood, J. W.; Redin, R. D. and Ashworth, T. *Calorimetric and Photoacustic Investigation of $KNO_3$ phase Transition.* J. App. Phys., **(1993)**, 73, 11, 7302-7310.

80. Harmealin, M. *Relation of Quantitative Differential Thermal Analysis to Study on Polymorphism of Potassium Nitrate at Atmospheric Pressure.* J. Therm. Anal., **(1972)**, 4, 4, 403.

81. Font J.; and Muntasell, J. *Thermobarometric Study of KNO3 Phase Transitions.* Thermochim. Acta, **(1997)**, 293, 1-2, 167-170.

82. Shimada, S.; Katsuda, Y. and Inagaki, M. *Phase Transition of Potassium Nitrate Monitored by Acoustic Emission Technique and the Healing Effect on the Gamma-Alpha. Transition.* J. Phys. Chem., **(1993)**, 97, 34, 8803-8807.

83. Belomestnykh, V. N.; and Botaki, A. A. *Polymorphism of Nitrates of Univalent Metals and Ammonium from Acoustic Data - Potassium and Sodium Nitrates.* Fizika Tverdogo Tela, **(1992)**, 34, 1.

84. Christensen, A. N.; Norby, P.; Hanson, J. C. and Shimada, S. *Phase Transition of $KNO_3$ Monitored by Sincrotón X-Ray Powder Diffraction.* App. Cryst., **(1996)**, 29, 265-269.

85. Benages, R.; Calvet, T. and Cuevas-Diarte, M. A. *Does the Solidus and Liquidus Intersect?,* **(in preparation)**.

86. Asadov, Y. G.; Nasirov, V. I. and Jarailova, G. A. *Morphology of Crystal Growth at Polymorphic Transformations in $KNO_3$, $AgNO_3$ and $NH_4NO_3$ Single Crystals.* J. Cryst. Growth, **(1972)**, 15, 45-50.

87. Kawashima, R.; Katsuki, K. and Suzuki, K. *Temperature Dependence of Optical Absorption near the Structural Phase Transition of Potassium Nitrate.* Phys. Status Sol., **(1985)**, 129, 2, 697-705.

88. Nagase, A.; Takeuchi, Y. and Takagi, Y. *Brillouin Scattering Study on $KNO_3$ Crystal: Appearance of Intermediate Phase on Heating.* Jpn .J. Appl. Phys. Part 1, **(1996)**, 35, 5B, 2903-2906.

89. Cornelison, S. G.; Gauss, A.; Krane, J. and Hardy, J. R. *Centimeter-Wave Reflection in the Nitrates and Nitrites of Sodium and Potassium: Experiment and Theory.* J. Appl. Phys., **(1997)**, 81, 3.

90. Westphal, M. J. *Particle Size and Cooperative Behaviour Effects on $KNO_3$ Phase Transitions.* Appl. Phys., **(1993)**, 74, 10, 6107-6114.

91. Sieradzki, A.; Komar, J.; Rysiakiewicz-Pasek, E.; Cizman, A. and Poprawski, R. *Calorimetric Investigations of Phase Transitions in $KNO_3$ Embedded into Porous Glasses.* Ferroelectrics, **(2010)**, 402, PII 929912804.

92. Baryshnikov, S. V.; Charnaya, E. V.; Milinkiy, A. Y.; Stukova, E. V.; Tien, C. and Michel, D. *Phase Transition in $K_{1-x}Na_xNO_3$ Embedded into Molecular Sieves.* J. Phys. C, **(2009)**, 21, 325902.

93. Yadlovker, D.; and Berger, S. *Reversible Electric Field Induced Nonferroelectric to Ferroelectric Phase Transition in Single Crystal Nanorods of Potassium Nitrate.* Appl. Phys. Lett., **(2007)**, 91, 17, 173104.

94. Kumar, N.; and Nath, R. *Thermal and Ferroelectric Properties of Potassium Nitrate: Polyvinyl Fluoride Composite Films.* IEEE Trans. Dielectr. Electr. Insul., **(2005)**, 12, 6.

95. Kumar, N.; and Nath, R. *Ferroelectric Phase Stability Studies in Potassium Nitrate: Polyvinylidene Fluoride Composite Films.* J. Appl. Phys., **(2005)**, 97, 2, 024105.

96. Dabra, N.; Hundal, J. S.; Sekhar, K. C.; Nautiyal, A. and Nath, R. *Ferroelectric Phase Stability Studies in Spray Deposited $KNO_3$:PVA Composite Films.* J Am Ceram Soc., **(2009)**, 92, 4, 834-838.

97. Dabra, N.; Hundal, J. S.; Sekhar, K. C.; Nautiyal, A. and Nath, R. *Preparation and Characterization of the Ferroelectric Potassium Nitrate: Poly(Vinyl Alcohol) Composite Films.* IEE Trans.on Ultrasonics Ferroel. Freq. Control, **(2009)**, 56, 8.

98. Fermor, J. H.; and Kjekshus, A. *On the Electrical Properties of $KNO_3$.* Acta Chem. Scand., **(1967)**, 21, 5, 1265-1276.

99. Shimada, S.; and Aoki, T. *Stabilization of the Ferroelectric G-Phase by Doping with $Na^+$, Determined by the Acoustic Emision Method.* Chem. Let., **(1996)**, 393-394.

100. Westphal, M. J. *Cooperative Behavior during Ferroelectric Transition in $KNO_3$ Powder.* J. of App. Phys., **(1993)**, 74, 5, 3131-3136.

101. Swaminathan, S.; and Srinivasan, S. *A Probable Crystallographic Path for the Thermal Phase Transition in Single Crystal of $KNO_3$.* Acta Cryst., **(1975)**, A31, 628-634.

102. Lu, H. M.; and Hardy, J. R. *First-Principles Study of Phase Transition in $KNO_3$.* Phys. Rev. B., **(1999)**, 44, 14, 7215-7224.

103. Erdinc, B.; and Akkus, H. *Ab-Initio Study of the Electronic Structure and Optical Properties of $KNO_3$ in the Ferroelectric Phase.* Phys.Scripta, **(2009)**, 79, 2, 025601.

104. Dieguez, O.; and Vanderbilt, D. *Theoretical Study of Ferroelectric Potassium Nitrate.* Phys. Rev. B., **(2007)**, 76, 13, 134101.

105. Aydinol, M. K.; Mantese, J. V. and Alpay, S. P. *A Comparative Ab Initio Study of the Ferroelectric Behaviour in $KNO_3$ and $CaCO_3$.* J. Phys.C., **(2007)**, 19, 49, 496210.

106. Kipp, S.; and Lacmann, R. *Cooling Crystallization Experiments Observed by in Situ Scanning Force Microscopy.* J. Cryst. Growth, **(1996)**, 160, 3-4, 320-329.

107. Rolfs, J.; Lacmann, R. and Kipp, S. *Crystallization of Potassium Nitrate ($KNO_3$) in Aqueous Solution .1. Growth Kinetics of the Pure System.* J. Cryst. Growth, (**1997**), 171, 1-2, 174-182.

108. Herden, A.; and Lacmann, R. *The Crystallization of Potassium Nitrate .2. Growth Rate Dispersion.* J. Cryst. Growth, (**1997**), 179, 3-4, 592-604.

109. Helt, J. E.; and Larson, M. A. *Effects of Temperature on the Crystallization of Potassium Nitrate by Direct Measurement of Supersaturation.* AIChE J., **(1977)**, 23, 6, 822-830.

110. Kipp, S.; Lacmann, R. and Rolfs, J. *Crystallization of Potassium Nitrate ($KNO_3$) in Aqueous Solution. 2. Kinetical Studies under the Influence of Additives.* J. Cryst. Growth, (**1997**), 171,1-2, 183.

111. Pradell, D. G. *Single Crystal Crystallization of Potassium Nitrate.* **, (1999),** Master Thesis**,** Universitat de Barcelona. .

112. Tanneberger, U.; Lacmann, R.; Herden, A.; Klapper, H.; Schmiemann, D.; Becker, R. A.; Mersmann, A. and Zacher, U. *The Dispersion of Growth Rate as a Result of Different Crystal Perfection.* J. Cryst. Growth, **(1996)**, 166, 1-4, 1074-1077.

113. Herden, A.; and Lacmann, R. *The Crystallization of Potassium Nitrate .1. Etch Pit Density and Microhardness of Potassium Nitrate in Comparison with some other Ionic Crystals.* J. Cryst. Growth, **(1997)**, 173, 3-4, 481-486.

114. Wang, S.; and Mersmann, A. *Initial-Size-Dependent Growth Rate Dispersion of Attrition Fragments and Secondary Nuclei.* Chem. Eng. Sci., **(1992)**, 47, 6, 1365-1371.

115. Huang, P.; Huang, D. C.; Xu, N. P. and Shi, J. *Quantitative Identification of Nucleation and Crystal Growth Stages in Batch Crystallization from Solution.* Chem. J. Chin. Uni., **(2004)**, 25, 3-8.

116. Zarkadas, D.; and Sirkar, K. *Solid Hollow Fiber Cooling Crystallization.* Ind. Eng. Chem. Res., **(2004)**, 43, 22, 7163-7180.

117. Soltsberg, L. J.; Fappiano, S. A.; Griffith, L. D.; Hidek, L. E.; Ofek, S. A. and Suarez, L. L. *Mechanism of Crystal Dendrite Formation in $KNO_3$.* Acta Cryst. B., **(1994)**, 40, 518-524.

118. Fujiwara, M.; Tokunaga, R. and Tanimoto, Y. *Crystal Growth of Potassium Nitrate in a Magnetic Field of 80 kOe.* J Phys Chem B., **(1998)**, 102, 31, 5996-5998.

119. van der Voort, E. *Observations on Growth Forms and Habits of Potassium Mitrate as a Function of Temperature.* J. Cryst. Growth, **(1990)**, 100, 539-544.

120. van der Voort, E. *The Theoretical Growth from of Potassium Nitrate from an Aqueous Solution.* J. Cryst. Growth, **(1991)**, 110, 4, 653-661.

121. Soltzberg, L. Z.; Carneiro, O.; Joseph, G. S.; Khan, Z.; Meretsky, T. M.; Ng, M. M. and Ofek, S. A. *Prediction of Early- and Late-Growth Morphologies of Ionic Crystals.* Acta Cryst. B., **(1998)**, 54, 384-390.

122. Lovik, O. M.; Jensen, T. L.; Moxnes, J. F.; Swang, O. and Unneberg, E. *Surface Stability of Potassium Nitrate ($KNO_3$) from Density Functional Theory.* Comp. Mat. Sci., **(2010)**, 50, 356-362.

123. Ahtee, M.; and Hewat, A. W. *Structures of the High Temperature Phases of Rubidium Nitrate.* Phys. Status Sol., **(1980)**, 58, 2, 525-531.

124. Pohl, J.; Pohl, D. and Adiwidjaja, G. *Phase-Transition in Rubidium Nitrate at 346-K and Structure at 296 K, 372 K, 413 K and 437 K.* Acta Cryst. B., **(1992)**, 48, 160-166.

125. Shamsuzzoha, M.; and Lucas, B. W. *Structure (Neutron) of Phase-IV Rubidium Nitrate at 298 K and 403 K.* Acta Cryst. B., **(1982)**, 38, 2353-2357.

126. Zhou, B.; Giavani, T.; Bildsoe, H.; Skibsted, J. and Jakobsen, H. J. *Structure Refinement of $CsNO_3$(II) by Coupling of N-14 MAS NMR Experiments with WIEN2k DFT Calculations.* Chem. Phys. Let., **(2005)**, 402, 1-3.

127. Shamsuzzoha, M.; and Lucas, B. W. *Polymorphs of Rubidium Nitrate and their Crystallographic Relationships.* Can. J. Chem., **(1988)**, 66, 4, 819-823.

128. Shinnaka, Y.; and Yamamoto, S. *X-Ray Study of Orientational Disorder in Cubic $RbNO_3$.* J. Phys. Soc. J., **(1981)**, 50, 6, 2091-294.

129. Stromme, K. *Crystal Structures of High-Temperature Phases of Rubidium Nitrate, Cesium Nitrate, and Thallium Nitrate.* Acta Chem. Scand., **(1971)**, 25, 1, 211-215.

130. Yamamoto, S.; Suematsu, Y. and Shinnaka, Y. *X-Ray Study of Phase-Transition in $RbNO_3$.* J. Phys. Soc. J., **(1977)**, 43, 6, 1962-1967.

131. Shamsuzzoha, M.; and Lucas, B. W. *New Crystal Data (Neutron) for Phase-II Rubidium Nitrate at 513 K.* J. Appl. Crystallogr., **(1988)**, 21, 74-74.

132. Fermor, J. H.; and Kjekshus, A. *Solid State Transitions in Univalent Nitrates Below Room Temperature.* Acta Chem. Scand., **(1968)**, 22, 6, 2054-2055.

133. Owen, W.; and Kennard, D, C. *Comment on Phase Transitions of Caesium and Rubidium Nitrate below Room Temperature.* Aust. J. Chem., **(1971)**, 24, 6, 1295-1299.

134. Kawashima, R.; and Uchiumi, T. *Temperature and Frequency Dependence of Electric Conductivity near the Successive Phase Transition Points of Rubidium Nitrate Crystal.* S. State Com., **(1986)**, 58, 9, 625-627.

135. Kawashima, R. *The Study of AC Conductivities on the Dynamical Properties Near the Successive Phase-Transition Points of Rubidium Nitrate Crystal.* J. Phys. Soc. J., **(1988)**, 57, 8, 2841-2851.

136. Kawashima, R.; Katsuki, K. and Suzuki, K. *Electric Properties Near the 1st Order Phase-Transition Points of Rubidium Nitrate Crystal.* J. Phys. Soc. J., **(1986)**, 55, 9, 3143-3150.

137. Kawashima, R.; Katsuki, K. and Suzuki, K. *Electric and Optical Properties Near the Successive Phase-Transition Points of Rubidium Nitrate Crystal.* J J. Phys. Soc. J., **(1985)**, 54, 5, 2057-2058.

138. Liu, J. J.; Duan, C. G.; Ossowski, M. M.; Mei, W. N.; Smith, R. W. and Hardy, J. R. *Molecular Dynamics Simulation of Structural Phase Transitions in $RbNO_3$ and $CsNO_3$.* J. Solid State Chem., **(2001)**, 160, 1, 222-229.

139. Sadananda C., A.; and Narender R., S. *Effect of Structural Changes on DC Ionic Conductivity of Rubidium Nitrate Single Crystals.* Phys. Status Solidi, **(1998)**, 208, 2, 349-352.

140. Dean, C.; Hambley, T. W. and Snow, M. R. *Structures of Phase-IV Rubidium Nitrate, $RbNO_3$, and Phase-II Cesium Nitrate, $CsNO_3$.* Acta Cryst. C., **(1984)**, 40, 1512-1515.

141. Treivus, E. B.; and Franke, V. D. *Crystallization Kinetics of some Anhydrous Nitrates.* Kristallografiya, **(1976)**, 21, 5, 1002-1005.

142. Lucas, B. W. *The Structure (Neutron) of Phase-Ii Cesium Nitrate at 298-K, $CsNO_3$.* Acta Cryst. C., **(1983)**, 39-43.

143. Pohl, D.; and Gross, T. *Cesium Nitrate (II) at 296-K.* Acta Cryst. C., **(1993)**, 49, 316-318.

144. Wacharine, S.; Hellali, D.; Zamali, H.; Rogez, J. and Jemal, M. *The Phase Diagram of $CsNO_3$-$RbNO_3$.* J. Therm. Anal. Cal., **(2012)**, 107, 2, 477-481.

145. Stromme, K. O. *The Crystal Structure of Sodium Nitrate in the High Temperature Phase.* Acta Chem. Scand., **(1969)**, 23, 1616-1624.

146. Stromme, K. O. *On the Crystal Structure of Potassium Nitrate in the High Temperature Phases I and III.* Acta Chem. Scand., **(1969)**, 23, 1625-1636.

147. Korhonen, U. Annales Academiae Scientiarum Fennicae Series A II Chemica, **(1953)**, 250, 1-16.

148. Charrier, E.; Charsley, E. L.; Laye, P. G.; Markham, H. M. and Griffiths, T. T. *Determination of the Temperature and Enthalpy of Solid-Solid Phase Transition of Caesium Nitrate by Differential Scanning Calorimetry.* Thermochim. Acta, **(2006)**, 445, 36-39.

149. Chary, A. S.; Reddy, S. N. and Chiranjivi, T. *Structural Phase-Transition in $CsNO_3$ - Dielectric Studies.* Solid State Ionics, **(1993)**, 62, 3-4.

150. Kawashima, R.; and Hirai, K. *Electrical-Properties near the Structural Phase-Transition of Crystalline Cesium Nitrate.* Phil. Mag. B., **(1988)**, 58, 6, 663-669.

151. Kawashima, R. *AC Conductivities Near the Structural Phase-Transition Point of Cesium Nitrate Crystal.* J. Phys. Soc. Japan, **(1989)**, 58, 9, 3236-3242.

152. Takagi, Y.; Kimura, S. and Takeuchi, Y. *Structural Phase Transition of $CsNO_3$ Crystal-Spontaneous Polarization.* Ferroelectrics, **(2003)**, 284.

153. Nautiyal, A.; Sekhar, K. C.; Pathak, N. P. and Nath, R. *Ferroelectric and Phase Transition Studies in Cesium Nitrate: Poly(Vinyl Alcohol) Composite Films.* App. Phys., **(2009)**, 97, 1.

154. Kalliomäki, M. S.; and Meisalo, V. P. J. *Structure Determination of the High Pressure Phases $RbNO_3$ V, $CsKNO_3$ III, and $CsNO_3$ IV.* Acta Cryst. B., **(1979)**, B35, 2829-2835.

155. Gottlicher, S.; and Knochel, C. D. *Crystal-Structure of Sodium-Nitrate.* Z. Kristall., **(1978)**, 148, 1-2, 101-105.

156. Holden, K. R.; and Dickinson, C. W. *Crystal Structures of Three Solid Solution Phases of Ammonium Nitrate and Potassium Nitrate.* J. Phys. Chem., **(1975)**, 79, 3, 249-256.

157. Shamsuzzoha, M.; and Lucas, B. W. *Single-Crystal (Neutron) Diffraction Structure of Iii-Rubidium Nitrate.* Acta Cryst. C., **(1987)**, 43, 385-388.

158. Voskresenskaya, N. K.; Evseeva, N. N.; Berul, S. I. and Vereshchetina, I. P.. *Handbook of Solid-Liquid Equilibria in Systems of Anhydrous Inorganic Salts,*. Voskresenskaya, N. K. ed., 1st ed. Jerusalem: Keter Press, **(1970).**

159. Dessureault, Y.; Sangster, J. and Pelton, A. D. *Evaluation Critique Des Donées Thermodynamiques et des Diagrammes de Phases des Systèmes AOH-AX, $ANO_3$-AX, $ANO_3$-$BNO_3$, AOX, BOX où A, B = Li, Na, K et X = Cl, F, $NO_3$, OH.* J. Chim. Phys., **(1990)**, 87, 407-453.

160. Drira, N. B.; Zamali, H. and Jemal, M. *Diagramme De Phases Du Systeme Binaire $LiNO_3$-$NaNO_3$.* J. Thermal Anal., **(1996)**, 46, 1449-1458.

161. Maeso, M. J.; and Largo, J. *The Phase Diagrams of $LiNO_3$-$NaNO_3$ and $LiNO_3$-$KNO_3$: The Behaviour of Liquid Mixtures.* Thermochim. Acta, **(1993)**, 223, 145-156.

162. Xu, K. *Raman Evidence for the Congruently Melting Compound $KLi(NO_3)_2$ in the $LiNO_3$-$KNO_3$ System.* J. Phys.Chem. Solids, **(1999)**, 60, 5-11.

163. Zhang, X. *The Phase Diagram of $LiNO_3$-$KNO_3$.* Thermochim. Acta, **(2002)**, 385, 1-2. 81.

164. Xu, K.; and Chen, Y. *Structural Features of the Congruently Melting Compounds $MLi(NO_3)_2$ (M=K, Rb, Cs) Inferred from their Raman Spectra.* J. Phys. Chem. Solids, **(1999)**, 60, 3, 317-324.

165. Xu, K. *Application of Raman in Phase Equilibrium Studies: The Structure of Subtitutional Solid Solutions of $KNO_3$ by $RbNO_3$.* J. Mat. Sci., **(1999)**, 34, 3447-3453.

166. Belaid Drira, N.; Zamali, H. and Jemal, M. *Phase Diagram of the Binary System $CsNO_3$-$LiNO_3$ - Activities in the Liquid.* J. Thermal Anal. Calorimetry, **(1999)**, 58, 3, 607-615.

167. Jriri, R.; Rogez, J. and Mathieu, J. C. *Diagramme de Phases $NaNO_3$-$CsNO_3$.* Comptes Rendus, **(1995)**, 321, 4, 163-165.

168. Zamali, H.; and Jemal, M. *Diagrammes de Phases des Systemes Binaires $KNO_3$-$CsNO_3$ et $KNO_3$-$NaNO_3$.* J. Thermal Anal., **(1994)**, 41, 1091.1099.

169. Secco, E.; and Secco, R. *Heats of solution/substitution in $TlNO_3$ and $CsNO_3$ Crystals and in $RbNO_3$ and $CsNO_3$ Crystals from Heats of Transition: The Complete*

*Phase Diagrams of $TlNO_3$-$CsNO_3$ and $RbNO_3$-$CsNO_3$ Systems.* J. Phys. Chem. Solids, **(2002)**, 63, 3, 433-440.

170. Nasirov, V. I.; Khazieva, A. F. and Asadov, Y. G. *Polymorphic Single Crystal Single Crystal Transformations in $Rb_{0.975}Cs_{0.025}NO_3$.* Crystal. Rep., **(2011)**, 56, 6, 1077-1081.

171. Asadov, Y. G.; and Nasirov, E. V. *Polymorphic Single Crystal a Dagger" Single Crystal Transition in $K_{0.975}Rb_{0.025}NO_3$.* Crystal. Rep., **(2010)**, 55, 5, 892-895.

172. Nasirov, V. I.; Khazieva, A. F.; Asadov, Y. G.; Amirov, A. S. and Alyev, Y. I. *Growth of $Rb_{0.90}Cs_{0.10}NO_3$ Crystals and their X-Ray Diffraction Analysis.* Crystal. Rep., **(2012)**, 57, 6, 869-872.

173. Nasirov, E. V.; and Asadov, Y. G. *Kinetics of the II -> III Polymorphic Transformation in $KNO_3$-$RbNO_3$ Solid Solutions.* Inorg. Mat., **(2010)**, 46, 8, 885-888.

174. Oonk, H. A. J. *Solid-State Solubility and its Limits. the Alkali Halide Case.* P. App. Chem., **(2001)**, 73, 5, 807-823.

# CHAPTER 2

## NITRATINE ($NaNO_3$) THEORETICAL MORPHOLOGY.

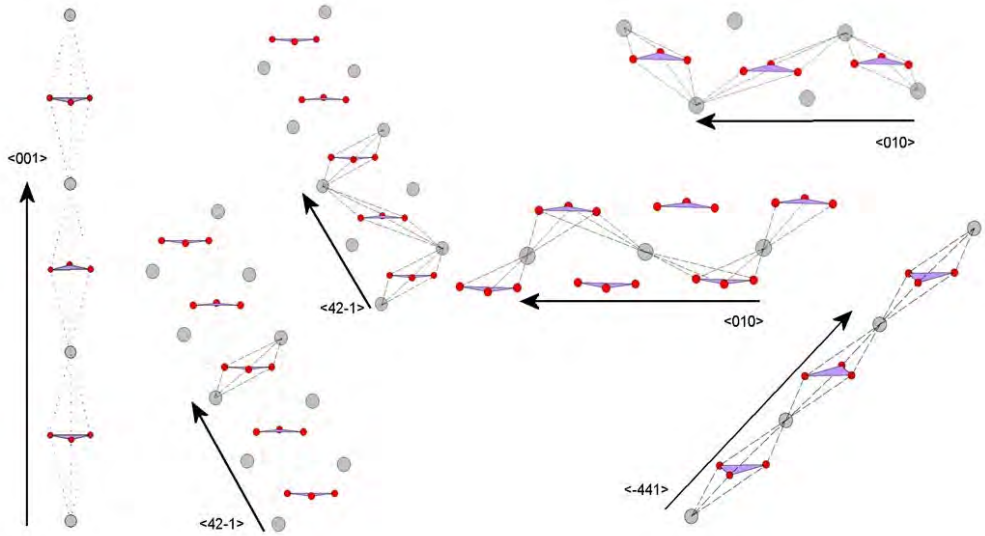


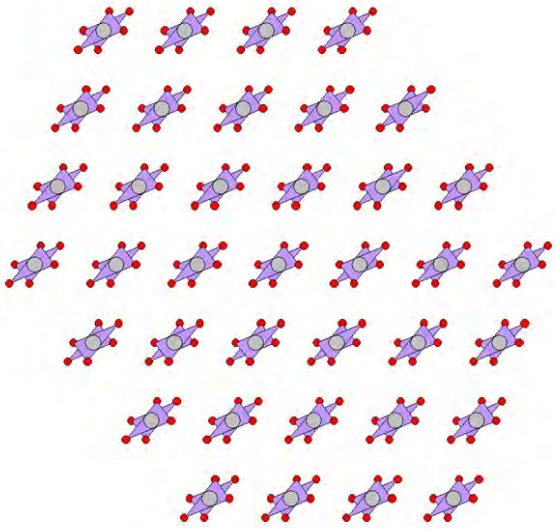

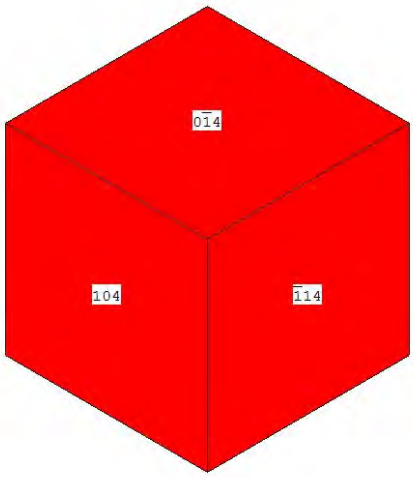

## 2.1. GENERAL INTRODUCTION

In this chapter we are focused in the study of theoretical morphology of sodium nitrate or nitratine ($NaNO_3$). Experimental morphology will be treated in chapters 3 and 4, however here we will also introduce it to compare with the one derived in this chapter. It is difficult to find sodium nitrate in nature because it is mainly formed in a dry and cold ambient inside caves due to a percolation from superior levels, it is basically found in Chile, India and the USA. In the geological description it is reported as granular or massive white crystals.[1] In industrial processes sodium nitrate is commonly used as a fertilizer, in pesticide formulations, in fireworks, in the food industry, and in the energy industry.

Crystals are ordered solids that can be obtained from solid, liquid or vapour phase. Except for solid phase and melt growth, all other growth media (and related techniques) yield crystals with well-developed faces (if some parameters are controlled) which represent the crystal medium interface during growth. Consequently, crystal faces contain information about the nature of the interface as well as about the phenomena taking place at the interface.

Morphology change and its control are important for a great variety of processes. For industrial applications it is not only an economic reason but also of the specific properties of a definite morphology. In industrial production, a solid product usually consists of large quantities of small crystallites, forming powders or grains. In this environment many factors besides morphology determine the solid state properties. The most important are aggregation behaviour, adhesiveness, compactness and particle size distribution. Mostly, a bulky habit, or isotropic morphology, is preferred for several reasons. First and foremost, bulky crystals are most suitable for filtration. Filtration after crystallization is one of the best and most commonly used methods of product purification. Needle-like and plate-like habits have the tendency to clog filters. Furthermore, because of solvent adhesion at the surface, drying the product is easiest if the crystals have a relatively small surface area (big crystals). Finally, bulky crystals are least vulnerable to physical stress. In other words, needles and plates break more easily during product handling, causing them to dust more. Sometimes, a plate-like habit is preferred, for instance in the case of pigments. Because the response to light-reflectivity and light-absorption are non-isotropic properties of crystals, there is always an optimal

orientation of the crystals relative to the incoming light. Because platelets tend to lie down, the maximal optical response is preferentially engineered to be perpendicular to the flat side of the plates. In the pharmaceutical field, habit control is still more important. For the crystallization of drug substances several parameters must be taken into account because they determine a number of important properties of the drug substance, namely the purity and residual solvent content, the polymorphic form, crystal size and size distribution, and it affects downstream processes such as drying, ease of delivery inside the body and formulation of the final drug product. A classic example is that of acetaminophen (gelocatil) which has three polymorphs. One unstable polymorph is preferred by the industry because it is easier (cheaper) to compact in tablets only due to its structure.

Nowadays it is accepted that the habit of a crystal is determined by the relative growth rates of the various crystal faces bounding the crystal. It is therefore dependent on several factors that can be classified in internal and external factors. Internal factors are those that are associated with the crystal itself, such as crystal structure, dislocations and twin boundaries. External factors are all other factors imposed on the crystal by the crystallization conditions, such as temperature, pressure, supersaturation, presence of non-crystalline material (fluid inclusion, etc.), and the flow or convection pattern. Strictly speaking there is not such a thing as the habit of a crystal. But it is possible to define a theoretical habit which is determined in a certain way by the properties of the ideal crystal structure. If this habit can be obtained, then the influence of external factors can be better understood or even quantitatively determined.

Now, one should ask: what are the most stable faces from the thermodynamic point of view? Or what forms do appear in the hypothetical equilibrium morphology of a crystal? Equilibrium morphology is seldom directly relevant to observation but needs to be understood as a basis for interpreting the growth or dissolution morphologies we usually observe. The classical rule that the bounding facets of a crystal in equilibrium are those which are most closely packed receive a reinterpretation and sharper definition in the recognition of F, S and K faces, which will be defined down here.

The theoretical morphology of a crystal can be obtained by two approaches, the Bravais-Friedel-Donnay-Harker (BFDH) and the PBC analysis through the Hartman-Perdok (HP) theory.

The first (BFDH) was postulated by Bravais and developed by Friedel[2] and successively improved by Donnay-Harker (BFDH).[3] The authors had the idea that the lattice type may be deduced from the morphological data of the crystal. It was believed that if all available morphological data of a mineral were treated statistically, and an idealized morphology abstracted, this should reflect the lattice or structural type of the crystal. This morphology is not the equilibrium morphology of the crystal, since it has no relation to any thermodynamic parameters. This theory was essentially phenomenological, since it was postulated by observing macroscopic natural crystals. On the contrary, when equilibrium morphology is calculated by thermodynamics the surface energy must be taken into account because it is comparable to that of the crystal bulk. In this sense it cannot be neglected because it has an important role in the total crystal free energy. Later, in the 1950's Hartman postulated his theory that the crystal faces might be built by only strong bonds; in fact the edges will be built up by a strong bonding direction.

In these theories, the morphology is deduced based on structure alone (BFDH) or qualitatively evaluated bond strengths, entirely neglecting growth parameters. The theoretical (or structural) morphology thus deduced is used as a criterion to analyse the actually observed morphology of a particular crystal i. e. the growth form. If growth forms differ from the structurally deduced morphology, the probable cause for that modification is sought. Such probable causes should be growth parameters which may influence, say PBCs, in the Hartman Perdok analysis. Thus impurities, including solvents, can be the only agents to modify the morphology of a particular crystal, since they may have an effect upon bonding. The influence of impurities in the growth form is introduced in chapter 4.

Here we will describe two approaches for the prediction of the crystal habit: the Bravais-Friedel-Donnay-Harker (BFDH) rule and the Hartman Perdok theory. And further they will be applied to $NaNO_3$.

### 2.1.1. The Bravais-Friedel-Donnay-Harker (BFDH) approach.

The Bravais-Friedel-Donnay-Harker (BFDH) theory is described elsewhere, so we will base this section on Prywer's paper.[4] According to this theory the crystal would be bounded by faces located at a distance proportional to their surface energies, the largest faces are expected to be the faces with the lowest surface energies, such faces are also those with the greatest interplanar distances $d_{hkl}$. In other words, the larger the interplanar distance ($d_{hkl}$) the larger the morphological importance (MI) of the corresponding *hkl* face. This may be stated as:

$$d_{h_1k_1l_1} > d_{h_2k_2l_2} \rightarrow MI_{h_1k_1l_1} > MI_{h_2k_2l_2}$$

It may also be stated as: $R_{hkl} \propto \frac{1}{d_{hkl}}$ where $R_{hkl}$ is the growth rate of the specific (hkl) face.

However, the symmetry elements due to space group symmetry must be taken into account, since they determine the effective interplanar spacing. Thus based on unit cell parameters, space group and hence extinction condition the morphological importance of the different lattice planes of the structure could be modified. Using the reciprocal of the interplanar distances, $1/d_{hkl}$, as the distances (growth rates) from the centre of the crystal to the respective *hkl* surfaces, one may obtain a theoretical BFDH morphology.

Having explained this rather geometric rule,, we move to the Hartman and Perdok theory which has a more physical meaning behind it, even though it begins with a geometric description.

### 2.1.2. The Hartman Perdok (HP) approach.

This section is based on two book chapters written by Hartman.[5, 6] The Hartman Perdok theory is based on the assumption that the habit can be deduced by searching for periodic bond chains (PBCs) within a slice (parallel to a given crystal face) of a given thickness. Crystal growth can be considered as the formation of bonds between crystallizing particles. Because these particles have to come close together in order to

form a crystal, only strong bonds are considered, i. e. those in the first coordination sphere. In a first approximation the criterion is geometrical rather than based on bond energies. However, energetic calculations can be performed a posteriori to discriminate the importance of different faces.

If we consider a two-dimensional growth layer, bounded by straight edges, the question is why from all crystallographic possible lattice rows only these are straight. Figure 1 shows a layer and the crystallizing units that are represented by small identical building units, the so called Kossel crystal. Growth occurs by filling kink sites. A next building unit can be attached in a terrace, ledge or kink. The probability of attachment in a kink is higher than in a ledge or on a terrace, so that the kink site is favoured on growth because here the building unit has three bonds with the bulk crystal.

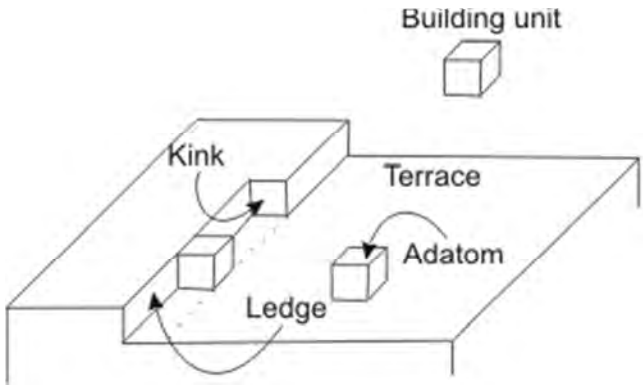


**Figure 1.** Simplified model of an F face which have terraces, a ledge (steps) and a kink. Kinks are the growing sites for the face.

The straight edge is parallel to a lattice row [uvw] in which identical building units are bonded by strong bonds. This means that there is an interrupted chain of strong bonds, a PBC parallel to [uvw] direction. Using this concept, three categories of faces present themselves (figure 2):

- F faces: a slice $d_{hkl}$ contains two or more PBCs.
- S faces: a slice $d_{hkl}$ contains only one PBC.
- K faces: a slice $d_{hkl}$ contains no PBC at all.

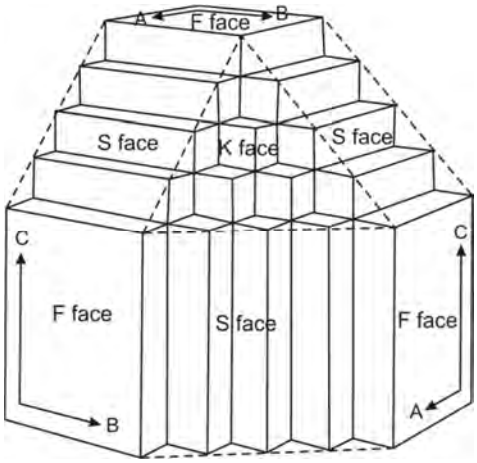


**Figure 2.** The three kinds of surfaces: F faces have 2 PBCs (AC, BC or AC). S faces have only one PBC (A, B or C). K faces do not have any PBC at all.

The slice of thickness $d_{hkl}$ is the interplanar distance of the face (hkl). Because the surface structure of a crystal is determined by the minimum specific surface energy, $d_{hkl}$ represents the repeat distance of this energy. As a consequence $d_{hkl}$ may be a submultiple owing to the centring of the lattice, the presence of screw axes or glide planes perpendicular to the face (hkl). Thus the same X-ray diffraction extinction rules are valid.

The F faces are able to grow according to the layer mechanism, so that their growth rate is small. A small growth rate means a higher probability to be a face remaining on the growth morphology of the crystal. Therefore they determine the theoretical habit, although it does not imply that all F faces should be present in the habit. The growth of K faces can occur everywhere on the surface without nucleation (surface diffusion is null because the coverage degree of kinks equals the unity) so the growth rate is high and faces do not occur on the crystal. The S faces are intermediate between F and K, they would need a one dimensional nucleation, but because in practice at all temperatures there are sufficient kinks present, they also grow fast and normally do not occur on the crystal.

It should be noted that PBC analysis not only defines the character of the face (F, S or K faces) but it also defines at the same time the atomic configuration at the surface. Moreover, if the growth fronts on a face are poligonized, the straight direction should be

parallel to the PBCs running in the slice parallel to the face. However, the argument cannot be reversed: a flat face is not automatically an F face and a straight step of a growth layer is not necessarily parallel to PBC. F faces and PBCs cannot be determined by observation or by experimentation, but have to be deduced from the crystal structure.

There are two methods to find PBCs and F faces: a visual one, making use of projections of crystal structures and a computational method. We shall only describe the first because this is the one employed in this work.

We start by solving the crystal structure of the compound of interest. Then the first coordination sphere must be determined (eventually the second coordination sphere may also be taken into account), and from this all bonds in a primitive unit cell must be listed. Then a projection of the structure on a plane perpendicular to a possible PBC is made. With the aid of the list of bonds, primitive PBCs are sought in the projection direction, the symmetrically equivalent PBCs are sketched and these are combined, eventually by adding loose atoms, to complete PBCs. Then, possible bonds between complete PBCs are sought so as to construct slices $d_{hkl}$. Often such slices are more easily recognised than PBCs. In doing so, the intersection of two slices may constitute a PBC. It should be noted here that the slices in the projection are not necessarily bounded by straight lines a distance $d_{hkl}$ apart. The boundary between successive slices may be curved, so if it is too irregular slices tend not to be recognized by the visual method. Once slices parallel to a [uvw] direction have been found, primitive PBCs in these slices can be sought and projections parallel to these directions are made. This procedure is repeated until a self-consistent set of PBCs and F faces are obtained. The slices must be stoichometrical and they do not have an electrostatic dipole moment perpendicular to its direction. Otherwise the related face cannot exist due to the repulsion forces between slices; in this case various reconstructions can be performed onto the face in order to stabilize it.

Applying the Hartman Perdok theory we can discern the most important faces in a particular structure, but this theory does not predict anything about the relative importance of them. However it gives surface structures that afterwards can be employed to calculate the specific surface energy for the F faces. Finally, by the application of the Wulff plot we can construct the equilibrium morphology of crystals.

Through the Hartman Perdok theory we can discern the most important faces in a particular structure, but this theory does not predict "a priori" anything about the relative importance of them. To do that, one can calculate the attachment energy, $E_{att}(hkl)$, for each (hkl) face, i.e: the energy released, per growth unit, when a new slice $d_{hkl}$ forms on a pre-existing face. As a matter of fact, the main HP hypothesis is that the growth rate $R_{hkl}$ of a (hkl) face is proportional to the attachment energy: hence, one can predict, in a preliminary way, the growth shape of a crystal by applying the simple relation:

$$R_{hkl} \approx E_{att}(hkl)$$

Moreover, the HP theory allows obtaining the surface structures that afterwards can be employed to calculate the specific surface energy, $\gamma_{hkl}$, for the F faces. Finally, by the application of the Wulff's plot we can construct:

- the equilibrium shape of crystals, through the $\gamma_{hkl}$ values,
- the related growth shape through the $E_{att}(hkl)$ values.

### 2.1.3. Surface energy.

In GULP manual[7] there is an interesting part about surface properties, so we summarize it here. The properties of surfaces are as important as those of the bulk since they control the interaction between the crystal and the external environment. It is worth remembering that the shape of a particle or crystallite is determined by the properties of the surface relative to the bulk. Due to this fact surface modeling using atomistic simulation has been being developed for many years.

There are two steps to any surface calculation: the creation of the surface from the bulk material and the subsequent calculation of its optimized structure and properties. When a surface is cleaved, there are also other important aspects to take into account, particularly the type of surface itself. There are three basic types of surface, depicted schematically in figure 3. Here the plane charges distribution (q) is presented on the right hand of each plane and the repetition unit is shown on the left.

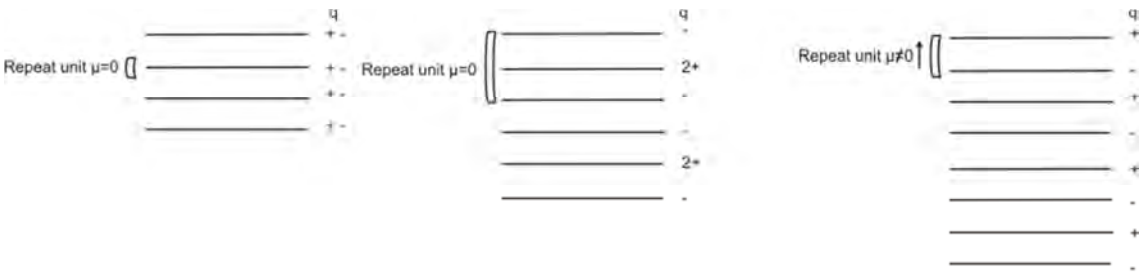


**Figure 3.** The three types of ionic surfaces according to charge distribution within the repetition unit, after Tasker.[8] Type 1: neutral planes; type 2: symmetric charged planes; type 3: charged planes with a perpendicular dipole moment.

In type 1 the atomic structure consists of charged neutral sheets of ion parallel to the surface plane and thus all shifts are guaranteed to yield a surface without a dipole moment normal to the surface.

In type 2 surfaces there are combination of layers of cations and anions that possess zero net dipole moment in the appropriate direction. A non-polar surface can be obtained in this case.

In type 3 all cleavage planes result in dipolar surface, which is therefore likely to be less stable. These surface types are reconstructed in order to erase the dipole moment. This typically involves the creation of cation or anion vacancies at the surface.

There are two practical approaches that are widely used to determine the surface energy by computational means.[7] In the first, a two-dimensional slab of material is created from the bulk, thus creating two surfaces. In this method it becomes necessary to assess whether the slab is thick enough since the properties must converge to those of the bulk at the centre of the slab. In the second method, a single surface is created by employing a two region strategy. Here the solid is divided into region 1, which contains the surface and all the layers of atoms below it that exhibit significant atomic relaxation, and region 2, which contains the rest of the bulk material where it is assumed that no displacements from the three-dimensional crystal structure are induced. In practice, only the atoms of region 2 that have an interaction with region 1 need be explicitly considered, so the depth of region 2 is controlled by the cut-offs of the force field. This second method is the most efficient and precise for atomistic techniques. However, it is considerably harder to extend to quantum mechanical methods since electronic perturbations may extend further into the bulk.

Once the specific surface energy is calculated we may draw the morphology of the crystal by the application of the Wulff plot as is described below.

### 2.1.4. Equilibrium form: the Wulff's plot.

Kern introduced the Wulff's plot with a historical note.[9] In late 19th century, some physicists tried to understand how crystals grow applying energetic concepts rather than geometrical (in that time crystallography was at its origins, X-ray diffraction was not discovered yet, and thermodynamics was being developed, evidently BFDH and HP approaches were not yet formulated). They looked for some invariant during the process that turned out to be the equilibrium since only one solution could be found. Curie and Gibbs at that time generalized Young's surface tension concept to anisotropic bodies, seeking for a crystal form of total minimal surface tension. Wulff stated his law on a wrong basis but later von Laue and Dinghas gave clear demonstrations of Wulff's statements.

Crystal morphologies can be calculated based on either the surface energy or attachment energy, which are typically taken to represent growth under thermodynamic or kinetic control respectively. In the first, equilibrium morphology, the contribution of a given plane to the total surface area is inversely proportional to its surface energy. For the second, the growth morphology, the surface area contribution is proportional to the negative of the attachment energy this is because surfaces with highly exothermic attachment energy will rapidly grow out of the morphology to leave the slow growing bounding surfaces.

In order to draw quantitatively the habit of a crystal we use the Wulff plot which is a phenomenological approach that helps us to obtain the equilibrium form of a crystal, i. e. the habit that at constant volume has the minimum of the total surface energy. So we can write:

$$\Phi = \sum \gamma_i A_i = \min \text{ at V=const.}$$

Where $\gamma_i$ is the specific surface energy and $A_i$ is the surface area of the $i^{th}$ face.

Solving the problem we arrive at the condition that:

$$\frac{\gamma_1}{h_1}=\frac{\gamma_2}{h_2}=\ldots=\frac{\gamma_i}{h_i}=\lambda$$

Where $\gamma_i$ is the surface energy of the face (a differential quantity measuring the change of the free energy of the condensed phase when its surface is increased), $h_i$ is the normal distance from an arbitrary point inside the form to the face i and $\lambda$ is a scalar number.

Drawing heights $h_i$ proportional to $\gamma_i$ from an arbitrary point O on the normal of the potential faces, the normal planes passing at the ends of these lengths determine concentric volumes. Therefore, for a given volume of the crystal, the equilibrium form is the most inner polyhedron of all concentric ones.

This means that for knowing the equilibrium form of the crystal we first have to know the surface energy values of the different crystal forms. Unfortunately it is not an easy quantity to measure due to the elastic properties of the solids. Moreover due to the intrinsic anisotropy of different faces it follows that the surface energies also became anisotropic. Therefore, we computed some semi-empirical calculations as described above.

We have already defined the background of the problem about determinations of theoretical morphology. Therefore, we can proceed with our problem: what is the theoretic morphology of $NaNO_3$? We will start reviewing previous works about $NaNO_3$ morphology, then we will continue by explaining some useful aspects in the space group of $NaNO_3$, $R\bar{3}c$. And finally, we will apply the BFDH and HP approaches to get and compare results for the respective theoretic morphology.

## 2.2. INTRODUCTION TO THE $NaNO_3$ SYSTEM

In this section we expose the previous works about sodium nitrate morphology and then we introduce the crystallography of the $R\bar{3}c$ space group. Finally the problem of the {104} and {012} forms is presented.

### 2.2.1. Previous works.

Benages et al.[10] studied the crystal growth morphology finding that single {104} rhombohedral crystals grow systematically from pure aqueous solution, see figure 4. The theoretical athermal equilibrium morphology, taking into account the surface energy published in Benages et al.,[10] is a simple cleavage {104} rhombohedra.

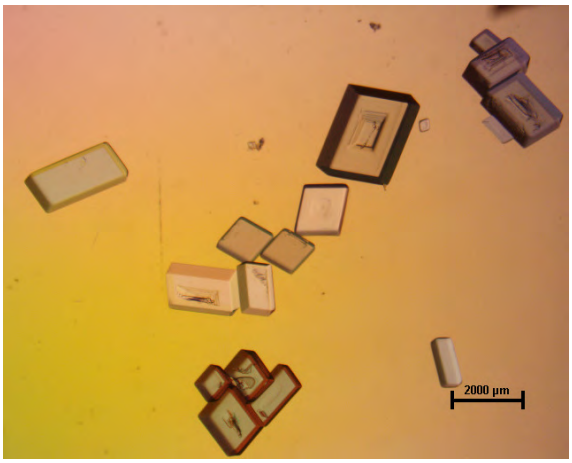


**Figure 4.** $NaNO_3$ crystals grown from pure saturated water solution at 300 K. Crystallization temperature 293 K, time: 2 days.

### 2.2.2. A crystallographic description of R$\bar{3}$c space group.

The atmospheric and room temperature phase of $NaNO_3$ or nitratine belongs to the R$\bar{3}$c space group.

The R$\bar{3}$c or R$\bar{3}$2/c space belongs to $\bar{3}$m Laue (crystal) class. It has an $\bar{3}$ inversion axis parallel to **z** direction. It has three symmetry equivalent axes of order 2 parallel to **x, y** and **w** directions, respectively. The glide plane "c", parallel to **z**, made a translation of ½ $c_0$. This set of basic symmetry operations generates many other symmetry operations such as screw axes and diagonal glide planes.

The symbol 'R' is used because we employ a hexagonal description of the rhombohedral primitive cell (with Z = 2). The triple R cell corresponds to the 'hexagonal description' of the rhombohedral lattice. So, we have six unit formulas per cell (Z = 6). In figure 5 we show this primitive cell with the atoms inside and also a schematic drawing of the relation between the rhombohedral and hexagonal cell.

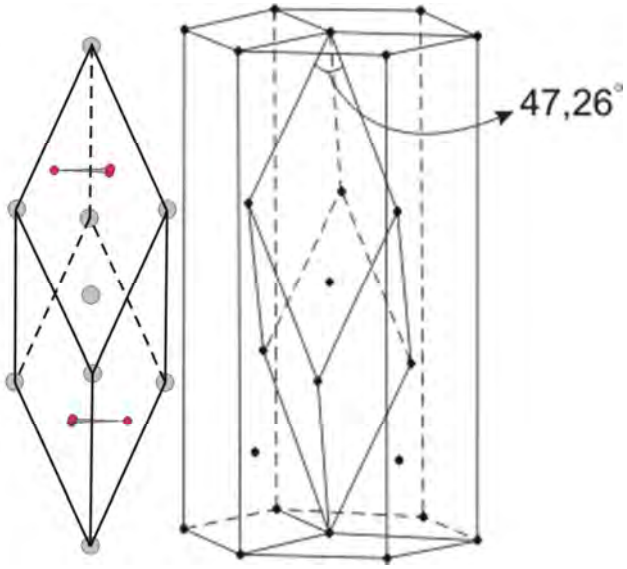


**Figure 5.** Left: the primitive unit cell of $NaNO_3$. Right: Relation between the primitive cell and the hexagonal cell in the same compound. In this case only sodium atoms are depicted.

Crystals in this space group can be described in two different reference frames depending on if the description is made in a rhombohedral unit cell or in the hexagonal

frame. In order to transform from one to another we can use the following matrices where the subscripts *rh* are for rhombohedral settings and *hex* is for hexagonal settings.

$$\begin{pmatrix} a_{rh} \\ b_{rh} \\ c_{rh} \end{pmatrix} = \begin{pmatrix} \frac{2}{3} & \frac{1}{3} & \frac{1}{3} \\ -\frac{1}{3} & \frac{1}{3} & \frac{1}{3} \\ -\frac{1}{3} & -\frac{2}{3} & \frac{1}{3} \end{pmatrix} \begin{pmatrix} a_{hex} \\ b_{hex} \\ c_{hex} \end{pmatrix}$$

$$\begin{pmatrix} a_{hex} \\ b_{hex} \\ c_{hex} \end{pmatrix} = \begin{pmatrix} 1 & -1 & 0 \\ 0 & 1 & -1 \\ 1 & 1 & 1 \end{pmatrix} \begin{pmatrix} a_{rh} \\ b_{rh} \\ c_{rh} \end{pmatrix}$$

The $NaNO_3$ structure in the hexagonal framework is described by the following atomic positions:

- Sodium has the Wyckoff position 'b'. It is in $\bar{3}$ inversion axe with six equivalent positions by symmetry. The coordinates are: 0, 0, 0; 0, 0, ½.
- Nitrogen has the Wyckoff position 'a' with symmetry 32 with six equivalent positions by symmetry. The coordinates are: 0, 0, ¼; 0, 0 ,¾.
- Oxygen has the Wyckoff position 'e' with symmetry 2 with eighteen equivalent positions by symmetry. The coordinates are: x, 0, ¼; 0, x, ¼; $\bar{x}$, $\bar{x}$, ¼; $\bar{x}$, 0, ¾; 0, $\bar{x}$, ¾; x, x, ¾.

The hexagonal cell determined by X-ray diffraction have six $NaNO_3$ groups with parameters $\mathbf{a_0}$ = 5.070 Å, $\mathbf{c_0}$ = 16.82 Å at 293 K.[11]

In this work we have to calculate some vector modules. In the hexagonal cell we cannot employ the Pythagoras theorem because we are not in an orthonormal reference system. Instead, we have to use the metric matrix G defined as:

$$G = \begin{pmatrix} a_i a_i & a_i b_i & a_i c_i \\ b_i a_i & b_i b_i & b_i c_i \\ c_i a_i & c_i b_i & c_i c_i \end{pmatrix} = \begin{pmatrix} a^2 & abcos120^o & 0 \\ bacos120^o & b^2 & 0 \\ 0 & 0 & c^2 \end{pmatrix} = \begin{pmatrix} 25{,}7049 & -12{,}85245 & 0 \\ -12{,}85245 & 25{,}7049 & 0 \\ 0 & 0 & 282{,}9124 \end{pmatrix}$$

Where $\mathbf{a}_i\mathbf{a}_i$, $\mathbf{a}_i\mathbf{b}_i$… are the scalar product of the unit cell vectors. Now the module of a certain vector *v* is defined as:

$$\|v\|^2 = v \cdot G \cdot v^t$$

In this space group we have the following systematic extinctions:

- hkil → $\bar{h} + k + l = 3n$
- hh2$\bar{h}$ → $(l = 3n)$
- h$\bar{h}$0l → $(h + l = 3n); l = 2n$
- hkil → $2n$

People working with the structure determination adopted a small rhombohedral unit cell containing only two $NaNO_3$ units per cell. This corresponds to an acute rhombohedron with $\mathbf{a_{rh}}$ = 6,48 Å and $\boldsymbol{\alpha}$ = 47,26º.[12] However, this choice is not suitable for our purposes and then we will use the hexagonal cell ($\mathbf{a_0}$ = 5.070 Å, $\mathbf{c_0}$ = 16.82 Å) which contains six formula units and allows to refer all the crystal forms to the {10.4} cleavage rhombohedron, that has an important morphological meaning. One can imagine this rhombohedron as a distorted cube, elongated or compressed across one of the $A_3$ symmetry axis. Therefore, it is possible to describe the $NaNO_3$ structure in analogy with that of halite (FCC cubic cell with Z = 4) changing the spherical Cl ions for the planar $NO_3$ groups maintaining the sodium positions. The $NO_3$ group is an equilateral triangle with oxygen in the vertexes and nitrogen in the centre. They are perpendicular to the [001] direction which is the analogue of [111] direction in NaCl structure. In $NaNO_3$ structure the $NO_3$ groups are alternatively rotated 60º in order to allow that Na ions have a coordination number 6 to the oxygen atoms; in this case there are not repulsive forces. This is the reason why the repeat period of $NaNO_3$ is double i.e. in one repeat period there are two sodium ions and two nitrate groups, while in NaCl only one ion of each appears. In figure 6 we show a projection of $NaNO_3$ with [001] direction in vertical and NaCl projection with the [111] direction vertical. Na atoms are the grey spheres, Cl ions are blue spheres, O atoms red spheres and N atoms are not depicted. As will be seen throughout the chapter, $NO_3$ groups are represented by a triangle. The repetition units in these directions are also highlighted.

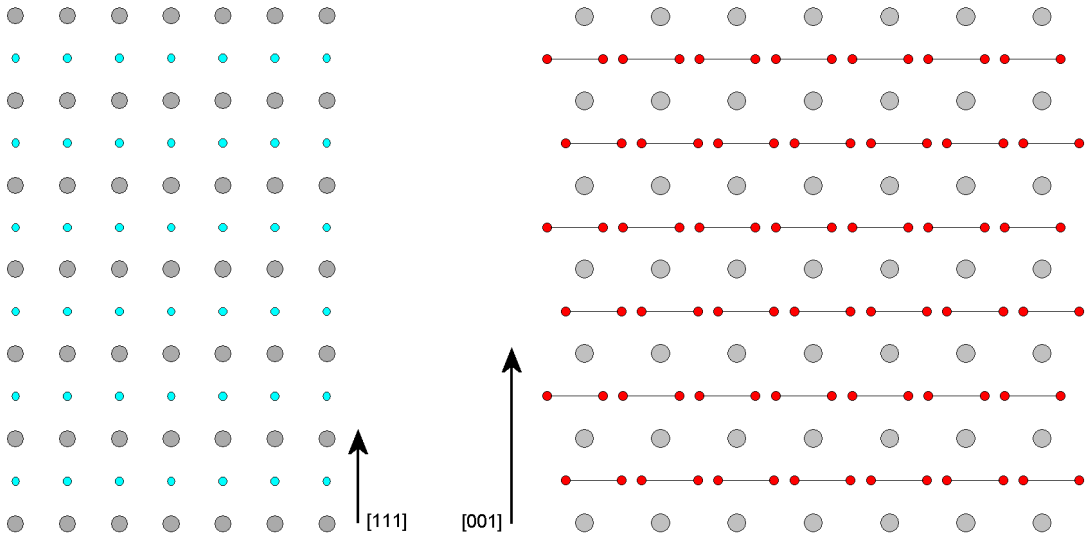


**Figure 6.** Comparison between the NaCl structure (left) and $NaNO_3$ structure. It can be seen that in these orientations, the gravity centre of the ions are located in the same position in the two structures.

In figure 7 we show the stereographic projection of the {012} form, the steep rhombohedron, as an example. There is also a picture of the {012} form with some of the main directions depicted. From here we can extract that the 'c' plane is the set of planes {210} that cuts the edges of the {012} rhombohedron. We also highlight in advance that the vertex directions converging in the apex are built by the <42$\bar{1}$> PBCs as will be analysed later.

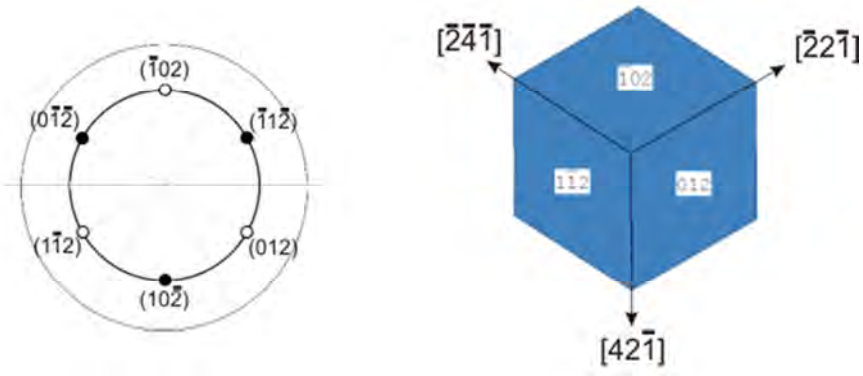


**Figure 7.** Stereographic projection showing the equivalent faces on {012} form (left) and the related morphology with some calculated directions (right) of the {012} form of $NaNO_3$.

### 2.2.3. The {104} and {012} problem.

We have already seen in the previous section that the $<42\bar{1}>$ set of equivalent direction define the {012} rhombohedral edges. Similarly, the {104} form edges are defined by the $<48\bar{1}>$ set of equivalent directions. Therefore, we can calculate the angle that defines both rhombohedra by the relation:

$$\cos\alpha = \frac{u_1 \cdot G \cdot u_2}{\|u_1\| \cdot \|u_2\|}$$

Where the numerator is the scalar product of two adjacent equivalent directions of the form and $\|u_i\|$ is the module of the corresponding vectors.

For the acute angle we have obtained that:

- Angle for the {012} form is 77.43º.
- Angle for the {104} form is 77.28º.

This leads to the following surprising result: if one examines only one face of a {104} or a {012} rhombohedron, it is practically impossible to make a distinction between them, if one only measures the angles on the face. There are two ways for solving this ambiguity:

- Observing the growth or the dissolution pattern on the surface of the face. In fact the symmetry **c** plane bisects the acute angle on the {012} and the obtuse one on the {104} rhombohedron.
- Observing the face in the context of other adjacent faces; as a matter of fact, the neighbouring faces are completely different in the two cases.

For the isostructural mineral calcite Aquilano et al.[13] and references therein have demonstrated that the most stable form is {104} so that it is the largest form that appears in the athermal equilibrium shape. In this chapter we demonstrate that the {104} has by far the most stable surface profile so that it is the only one that appears in the athermal equilibrium form of sodium nitrate due to its incredible low surface energy as has been calculated earlier.[10]

## 2.3. DETERMINATION OF THE THEORETICAL MORPHOLOGY OF $NaNO_3$

As described above in this chapter we are comparing the theoretical shape of $NaNO_3$ crystal determined by the BFDH and HP approaches.

### 2.3.1. The Bravais-Friedel-Donnay-Harker approach.

The morphologic importance (MI) of the {hkl} forms of nitratine according to the Bravais-Friedel-Donnay-Harker approach can be evaluated by calculating the $(d_{hkl})^{-1}$ values (see Table 1) and drawing the corresponding Wulff's plot,[14] the minimum among the $(d_{hkl})^{-1}$ values being assumed as a reference.

**Table 1.** X-ray indexed diffraction for $NaNO_3$. The inverse of lattice spacing and the ratio to the minimum are essential to calculate the BFDH growth shape.

| Form {hkl} | Allowed $d_{hkl}$ value (Å) | $(d_{hkl})^{-1}$ $(Å)^{-1}$ | Ratio to the minimum $(d_{hkl})^{-1}$ value |
|---|---|---|---|
| 012 | $d_{012} = 3.8922$ | 0.2569 | 1 |
| 104 | $d_{104} = 3.0369$ | 0.3293 | 1.2818 |
| 001 | $d_{006} = 2.8033$ | 0.3567 | 13885 |
| 110 | $d_{110} = 2.5350$ | 0.3945 | 1.5356 |
| 113 | $d_{113} = 2.3099$ | 0.4329 | 1.6851 |
| 101 | $d_{202} = 2.1242$ | 0.4708 | 1.8326 |
| 018 | $d_{018} = 1.8963$ | 0.5273 | 2.0525 |
| 116 | $d_{116} = 1.8802$ | 0.5319 | 2.0705 |
| 211 | $d_{211} = 1.6515$ | 0.6055 | 2.3569 |
| 122 | $d_{112} = 1.6282$ | 0.6142 | 2.3908 |
| 214 | $d_{214} = 1.5437$ | 0.6478 | 2.5216 |
| 119 | $d_{119} = 1.5042$ | 0.6648 | 2.5878 |
| 125 | $d_{125} = 1.4883$ | 0.6719 | 2.6154 |
| 100 | $d_{300} = 1.4636$ | 0.6832 | 2.6594 |

Hence, the theoretical growth shape is built by considering only those spacing that fulfil the systematic extinction rules of nitratine space group, $R\bar{3}c$. It is clear, from figure 8 that the forms that appear in the growth shape are {012}, {$01\bar{2}$} forms, evidently with the same MI because $d_{012} = d_{01\bar{2}}$. In contrast to the expected result, the second most important form {014}, {$10\bar{4}$} actually does not appear. This drawback is only due to geometrical reasons. However, the {001} form also appears. It is exactly the same growth morphology derived by the BFDH method for calcite.[15] This contrasts with the equilibrium athermal morphology determined by HP approach and the different experimental growth shape of calcite and nitratine (see below).

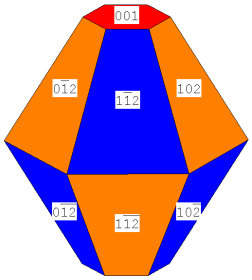


**Figure 8.** The growth shape of $NaNO_3$ according to the BFDH approach. The {012} and the {$01\bar{2}$} forms have the same importance. The {001} form also appears in the growth morphology.

### 2.3.2. The Hartman-Perdok approach.

#### 2.3.2.1. Building units of $NaNO_3$.

Following the Hartman-Perdok procedure we analyse the first (shorter) coordination sphere in the $NaNO_3$ structure, the second coordination sphere is added because it has been demonstrated to play an important role in the equilibrium shape prediction of calcite (see Aquilano et al.[13] and references therein for a complete discussion about calcite equilibrium morphology). As can be seen in Table 2, one cannot exclude δ bonds without also excluding γ bonds; these bonds are considered in the second coordination sphere and are very important. We can separate the bonds into two kinds of clusters. The building unit 1 ($BU_1$) is the strongest with three different Na-O bond lengths (α, β and γ bonds) and the shortest Na-N interatomic distance (ε bond), and the building unit 2 ($BU_2$) with three equal Na-O bond length (δ bond) and the largest Na-N bond length (π bond).

**Table 2.** Bond distances of first and second coordination sphere.

| | Bond | Length (Å) |
|---|---|---|
| $BU_1$ | α (Na-O) | 2,4038 |
| | β (Na-O) | 3,4750 |
| | γ (Na-O) | 4,2864 |
| | ε (Na-N) | 3,2455 |
| $BU_2$ | δ (Na-O) | 4,3846 |
| | π (Na-N) | 4,2050 |

In figure 9 we show the main bonding directions that can be found by the combination of $BU_1$ and the $BU_2$ constructions. Here we drew bonds for 1.5 repetition units, the arrows beside every construction mark a set of equivalent PBCs directions and the vector length. The chains are a little bit tilted to visualize better the different nitrate group orientations. In this figure (and throughout the text) α, β and γ bonds are marked by a dashed line and δ bonds are marked by a dotted line. It is worth remembering the different $NO_3$ group orientations in the repetition unit for both kinds of BUs. These directions can be found from the unit cell following the HP procedure. We start with

$Na_1$ atom in the centre, then we search for the shortest Na-O bond (α-bond) and then complete the bonding with the other $Na_1$-$O_i$ bonds within the same nitrate group (with the $N_1$), thus we have bonds $Na_1$-$O_2$ and $Na_1$-$O_3$. This nitrate group now becomes the centre, and then we search for the shortest $N_1$-O (ε-bond) in order to construct bonds between $O_1$-$Na_2$, $O_2$-$Na_2$, and $O_3$-$Na_2$. In continuation, $Na_2$ atom becomes the centre and we repeat the first step. This procedure is repeated until a complete set of PBCs is obtained so that we can make projections along them to verify if parallel PBCs are bonded together within a certain slice of thickness $d_{hkl}$ to create an F face. All the directions depicted in figure 9 can be found in this way except for <001> directions that are bonded only with $BU_2$. In this last case we should look exclusively for δ bonds. In the case of <42$\bar{1}$> we should find first the construction in which only $BU_1$ are involved; the alternative construction with δ bonds can be derived after making an appropriate projection as is depicted in figure 9.

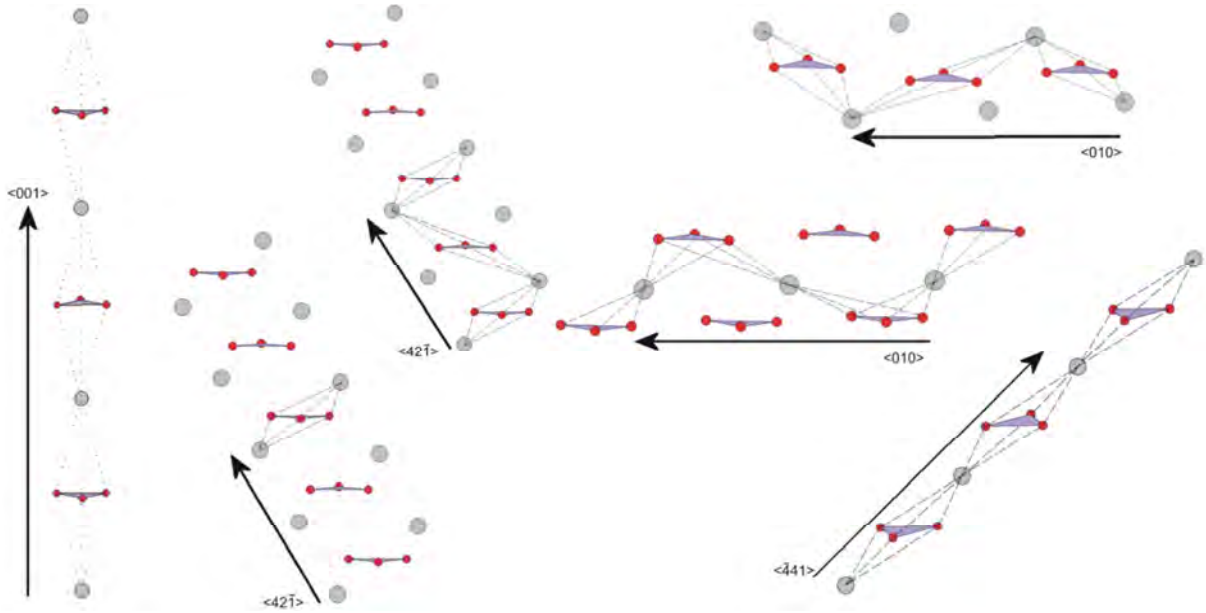


**Figure 9.** Main PBC's directions and their different constructions in the $NaNO_3$ structure.

Now we will describe the main features of the principal PBC's directions showed in figure 9.

- The $<\bar{4}41>$ directions are constructed only by $BU_1$, and so they are the strongest bonding directions. The periodicity of this chain is $1/3[\bar{4}41] = 12{,}98$ Å.

- The $<42\bar{1}>$directions are composed, as can be seen in figure 9, by a combination of $BU_1$ and $BU_2$ so it is a weaker direction in respect to the $<\bar{4}41>$ direction. It has a repetition unit of $1/3\ [42\bar{1}] = 8.11$ Å. This direction can also be constructed by $BU_1$ only. As is pointed out in figure 8, this chain is intrinsically polar in the sense that the charges do not lie in the same plane as can be viewed in figure 9 and in the projection along $<42\bar{1}>$ below (figure 10).

- The <010> directions as depicted in figure 9 are built only by $BU_1$. They can be constructed in two ways: sodium ion or nitrate group on the borders. In the former case, all the nitrate groups are pointing to the same direction. This situation can be overcome if we look at the nitrate group terminated chain, the nitrates on both sides are pointing in opposite directions. In <010> direction we have to highlight that one out of every two border ions are missing as can be clearly seen in the figure 9 following the bonds. It has a unit repetition of $2\cdot[010] = 10.14$ Å. As in the case of $<42\bar{1}>$ chains, the <010> directions are intrinsically polar for the same argument.

It is interesting to highlight here that the strongest $<\bar{4}41>$ bond directions has the largest periodicity of the three PBCs described so far. This fact is due to the charge alternation that gives a non-polar chain. Furthermore $<\bar{4}41>$ directions can only be constructed in one and the same way while $<42\bar{1}>$ and <010> can be built in different ways. Finally, these last two sets of directions ($<42\bar{1}>$ and <010>) have a 'zigzag profile' while $<\bar{4}41>$ directions are 'linear'.

- The [001] direction is constructed only by $BU_2$, as can be seen in figure 9, which have the longest Na-O bonds considered so far (δ-bonds), hence it is the weaker bond direction. It has a repetition unit of [001] = 16.82 Å.

Now that we have defined the stronger bond directions in $NaNO_3$, we can continue with the projections along them as HP theory indicates.

### 2.3.2.2. PBC analysis of $NaNO_3$ structure.

Following the strongest bond directions derived above and the Hartman Perdok theory [16-18] we made the projection along the directions <$\bar{4}41$>, <$42\bar{1}$>, <010> and <001> in order to search bonding between these PBCs and, thus, find the faces and their character.

#### 2.3.2.2.1. The [$\bar{4}41$] direction.

Figure 10 shows the $NaNO_3$ structure projected along [$\bar{4}41$] direction. We can observe a series of parallel periodic bond chains. As it is said above these chains are built with the $BU_1$.

Two considerations are necessary:

a) The structural analogy between NaCl and $NaNO_3$ permits us to reveal the correspondence between <100> direction in NaCl and <$\bar{4}41$> direction in $NaNO_3$. In both cases bonds are constituted by the alternance of aligned positive and negative charges. Moreover the anisotropy of the $NO_3$ ions implies a doubled period in the chain (11.08 Å in $NaNO_3$ while 5.64 Å simple period in NaCl holds).

b) By analogy of calcite calculations, in which the end chain energy of <$\bar{4}41$> direction is attractive, it is reasonable to assume that the same holds also for the <$\bar{4}41$> direction in $NaNO_3$ and hence it is a true PBC according to the Hartman-Perdok theory. This statement must be true because <$\bar{4}41$> direction is the strongest bond direction. If it is not true the crystal itself will not exist.

When analysing this projection we can see many features that must be noticed always referring to figure 10.

- In the direction [100] or its equivalent [010] (blue lines) we can see that the [$\bar{4}41$] PBC has an interrupted series of bonds in the slice of thickness $d_{104}$.

Consequently, we have (at least) two non-parallel PBCs and hence the face (104) has an F character.

- In the direction [110] (green solid lines) we can observe that [$\bar{4}41$] PBCs are not connected with any bond within the slice $d_{018}$. It gives a first notion that the (018) face has an S character.

An interesting fact can be extracted when we take the double spacing $2d_{018}$. Then we can construct a continuous series of bonds in the equivalent directions <010> that would play an important role in the formation of screw dislocations in this face. It is constructed by a series of strong bonds.

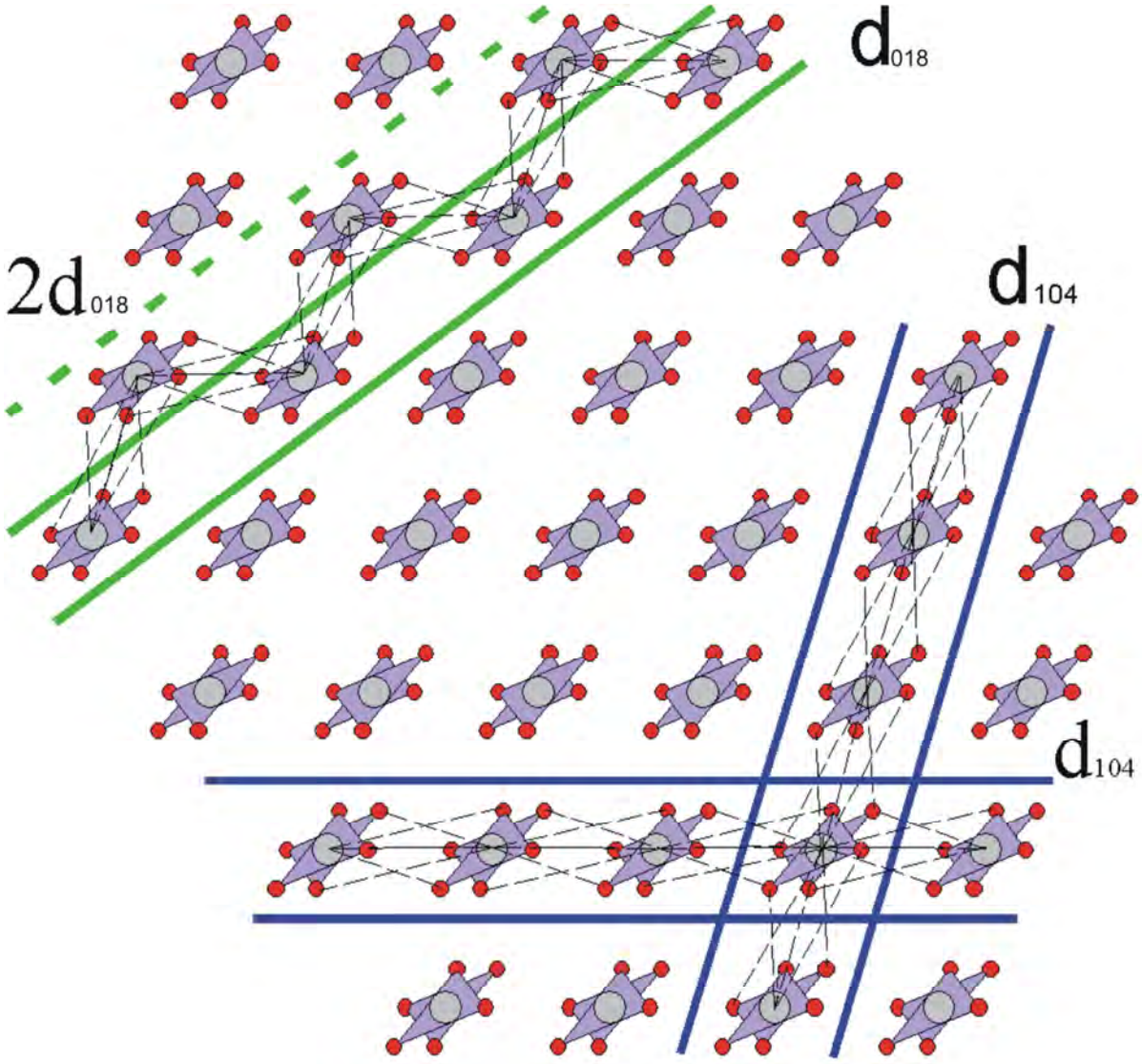


**Figure 10a.** Projection along the [$\bar{4}41$] direction. The (104) face is outlined by blue lines and the (018) face with green lines.

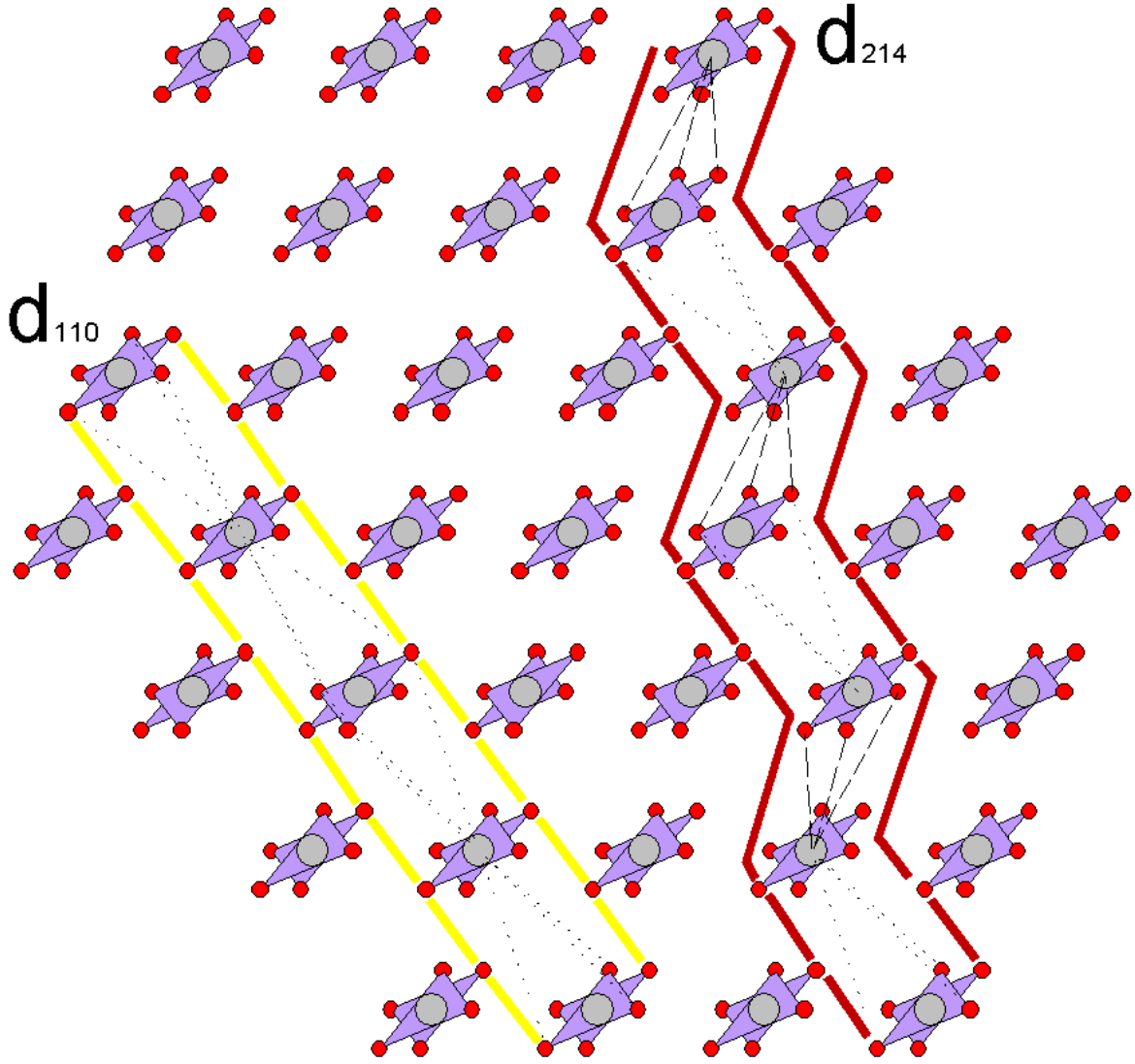


**Figure 10b (cont.).** Projection along the $[\bar{4}41]$ direction. The (110) face is outlined by yellow lines and the (214) 'zig-zag' face with brown lines.

- If we look at the [001] direction (yellow lines) we find that the $[\bar{4}41]$ PBCs are bounded by the weaker δ bonds. So in the slice $d_{110}$ we have a strong PBC and a weak PBC, therefore the prism {110} has a weak F character.
- When dealing with a $d_{214}$ slice we do not find a simple bond. Similarly to what we found in the {018} form, the (214) face is formed by a complex 'zigzag reconstruction' where a succession of PBC bonds that belong to (110) face and (104) face, weak and strong bonds respectively, holds. Therefore this face cannot be considered as F by itself but can be considered as a summation of (110) and (104) microfacets.

#### 2.3.2.2.2. The $[42\bar{1}]$ direction.

Figure 11 shows the projection along $[42\bar{1}]$ direction with the PBC analysis drawn on it. As said above and already seen in figure 9 this PBC is polar because charges are not aligned. The presence of this PBC may be the reason for apparition of polar faces; they must be reconstructed in order to exist. From figure 11 we can highlight the following facts:

- We clearly observe that the $[42\bar{1}]$ PBCs are bonded in the direction [001] (yellow lines) to give the $(1\bar{2}0)$ face equivalent to (110) face in the positive octant within a slice of thickness $d_{110}$. So, the prism {110} form is shown again to have a weak F character.
- The PBC $[42\bar{1}]$ is bonded through [010] direction within a slice of $d_{104}$. All the bonds are inside this slice. Thus {104} form takes another PBC, and so, it has a marked F character.

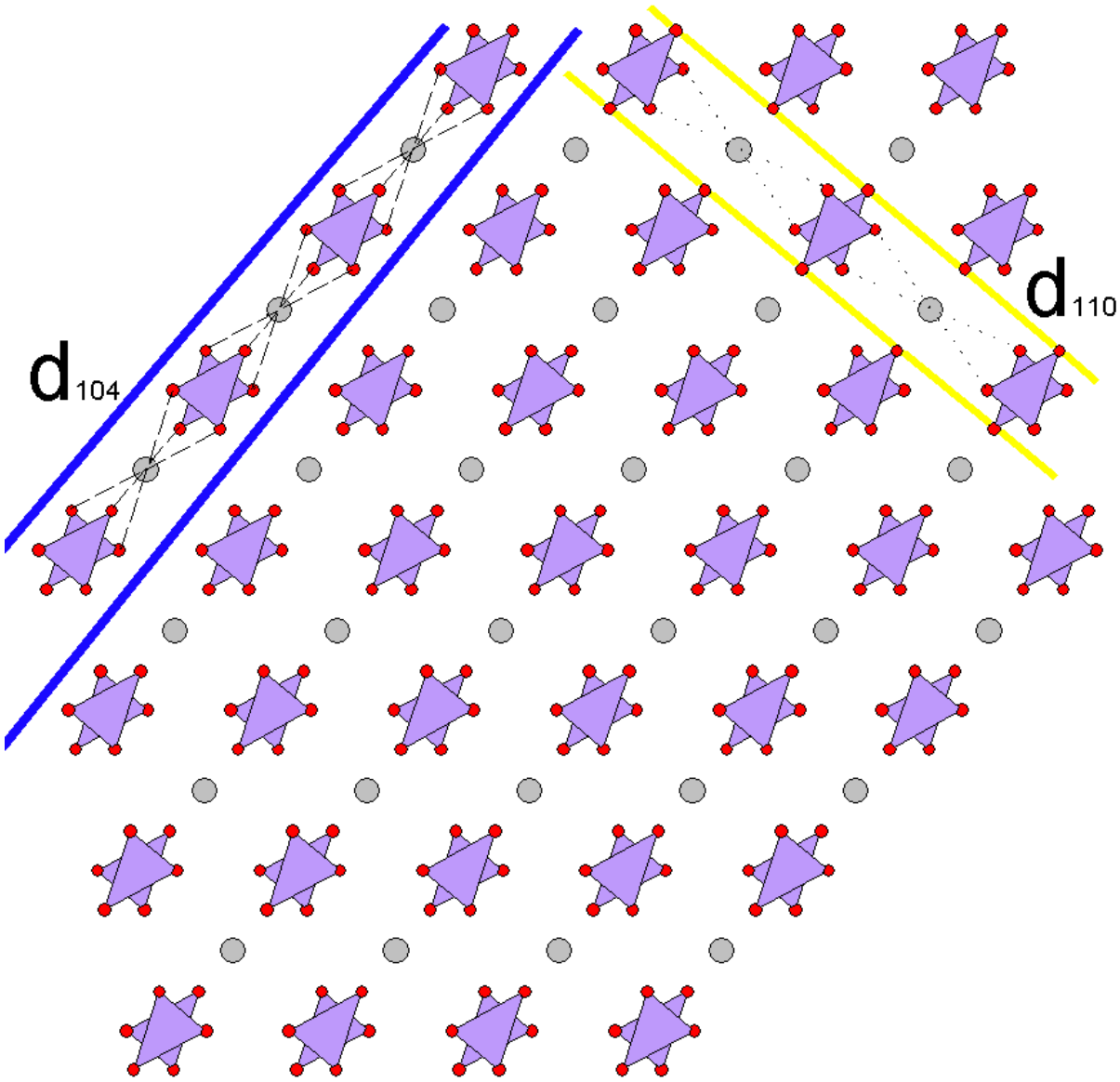


**Figure 11a.** Projection along the $[42\bar{1}]$ direction. The (104) face is outlined by blue lines and the (110) face with yellow lines.

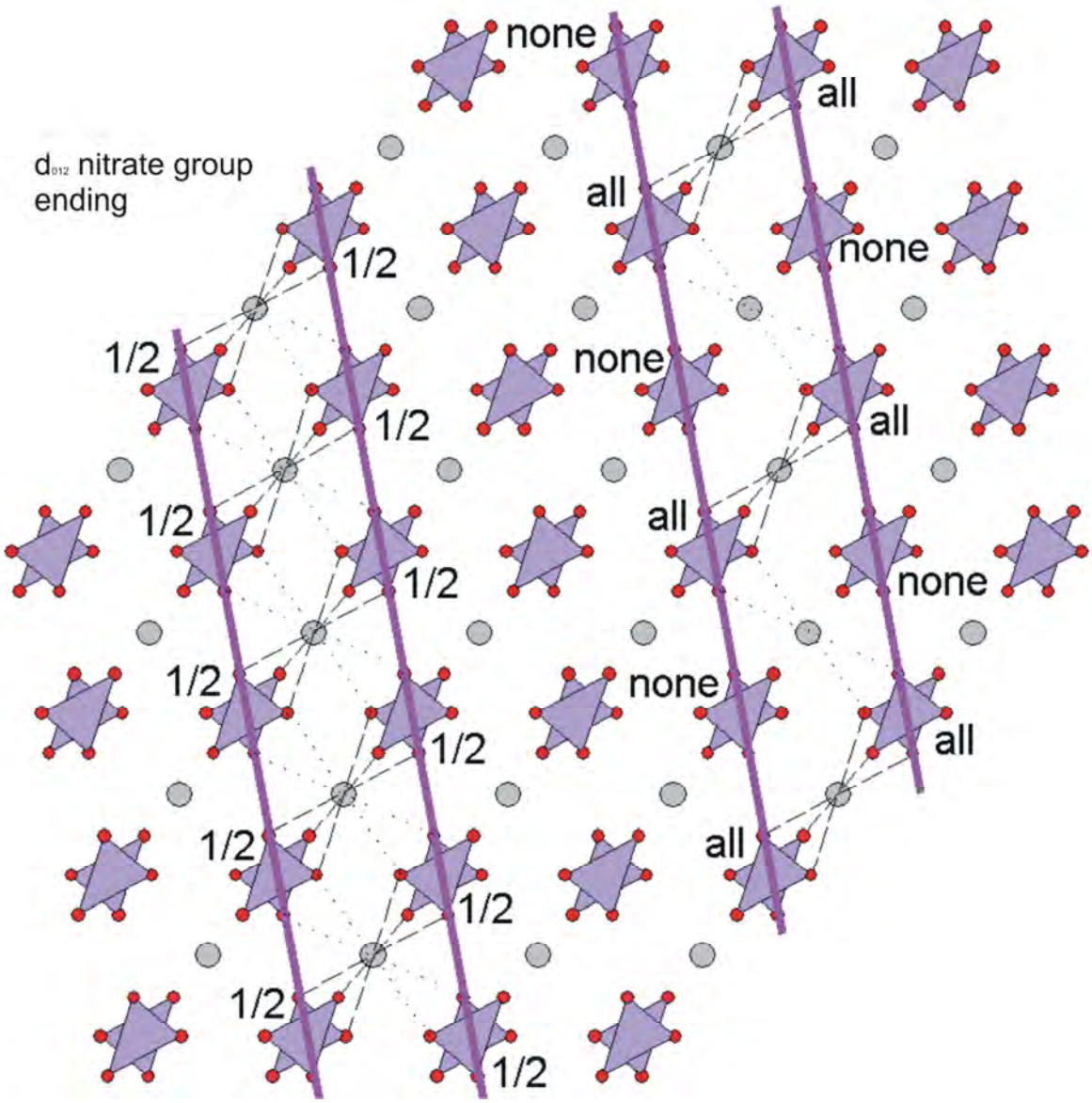


**Figure 11b (cont).** Projection along the $[42\bar{1}]$ direction. The (012) face must be reconstructed. Here we show the nitrate ion ending reconstruction.

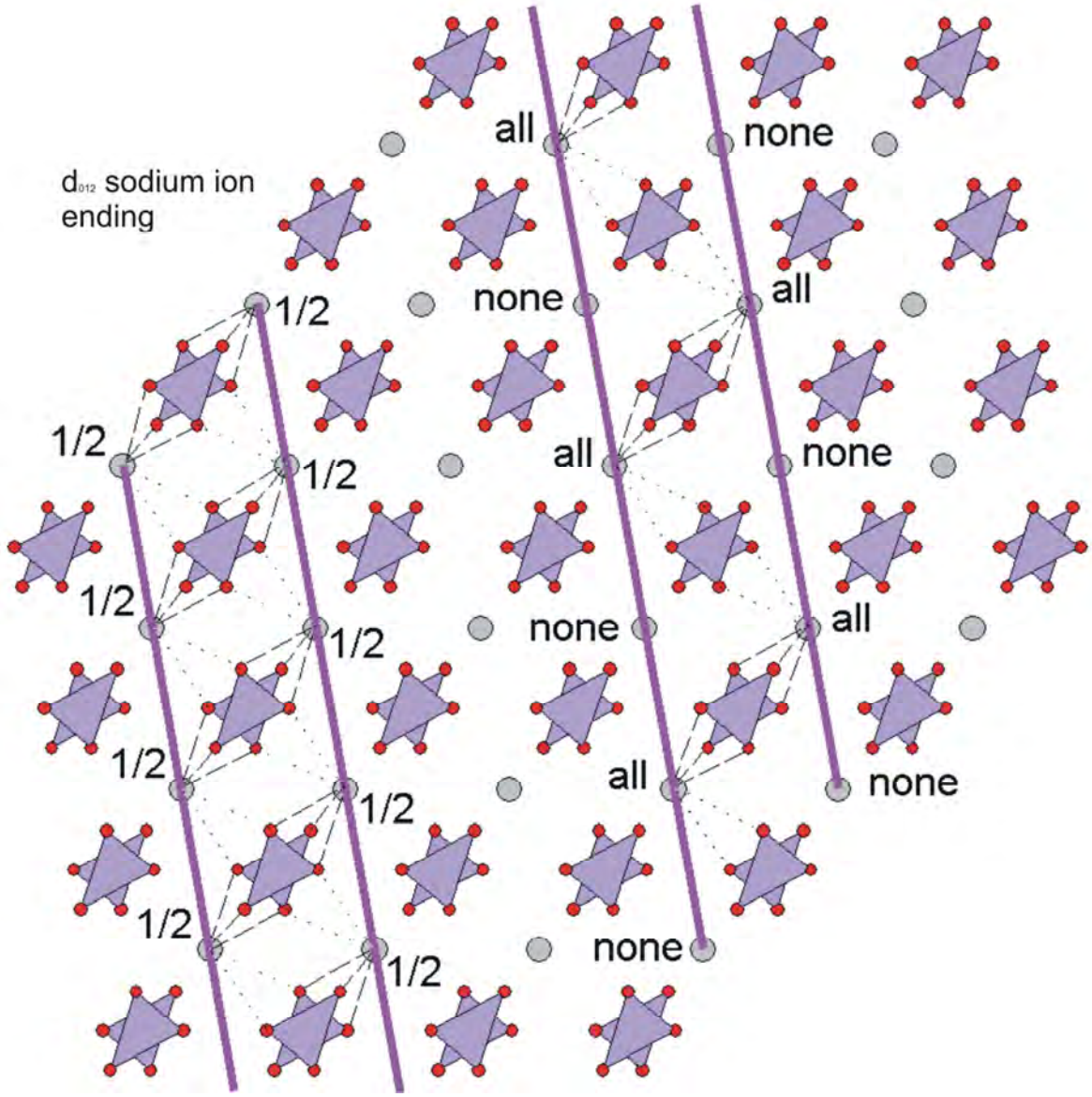


**Figure 11c (cont).** Projection along the $[42\bar{1}]$ direction. The (012) face must be reconstructed. Here we show the sodium ion ending reconstruction.

- We can observe that within the slice $d_{012}$ there is a complex bonding that runs across the direction [211] (purple lines). The slice is a sum of <001> and <010> directions. Some problems may arise with this form: the steep {012} rhombohedron. First the slice is polar because it is built by alternating planes of opposite charges, it is a type 3 surface in the Tasker classification.[8] In that sense it breaks the PBC rules for a good slice. So the corresponding surface must be reconstructed.

The surface reconstruction is not immediate. Following the work of Bruno et al.[19] this kind of faces can finish in four different profiles. These are sodium (figure 11c) or nitrate (figure 11b) terminated and respecting or not the surface symmetry. In the quoted

paper about calcite, the most stable profile is that based on a carbonate terminated, [010] x 1/3[211] rectangular mesh, symmetrical with respect to the c glide plane of the crystal and, hence fulfilling the 2D symmetry of the face.

In figure 11b and 11c we have drawn the four terminations. For the left hand terminations (both sodium and nitrate terminated) we take all the possible bonds but in order to avoid the polarity we can only have 1/2 of nitrate group or sodium ions respectively in the direction $[42\bar{1}]$ (i. e. perpendicular to the paper as it is the projected direction). In this sense we have a never ending spiral in this direction. It is worth noting that the 'border' groups (those below the purple line) are also positioned alternatively on the $[211]$ direction in the sense that within the same height the occupancy is also 1/2. For the right hand termination (figure 11b and c) a different approach is considered to erase the polarity. Here we have eliminated one out of every two $[42\bar{1}]$ rows. So the repetition vector along $[211]$ is the same as in the other termination. But here we cannot construct a spiral running in the $[42\bar{1}]$ direction.

In figure 12 we have projected all the atoms belonging to the sodium terminated slice onto the plane perpendicular to the face (012). We show three different reconstructions of the (012) face. In this figure fainted (and not bonded) sodium atoms are those eliminated in order to erase the face polarity. For the drawing on the left we have eliminated 1/2 of the sodium atoms in each [010] rows (vertical). We observe that all the [010] rows are linked by never ending spirals constructed by strong bonds. Adjacent spirals are bonded by δ bonds that run along the [001] direction ([211] projected direction in figure 12). This construction corresponds to the left part of figure 11c.

For the picture on the right side of figure 12 we eliminated 1/2 of the complete [010] rows, so 2 sodium rows disappear and the other 2 sodium rows remain in the face. In this case, sodium atoms are bonded in a double spiral through nitrate groups by strong bonds. If we only consider strong bonds (dashed lines in figure 12) there is only 1/2 of the nitrate groups bounded, i.e. 1 out of every 2 [010] nitrate rows. Only when we consider δ bonds, all atoms become linked in a very regular way. This construction corresponds to the right slice of figure 11c. The middle picture of figure 12 shows an example of a complex asymmetric reconstruction. In this case we have erased half of the sodium [010] rows (as in the preceding case but in a different way). This gives a zigzag of strong bonds between contiguous nitrate groups in the [010] direction. These 'zigzag' rows are bonded laterally by δ bonds but not in a symmetric way like the other two reconstructions.

The second reconstruction described may be the weakest because one half of the nitrate group rows are strongly bonded (by two strong bond spirals) while the other half is only weakly bonded by δ bonds. In contrast this reconstruction has the lowest surface energy in calcite as reported by Bruno et al.[19]

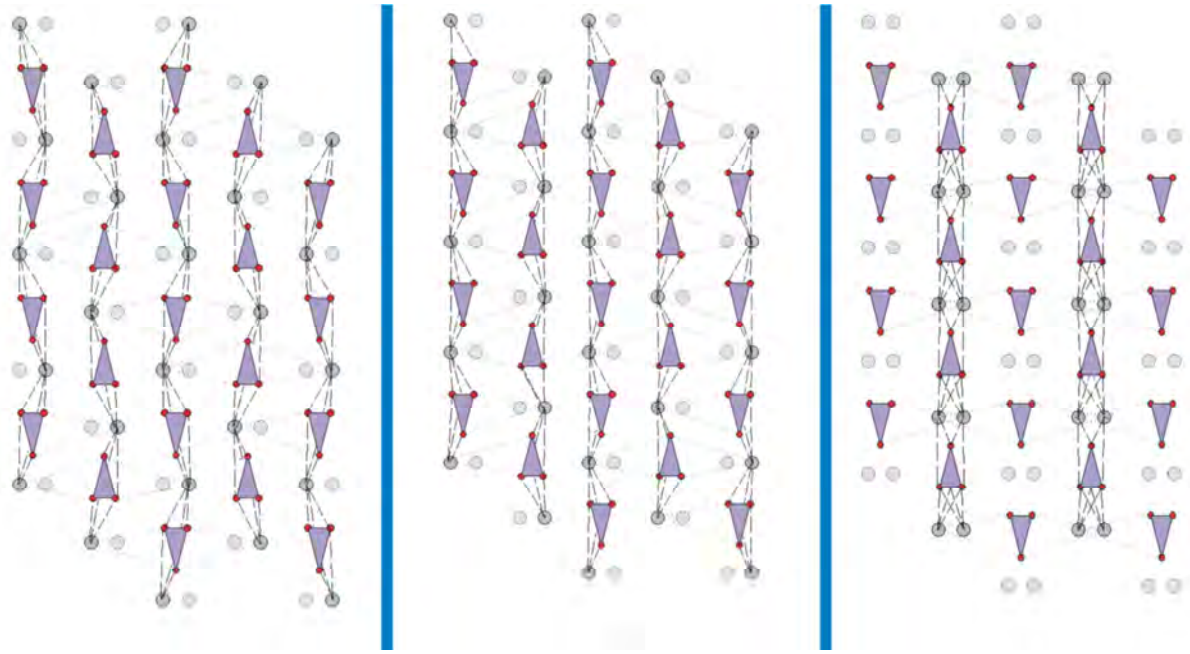

**Figure 12.** Front view of a slice on the (012) face. The three possible reconstructions of the face are shown here, see text for an explanation.

To observe the surface unit cell the projection shown in figure 13 is better. Here, for the sake of simplicity, we have deleted the back row of sodium atoms; thus, this projection only has those sodium atoms that are below one purple line in figure 11c and the nitrate groups inside the slice. It is how the theoretical surface should appear at 0 K without relaxation. In figure 13 we show three possible surface unit cells. The left and the middle picture are obtained by eliminating one half of the sodium atoms in the [010] direction. In this sense one half of the sodium rows in the directions $[2\bar{2}1]$ and [241] respectively have disappeared. It turns out that these surface reconstructions are equivalent because they have the same oblique unit cell. The right image (figure 13) is achieved by erasing a half of the [010] rows in order to obtain a rectangular surface cell 1/3 [211] x [010] which is, as exposed above, the best surface reconstruction.

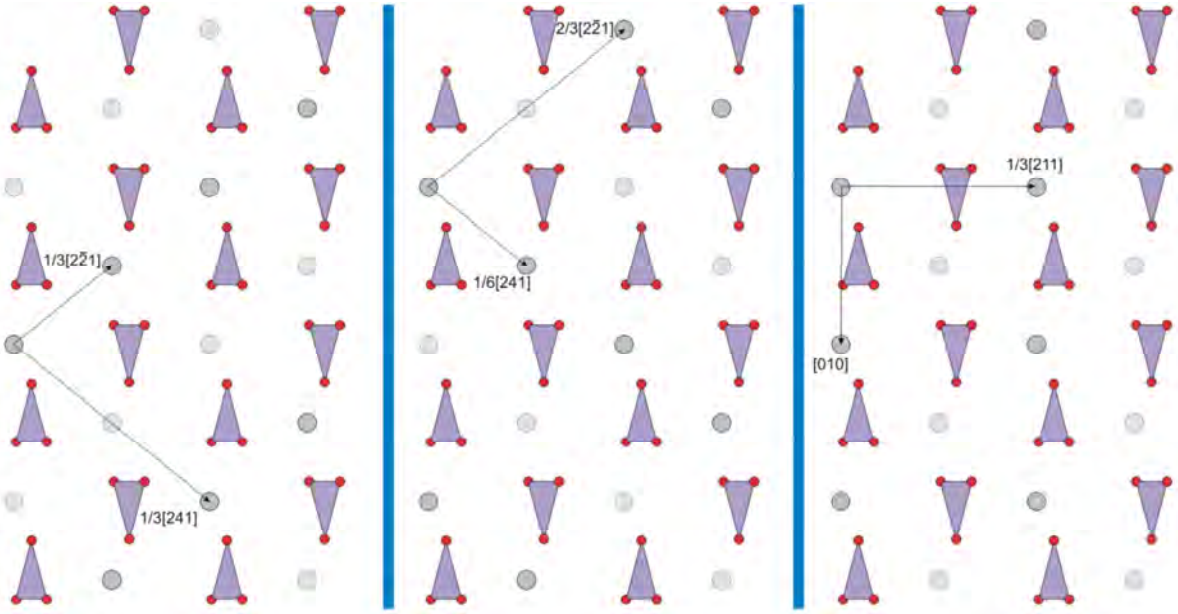


**Figure 13.** Front view of a slice on the (012) face. Here we mark the three possible surface cells depending on the reconstruction performed (see text).

#### 2.3.2.2.3. The [010] direction.

In figures 14a-e we show projections along [010] direction with different PBC constructions depicted. Looking at them, we can make the following considerations.

- If we take the slice of thickness $d_{018}$ we observe that a PBC runs across the direction [$\bar{4}\bar{8}$1] (green lines). This is the only PBC that can be found within the slice of thickness $d_{018}$. A double layer of thickness $2 \times d_{018}$ is needed in order to have a connection for this PBC, as was outlined above in the [$\bar{4}$41] projection (figure 10a green lines). It is exactly the same problem but viewed from another point of view. So, the {018} form has an S character.

- If we look at [$\bar{4}$41] (blue lines) direction, we can easily find that a PBC runs within a slice $d_{104}$. This is not surprising since it is the 'reciprocal' projection of the [$\bar{4}$41] first considered before. It is worth remembering here that the [$\bar{4}\bar{8}$1] (green lines) and [$\bar{4}$41] (blue lines) directions are symmetrically equivalent.

- If we take into account the direction [211] we observe that in a slice $d_{012}$ runs a complex PBC. As in the [42$\bar{1}$] projection we observe that the (012) face has to be reconstructed in the same way, and therefore it is consistent with the previous results. It means that it can be sodium or nitrate terminated respecting or not the face symmetry. All projections show that (012) face is complicated from the structural point of view meaning that it can be finished in 4 different ways.

- Along the direction [$\bar{1}$11] (orange lines) there is a PBC with an allowed thickness of $d_{202}$. This slice is polar because opposite charges are centred in different planes: positive-negative-positive within its thickness. It has strong and weak bonds and can also be sodium or nitrate terminated. The (101) surface, which belongs to the {101} acute rhombohedron, presents exactly the same problem as the (012) surface. Therefore, the surface reconstruction may proceed in a similar way. This surface is, therefore, another example of type 3 surfaces according to Tasker classification.[8]

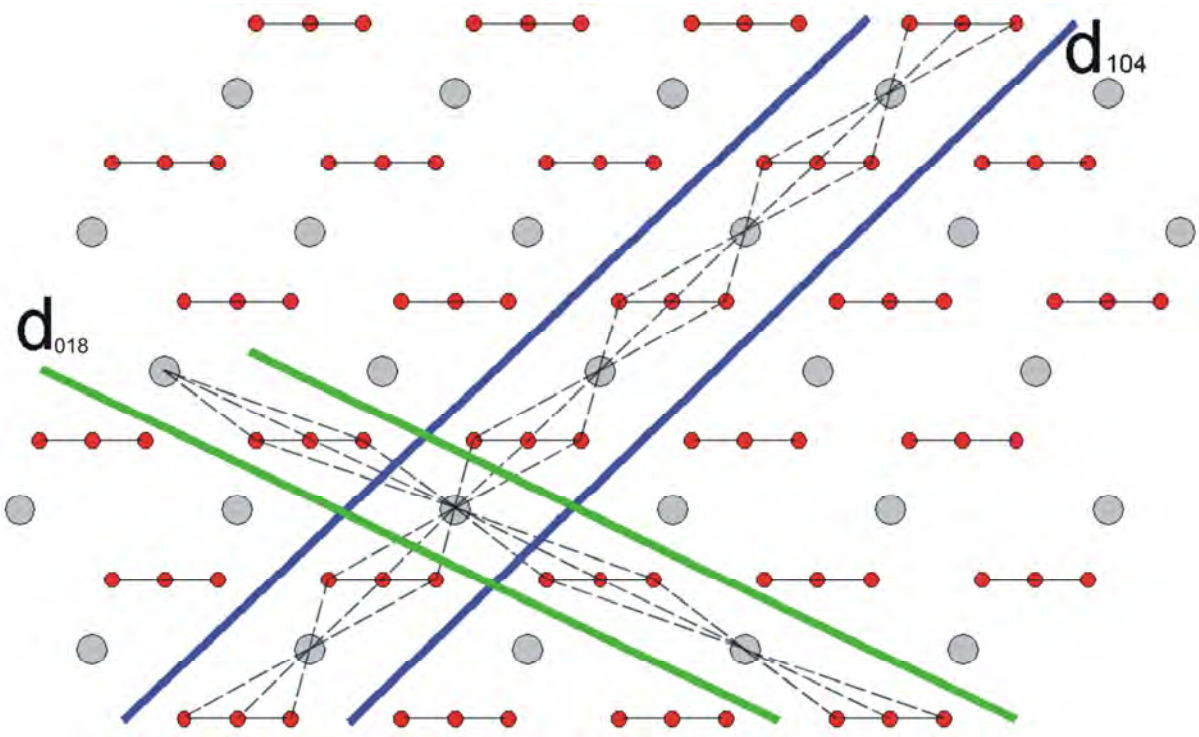


**Figure 14a.** Projection along the [010] direction. The (104) face is outlined by blue lines and the (018) face with green lines.

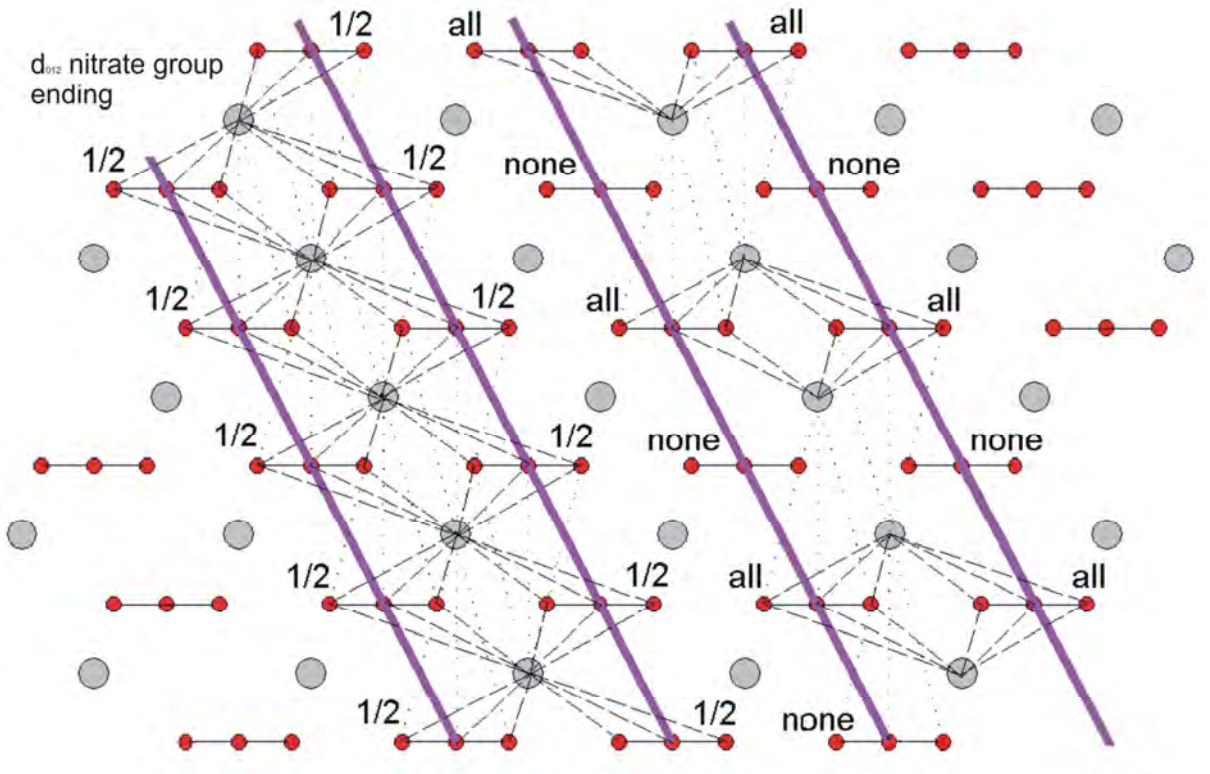


**Figure 14b (cont.).** Projection along the [010] direction. The (012) face must be reconstructed. Here we show the nitrate ion ending reconstruction

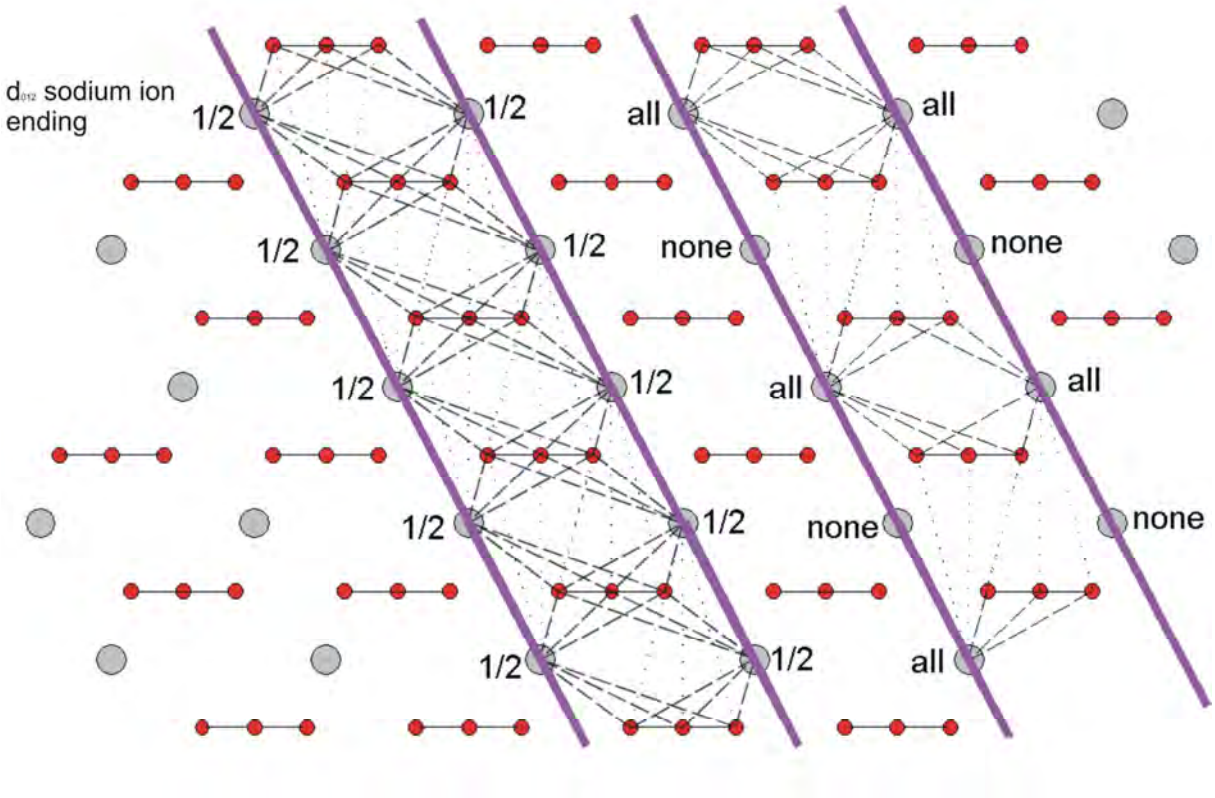


**Figure 14c (cont.).** Projection along the [010] direction. The (012) face must be reconstructed. Here we show the sodium ion ending reconstruction

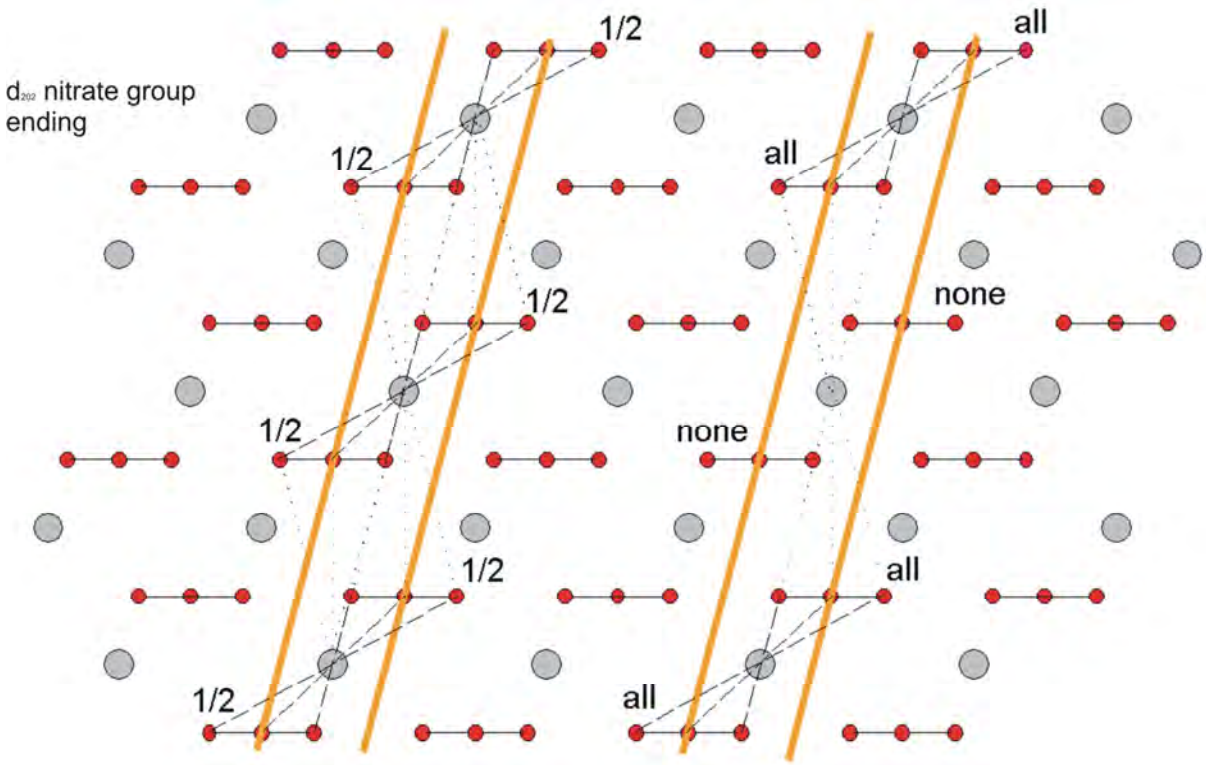


**Figure 14d (cont.).** Projection along the [010] direction. The (101) face must be reconstructed. Here we show the sodium ion ending reconstruction

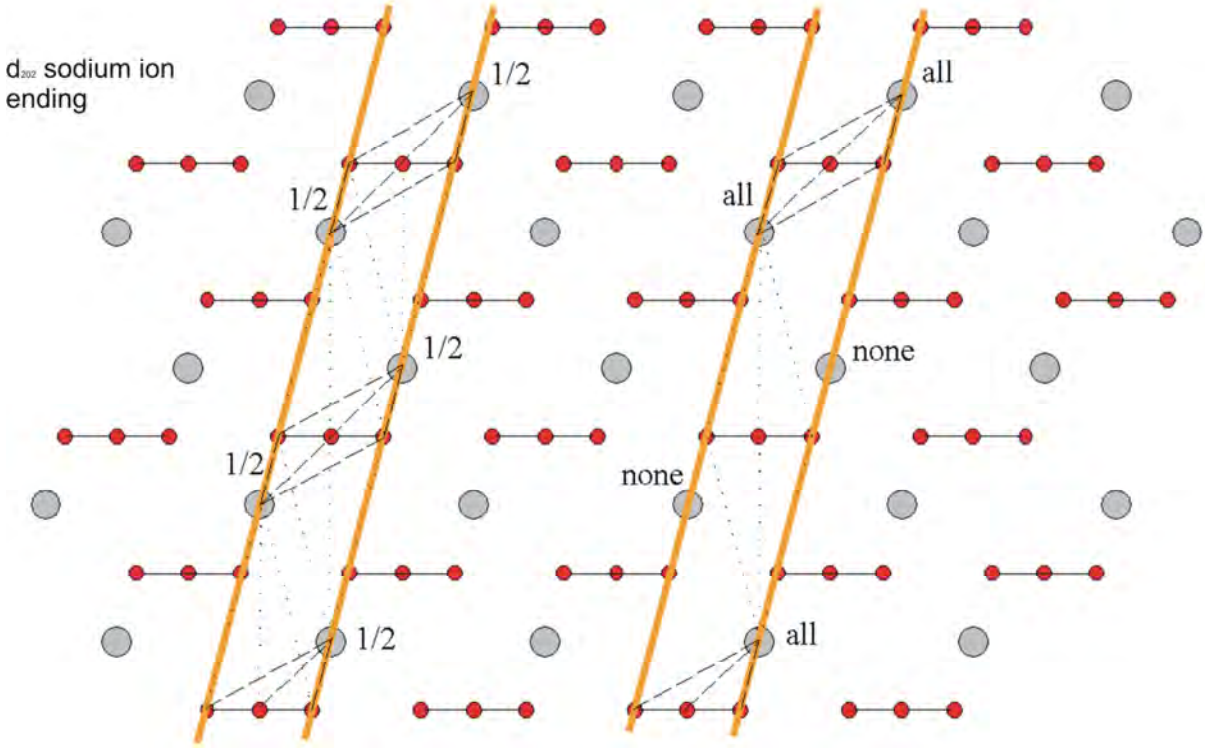


**Figure 14e (cont.).** Projection along the [010] direction. The (101) face must be reconstructed. Here we show the sodium ion ending reconstruction

We show in figure 15 a front view of the face (101) with three different reconstructions. For the sake of simplicity we only work with sodium terminated slice projecting all the atoms onto the surface plane, as we have already done with the (012) surface. In these reconstructions excluded sodium atoms in each type of reconstruction appear faint and not bonded. In this case we show the three possible reconstructions.

In the left hand picture of figure 15 we have eliminated one half of the sodium atoms in the [010] row (corresponding to the reconstruction on the left in figure 14e). In this case we see a spiral made by strong bonds where all the spirals are linked together by δ bonds. In the middle reconstruction of figure 15 (corresponding to the reconstruction on the right in figure 14e) we observe a double spiral of strong bonds bonded together by a complete $BU_2$, this means that half of the nitrate groups are strongly bonded while the other part has only weak bonds. On the right part of the figure 15 we see a reconstruction where sodium atoms present are those on only one side of the slice. In this case we observe zig-zag structures bonded by strong bonds; nonetheless these are bonded together by δ bond bridges constituted by only 1/2 $BU_2$. This last reconstruction is not depicted in figure 14 above.

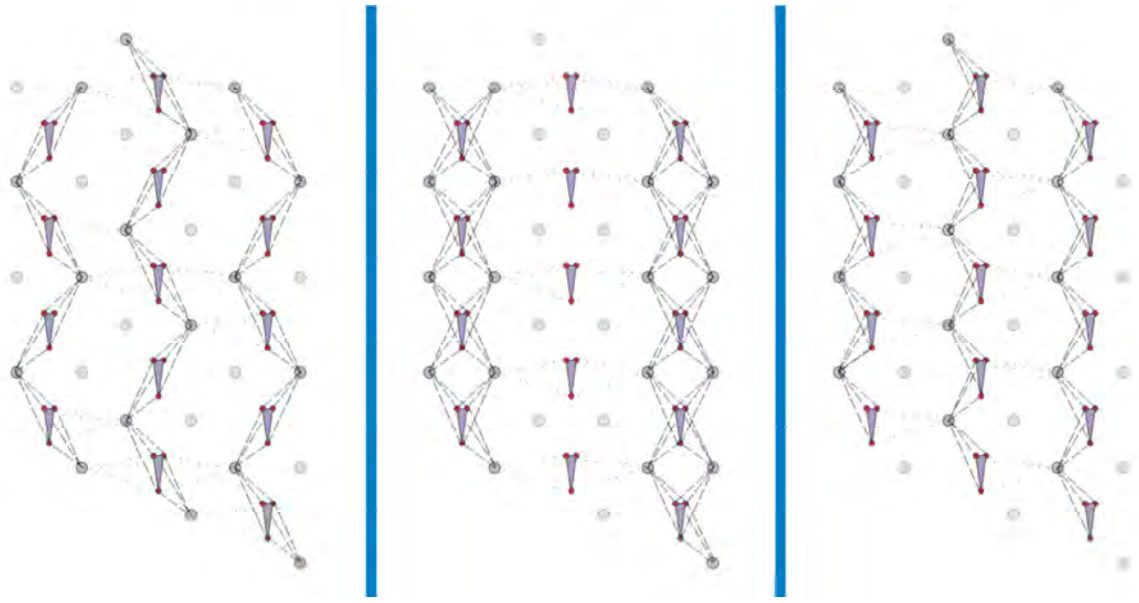

**Figure 15.** Front view of a slice of the (101) face. In the left picture we erased one out of every two sodium atoms in the [010] row while in the middle and right picture we erased one out of every two [010] rows in different ways (see text).

In order to recognize the surface unit cell we proceed as in the (012) face. In figure 16 we only projected sodium atoms below one orange line and nitrate rows. As we did in

the (012) we show here two different reconstructions erasing 1/2 of sodium atoms in the [010] directions. It conducts, according to the figure 15 above, to different orientation of the helix, so the oblique surface unit cells are equivalent. For the right reconstruction, eliminating 1/2 sodium atoms rows, we obtain a rectangular surface cell.

.

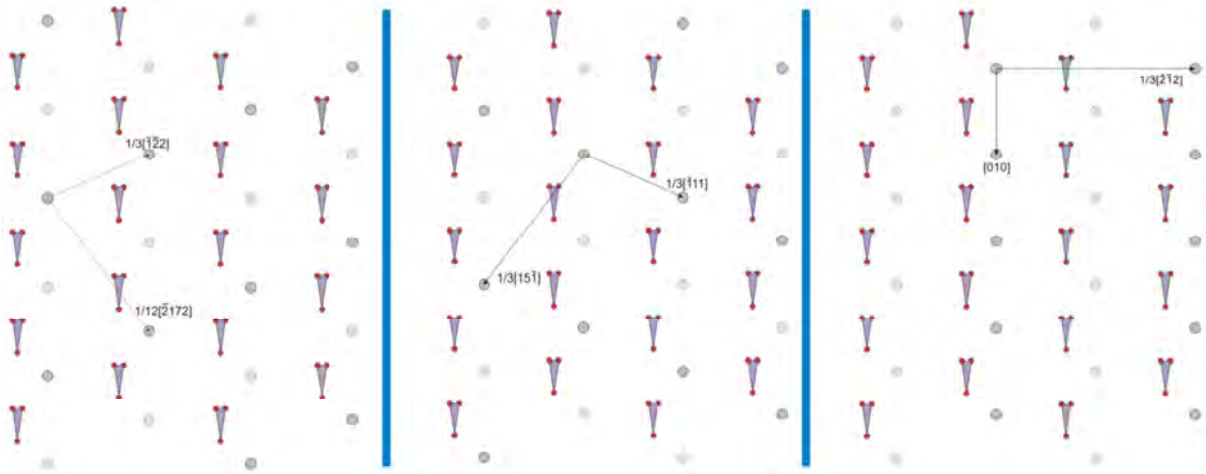


**Figure 16.** Front view of a slice on the (101) face. Here we mark the three possible surface cells depending on the reconstruction performed (see text).

#### 2.3.2.2.4. The [001] direction.

Figure 17 shows the [001] projection of nitratine structure. Here we highlight the following statements.

- The [010] PBC is not bonded along its equivalent direction [100] within a slice of thickness $d_{300}$. We have to note that the profile of faces (100) or (010) may not have a flat aspect. In this case the extinction rules impose that the slice, to have an F face, must have a thickness equal to $d_{300}$. Therefore, the wavy profile allows cancelling out the possible polarity. In this sense the {001} form has not, in principle, an F character because we cannot draw bonds between PBCs within the slice of thickness $d_{300}$. However, Bruno et al.[20] demonstrated in the isostructural mineral of calcium carbonate (calcite) that the {100} form enters in the athermal equilibrium shape of calcite.
- We observe that the [110] PBC is bonded within a slice of thickness $d_{110}$.

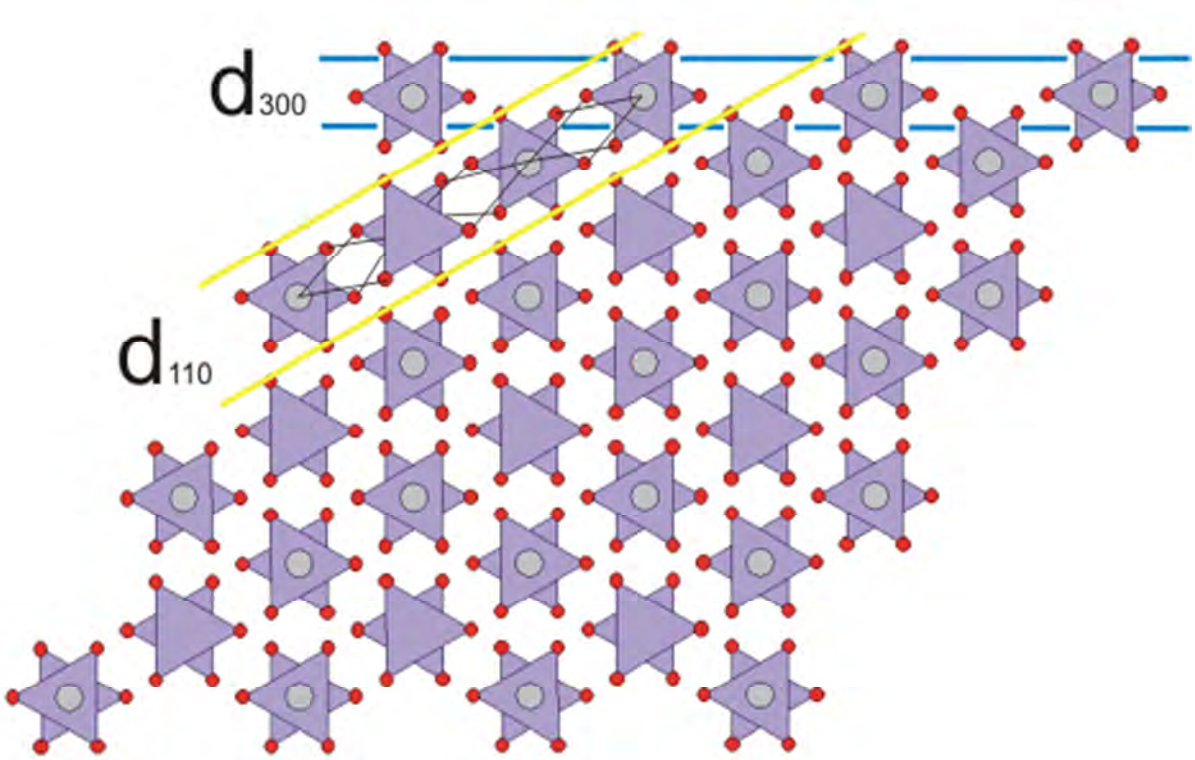


**Figure 17.** Projection along [001] direction. The [001] PBCs has no connection within a slice of thickness $d_{300}$.

Now the complete PBC analysis is finished. Therefore, gathering the information extracted from the different projections, we can summarize the face character in Table 3. This Table is ordered in decreasing value of the allowed thickness in order to compare it with Table 1.

**Table 3.** Face character of the most important faces in nitratine together with the PBC directions that can be found within the allowed thickness in the face.

| Face | Allowed thickness | PBC directions | Character |
|---|---|---|---|
| (012) | $d_{012} = 3.8922$ | $<42\bar{1}>$; <010> | F |
| (104) | $d_{104} = 3.0369$ | $<\bar{4}41>$;$<42\bar{1}>$; <010> | F |
| (001) | $d_{006} = 2.8033$ | None | K |
| (110) | $d_{110} = 2.5350$ | $<\bar{4}41>$; $<42\bar{1}>$; <001> | F |
| (101) | $d_{202} = 2.1242$ | <010> | F |
| (018) | $d_{018} = 1.8963$ | $<\bar{4}41>$ | S |
| (214) | $d_{214} = 1.5437$ | microfacets | K |
| (100) | $d_{300} = 1.4636$ | <001> | S |

Now we can remember the relative strength of important PBC directions. They can be ordered, in a first approximation, from the strongest to weakest as:

$$<\bar{4}41> \rightarrow <42\bar{1}> \rightarrow <010> \rightarrow <001>$$

Therefore, we can also order the morphological importance of different faces by only applying the geometrical description proposed in the HP approach. Our proposal is:

$$\{104\} > \{110\} > \{012\} > \{018\} > \{101\} > \{100\} > \{214\} \sim \{001\}$$

Now that we know the most probable faces that can enter in the theoretical shape of sodium nitrate by the HP method we can proceed with surface energy calculations.

#### 2.3.2.3. The theoretical equilibrium morphology of $NaNO_3$ calculated in a vacuum.

To approach the equilibrium shape of the $NaNO_3$ crystal, the {001} and {104} surfaces were studied by using the 2D - slab model: 001 and 104 slabs of varying thickness were generated by separating the bulk structure along the plane of interest. The geometry optimization was performed at DFT level (B3LYP Hamiltonian, which contains a hybrid Hartree-Fock/Density-Functional exchange term) by following considerations:

i) a modified conjugate gradient algorithm implemented in the CRYSTAL06 package,[21] considering the slab limited by two centre-symmetry related surfaces, and

ii) allowing the relaxation of the positions of all of the atoms.

Geometry optimization is considered converged when each component of the gradient and of the displacement (TOLDEG, TOLDEX parameters in CRYSTAL06) is smaller than 0.00030 hartree $bohr^{-1}$ and 0.0012 bohr, respectively. Na, N and O are respectively described with the 8-511G*, 6-21G* and 8-411G* basis sets.

Relaxed and athermal surface energies (surfaces energies at T = 0 K), $\gamma$, have been calculated by using the relation:

$$\gamma = \lim_{n\to\infty} E_s(n) = \lim_{n\to\infty} \frac{E(n) - n[E(n) - E(n-1)]}{2A}$$

where *n* is the number of layers in the slab and E(n) is the energy of a n-layer slab; the factor 2 accounts for the upper and lower surfaces of the slab. $E_s(n)$ is thus the specific energy required to form the surface from the bulk. As more layers are added in the calculation ($n \rightarrow \infty$), $E_s(n)$ will converge to the specific surface energy.

The {001} surfaces are dipolar ones, being composed of alternating layers of Na ions and $NO_3$ groups if observed along the [100] direction. This means that the potential energy near the surface diverges with the thickness of an infinite (001) crystal slab and then the surface itself cannot exist. Therefore, in order to stabilize the surface it is necessary to quench the macroscopic dipole moment in some way. In this work this is done by modifying the density of ions in the outermost layers of the crystal by the introduction of vacancies: the octopolar Lacmann's model[22] was considered, which was already proposed by Hartman[23] for NaCl-like lattices. This type of reconstruction respects the bulk symmetry of the crystal and was carried out by removing 3/4 of the ions in the outermost layer and 1/4 in the second last one, respectively (according to the Curie's principle, the symmetry group of a reconstructed surface must be a subgroup of the symmetry of the bulk crystal viewed along the normal to the surface). The octopolar Na- terminated {001} form resulted to be highly more stable than the $NO_3$ terminated one: in fact $\gamma(001)_{Na}$ = 695 erg/cm$^2$ and $\gamma(001)_{NO3}$ = 1535 erg/cm$^2$, respectively. It ensures that the {001} form does not enter the theoretical athermal equilibrium shape, since the touchstone of all surface energies of nitratine, i.e. $\gamma(104)$, barely reaches 160 erg/cm$^2$. This result unambiguously proves that the athermal equilibrium shapes of nitratine should only have the {104} form.

Effectively when introducing these surface energy values in the Wulff plot we observe that (figure 18), as we have expected for the large difference in the values in the surface energy, only the {104} form appears in the athermal equilibrium morphology.

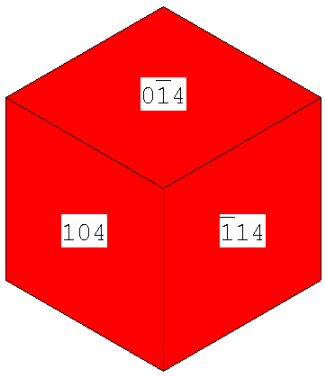


**Figure 18.** Equilibrium morphology of $NaNO_3$ taking into account the surface energy values calculated at semi-empirical level.

## 2.4. DISCUSSION

We have determined the theoretical $NaNO_3$ morphology using two different approaches: the Bravais-Friedel-Donnay-Harker method, and the Harman Perdok theory of periodic bond chains.

It is worth remembering here the ordered list of the most important forms by applying both methods. First, we deal with only geometric considerations, and later, we see if this classification corresponds to the forms that appear in the theoretical shape after applying the Wulff plot. Finally, we compare them to the experimental growth morphology.

For the BFDH method we have obtained the X-ray diffraction list:

$$\{012\} > \{104\} > \{001\} > \{110\} > \{113\} > \{101\} > \{018\} > \{016\}\ldots$$

When we plot the theoretical morphology, the situation is totally different. The {104} form disappears and the polyhedron is formed only by the forms:

$$\{012\} = \{01\bar{2}\} > \{001\}$$

where we have stated the relative importance.

On the contrary, when we apply the HP procedure, we can also order the morphological importance of different faces by only applying the geometrical description, remembering that the PBC relative strength is: $<\bar{4}41> \rightarrow <42\bar{1}> \rightarrow <010> \rightarrow <001>$. So that our proposal is:

$$\{104\} > \{110\} > \{012\} > \{018\} > \{101\} > \{100\} > \{214\} \sim \{001\}$$

The situation changes when applying the Wulff plot after the calculation of the specific surface energies. In this case, the only form that appears in the equilibrium morphology is {104}. This form has a very low surface energy so that it is very stable. We think that is quite difficult that other forms can enter in the equilibrium form because in comparison with calcite calculations the other important forms have higher surface energies. In calcite {018}, {001}, and {100} forms have similar surface energies. For nitratine we have only calculated the {001} surface energy. It reaches 695 erg/cm$^2$, so that we can estimate that $\gamma_{\{001\}} \approx \gamma_{\{100\}} \approx \gamma_{\{018\}} \approx 700$ erg/cm$^2$ for nitratine.

In figure 19 we put together the theoretical morphology calculated by the two methods and that obtained experimentally. From this figure it is clear that the theoretical morphology is different depending on the method used. Furthermore, only the HP approach in this case simulates correctly the experimental morphology. In the impurity effect chapter we will focus our attention on the difficulty of changing $NaNO_3$ morphology. The reason for this complication is now clear; we have to lower the specific surface energy by about 400 erg/cm$^2$ in order to obtain an extra face.

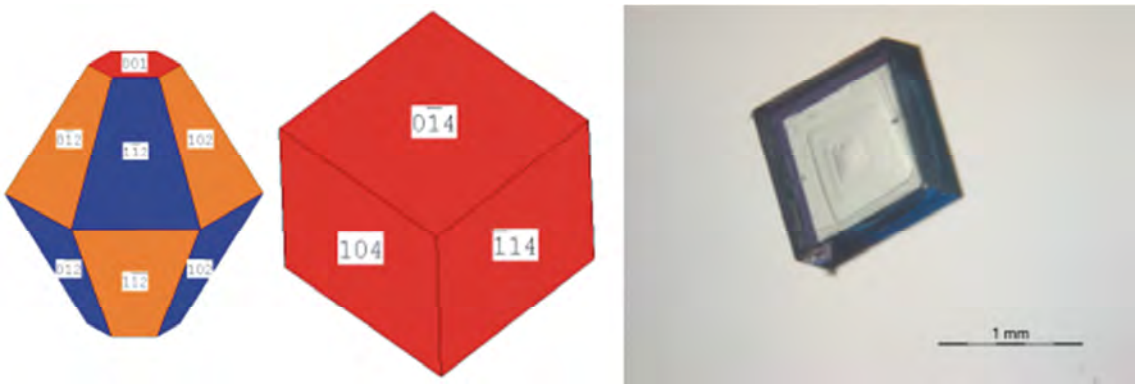


**Figure 19.** Theoretical morphology applying the BFDH method (left) and the HP method (center). Right: experimental morphology, from pure aqueous solution growth, built by {104} rhombohedron.

The scenario totally changes when surface energy is considered. For calcite many surface energies have been calculated[24] giving somewhat different order in the morphological importance of faces, we order here in increasing value of surface energy:

$$\{104\} > \{018\} \sim \{001\} \sim \{100\} > \{012\} \sim \{214\} >> \{110\}$$

This last classification is for calcite only, and it probably does not hold for sodium nitrate because they have quite different electrical fields on the surfaces due to the different ion charges. Calculation of other surface energies in nitratine will be useful to compare whether the same tendency holds or not. It would help us to clarify what is the most important aspect to derive the theoretical morphology: geometry and surface charge. Calcite and nitratine geometry is practically equal because they are isostructural, however, the surface charges in calcite is doubled in respect to nitratine. If the geometry is the most important aspect then a similar surface energy ordering of surfaces will be

encountered in $NaNO_3$. Conversely, if the surface charge is the most important aspect then the $NaNO_3$ surface energy will be totally different.

We have to highlight the difference between the BFDH and the HP theoretical morphology. According to the HP way of analysing the structure, the most important face is not that of the thickest interplanar distance: $d_{012}$. This is, in fact, not surprising after analysing the strongest bonds. For a slice of thickness $d_{104}$ there are three strong PBCs, what is more, two of them (<$\bar{4}41$> and <$42\bar{1}$>) lay exactly inside its thickness. Therefore, in this form there is not a problem of polarity and surface reconstruction as in the {012} and {101} forms.

The forms that enter into the morphology calculated by the BFDH method are the {012} = {$01\bar{2}$} and the {001} forms. These have one and zero PBC directions within their respective thicknesses, so that they are not expected to enter into the equilibrium form according to HP. However, {001} form is in the equilibrium of calcite (isostructural with nitratine) after applying the octopolar reconstruction.[22] Nonetheless, we do not expect that the {001} enters into the nitratine morphology because its surface energy is 4.3 times larger than that of the lowest face (104).

Similarly, it is thought that the negative forms of nitratine will not enter into the equilibrium form because we expect that they have, by resemblance with calcite, higher surface energies than the respective positive.[15]

## 2.5. CONCLUSIONS

The theoretical morphology of $NaNO_3$ has been calculated applying the Bravais-Friedel-Donnay-Harker and Hartman Perdok approaches independently.

From the first approach, we obtain that {012}, $\{01\bar{2}\}$, and the {001} forms appear. We highlight that 'positive' and 'negative' faces emerge with the same morphological importance in the calculated morphology.

From the HP approach and after calculating surface energies we have obtained that only {104} form is able to enter into the equilibrium morphology i.e. that calculated at 0 K in a vacuum. The calculated surface energy for this form is so low that it practically excludes the possibility of other forms to enter into the morphology. Moreover, by similarity between $NaNO_3$ and $CaCO_3$ we can definitely eliminate the possibility of negative forms entering into the equilibrium morphology of nitratine. It is worth remembering that negative forms always have higher surface energies in respect to the positive in the case of calcite.[15]

Only the HP approach in this case simulates correctly the experimental morphology: only the {104} form appears.

## 2.6. BIBLIOGRAPHY

1. *Web Mineral: http://webmineral.com/data/Nitratine.Shtml 2013.*

2. Friedel, M. G. *Études Sur La Loi De Bravais.* Bull. Soc. Franc. Min. Crist., **(1907)**, 30, 326-455.

3. Donnay, J.; and Harker, D. *A New Law of Crystal Morphology Extending the Law of Bravais.* Am. Mineral., **(1937)**, 22, 5, 446-467.

4. Prywer, J. *Explanation of some Peculiarities of Crystal Morphology Deduced from the BFDH Law.* J. Cryst. Growth, **(2004)**, 270, 3-4, 699-710.

5. Hartman, P. *Structure and Morphology, in* Crystal growth: an introduction. Hartman, P. ed., 1st ed. Amsterdam: North-Holland, **(1973)**, 367-402.

6. Hartman, P. *Modern PBC Theory, in* Morphology of crystals. Sunagawa, I. ed., Tokyo: Terra Scientific Publishing Company, **(1987)**, 269-320.

7. Gale, J. D. *General Utility Lattice Program (GULP) User's Manual. Version 3.1.*

8. Tasker, P. W. *The Stability of Ionic Crystal Surface.* J. Phys. C., **(1979)**, 12, 1979-1984.

9. Kern, R.:*The Equilibrium Form of a Crystal, in* Morphology of crystals. Sunagawa, I. ed., Tokyo: Terra Scientific Publishing Company, **(1987)**, 77-206.

10. Benages, R.; Costa, E.; Bruno, M.; Cuevas-Diarte, M. A.; Calvet, T. and Aquilano, D. *Experimental and Theoretical Aspects of the Growth and Equilibrium Morphology of $NaNO_3$.* Cryst. Res. Tech., **(2011)**, 1-6.

11. Paul, G. L.; and Pryor, A. W. *Study of Sodium-Nitrate by Neutron Diffraction.* Acta Cryst. B, **(1972)**, 28, 15, 2700-2702.

12. Kern, R.; Le Lay and; Metois, J. J.: *Basic Mechanisms in the Early Stages of Epitaxy, in* Current topics in material science. Kaldis, E. ed., Amsterdam: North Holland, **(1979)**, 131-419.

13. Aquilano, D.; Bruno, M.; Massaro, F. R. and Rubbo, M. *Theoretical Equilibrium Shape of Calcite. 2. [$\bar{4}$41] Zone and its Role in Biomineralization.* Cryst. Growth Des., **(2011)**, 11, 9, 3985-3993.

14. Wulff, G. *On the Question of Speed of Growth and Dissolution of Crystal Surfaces.* Z. Kryst. Min., **(1901)**, 34, 5/6, 449-530.

15. Aquilano, D.; Benages-Vilau, R.; Bruno, M.; Rubbo, M. and Massaro, F. R. *Positive and Negative Form of Calcite Crystal ($CaCO_3$) in the Light of Bravais-Friedel-Donnay-Harker and Hartman-Perdok Approach.* in Press.

16. Hartman, P.; and Perdok, W. G. *On the Relations between Structure and Morphology of Crystals. I.* Acta Cryst., **(1955)**, 8, 49-52.

17. Hartman, P.; and Perdok, W. G. *On the Relations between Structure and Morphology of Crystals. II.* Acta Cryst., **(1955)**, 8, 52-55.

18. Hartman, P.; and Perdok, W. G. *On the Relations between Structure and Morphology of Crystals. III.* Acta Cryst., **(1955)**, 8, 55-59.

19. Bruno, M.; Massaro, F. R. and Prencipe, M. *Theoretical Structure and Surface Energy of the Reconstructed {01.2} Form of Calcite ($CaCO_3$) Crystal.* Surf. Sci., **(2008)**, 602, 16, 2774.

20. Bruno, M.; Massaro, F. R.; Prencipe, M. and Aquilano, D. *Surface Reconstructions and Relaxation Effects in a Centre-Symmetrical Crystal: The {00.1} Form of Calcite ($CaCO_3$).* Cryst. eng. comm., **(2010)**, 12, 11, 3626-3633.

21. Dovesi, R.; Saunders, V. T.; Roetti, C.; Orlando, R.; Zicovich-Wilson, C. M.; Pascale, F.; Civalleri, B.; Doll, K.; Harrison, N. M.; Bush, I. J.; D'Arco, P. and Llunell, M. *CRYSTAL06 User's Manual (University of Torino, Torino, 2006).*

22. Lacmann,R. :*Gleichgewichtsform Und Oberflächenstruktur Von NaCl Kristallen, in* Adsorption et Croissance Cristalline. Kern, R. ed., Nancy: Colloques Internationaux du CNRS; N°152, **(1965)**, 195-214.

23. Hartman, P. Bull. Soc. Franc. Min. Crist.,**(1959)**, LXXXII, 158.

24. Massaro, F. R.; Bruno, M. and Aquilano, D. *The Effect of Surface Relaxation on the Theoretical Equilibrium Shape of Calcite. I. the [001] Zone.* Cryst. Growth Des., **(2010)**, 10, 7, 2870-2878.

# CHAPTER 3

## GROWTH KINETICS OF THE {104} FACES OF NITRATINE ($NaNO_3$)

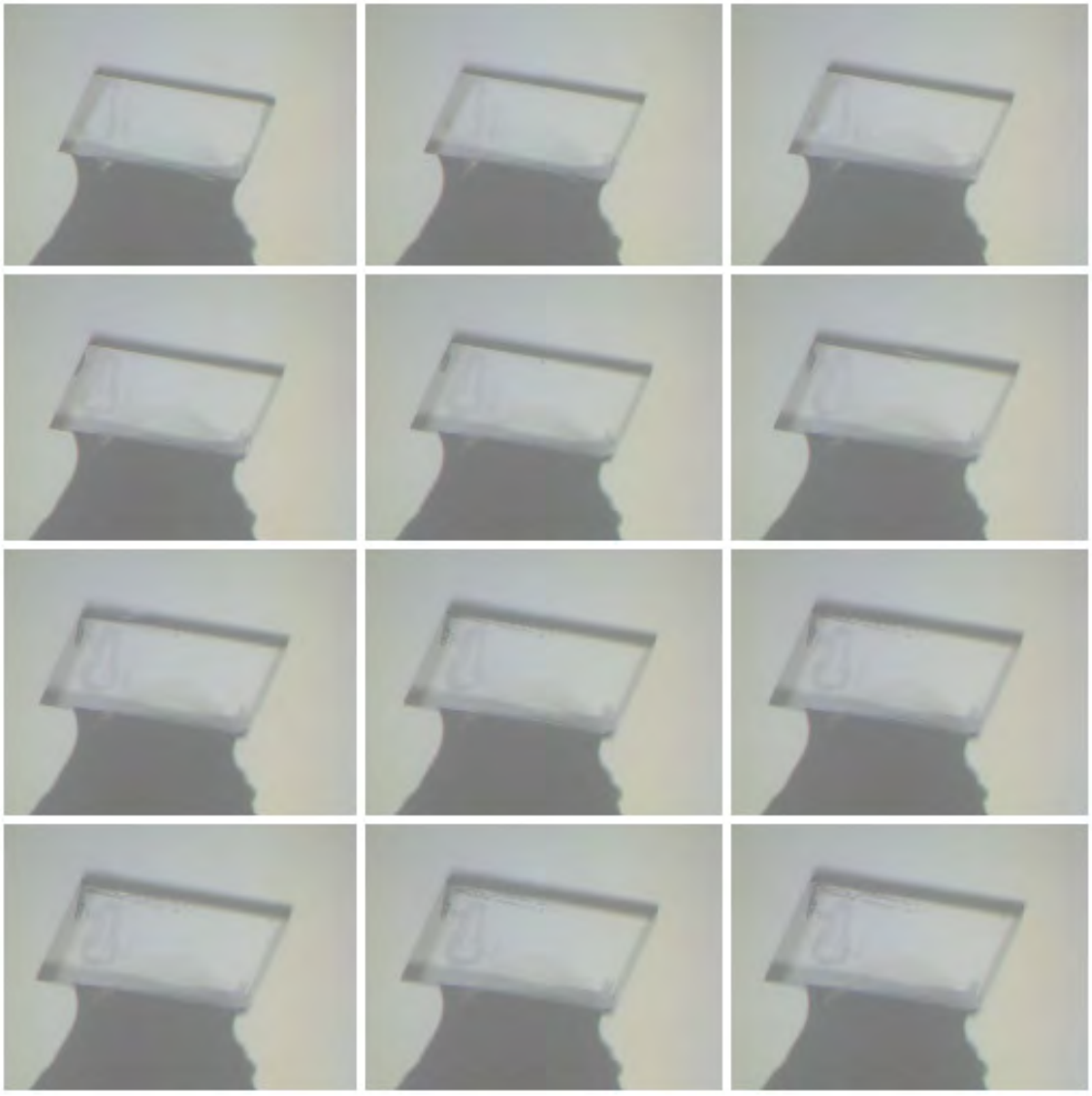

## 3.1. GENERAL INTRODUCTION

Molecular level understanding of the crystallization processes provides the capability to quantitatively model the crystallization and hence control it. Then we can control the crystal morphology, the crystal size and its distribution, etc.

Following the Kossel crystal model, the elementary act of growth of crystals is the attachment of building units (atoms, molecules, ions, etc.) in the sites called kinks, in which incoming building units have one half of the neighbors in respect to the bulk. Calculating the mean evaporation energy (per building unit) of the crystal, one can find that its value coincides with that necessary to extract a building unit from a kink-site: it follows that the kink site is in equilibrium with the mother phase, and then the incorporation of new building units into it does not affect the surface free energy of the crystal (figure 1). Consequently, the kinks are special sites for growth because from the calculations exposed in Mutaftschiev,[(1)] they have the highest coverage degree (being 1/2) among the building units that are able to enter into the crystal (i.e. 1 bond: adsorbed on a terrace; 2 bonds: adsorbed in a ledge; 3 bonds: in a kink site) and have the lowest exchange frequency.

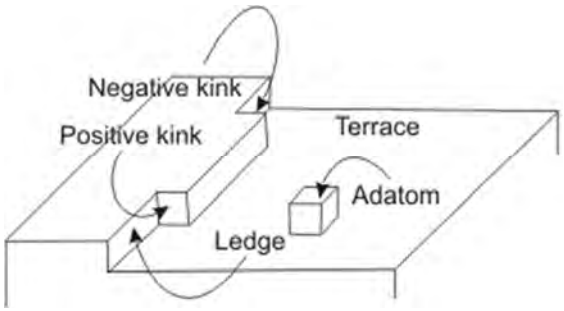


**Figure 1.** The main sites on the crystal surface. Terrace, step, and kink (positive and negative).

The rate of growth of a crystal face is determined by two factors: the kink density of the face and the barriers, both entropic and enthalpic, for an incorporation of a new building unit into the kink. The density of kinks on a face depends mainly on its character (F, S, and K faces, see chapter 2). In general and taking into account the kink density (let us define this quantity as Ω), kinked faces have the highest growth rate while faceted faces are the slowest, and so the following tendency holds:

$$\Omega_K > \Omega_S > \Omega_F \quad \rightarrow \quad R_K > R_S > R_F$$

where $R_K$, $R_S$ and $R_F$ are the growth rate of kinked, stepped, and flat faces, respectively. On the other hand, the growth rate of a certain face is also a function of the dislocation density and of the quality of the face (the presence of impurities which poison the kink sites) and hence the growth rate can be lowered so that in the final morphology we can seldom observe K-faces that are not theoretically predicted.

According to the Hartman and Perdok (see chapter 2) concept of periodic bond chains (PBC) F faces are smooth on a molecular level and contain a low density of kinks while S and K faces are rough and contain higher densities of kinks. Therefore, the growth of F face is possible only when growth layers emitted by dislocation emerging on the surface, or 2D nuclei forming on it, provide the necessary kinks for the attachment of growth entities. Because of their roughness, S and K faces do not require the presence of dislocations or 2D nucleation to grow.(3) These authors had the idea that the advancement rate ($R_{hkl}$) of a (hkl) face is proportional to its attachment energy $E^{att}_{hkl}$, i.e. the energy released per formula unit when a $d_{hkl}$ layer attaches on the pre-existing substrate during growth. In other words, the higher the $E^{att}_{hkl}$ value, the higher the corresponding $R_{hkl}$ and, consequently, the lower the morphological importance of a face.(4)

Here, we only describe the growth of F faces because they are the most important from the morphological point of view and as we have already viewed in the morphology chapter (and confirmed in this chapter) they are the only ones that we found in the crystallization of $NaNO_3$ pure system.

A crystal can grow whenever its building units arrive at the surface and integrate into the growing seed. Obviously, for growing there must be a driving force which is the supersaturation. This conduces, in fact, to a descending of the free energy of the system. The growth of F-faces occur by capture of building units into kinks on steps. Such a building unit can diffuse over the surface and then leave it, or if the unit lands close enough to a step (which has a high concentration of kinks due to thermal roughening), it can enter the step and finally join the kink. Once there, its probability of escape is low.

The process is far from easy and can be decomposed in many sub-processes as is depicted in figure 2.

Crystal growth proceeds basically in five steps, as can be seen in figure 2:

i) Bulk diffusion of the building unit from the bulk to the unstirred layer.

ii) Diffusion in the unstirred layer to the surface ($w_{VD}$).

iii) Adsorption of the building unit on a terrace, with the subsequent loss of solvent ($w_{ADS}$).

iv) Surface diffusion from a terrace to a ledge ($w_{SD}$, another solvent molecule is lost). Alternatively, the building unit returns to the solution ($w_{DEADS}$).

v) Adsorption in the ledge with a subsequent loss of other molecules of solvent ($w_E$).

vi) Ledge diffusion from a step to a kink ($w_{LD}$).

vii) Integration of the building unit to the crystal. Transport of the released heat of reaction and solvent molecules from the solvated atoms/molecules ($w_K$).

In figure 2 there is also depicted the possibility of de-adsorption of the building unit. This is, in fact, quite probable as the rate of interchange between F faces and the solvent is quite high. The fact that the building unit adsorbs preferentially onto a terrace is only for a statistical reason: the bigger the terrace the greater the probability. In this sense adsorption directly onto the ledge is less probable, and directly onto a kink is even less probable. It is worth remembering that we are talking about the general case of a flat face.

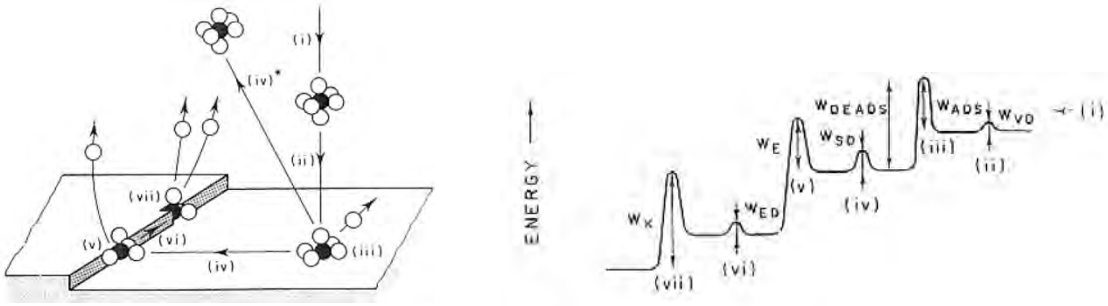


**Figure 2.** Left: general path for the incorporation of a building unit in a crystal. Right: scheme of the activation energy (w) for each process (see text). After Madsen.[5]

Every step, like every reaction, has its own activation energy (defined in point 4.2) and can be the rate determining step. In general, volume and surface diffusion are the rate dependent steps, thus growth models have been developed to describe the process.

The general trend is that at low supersaturation the free energy variation needed to create a 2D nucleus on a crystal surface is not high enough, so the crystal can only grow

by spiral growth as first proposed by Burton, Cabrera and Frank; it is the parabolic law.[6] When the free energy variation is enough to create 2D islands, the activation energy can be overcome and hence the mechanism becomes a 2D nucleation as first proposed by Becker and Döring,[7] it is the first linear law.

Growth rate is an anisotropyc parameter that determines the form of the (polyhedral) crystal. It is determined by the state of interfaces, the growth mechanism, and the driving force. In figure 3 the vertical axis represent the growth rate while the horizontal axis is the driving force. Curves a, b, and c correspond to the expected growth rate versus driving force relations for spiral growth, 2D nucleation growth and adhesive growth type mechanism repectively.

At points indicated by one and two stars we see boundaries between the proposed growth mechanism where two curves cross. Above the two star point, the interface will be rough, and below smooth. In the region between the one star and two star points we observe predominately 2D nucleation growth, and below the one star line only a dislocation growth. The position of the stars depends on many factors such as solute–solvent interaction energies, crystallization mode (from the melt, solution or vapour), supersaturation, temperature, pressure, impurities, and the size of the crystals. It also depends on the crystallographic direction and crystal faces.

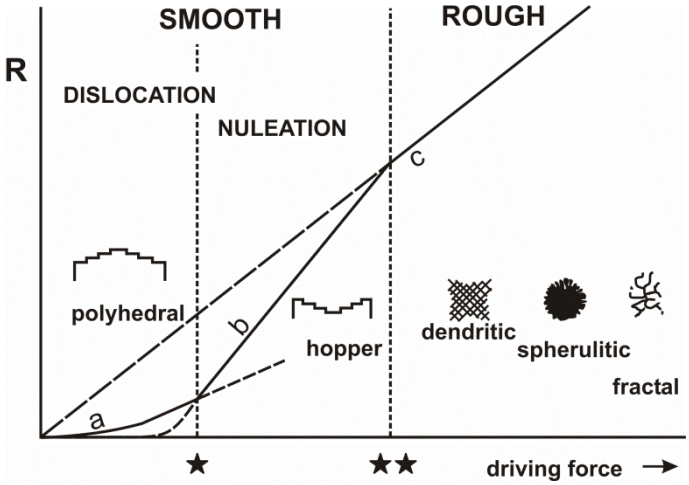


**Figure 3.** General scheme of crystal growth morphology as a function of the driving force, after Sunagawa.[8] The lower the driving force, the more perfect the crystal (polyhedral) is: it grows according to the parabolic law (a). When the driving force is higher we obtain hopper crystals and the first linear law (b). Finally, when the driving force is even higher, crystals grow without surface diffusion and we get dendritic, spherulitic or fractal cristals.

In the region below the one star line, growth is controlled by the spiral growth mechanism. The normal growth rate of a face in this region is determined by the height of spiral growth layers, step separation and the advancing rate of the spiral steps. The habit of crystals is determined by the relative ratio of the normal growth rate of the crystal faces: faces with higher normal growth rate develop smaller, and those with the slower normal growth rate develop larger. The factors that cause a variation of the habit also affect the step height, step separation, and advancing rate. The step height is determined by lattice spacing, the step separation is related to critical radius of 2D nucleation, which, in turn, is related to both the edge free energy and the driving force; and the step advancing rate is related to the edge free energy and the driving force.[8]

Thermodynamic parameters strongly influence the growth mechanism while kinetic parameters determine the growth kinetics and the generation of defects.

If the supersaturation of a flat face is low in the center and high near the edges (the so called Berg-effect), growth layers will preferentially generate near the edges of a face and advance inwards in the region between the one star and two star points. The crystal will be bound by stepwisely depressed faces (a hopper crystal). The same situation is expected when dislocation outcrops concentrate along the edges, since the advancing rate of spiral layers are high and the step separations are narrower near the edges where higher supersaturation is present.

In the region above the two star line, the controlling growth mechanism is of the adhesive type and the interface is rough and curved, morphological instability of the interface becomes important. Crystal morphology is then dendritic, spherulitic or fractal.

## 3.2. INTRODUCTION TO THE $NaNO_3$ CRYSTAL GROWTH

The $NaNO_3$ (nitratine) crystal structure consists of alternating layers of sodium ions and nitrate groups; nitrate ion layers are rotated by 60º with respect to each other around the triad axis, the crystal space group being $R\bar{3}c$.[9] Each Na has an octahedral coordination with oxygen atoms. Nitratine is iso-structural with calcite but its athermal equilibrium shape (ES), calculated using a semi-empirical potential, is very different from that of calcite as only the {104} cleavage rhombohedron is present because its surface energy is very low with respect to the other crystal forms. $NaNO_3$ is easy to crystallize from an aqueous solution and the {104} rhombohedron always appears.

$NaNO_3$ crystal growth has not been widely studied over the years. The earliest research found was made by Sipyagin and Chernov[10] who measured the crystal growth as a function of temperature (273 - 323 K) at a constant sub-cooling of $T - T_{eq} = 0.3$ K. They found that the growth rate of single crystal faces was always below 12·µm/min. They highlighted anomalies in this system: a non-monotonic increase in crystal growth when temperature was raised. Some year later Kirkova and Nikolaeva[11] measured the growth rate of the face of nitratine as a function of the flow rate at different supersaturations. Results were essentially the same as those reported by Sipyagin and Chernov. Two drawbacks affected these measurements: firstly, the indexes of the growing faces were ambiguous in both cases and, secondly, neither of these two researchers measured an isothermal growth rate that is necessary to discriminate the $NaNO_3$ crystal growth mechanism. Treivus[12] put forward that the $NaNO_3$ solution growth proceeds according to the dislocation mechanism in a free convection regime. Jones and Larson[13] characterized statistically the growth rate dispersion of secondary nuclei. They used a 5 ml isothermal chamber for growth experiments. With this setup, as we demonstrate in this chapter, is impossible to maintain constant the supersaturation, thus the growth rate is time dependent. The initial growth rate they measured is about 20 µm/min. Furthermore, Jones and Larson[14] developed a model which predicts the dependence between growth rate and dislocation density and strain. Ristic et al.[15] used Michelson interferometry to investigate the growth rate of strained crystal by means of synchrotron radiation. They concluded that the growth of 150 µm of new material is enough to recover the normal growth rate, i.e. equivalent to a non-irradiated crystal; the tangential growth rate of steps was about 750 µm/min with a supersaturation $\sigma = (c-c_{eq})/c_{eq} = 0.2$ %. Ristic et al.[16] also studied the influence of tensile strain on

growth behaviour. In this case they used a special cell in which tensile strain can be applied during growth. According to these authors the application of tensile strain on the crystal decreases the growth rate. The face advancement rate ($R_{hkl}$) published was about 5 µm/min at $\sigma$ = 0.4 %. Jones et al.[17] studied the strain in $NaNO_3$ secondary nuclei as a function of supersaturation. They reported that strain effect on the growth rate (measured by laser interferometry) was more pronounced at high supersaturations levels. The face growth rate ($R_{hkl}$) were between 0.6 and 6 µm/min depending on the relative supersaturation. They proposed a BCF model even though they did not work under isothermal conditions. Graber et al. studied the mass transfer and growth in industrial crystallization.[18] And finally, Oosterhof et al. experimented with isopropoxyethanol-water mixtures.[19] Regarding the growth from the melt, Komnik and Startsev[20] (see reference therein) grew $NaNO_3$ single crystals from the melt. More recently, Gopalakrishnan et al.[21] were able to grow 40 x 10 mm cylindrical $NaNO_3$ single crystals from the melt with a specially designed strip heater in a travelling zone method with a dislocation density of about $10^3$ - $10^4$ $cm^{-2}$. Sawada and Shichiri[22] found that $NaNO_3$ crystals growing from the melt developed a non-faceted morphology at low subcooling and dendritic behavior at higher subcooling.

In this work, we aim at assessing the growth mechanisms from aqueous solution of the {104} $NaNO_3$ crystal faces: to this end, different growth isotherms are measured in order to find both the best fit between the experimental curves ($R_{hkl}$ vs $\sigma$) and one among the theoretical models proposed, and to obtain the temperature dependence of the kinetic coefficients.

## 3.3. EXPERIMENTAL

Our main goal is to determine the normal crystal growth kinetics ($R_{104}$) under isothermal conditions in the temperature interval 288 K - 297.5 K and hence the most probable growth mechanisms. For each isotherm, the temperature of crystallization ($T_{growth}$) is maintained constant while supersaturation is varied by changing the saturation temperature ($T_{eq}$) of the growth solution. This method allows for a very precise determination of the supersaturation.[23] The temperature interval $\Delta T = (T_{eq} - T_{growth})$, corresponding to the supersaturation range we choose is $0.1 < \Delta T < 0.8$ K. It is worth remembering here that 3D-nucleation occurs when settings are $\Delta T \geq 0.4$ K, so the zone where crystals only grow is very narrow, as was already determined by Benages et al.[24]

At the end of the chapter we will describe the first experiments on the (104) surface dislocation movement during the growth visualized by laser confocal differential interference contrast microscopy (LCM-DIM). The device was temporally installed in a recently developed confocal differential interference contrast microscope (LCM-DIM) in Laboratorio de Estudios Cristalográficos of Instituto Andaluz de Ciencias de la Tierra (LEC-IACT) belonging to the Centro Superior de Investigaciones Científicas (CSIC). With this technique we can observe elementary steps (up to 3 nm height[25]), and at the same time, a large area of the growing crystal surface (800 µm x 800 µm). The setup is built around a confocal system (FV300, Olympus) attached to an inverted optical microscope (IX70, Olympus) with a 10x objective lens and equipped with a Nomarski prism introduced in the optical path and a partially coherent super-luminescent diode (Amonics Ltd.,model ASLD68-050-B-FA: 680 nm) to eliminate diffraction noise. More details about this experimental setup can be found in Van Driessche[26] and references therein.

Additionally, we have also observed the growth in a stagnant circular cell (18 mm diameter and about 2 mm height). It was made out of two sandwiched glass plates of 0.17mm thickness separated by 2-mm-thick Teflon ring glued by vacuum grease. This observation cell was mounted inside a copper sample stage which completely surrounded it except for the observation area (Ø = 7 mm) at the bottom side. The precision of the temperature control in the studied temperature range (283 - 298 K) was ± 0.1 K. Deeper experimentation must be performed in order to understand the growth rate behaviour of $NaNO_3$.

### 3.3.1. The growth setup.

In order to measure crystal growth kinetics we have constructed a device to observe the face advancement with a microscope. Its diagram is shown in figure 4 together with a picture.

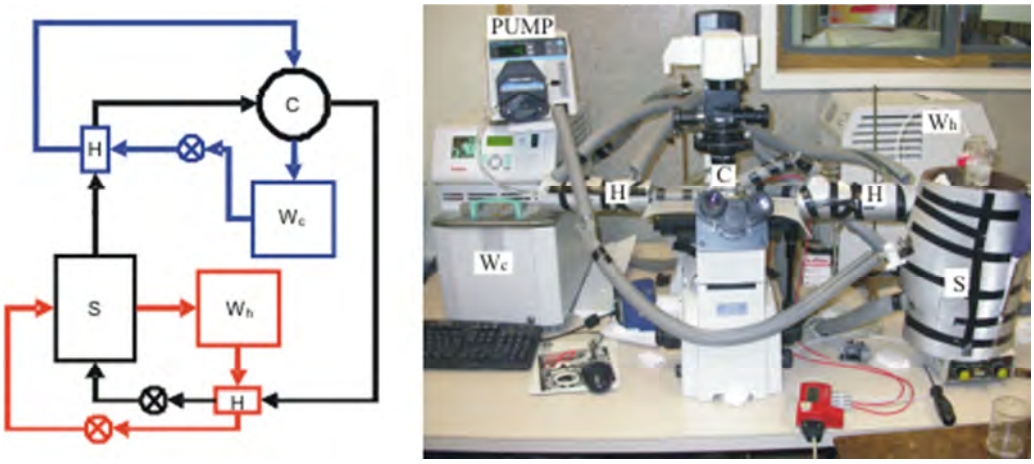


**Figure 4.** Flow diagram (left) and photograph (right) of the constructed growth cell device. Observation cell (C), peristaltic pump (⊗, pump), thermostat baths ($W_h$, $W_c$), countercurrent concentric tube heat exchangers (H) and a reservoir (S).

The unit consists of five main bodies: an observation cell (C), a peristaltic pump (⊗, or PUMP), two thermostat baths ($W_h$, $W_c$) with two counter-current concentric tube heat exchangers (H) and a reservoir (S). As is seen in figure 1, the whole system is thermally insulated to avoid temperature fluctuations. In the following we describe the elements of the device built for studying the growth of single crystals.

The device has been built in AISI 304 stainless steel due to corrosive properties of $NaNO_3$ solutions, aluminium being unable to resist such a solution. The reservoir was built of glass and the connections and valves were of PP. Finally, tubing was of PVC and Tygon® for the pump section.

- The cell.

A detailed image of the observation cell is shown in figure 5. The solution flows into it from the right to the left of figure 5 through an internal section of 0.6 x 1 $cm^2$. In order to maintain a constant temperature a double-walled stainless steel circular block with thermostatic water is required. The seed glued on the sample holder can be observed

between 2 glass windows mounted with “viton” gaskets. In the back part there are two temperature probes.

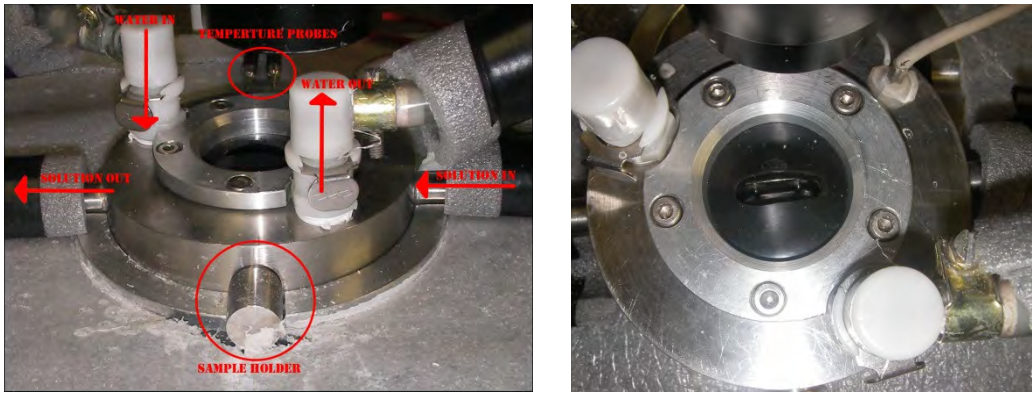


**Figure 5.** A detailed vision of the growth cell.

- The sample holder

The sample holder is a cylinder that ends in a ~ 1 mm diameter flat cone. As shown in figure 6 it has 2 Viton rings to prevent any leakage of the solution. Finally, it has a hole in the outer side that permits tilting the crystal inside the cell in order to obtain the best orientation.

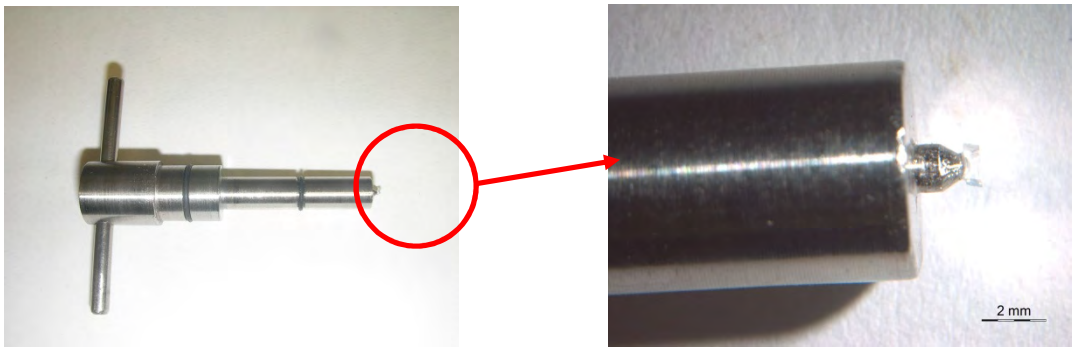


**Figure 6.** The sample holder.

- The reservoir.

The reservoir is a double-walled 1.3 litre vessel. It has the solution exit at the bottom of the internal glass wall and the solution inlet at the upper part at 90º. The vessel is closed on top by a lid with three holes. One is used to introduce a temperature probe, the second is only used for filtering the solution with the system shown in figure 7, while the third one was not used in these experiments. It is essential to buffer the solution concentration throughout the measuring time.

**Figure 7**. Vacuum filtration inside the reservoir.

- The temperature control.

Temperature inside the system must be constant, so thermal insulation is essential to have a good performance. Two thermostatic baths are connected, as figure 4 shows, to control the temperature in the system. The first thermostat is connected to one heat exchanger and to the cell in order to maintain the temperature constant inside it during the experiments. This is the thermostat devoted to adjust the temperature ($T_{growth}$) inside the cell during all the measurements. The other thermostat is used to prevent crystallization in the reservoir and to heat the solution (with the aid of a heat exchanger) just after the solution passes through the cell. In this case, during experiments, its temperature is maintained constant. It is only adjusted when $T_{growth}$ is varied.

The temperature in the system is recorded every 5 seconds through four temperature probes. Two probes are inserted into the cell just before and after the growing crystal (at about 5 mm distance), and a third one into the cooling bath. There is another temperature probe in the solution reservoir. A typical temperature record is shown in figure 8 where S1 and S2 are the probes inside the cell (there is a mismatch of 0.2 K due to the calibration). S3 is the record of the probe inserted in the cooling water and S4 is in the reservoir. It can be clearly seen in figure 8 that the temperature inside the cell is constant and its standard deviation is less than 0.05 K. In contrast, for the S3 record a relatively higher variation, due to the variation of the room temperature which is close to 291 K, is observed.

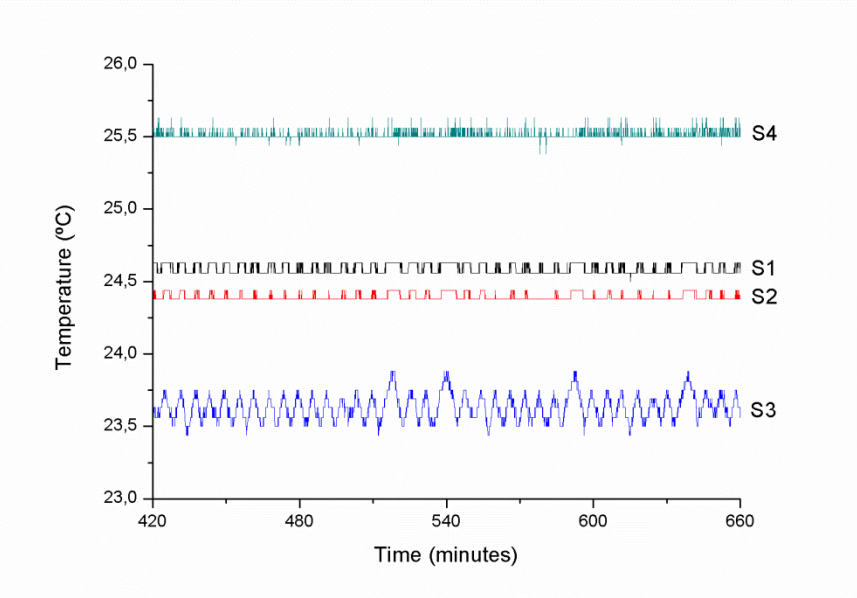


**Figure 8**. A typical temperature recording during the experiments. S1 and S2 are the solution temperatures, measured near the crystal. S3 is the temperature of the thermostatic water flowing into the cell and S4 is the temperature of the reservoir.

The solution (of known concentration) leaves the reservoir at a temperature somewhat higher than that of the target temperature ($T_{growth}$) with the aid of the pump (pumping rate 40 mL/min). It goes through a heat exchanger directly to the observation cell, where a seed crystal is glued. The temperature inside the cell is controlled and adjusted to $T_{growth}$ with the $W_c$ thermostat. Immediately after leaving it, the solution temperature is raised again with the other heat exchanger that conducts it back to the reservoir. The system is equipped with two valves: one in the reservoir exit and the other in the inlet.

### 3.3.2. Source of material.

$NaNO_3$ (analytical grate) was supplied by Quality Chemicals. According to the manufacturer the major impurities are phosphorous and sulphur atoms. Its purity was checked by ionic coupled plasma (ICP) with a mass detector, our results shows that these compounds are below the detection limit (500 ppm), however we have found 21.7 ppm of titanium and 0.22 ppm of manganese. Powder X-ray diffraction informs that the product is a single II-$NaNO_3$ phase.

### 3.3.3. Preparation of seed crystals.

Seed crystals were grown by water evaporation at 291 K in a Petri capsule. The best crystals of less than 2 x 2 x 1 $mm^3$ were picked up with tweezers from the solution, dried on a filter paper and then stored at room temperature. The crystallization process takes at least 2 days.

When necessary, the best crystals were glued to the sample holder tip with a two component epoxy resin. We have used a magnifying glass to assure a good contact between the crystal face and the sample holder. The upper part of the crystal is glued to the sample holder.

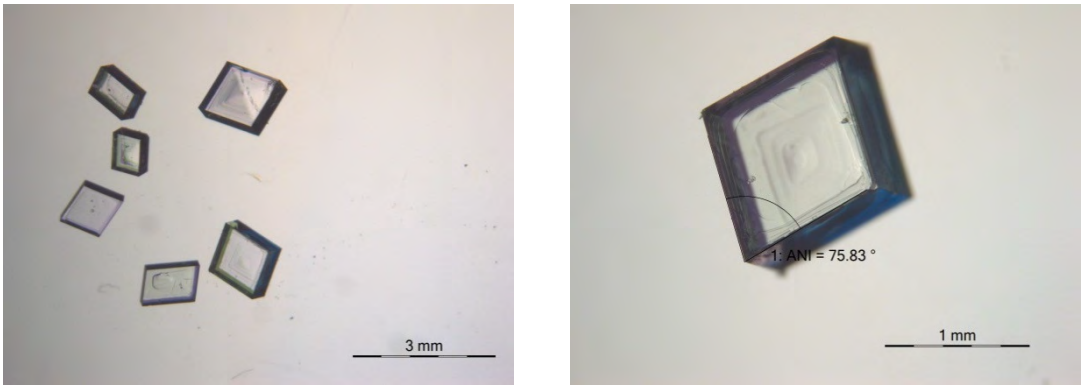


**Figure 9**. Left: $NaNO_3$ seed crystals grown by water evaporation at 291 K. All the crystals measured less than 2 x 2 mm Right: a detailed image showing an angle of 75.83º which is characteristic of the (104) face, as it comes out from the intersections of the set of $<\bar{4}41>$ directions limiting the face.

### 3.3.4. Batch preparation.

For solution preparation we relied on the solubility curve determined by Xu and Pruess:[27]

$$X = 0.0022 \times T - 0.1757 \qquad \textbf{equation 1}$$

where X is the mass fraction and T the absolute temperature. We weighed the required amounts of water and sodium nitrate to have 1600 g of solution. Then it was dissolved in a 2 litre glass. When the solution was transparent it was directly vacuum filtered into

the reservoir; in this case the two valves were closed in order to achieve a pressure reduction.

The reservoir temperature was set at a temperature above the predicted equilibrium temperature with the aid of the second thermostat to avoid any crystallization during the filtration.

We prepared 2 batches. The first was used to measure the crystal growth at 288 K and the second was used to obtain results at 297.5 K and, after diluting with water, at 292.5 K.

To demonstrate that this high amount of material is required, we calculate the mass that crystallises at 300 K by a decrease of 0.1 K by applying the Xu and Pruess[27] solubility curve (equation 1) where we have added the total mass (M) to obtain $NaNO_3$ mass directly.

$$g^{T}_{NaNO_3} = M(0.0022 \cdot T - 0.1757)$$
$$g^{300.1K}_{NaNO_3} = 1600 \cdot (0.0022 \cdot 300.1 - 0.1757) = 775.2326g$$
$$g^{300K}_{NaNO_3} = 1600 \cdot (0.0022 \cdot 300 - 0.1757) = 774.88g$$

where $g^{T}_{NaNO_3}$ is the mass of $NaNO_3$ at equilibrium temperature T. This means that if we decrease the temperature by 0.1 K we are able to crystallise a mass of 0.352 g. Instead, if we compare it with a 5 ml solution described in the Jones and Larson[13] paper, we get that only with $1.4 \cdot 10^{-3}$g of crystallized matter, the equilibrium temperature is changed by 0.1 K.

In conclusion, with 1600 g of solution we assure the concentration stability throughout the growth experiments. Experimentally, it has been noticed that the addition of 1 ml of water can decrease the equilibrium (saturation) temperature almost 0.1 K, showing once again that the system is very sensitive to the boundary conditions (solution concentration, temperature, supersaturation).

### 3.3.5. Sample introduction and replacement.

The seed is introduced into the growth cell at about 1 K above the $T_{eq}$ to avoid unwanted nucleation during the process. First, we stopped the peristaltic pump. Second, the sample holder is taken out and we waited for the solution drain. Then a sample holder with a new crystal is introduced. Finally, the pump is started and the cell is filled again taking care that no air bubbles remain inside. It has to be pointed out that during the process there is no loss of solution. The new crystal is then oriented properly and dissolved a little bit (at $T_{eq}$ + 0.5 K) to erase surface defects. Now the system is ready for a new measurement by adjusting the temperature of interest. It is worth saying that during this whole process only the first thermostat is manipulated to change the cell temperature. The temperature in the reservoir remains constant while changing the cell temperature.

If an unwanted nucleation event takes place during the process, the cell is reheated in order to dissolve all the crystals and the process is repeated again.

Finally, with this system we were able to measure "simultaneously" the kinetics of two different faces that belong to the same {104} form. The difference is their position in respect to the solution flow. Figure 10 shows an image of a growing crystal where we define the parallel (P) and perpendicular (N) faces.

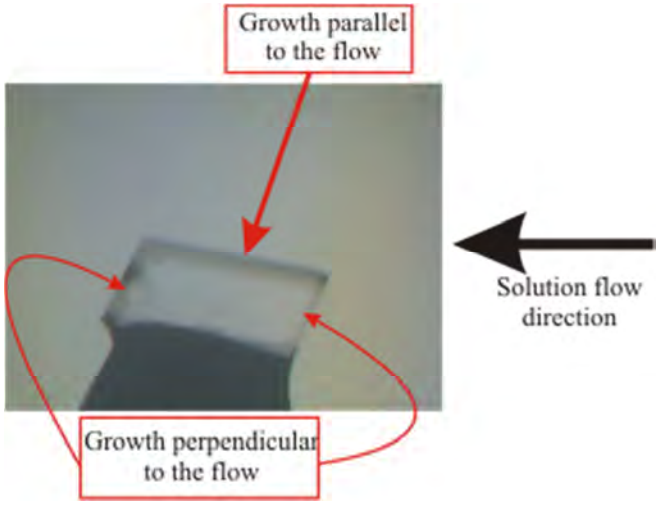


**Figure 10.** Definition of the growth of parallel (P, $R^{p}_{104}$) and perpendicular (N, $R^{N}_{104}$) faces in respect to the flow.

### 3.3.6. Determination of equilibrium and growth temperature.

Once the system is equilibrated we proceed to the growth rate determination:

- By adjusting the first thermostat we are able to determine the equilibrium temperature ($T_{eq1}$), by applying the Boistelle method.[23, 28]
- The temperature in the growth cell is decreased up to 0.8 K to achieve the required growth temperature ($T_{growth}$) adjusting the first thermostat and, successively, images of the oriented seed crystal are captured at regular time intervals to measure the face advancement rate.
- To change the supersaturation we add water directly into the reservoir to achieve a second equilibrium temperature $T_{eq2} = T_{eq1} - 0.1$ K. With this new concentration we set the difference $\Delta T = (T_{eq2} - T_{growth})$ to determine a second point, at lower supersaturation value, in the isothermal growth rate. This is repeated until, in practice, $T_{eq} = T_{growth}$.
- The crystal seed is changed when working at $T - T_{eq} > 0.4$ K or when 3D crystallization occurs, the growth cell is heated in order to dissolve nuclei and a new seed is then used. Additionally, if the seed becomes too large it is discarded. When seed is changed, the $T_{eq}$ is re-checked and adjusted adding water or $NaNO_3$ if required.

## 3.4. RESULTS AND DISCUSION

### 3.4.1. Calculation of Supersaturation.

As pointed out in the introduction, for the determination of the kinetics, it is necessary to construct a plot $R_{hkl}$ versus σ, i.e. what the dependence of the specific face ({104} form) with the supersaturation at different temperatures is. We have also reported that solubility of $NaNO_3$ is high (about 49 % in w/w at 298 K), so this system is far from being an ideal system. Therefore, a first step is to calculate the activity coefficient. The supersaturation of the solution is then defined as:

$$\sigma = \frac{\left(a_{Na^+} \cdot a_{NO_3^-}\right)_{eq}}{\left(a_{Na^+} \cdot a_{NO_3^-}\right)_{growth}} - 1 \qquad \textbf{equation 2}$$

where the nominator contains the actual value of the $NaNO_3$ concentration, in terms of molality. And the denominator is the $NaNO_3$ concentration at the crystallization temperature. The activity being:

$$a_{NaNO_3} = \nu_{Na^+} \cdot \nu_{NO_3^-} \cdot (\gamma_{NaNO_3} \cdot m_{NaNO_3})^2 \qquad \textbf{equation 3}$$

The calculation of activity coefficient is based on the work of Archer.[29] In this work Archer applies his modified Pitzer model[30] of ionic solutions to parameterize the equilibrium properties of the system $NaNO_3$ - $H_2O$. The equation they developed is given:

$$\ln\gamma_{\pm} = -|z_M z_X| A_\varphi \left(\frac{I^{1/2}}{1+bI^{1/2}} + \frac{2}{b}\ln(1+bI^{1/2})\right) + m\frac{2\upsilon_M\upsilon_X}{\upsilon}\left\{2\beta^{(0)}_{MX} + \frac{2\beta^{(1)}_{MX}}{\alpha^2 I}\left[1-\left(1+\alpha I^{1/2}-\frac{\alpha^2 I}{2}\right)e^{(-\alpha I^{1/2})}\right]\right\} +$$

$$m^2\frac{2\upsilon_M^2\upsilon_X\upsilon_Z}{\upsilon}\left\{3C^{(0)}_{MX} + 4C^{(1)}_{MX}\frac{\left[6-\left(6+6\alpha_2 I^{1/2}+3\alpha_2^2 I+\alpha_2^3 I^{3/2}-\frac{\alpha_2^4 I^2}{2}\right)e^{-\alpha_2 I^{1/2}}\right]}{\alpha_2^4 I^2}\right\} \qquad \textbf{equation 4}$$

where $\beta^{(0)}_{MX}$ , $\beta^{(1)}_{MX}$ , $C^{(0)}_{MX}$ , $C^{(1)}_{MX}$ are adjustable parameters (ion-interaction parameters) that are dependent on temperature and pressure. $z_M$ and $z_X$ are the charges of the cation and anion respectively; $\alpha$ and b were chosen to be constants with values 2.0 and 1.2 $Kg^{1/2}$ $mol^{1/2}$ respectively. $\nu_X$ and $\nu_M$ are the stoichiometric numbers of cations and anions formed upon complete dissociation and $n_w$ is the number of kg of water. Finally, m is the stoichiometric molality.

The parameters defined above are given in table 1, following Archer,[29] between 273.15 K and 373.15 K. The molality at saturation is also tabulated every five degrees in this temperature interval in the same paper. In order to calculate the logarithm of activity at the crystallization temperature we first calculate the dependence of $\beta^{(0)}_{MX}$, $\beta^{(1)}_{MX}$, $C^{(0)}_{MX}$, $C^{(1)}_{MX}$ values with temperature by spline interpolation of the values given in table 1. Then we calculated the molality of solution at the saturation temperature again by spline interpolation implemented in Matlab software. The ionic strength is calculated at the equilibrium temperature ($T_{eq}$) while the parameters of equation 2 are calculated at crystallization temperature ($T_{growth}$).

**Table 1.** Parameter values for the calculation of the activity coefficient from the modified Pitzer model for $NaNO_3$.[29]

| T / K | $A_\varphi$ ($Kg^{1/2}$ $mol^{1/2}$) | $\beta^{(0)}_{MX}$ (Kg/mol) | $\beta^{(1)}_{MX}$ (Kg/mol) | $1000\cdot C^{(0)}_{MX}$ (Kg/mol)^2 | $1000\cdot C^{(1)}_{MX}$ (Kg/mol)^2 |
|---|---|---|---|---|---|
| 273.15 | 0.376422 | -0.0121588 | 0.091059 | 0.499291 | -0.0934043 |
| 298.15 | 0.391476 | 0.00230499 | 0.211028 | 0.004126 | 0.0246091 |
| 323.15 | 0.410277 | 0.0123579 | 0.260857 | -0.286222 | 0.110253 |
| 348.15 | 0.433068 | 0.0186017 | 0.280054 | -0.418555 | 0.183839 |
| 373.15 | 0.459887 | 0.0218216 | 0.283146 | -0.443139 | 0.253879 |

At this point we have the values of supersaturation vs. growth rate at the three different growth temperatures. The data are given in table 2 where $R^N_{104}$ is the growth rate of the faces perpendicular to the flow and $R^p_{104}$ is the growth rate of the face parallel to the flow as they were defined in figure 10.

**Table 2.** Experimental growth rate at different supersaturations ($\sigma$) for perpendicular ($R^N_{104}$) and parallel ($R^p_{104}$) at the three temperatures.

| $\Delta T$ (K) | $\sigma$ ($x10^3$) | $R^N_{104}$ ($x10^7$cm/s) | $R^p_{104}$ ($x10^7$ cm/s) |
|---|---|---|---|
| 288.0 K | | | |
| 0.1 | 1.401 | 1.07 | 1.17 |
| 0.2 | 2.804 | 3.28 | 2.57 |
| 0.4 | 5.616 | 5.85 | 6.48 |
| 0.5 | 7.023 | 6.80 | 8.12 |
| 292.5 K | | | |
| 0.2 | 2.767 | 4.03 | 4.50 |
| 0.3 | 4.153 | 5.07 | 3.48 |
| 0.4 | 5.540 | 9.58 | 8.47 |
| 0.5 | 6.929 | 11.5 | 9.65 |
| 297.5 K | | | |
| 0.2 | 2.712 | 7.62 | 6.58 |
| 0.3 | 4.070 | 7.02 | 9.22. |
| 0.4 | 5.430 | 15.8 | 22.9 |
| 0.5 | 6.791 | 21.5 | 19.9 |
| 0.7 | 9.519 | 23.5 | 16.5 |
| 0.8 | 10.88 | 37.5 | 26.7 |

A plot for the three different temperatures is shown in figure 11 where a linear fit is sketched only for a general description. In these plots the red points indicate a measurement of the growth rate for the parallel ($R^p_{104}$) face with respect to the flow, likewise blue points indicate the growth rate for faces perpendicular to the flow ($R^N_{104}$) as have been explained in the introduction.

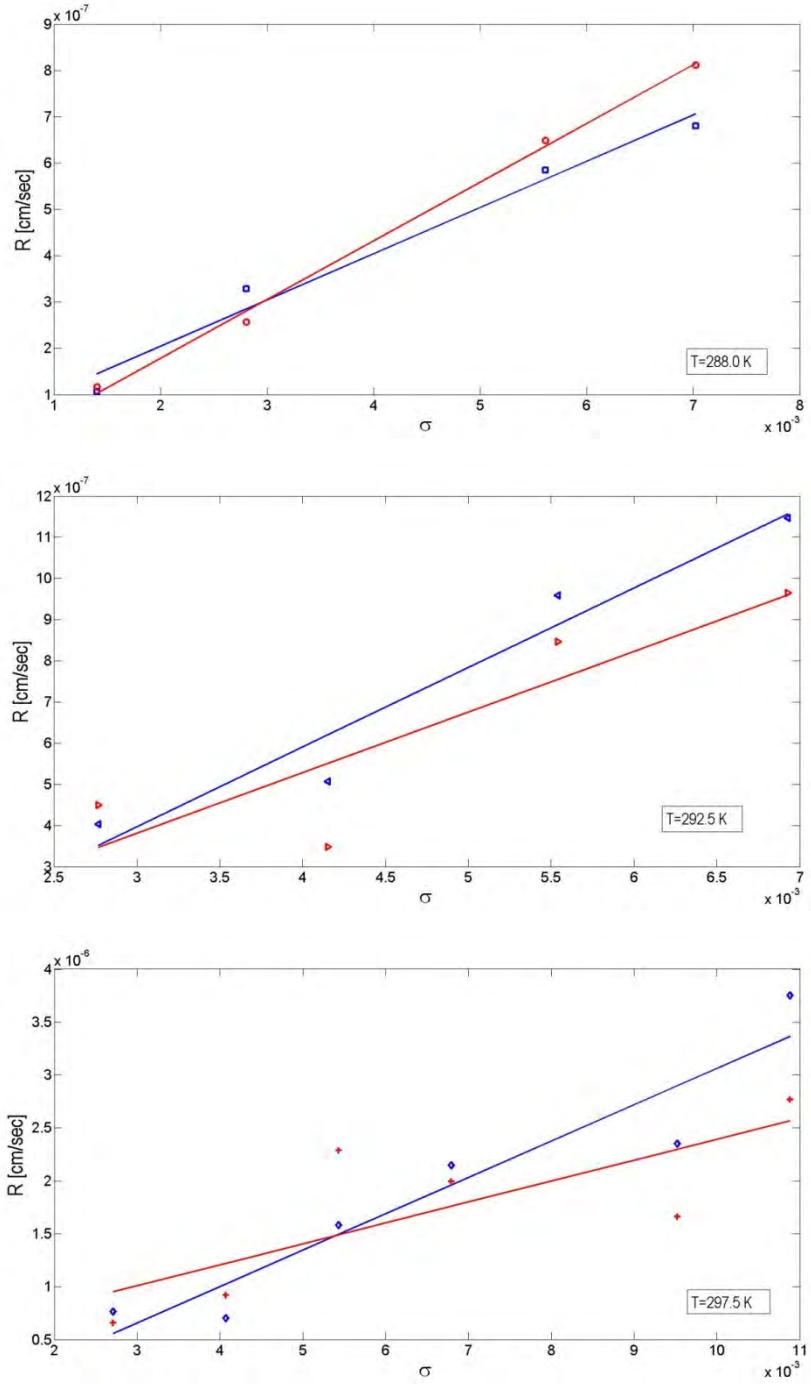


**Figure 11.** Kinetic measurements of the $NaNO_3$ {104} form at three different temperatures. Two hydrodynamic conditions hold in the experiment: parallel faces ($R^{p}_{104}$) with respect to the flow (red points) and perpendicular faces ($R^{N}_{104}$) with respect to the flow (blues points). Lines are only depicted for a discussion.

An unforeseen tendency comes out at first sight. We expected that, as we work with the same {104} form, both parallel and perpendicular faces have the same (or near the same) slope which would indicate similar activation energy, as we will present later on. In fact, the face parallel to the flux (red lines) seems to be tilted with respect to the other

measurement (blue lines) as the temperature is increased. This means that the growth rate of the parallel face, at a given supersaturation, which is the slowest (fastest) in respect to that of perpendicular face at 288.0 K becomes the fastest (slowest) at 297.5 K. This fact could be explained by many factors. First, the hydrodynamics are not the same. While in the perpendicular faces we have a 'thin' boundary layer in the parallel face, we would have turbulence due to the crystal itself and hence a somewhat 'thicker' boundary layer, so the parallel face growth rate would be the slowest. Another possible explanation is that this perpendicular face does not have a homogeneous environment due to its larger area in respect to the other faces. As Jones et al.[17] stated $NaNO_3$ has lots of dislocations within the volume and hence appearing on the surface. In this work we have used lots of seeds because the solubility is quite sensitive to the temperature and spontaneous nucleation appears at very low supersaturations, so normally more than one seed is used to determine each point. It is easy to suppose that the dislocation density is neither constant for different crystals nor for different faces. It might well introduce some dispersion in measurements. Another point of dispersion is the lack of reference point to make measurements on the parallel face, we generally use the sample holder as a reference but the delimitation line was not, in most of cases, clear so that it is source of experimental error. For perpendicular faces we calculated the mean velocity between the two faces, after realizing that the growth rate for the front and back face was similar (if this premise did not hold the measurement was immediately discarded). The crystal position in respect to the flow was another point of uncertainty, as can be seen by the comparison of the snapshots in figure 12. In the system built we have only one degree of freedom to orient the crystal (rotation in order to orient the perpendicular face). The parallel cannot be oriented and depends on the sample preparation. Seeds grow apparently without defects at least on the front face (right part of the crystal). Some defects were developed in certain cases on the parallel and back faces as can be observed in the figure 13. That the crystal environment is not homogeneous can be proven by the dissolution behavior showed in figure 14. It is clear that the front perpendicular face (on the right side of the crystal) dissolves quicker than the other two.

**Figure 12.** The relative orientation of the faces is not the same as in other images (see figure 13, 14, and figure 10). $T_{growth}$ = 292.5 K; $\Delta T$ = 0.4 K. Growth time 240 minutes.

**Figure 13.** Defects are mainly produced on the back face: dark part within the crystal in the image on the right. $T_{growth}$ = 297.5 K; $\Delta T$ = 0. 8 K. Growth time 120 minutes.

**Figure 14.** Dissolution experience, we clearly see that the right face dissolves faster than the others, therefore surrounding conditions are not constant.

Additionally, we would like to propose some considerations on the dispersion of the measured points. It is known that volume and surface diffusion can both contribute to the growth rate of a face. In solution growth the orientation of the face determines different hydrodynamic situations. Carlson[31] points out that turbulent flow may lead to starvation of faces whose normal is perpendicular to the solution flow (in this work

faces N, see figure 10) and convection plumes can lead to wedged crystals implying the formation of vicinal and even higher index faces.[32]

Moreover, the models we use to unravel a growth mechanism assume that the growth hillocks are made by a sequence of equally spaced steps as a consequence of neglecting the steps movements in respect to the rate of diffusion of the growth units towards the steps. As shown by the measurements (see below) on the face (104) of nitratine, even single spiral sides do not have a constant slope. This can be understood by considering that in the center of spiral there is only one source of dislocations (steps can be considered equally spaced) while near the spiral periphery the advancement rates of the steps is determined by crystal edges, steps from other sources, defects, etc. Consequently, step bunching occurs. It is also shown in some models[33] and theories.[34, 35] It follows that the measured growth rate of a crystal face is a mean over different domains of the same face where the step density and often the height are different. Finally, to measure a growth isotherm requires the use of several different crystals which may cause dispersion since each crystal has a different dislocation distribution and density. In conclusion, hydrodynamic factors and surface features at the nano scale, can explain both the dispersion of the growth rates and that the growth of faces with different orientation may be limited by different elementary processes i.e. they grow with different mechanisms. Notwithstanding the dispersion, in most cases, the processes limiting the growth rate can be identified as the experimental isotherms, growth rate (R) vs. supersaturation ($\sigma$), can be fitted by curves corresponding to proposed growth models and the derived activation energies for growth support the statistical analysis.

### 3.4.2. General equations for determining the growth mechanism.

In order to identify the growth mechanism of the $NaNO_3$ ($R^N_{104}$ and $R^p_{104}$) faces, we refer to the work of Gilmer, Ghez and Cabrera[36] who consider the stationary growth of a crystal due to combined volume and surface diffusion processes. The more general form of the growth rate, $R_{hkl}$, they obtained depends on the slope of the growth hillock, on transport properties in the bulk of the solution and crystal surface, and finally, on the kinetics of integration of the growth unit in the steps. Depending on the relative weight of the different fundamental processes: volume diffusion, surface diffusion and

integration rate of growth units in the steps, the general $R_{hkl}$ vs. $\sigma$ relation assumes specialized laws proposed by BCF,[6] Bennema[37] or Chernov.[38]

The Gilmer, Ghez and Cabrera master equation reduces to equation 5 in the case where the mean free path of growth units in solution ($\Lambda$) is much greater than that on the crystal face ($\lambda$). That $\lambda / \Lambda \rightarrow 0$ is expected as surface diffusion requires desorption of the growth units. This assumption will be justified a posteriori if we find a mechanism acceptable under this assumption.

$$R_{hkl} = \frac{N_0 \, \Omega D}{\Lambda + \delta + \frac{\Lambda \Lambda_s l}{\lambda^2} + \Lambda\left[\frac{l}{2\lambda}\coth\frac{l}{2\lambda} - 1\right]} \sigma \qquad \textbf{equation 5}$$

The meanings of the symbols in equation 5 are:

$N_0$: density of solute at equilibrium.

$\Omega$: volume of a formula unit in the crystal cell.

D: diffusion coefficient of growth units in solution.

$\sigma$: supersaturation of the solution.

$\Lambda$: mean free path of a growth unit in solution.

$\delta$: thickness of the boundary layer.

$\Lambda_s$: coefficient related to the transfer of growth units between steps and surface.

$\lambda$: mean free path of a growth unit on crystal face.

$l$: equidistance of steps.

$\tau_s$: the life time of a growth unit on the crystal surface before desorption.

The growth rate $R_{hkl}$ is limited by several impedances: first, the impedance of the adsorption reaction; second, the impedance to enter in the unstirred layer; third, the impedance for entering the steps; and forth, the surface diffusion impedance. They are in order in the denominator of equation 5.

In order to calculate the activation energy associated with the growth, it is necessary to express the temperature dependence of the phenomenological coefficients. Following the definitions in Bennema[37] we have:

$$D_v = a'^2 \frac{kT}{h} \cdot \exp - \frac{\Delta G^{\ddagger}_{vdiff}}{kT} \qquad \textbf{equation 6}$$

$$\Lambda = a' \cdot \exp \frac{\Delta G^{\ddagger}_{desolv} - \Delta G^{\ddagger}_{vdiff}}{kT} \qquad \textbf{equation 7}$$

$$D_s = a^2 \frac{kT}{h} \exp - \frac{\Delta G^{\ddagger}_{sdiff}}{kT} \qquad \textbf{equation 8}$$

$$\lambda = a \cdot \exp \frac{\Delta G^{\ddagger}_{des} - \Delta G^{\ddagger}_{sdiff}}{2kT} \qquad \textbf{equation 9}$$

$$\tau_s = \frac{\lambda^2}{D_s} = \frac{h}{kT} \cdot \exp \frac{\Delta G^{\ddagger}_{des}}{kT} \qquad \textbf{equation 10}$$

$$\Lambda_s = \frac{1}{2} a \cdot \exp \frac{\Delta G^{\ddagger}_{ks} - \Delta G^{\ddagger}_{vdiff}}{kT} \qquad \textbf{equation 11}$$

where the $\Delta G^{\ddagger}_i$ is activation energy for volume and surface diffusion ($\Delta G^{\ddagger}_{vdiff}$ and $\Delta G^{\ddagger}_{sdiff}$ respectively), desorption from the crystal surface to solution ($\Delta G^{\ddagger}_{des}$), partial desolvation from solution to crystal surface ($\Delta G^{\ddagger}_{desolv}$) and for entering the kinks from the surface ($\Delta G^{\ddagger}_{ks}$) (as were defined in figure 2).

The general expression to obtain the experimental value of the crystallization enthalpy from kinetic measurements is:

$$-R \frac{\partial ln b_{exp}}{\partial \frac{1}{T}} = \Delta H_{cr}^{exp} \qquad \textbf{equation 12}$$

where R is the gas constant value and $b_{exp}$ is the parameter that multiplies the supersaturation in accordance with a general growth rate law:

$$R_{hkl} = b(T) \times \sigma^n \qquad \textbf{equation 13}$$

here $R_{hkl}$ is the experimental growth rate and n is the growth rate order.

### 3.4.3. Calculation of some external parameters ($N_0$, Ω, $D_v$, δ).

There are parameters that are independent of the growth model proposed but depend on the temperature, basically.

### 3.4.3.1. Solute density at equilibrium ($N_0$).

The solute density at the equilibrium is related to molarity, m. It, in turn, is related to the molality, m, by the relation:

$$c = \frac{m \cdot \rho}{1 + m\frac{W}{1000}} \qquad \textbf{equation 14}$$

where ρ is the solution density and W is the solute molecular weight.

### 3.4.3.2. Molecular volume (Ω).

From the cell parameters, $NaNO_3$ crystallize in $R\bar{3}c$ space group with cell parameters **a** = 5.07 Å and **c** = 16,82 Å at 293 K with 6 molecules per cell (Z = 6)[9] So the calculation gives a volume of a unit formula (building unit) of $\Omega = 62.41 \cdot 10^{-24}$ $cm^3$.

### 3.4.3.3. Volume diffusion ($D_v$).

The magnitude of the diffusion coefficient was calculated by the Nernst equation, defined below (equation 15), at the three temperatures. The required data for the limiting equivalent conductivities was taken from Robinson and Stokes.[39]

$$D^0 = \frac{RT}{F^2}\frac{\nu_1+\nu_2}{\nu_1|z_1|}\frac{\lambda_1^0\lambda_2^0}{\lambda_1^0+\lambda_2^0} \qquad \textbf{equation 15}$$

In the equation 15, $\nu_1$ and $\nu_2$ correspond to the number of cations and anions with algebraic valence $z_1$ and $z_2$ respectively generated by the dissociation of a unit formula of electrolyte. $\lambda_1^0$ and $\lambda_2^0$ are the limiting equivalent conductivities, R and F are the gas and Faraday constants.

Its variation with the concentration is given by equation 16. Results are given in the table 3.

$$D_\nu = D^0\left(1 + \frac{d\log(\gamma_\pm)}{d\log(c)}\right) \qquad \textbf{equation 16}$$

**Table 3.** Volume diffusion coefficient for $NaNO_3$ saturated solution at the three temperatures of interest.

| T (K) | $D_v$ ($cm^{-1}$) |
|---|---|
| 288.8 | $8.4 \cdot 10^{-6}$ |
| 292.5 | $9.2 \cdot 10^{-6}$ |
| 297.5 | $10.3 \cdot 10^{-6}$ |

### 3.4.3.4. Thickness of the boundary layer (δ).

The boundary layer thickness is given by the equation:

$$\delta = \frac{3}{2}\left(\frac{kT\rho}{6\pi r\eta^2}\right)^{\frac{1}{3}}\left(\frac{\eta d}{\rho v}\right)^{\frac{1}{2}}. \qquad \textbf{equation 17}$$

where the values of density ρ and viscosity η, can be obtained using their parametric representations given in the paper by Xu and Pruess.[27] The molecular size r is known, while the rate of flow of the solution $v$ and the linear size of the crystal d, are experimental. It turns out that $\delta \cong 1.4 \times 10^{-2}$ cm.

### 3.4.4. Determination of the growth model and energetic parameters.

As we have two different hydrodynamic conditions for the growth of the equivalent (104) faces we ought to analyze them independently. We first consider perpendicular face, and after that, parallel faces. In this part we determine the most probable growth mechanism and some thermodynamic parameters that help us to validate the proposed theories.

### 3.4.4.1. Perpendicular faces.

The kinetic analysis is limited to the growth curves of the faces perpendicular to the solution flux ($R^N_{104}$). Indeed, the variation of the growth rates of the crystal faces parallel to the flux ($R^P_{104}$) shows variations with temperature and supersaturation ascribable to non-steady hydrodynamic phenomena. Anyway, we have also tried to fit the data to a linear model for the parallel face as can be seen later.

In order to identify a growth mechanism we tentatively tested several different hypothesis, as detailed in the following.

#### 3.4.4.1.1. Chernov model.

As the measured growth isotherms suggest a linear increase of the growth rate with supersaturation, we tested at first if the growth is limited by volume diffusion. When the volume diffusion parameter is larger than the thickness of boundary layer ($\Lambda >> \delta$) equation 5 transforms to equation 18 which is the Chernov model: growth rate determined by volume diffusion.

$$R_{hkl} = \frac{N_0 \Omega D \sigma}{\Lambda(\frac{\Lambda_s l}{\lambda^2} + \frac{1}{2\lambda}\coth\frac{1}{2\lambda})} \qquad \textbf{equation 18}$$

Two parameters were determined by non-linear least squares:

$$p_2 = \sigma\frac{1}{2\lambda} = \frac{\gamma a}{kT\lambda} \qquad \textbf{equation 19}$$

$$p_1 = \frac{2\Lambda_s}{\lambda} \qquad \textbf{equation 20}$$

here $\gamma$ is the mean specific edge energy (erg/cm) of a 2D nucleus on the (104) face, and a ($cm^2$) the area occupied by a growth unit onto the step ledge.

The order of magnitude of the diffusion coefficient is $D_v \cong 1.03 \cdot 10^{-5} cm^{-1}$. It was calculated above (see point 3.3).

A least squares test was made on the isotherm at 297.5 K. The values of $\Lambda$ were fixed and spanned several orders of magnitude. Only for values $\Lambda \cong 10^{-2}$ cm the least squares test converged. Although values of the parameters are affected by high variance values this law cannot be rejected on the grounds of a $\chi^2_{0.9}$ test with 4 degrees of freedom.[40]

As the Chernov model is obtained when $\Lambda >> \delta$, this mechanism should be definitively excluded. We assume that this also holds true for the two other isotherms, which will be further confirmed if we find a unique rate law describing the three growth isotherms.

### 3.4.4.1.2. Growth limited by volume transport and surface diffusion.

When we impose the condition that volume transport is smaller than the mean free path ($\Lambda_s \ll \lambda$) to equation 5, we arrive at equation 21:

$$R=\frac{N_0\,\Omega D}{\delta+\Lambda\frac{1}{2\lambda}\coth\frac{1}{2\lambda}}\sigma \qquad \textbf{equation 21}$$

Using the experimental value of δ, we tried to determine two parameters fitting this expression to the higher temperature isotherm without succeeding so it has to be excluded.

### 3.4.4.1.3. Growth limited by surface diffusion.

When the surface diffusion is the rate limiting step, from equation 5one obtains the B.C.F. growth law: equation 22.

$$R_{104}^{N}=\frac{p_1}{p_2}\tanh\left(\frac{p_2}{\sigma}\right)\cdot\sigma^2 \qquad \textbf{equation 22}$$

The parameters to be determined by least squares are:

$$p_1=\frac{D_s\Omega n_{s0}}{\lambda_s^2}=\frac{n_0\Omega}{\tau}; \qquad \textbf{equation 23}$$

$$p_2=\frac{\in}{c}\frac{\gamma a^2}{kT\lambda} \qquad \textbf{equation 24}$$

$$\frac{p_1}{p_2}=\frac{c}{\in}\frac{D_s\Omega n_{s0}kT}{\gamma\lambda_s a^2}; \qquad \textbf{equation 25}$$

We recall that the mean distance between steps is:

$$l=\frac{2\gamma a^2}{kT\sigma}. \qquad \textbf{equation 26}$$

where $D_s$ is surface diffusion coefficient ($cm^{-1}$); $\tau$ residence time of a growth unit on the surface before evaporation (s); $\gamma$ edge free energy (erg/cm); $a^2$ 2 - D area occupied by a growth unit in a mesh on a step ($cm^2$); $c/\epsilon$ is the ratio between the shape factor $c$ of the spiral growth and the number of dislocation in a bundle $\epsilon$ and $n_{s0}$ the concentration of adsorbed growth unit at equilibrium.

This $R^N_{(104)}$ vs. $\sigma$ relation is observed when the growth rate is limited by the diffusion of growth units on the crystal face while their integration in the kinks is relatively faster as well as the transport through the boundary layer.
As before, the parameters ($p_1$ and $p_2$) were determined by least squares analysis and the likelihood test is positive for the three isotherms. Results for both parameters at the three temperatures are given in table 4.

**Table 4.** Parameters determined for the BCF growth model for perpendicular faces at three temperatures.

| | 288.0 K | | 292.5 K | | 297.5 K | |
|---|---|---|---|---|---|---|
| | Value | Error | Value | Error | Value | Error |
| $p_1$ | $1.01\cdot10^{-4}$ | $5.9\cdot10^{-4}$ | $1.80\cdot10^{-4}$ | $8.6\cdot10^{-5}$ | $3.81\cdot10^{-4}$ | $1.0\cdot10^{-5}$ |
| $p_2$ | $6.36\cdot10^{-4}$ | $3.7\cdot10^{-3}$ | $3.40\cdot10^{-3}$ | $2.0\cdot10^{-3}$ | $6.32\cdot10^{-3}$ | $3.2\cdot10^{-3}$ |

In Figure 15 we show the BCF theoretical curve fitting the experimental values for the three temperatures (Blue: 297.5 K; red: 292.5 K; and green: 288.0 K). It is also shown the limiting growth rate (linear part of the BCF mechanism for very high $\sigma$) for 297.5 K mechanism. It is worth pointing at three facts in this figure. First: The parabolic parts of the curves are restricted to very low supersaturation values, the lower the temperature the shorter the parabolic region. Second, the transition from the parabolic part to the lineal is gradual as can be seen by the 297.5 K (blue line). And third, at very low supersaturations $\sigma < 0.002$ the three curves have a cross that might be related to the different parts of the curves in the three temperatures, as explained above.

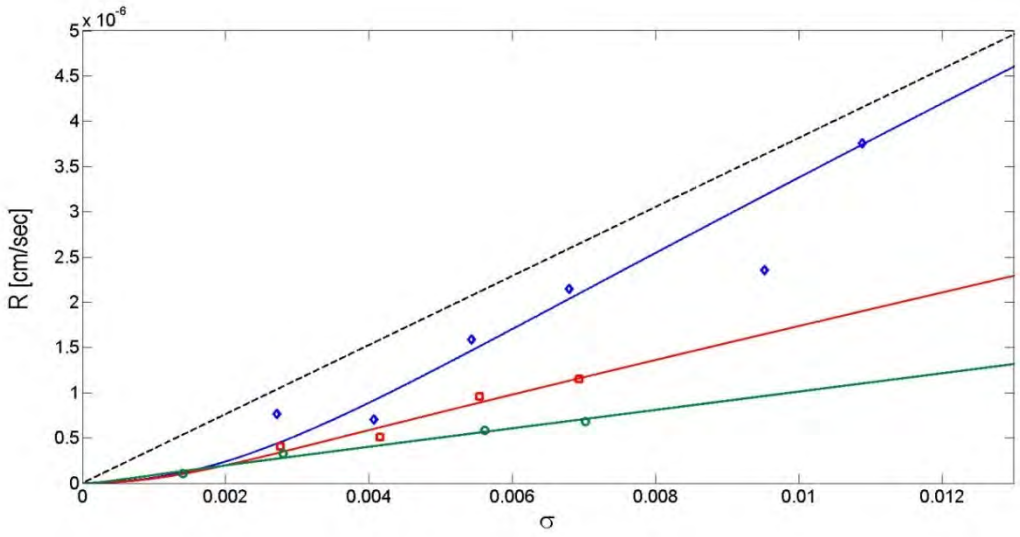


**Figure 15.** BCF plot on the perpendicular faces at three temperatures. Blue diamonds: 297.5 K; red squares: 292.5 K; and green circles: 288.0 K.

As concerns the growth of the N faces, we consider at first, the dependence of the parameter $p_1$ on temperature, shown in Figure 16. Here we fit an Arrhenius plot to calculate the activation energy.

The value of $p_1$ is related to the slope of $R^N_{(104)}$ at high supersaturation ($\sigma$). We limit the analysis to it as it is better constrained than the ratio $p_1 / p_2$. This is due to the lack of values at very low supersaturations as a result of the difficulty of accurate measurements at lower temperature: 288.0 K and 292.5 K.

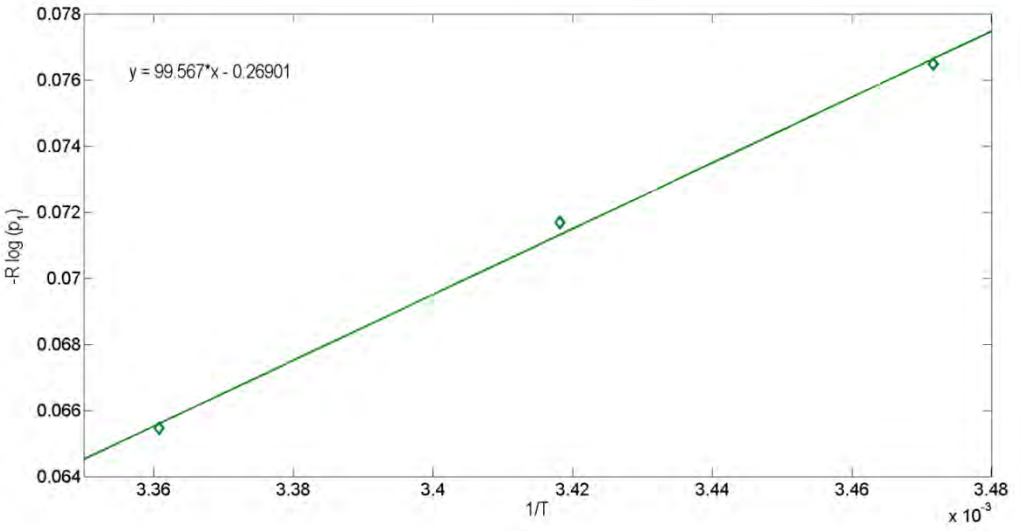


**Figure 16.** Arrhenius plot for determining the activation energy for $NaNO_3$ crystallization.

From a plot of the estimated ln $p_1$ against 1/T we obtain 99,6 kJ/mol. Its temperature dependence is expressed by the equation 27:

$$-R\frac{\partial \log p_1}{\partial \frac{1}{T}} = RT + \Delta H^{\ddagger}_{des} + \Gamma^0_1 s^0_2 \Delta H^0_{1des} + \Delta H^{\dagger}_{ks} \qquad \textbf{equation 27}$$

This comes from the definition of $p_1$ parameter $p_1 = \frac{n_0 \Omega}{\tau}$ where the molecular volume ($\Omega$) is taken as constant. When we take partial derivatives:

(a) the variation of residence time ($\tau$) with temperature: $-R\frac{\partial \log \tau^{-1}}{\partial \frac{1}{T}} = RT + \Delta H^{\ddagger}_{des}$, where $\Delta H^{\ddagger}_{des}$ represents the activation heat for desorption of a growth unit; and

(b) the variation of the concentration of adsorbed growth units at equilibrium ($n_0$) with temperature $-R\frac{\partial og}{\partial \frac{1}{T}} = \Gamma^0_1 s^0_2 \Delta H^0_{1des} + \Delta H^{\dagger}_{ks}$ where $\Delta H^{\dagger}_{ks}$ is the mean enthalpy to transfer a growth unit (component 2) from the kink (a crystal cell of 6 growth units) to the surface: on the surface the growth units occupy the area $s^0_2$ and they can be adsorbed if simultaneously $\Gamma^0_1 s^0_2$ molecules of solvent are desorbed with evolution of $\Gamma^0_1 s^0_2 \Delta H^0_{1des}$ joules.

Several equations[5, 41] have been proposed for the dependence of $n_{s0}$ with temperature. We chose the thermodynamical model of adsorbed layer developed by H.E. Madsen Obviously, $\Gamma^0_1 s^0_2 \Delta H^0_{1des} + \Delta H^{\dagger}_{ks}$, is a very difficult quantity to be calculated a priori for an adsorbed layer of electrolyte.[5, 41] Nevertheless, we can assess this value from a plot of the estimated $ln\ p_1$ against 1/T. As shown in figure 16 the slope we have obtained is: 99.6 kJ/mol.

Additionally, the calculated mean attachment energy per mol of formula unit on (104) face is 56.8 kJ/mol.[42] A fraction of this value represents the activation energy for the transition from the crystal surface to the solution. Assuming that the upper limit of the activation energy for desorbing a growth unit is of the order of the attachment energy per mol of formula units ($\Delta H^{\ddagger}_{des}$ ~ 56.8 kJ/mol) and considering the mean value of the crystallization temperature RT = 2.4 kJ/mol, we obtain the lower limit of: $\Gamma^0_1 s^0_2 \Delta H^0_{1des} + \Delta H^{\dagger}_{ks}$ = 40.4 kJ/mol, an order of magnitude which seems to be acceptable.

On the other hand, we can use $p_2$ to estimate the mean edge free energy of a 2D island ($\gamma$) on (104) faces by the relation $p_2 = \frac{\epsilon}{c}\frac{\gamma a^2}{kTx_s} = 0.0063$, at 297.5 K. $\epsilon$ depends on the number of interacting spirals of the same sign, c is the shape factor approximately equal to 4 for a lozenge shaped island.[33, 43] Assuming the mean free path of the growth units on (104) face is equal to $4 \cdot 10^{-6}$ cm and $\epsilon / c = 1$, we calculate $\gamma = 5.1 \cdot 10^{-7}$ erg/cm. This value looks to be of the correct order of magnitude.

In conclusion, we accept that the growth of the (104) faces whose normal is parallel to the solution flow is limited by surface diffusion.

#### 3.4.4.2. Parallel faces.

As we have described for the perpendicular faces we also sought to find a mechanism of growth for parallel face. A description is in the following.

##### 3.4.4.2.1. Growth limited by volume diffusion.

We did not try a fit with the BCF law used in case of the growth of the faces perpendicular to the solution flow. A different growth mechanism is, indeed, apparent. It is suggested from the curves R vs. $\sigma$ and the variation of their slopes. Because it was difficult to measure the advancement rates of this face with the same accuracy of those phases perpendicular to the solution flow we fitted the isotherms by a linear equation in respect to the parameters and supersaturation.
The linear law can be derived from equation 5 when the equidistance between steps is nearly zero ($l \to 0$) so that surface diffusion is negligible and the volume diffusion limits the growth rate. In equation 28 the value in parenthesis is the parameter 'a', and 'b' must be 0.

$$R = \left(\frac{N_0 \, \Omega D_V}{\delta + \Lambda}\right) \sigma \qquad \textbf{equation 28}$$

Where $N_0$ is the equilibrium concentration of growth units in solution, Ω is the volume of a formula unit in the kinks, $D_v$ is the diffusion coefficient in solution, δ the thickness of the solution boundary layer on the (104) face. The regression coefficients 'a' and 'b' are given in the table 5. Despite the high error in b parameter, fitted lines can be considered to pass through origin. In figure 17 we show the fitting.

**Table 5.** Calculated parameters for the linear law in the parallel face ($R^P_{104}$).

| | 288.0K | | 292.5K | | 297.5K | |
|---|---|---|---|---|---|---|
| | Value | Error | Value | Error | Value | Error |
| a | $1.28\cdot10^{-4}$ | $2.3\cdot10^{-5}$ | $1.47\cdot10^{-4}$ | $3.2\cdot10^{-5}$ | $1.98\cdot10^{-4}$ | $1.4\cdot10^{-4}$ |
| b | $-7.54\cdot10^{-8}$ | $1.1\cdot10^{-7}$ | $-6.16\cdot10^{-8}$ | $8.3\cdot10^{-8}$ | $4.16\cdot10^{-7}$ | $1.0\cdot10^{-6}$ |

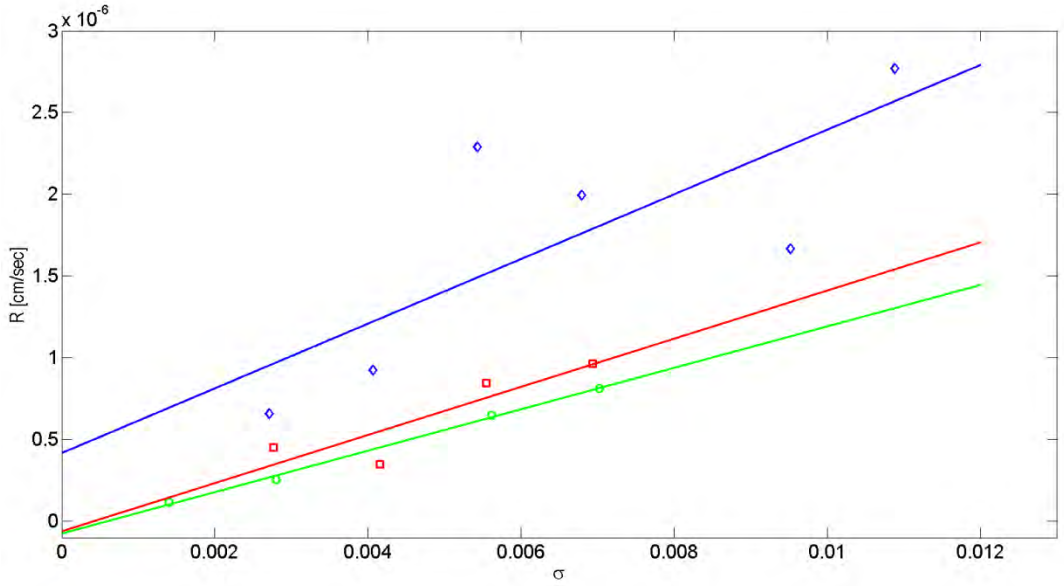


**Figure 17.** Faces P. Growth isotherms ($R^P_{104}$) refer respectively to: Green circles: 288.0 K, Red squares: 292.5 K, and Blue diamonds: 297.5 K.

In order to determine the experimental value of the crystallization enthalpy we have to apply the general equation 12 given above. Similarly to what we did with the perpendicular faces here we describe the thermodynamic parameters that can be extracted from the linear law. From the plot $-R\cdot\log(a)$ versus 1/T (figure 18) we get that the activation energy ($E_1^{\ddagger}$) is 33.5 kJ/mol.

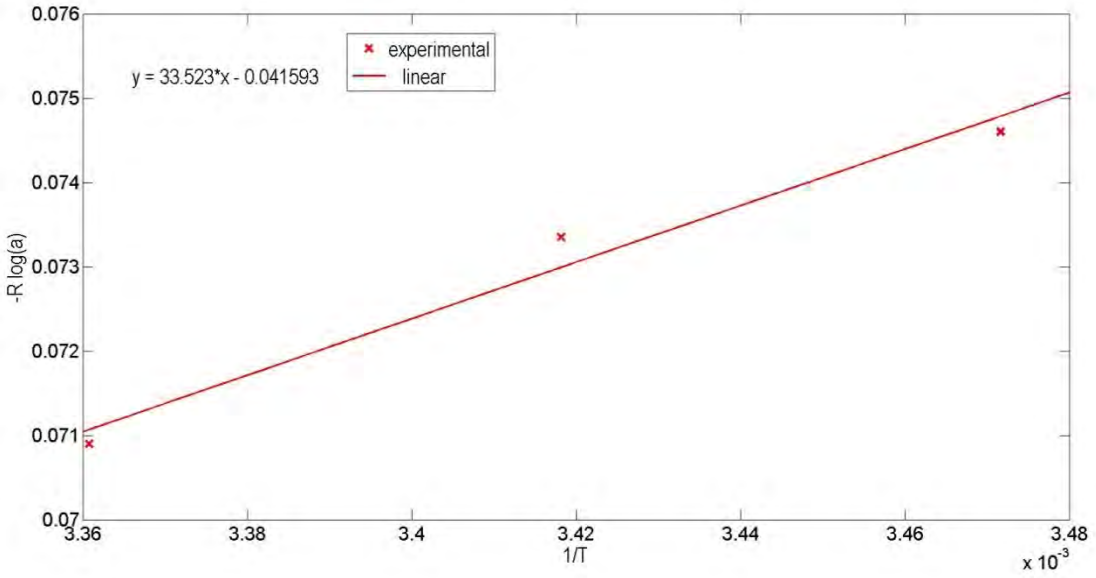


**Figure 18.** Data fitting for the linear law proposed in parallel face.

The expression of the activation energy for the linear law is obtained starting from $a=\frac{N_0\,\Omega D}{\delta+\Lambda}$. The molecular volume is considered constant. After arranging the partial derivatives we get:

$$E_l^{\ddagger}=-R\left\{\frac{\partial \log N_0}{\partial \frac{1}{T}}+\frac{\partial \log D_v}{\partial \frac{1}{T}}-\frac{1}{\delta+\Lambda}\left[\frac{\partial \delta}{\partial \frac{1}{T}}+a'\frac{\Delta H^{\ddagger}_{desolv}-\Delta H^{\ddagger}_{vdiff}}{R}\exp\frac{\Delta G^{\ddagger}_{desolv}-\Delta G^{\ddagger}_{vdiff}}{RT}\right]\right\}$$

where $\Delta H^{\ddagger}_{desolv}$ and $\Delta G^{\ddagger}_{desolv}$ are the activation enthalpy and free enthalpy of a growth unit that surmounts the activation barrier in the transition from the solution to the crystal face; we estimate $\Delta H^{\ddagger}_{desolv}$ = 50 kJ/mol.[44].

The first factor can be further developed:

$$-R\frac{\partial \log N_0}{\partial \frac{1}{T}}=-R\left\{\frac{\partial \log m}{\partial \frac{1}{T}}+\frac{\partial \log \rho}{\partial \frac{1}{T}}-\frac{M\times 10^{-3}}{1+mM\times 10^{-3}}\frac{\partial m}{\partial \frac{1}{T}}\right\}$$

where M is the molecular weight of the solute. The derivative of $m$ is calculated using the solubility by Archer.[29]

$$R\frac{M\times10^{-3}}{1+mM\times10^{-3}}\frac{\partial m}{\partial T^{-1}}=-0.0638 \text{ and}$$

$$-R\frac{\partial \log m}{\partial T^{-1}}=6.343.$$

The temperature dependence of ρ is calculated from the data by NIST:[29]

$$-R\frac{\partial \log \rho}{\partial T^{-1}}=-0.455\times10^{-3}$$

Therefore, the value of the first factor is 6.405 kJ/mol.

The second factor was calculated through the variation of the volume diffusion coefficient at the three crystallization temperatures. It gives $-R\frac{\partial \log D_v}{\partial \frac{1}{T}}=15.993$ kJ/mol by linear regression.

The mean value of $\delta + \Lambda = 0.0308$ cm is calculated from the isotherm at 292.5 K. The boundary layer dependence with temperature turns out to be $\frac{\partial \delta}{\partial \frac{1}{T}} = -4.1071$ cm·K, evaluated through the experimental values of solution flow rate (v), mean dimension of crystals (d), and data from NIST[29] to calculate the remaining quantities in the relation of the thickness of the boundary layer (equation 17).

Additionally, one can also estimate that the activation enthalpy for volume diffusion at 292.5 K. is $\Delta S^{\ddagger}_{vdiff} = 13.56$ kJ/mol.

The difference between the activation entropy for partial desolvation of the growth units entering the adsorbed layer and that for volume diffusion is acceptable as, in the activated state, the rate determining step is the relaxation of bonds between growth units and solvent molecules in both processes.

Therefore considering that during growth:

- P faces remain flat at the observation under the microscope and do not experience effects due to turbulent flow.
- The trend of the growth isotherm is linear.
- The thermodynamic analysis does not lead to inconsistencies;

Then we accept that the growth rate of the P faces is limited by the diffusion in the bulk of the solution.

## 3.5. SURFACE STRUCTURE VIEWED WITH ADVANCED MICROSCOPY

We describe here the initial experiences for the surface observation in a confocal differential interference contrast microscope (LCM-DCM) that led us to understand the arduous processes occurring on the surface. We have worked in two directions with this observation technique. First, we built the setup described in this chapter so that we have the same solution flow environment described throughout the chapter. Then, we followed working by small stagnant batches. Thus we can compare the results obtained.

Referring to flow tests, many experiments have been carried out at several temperatures between 283 K and 298 K. We show in figure 19 a sequence of snapshots in which we can observe the $NaNO_3$ complicated surface structure inside a solution flow. It is worth remembering here that the surface we are looking at is the bottom face of the crystal; therefore it is a parallel face in respect to the flow (P, $R^P_{104}$). As described above, the volume diffusion is the rate determining step on this face. It is consistent with the dislocation mesh found on the surface. Furthermore, the quality of seed crystal surface is very poor. Seed crystals exposed to ambient condition tend to be partially dissolved and present the surface topography showed in figure 19.

In figure 19 we observe in the initial snapshot (upper-left) a relatively flat surface with a macrostep (made by several steps) on the right part. As time passes lots of steps are generated onto the surface. Its main propagation direction is from bottom-right to upper-left. We observe, however, that the steps propagate with rounded shape surrounding holes (some are encircled in figure 19). This is the typical mechanism to overcome strongly adsorbed impurities.[45] Furthermore, on the right part of the crystal we observe a flat surface that is growing. On this part we have observed quick steps (marked with arrows in figure 19) running from the bottom to the upper part of the crystal with an impressive growth of 335 µm/min.

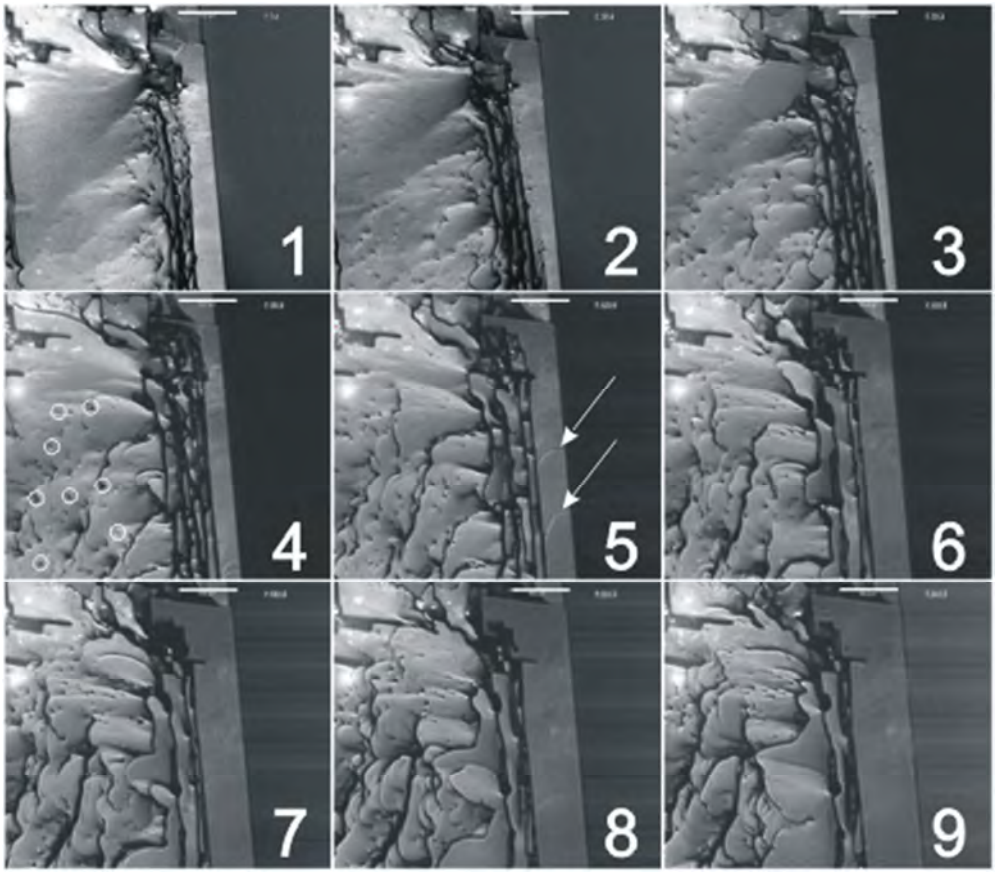


**Figure 19.** Macrosteps movement during the growth of $NaNO_3$ seed crystal at 285.9 K with a supersaturation corresponding to $\Delta T$ = 0.4 K. Morphological features and selected step growth rate are displayed on the image. Time between images is 300 seconds. Bar: 100 µm (brightness and contrast has been modified to display better surface characteristics).

We can conclude with this set of measurements at different temperatures and relative supersaturations that there is not a clear relationship between step velocity and the supersaturation. It seems to be more dependent on the height of the step. We must remember here that the step height cannot be measured by confocal microscopy, but differences in contrast give us an idea of relative observed heights.

This result is consistent with the previous findings: volume diffusion is the rate determining step on this face. We have observed here a lot of growing points; this led to a short mean free path on the surface ($\lambda$), so that a new building unit will quickly find a kink to be attached to the bulk crystal. More experiments have to be done for a deeper understanding.

We expose now the results obtained by the observation of $NaNO_3$ growth in stagnant solutions. Here we suppose that volume diffusion is the rate determinant step because the boundary layer in this situation tends to be larger than that with a stirred solution.
In this case we have worked at two different equilibrium temperatures around 286.5 K and different supersaturations. As can be observed in figure 20, we can distinguish essentially three different stages during $NaNO_3$ crystal growth. First, a macro-island appears from a relatively rough surface, then it grows until the crystal border is reached: a flat surface is formed (it has a roughness below 3 nm because it is the instrumental limit) and, finally the crystal further grows, although we cannot see any surface movement. We are sure that the crystal is still growing when it has a flat surface because, with time, we lose the focal plane.

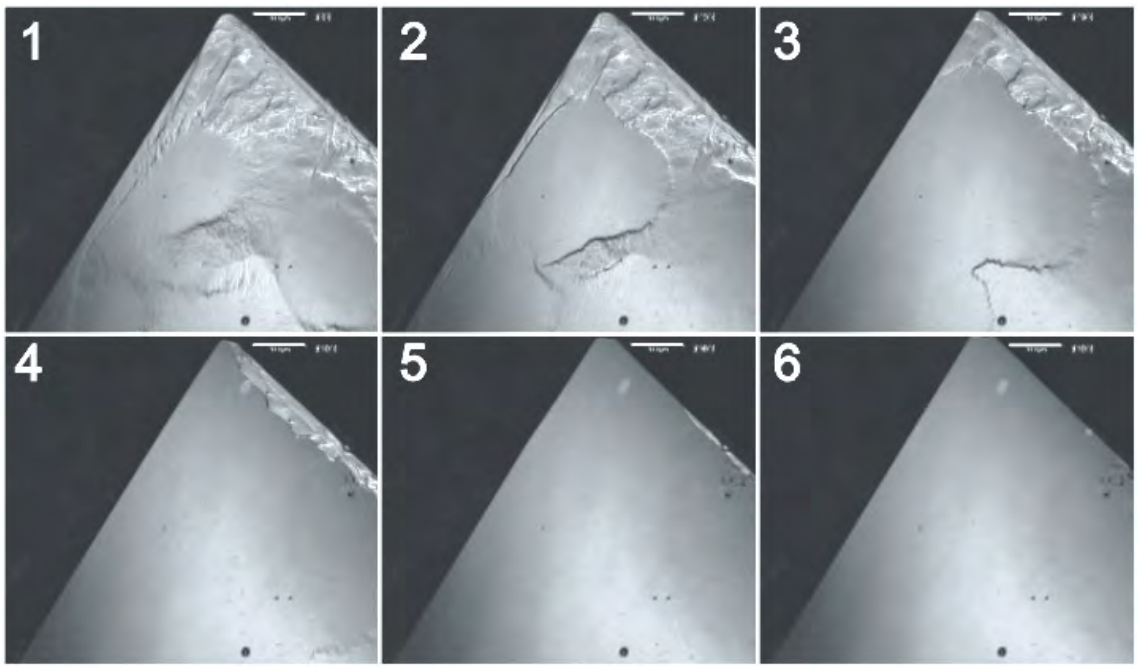


**Figure 20.** Formation of a flat face from a seed. Equilibrium temperature 286.9 K. supersaturation corresponding to $\Delta T$ = 0.3 K. Time between images: 180 seconds. Bar: 100 µm.

An additional experience has been performed by growing and dissolving a seed. The aim of these experiences is to measure the dependence of the step growth rate with the direction. We have worked at the same equilibrium temperature growing the same seed at different supersaturations corresponding to the temperature range: 0.1 K < $\Delta T$ <1.3 K. Between measurements the seed was partially dissolved in order to

obtain a rough surface. In figure 21 we show 3 snapshots of the process for a $\Delta T = 0.5$ K.

We observe that a macroisland is generated in the middle of the crystal. It grows in the set of equivalent directions <$\bar{4}41$>. These are parallel to crystal edges. We may define these directions here as their movement from the centre of the crystal: left, right, up, and down.

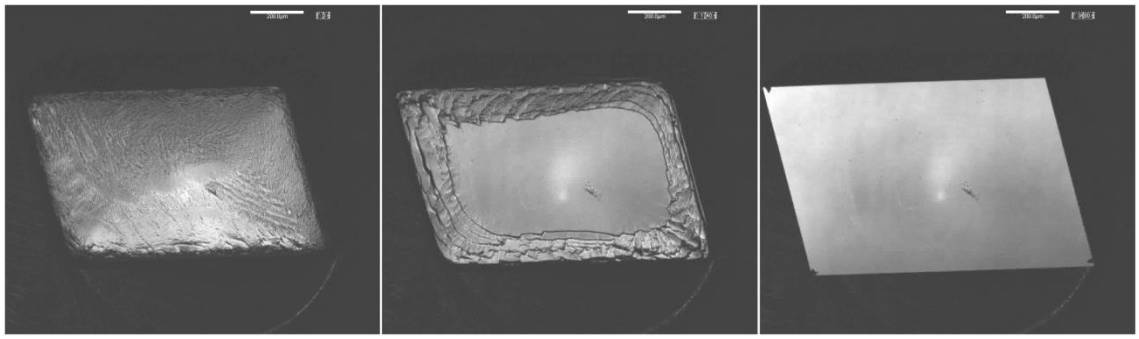

**Figure 21.** Visualization of the step growth of $NaNO_3$ crystal at 286.4 K and $\Delta T = 0.5$ K.

Repeating this experiment at several supersaturations we obtain the plot displayed in figure 22. Two expected results are extracted from this plot. First: the higher the supersaturation, the higher the step velocity. And second: the step rate order in the four directions is the same at high and low supersaturations, i. e. the downward direction is always the slowest.

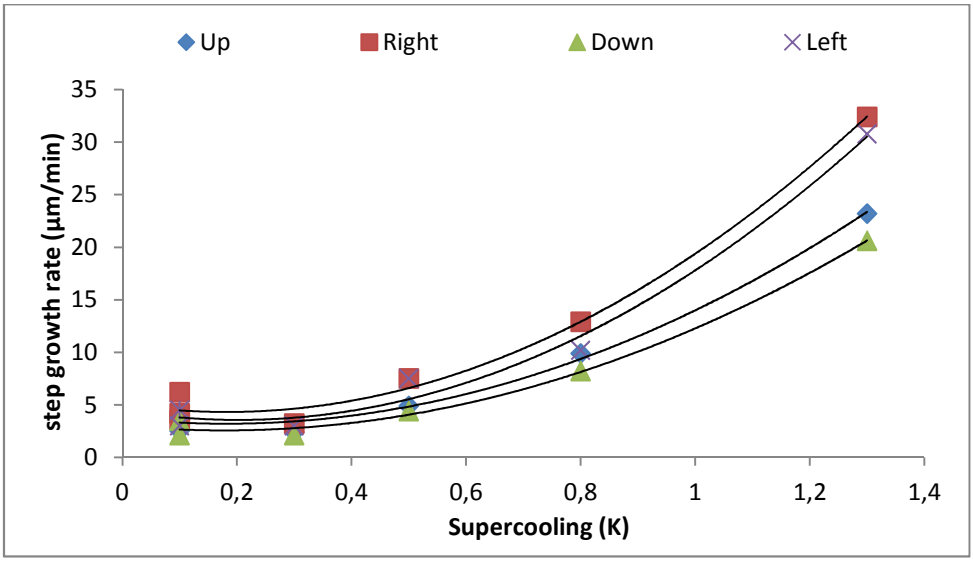


**Figure 22.** Step growth rate measurement at different supersaturations (supercooling) for the four main directions.

Finally, we point out that although we have worked at high supersaturations (corresponding to $\Delta T = 1.3$ K) only one (macro-) step is generated. Furthermore, the crystal surface always becomes flat due to the growing of this island.

## 3.6. CONCLUSIONS

In this chapter we have described the face specific growth of $NaNO_3$ under two different hydrodynamic conditions. We have seen in this system that the temperature control is essential because the growth rate of nitratine is very sensitive to the experimental parameters. In this sense we have built a device to precisely control the temperature around a growing crystal. We have measured three isotherms to obtain the growth mechanism. Therefore, we can assure that both volume (P faces) and surface diffusion (N faces) can limit the growth rate depending on the prevailing hydrodynamic conditions, conversely the integration of the growth units in the steps is not rate limiting. Furthermore, all the data recollected allows us to obtain useful information on the growth mechanism of the (104) faces of nitratine. Likewise, we estimated the edge energy of steps on (104) and the energy of transfer units from kinks and from solution to the adsorbed layer. All these were determined by the temperature dependence of the parameters adjusted by least squares.

Moreover, we have seen the arduous processes occurring on the surface by advanced microscopy (LCM-DCM). With this technique we can conclude that initial $NaNO_3$ growth rate is reconstructive in the sense the surface morphology becomes flat, the step height is below 3nm. Further experiments have to be done to observe the surface topography of sodium nitrate growing crystal.

## 3.7. BIBLIOGRAPHY

1. Mutaftschiev, B.: *The Atomistic Nature of Crystal Growth,*. Hull, R.; Osgood, Jr R. M.; Sazak, H. and Zunger, A., eds., 1st ed. Berlin: Springer, **(2001)**.

2. Vekilov, P. G. *What Determines the Rate of Crystal Growth of Crystals from Solutions?* Cryst. Growth Des., **(2007)**, 7, 12, 2796-2810.

3. Sangwal, K. *Effects of Impurities on Crystal Growth Processes.* Prog.Cryst. Growth Charac. Mat., **(1996)**, 32, 1-3, 3-43.

4. Hartman, P.: *Modern PBC Theory, in* Morphology of crystals. Sunagawa, I. ed., Tokyo: Terra Scientific Publishing Company, **(1987)**, pp. 269-320.

5. Madsen, H. E. L.; *Cinétique De Croissance Des Faces (001) des Crystaux d'Hexatriacontane en Solution.,* Thesis Université Aix-Marseille III. (**1978).**

6. Burton, W. K.; Cabrera, N. and Frank, F. C. *The Growth of Crystals and the Equilibrium Structure of their Surfaces.* Phil. Trans. Royal Soc. A, **(1951)**, 243, 866, 299-358.

7. Becker, R.; and Doring, W. *Kinetic Treatment of Germ Formation in Supersaturated Vapour.* Ann. Phys., **(1935)**, 24, 8, 719-752.

8. S Sunagawa, I. *Growth and Morphology of Crystals.* Forma, **(1999)**, 14, 147-166.

9. Paul, G. L. and Pryor, A. W. *Study of Sodium-Nitrate by Neutron Diffraction.* Acta Cryst. B., **(1972)**, 28, 15. 2700-2702.

10. Sipyagin, V. V.; and Chernov, A. A. *Anomalies of Temperature Dependence of Growth Rates of Faces of Crystals $KNO_3$, $NaNO_2$, $NaNO_3$, $NaClO_4$ and Rochelle Salt from Aqueous-Solutions.* Kristallografiya, **(1972)**, 17, 5, 1003-1009.

11. Kirkova, E.; and Nikolaeva, R. *Influence of the Flow Velocity, Supersaturation and Temperature on the Crystal-Growth from Solutions.* Cryst. Res. Tech., **(1983)**, 18, 6, 743-754.

12. Treivus, E. B. *The Oscillations of Crystal Growth Rates at their Formation in the Regime of Free Convection of a Solution; Statistical Investigation.* Cryst. Res. Tech., **(1997)**, 32, 7, 963-972.

13. Jones, C. M.; and Larson, M. A. *Characterizing Growth-Rate Dispersion of $NaNO_3$ Secondary Nuclei.* AIChE J., **(1999)**, 45, 10, 2128-2135.

14. Jones, C. M.; and Larson, M. A. *Using Dislocations and Integral Strain to Model the Growth Rates of Secondary Nuclei.* Chem. Eng. Sci., **(2000)**, 55, 14, 2563-2570.

15. Ristic, R. I.; Sherwood, J. N. and Shripathi, T. *The Influence of Tensile Strain on the Growth of Crystals of Potash Alum and Sodium Nitrate.* J. Cryst. Growth, **(1997)**, 179, 1-2, 194-204.

16. Ristic, R. I.; Sherwood, J. N. and Shripathi, T. *The Influence of Tensile Strain on the Growth of Crystals of Potash Alum and Sodium Nitrate.* J. Cryst. Growth, **(1997)**, 179, 1-2, 194-204.

17. Jones, C. M., Larson, M. A.; Ristic, R. I.; and Sherwood,. *The Role of Dislocations, Integral Strain, and Supersaturation on the Growth Rates of Sodium Nitrate.* J. Cryst. Growth, **(2000)**, 208, 1-4. 520-524.

18. Graber, T. A.; Taboada, M. E.; Alvarez, M. N. and Schmidt, E. H. *Determination of Mass Transfer Coefficients for Crystal Growth of Nitrate Salts.* Cryst. Res. Tech., **(1999)**, 34, 10, 1269-1277.

19. Oosterhof, H.; Geertman, R. M..; Witkamp, G. J.; and van Rosmalen G. M. *The Growth of Sodium Nitrate from Mixtures of Water and Isopropoxyethanol.* J. Cryst. Growth, **(1999)**, 198, 1. 754-759.

20. Komnik, S. N.; and Startsev, V. I. *On the Growth of Large Perfect Crystals of Sodium Nitrate.* J. Cryst. Growth, **(1969)**, 5, 207-209.

21. Gopalakrishnan, R.; Arivuoli, D. and Ramasamy, P. *Growth and Characterization of $NaNO_3$ Single-Crystals* Cryst. Res. Tech., **(1991)**, 26, 6, K141-K146.

22. Sawada, T.; and Shichiri, T. *Morphology and Kinetics in Ionic Crystals Growing from their Melts.* J. Cryst. Growth, **(1984)**, 67, 2, 233-240.

23. Rubbo, M.; and Sherwood, J. N. *An Improved Method for the Measurement of the Rates of Growth and Dissolution of Crystals Under Isothermal Conditions.* J. Cryst. Growth, **(1983)**, 61, 210-214.

24. Benages, R.; Costa, E.; Bruno, M.; Cuevas-Diarte, M. A.; Calvet, T. and Aquilano, D. *Experimental and Theoretical Aspects of the Growth and Equilibrium Morphology of $NaNO_3$.* Cryst. Res. Tech., **(2011)**, 1-6.

25. van Driessche, A. E. S.; Sazaki, G.; Otalora, F.; Gonzalez-Rico, F. M.; Dold, P.; Tsukamoto, K. and Najima, K. *Direct and Noninvasive Observation of Two-Dimensional Nucleation Behavior of Protein Crystals by Advanced Optical Microscopy.* Crys. Growth Des., **(2007)**, 7, 10, 1980-1987.

26. van Driessche, A. E. S.; Gavira, J. A.; Lopez, L. D. and Otalora, F. *Precise Protein Solubility Determination by Laser Confocal Differential Interference Contrast Microscopy.* J. Cryst. Growth, **(2009)**, 311, 3479-3484.

27. Xu, T.; and Pruess, K. *Thermophysical Properties of Sodium Nitrate and Sodium Chloride Solutions and their Effects on Fluid Flow in Unsaturated Media,* **(2001)**. E. O. Lawrence Berkeley National Laboratory, Berkeley, CA (US). DOI 10.2172/790019 .

28. Beckmann, W.; Boistelle, R. and Sato, K. *Solubility of the A, B, and C Polymorphs of Stearic Acid in Decane, Methanol and Butanone.* J. Chem. Eng. Data, **(1984)**, 29, 211-214.

29. Archer, D. G. *Thermodynamic Properties of the $NaNO_3$ $H_2O$ System.* J. Phys. Chem. Ref. Data, **(2000)**, 29, 5. 1141-1156.

30. Pitzer, K. Z. *Thermodynamics of Electrolytes. I. Theoretical Basis and General Equations.* J. Phys. Chem., **(1973)**, 77, 2, 268-277.

31. Carlson, A.:*The Fluid Mechanics of Crystal Growth from Solution, in* Growth and perfection of crystals. Doremus, R. H.; Roberts, B. W. and Turnbull, D., eds., New York: Wiley, **(1958)**, 421-426.

32. Bedarida, F.; Zefiro, L.; Boccacci, P.; Aquilano, D.; Rubbo, M.; Vaccari, G.; Mantovani, G. and Sgualdino, G. *Growth of Sucrose Crystals and Tapering Effect Studied by Holographic-Interferometry.* J.Cryst.Growth, **(1988)**, 89, 4, 395-404.

33. Rubbo, M.; and Aquilano, D. *Poligonized Spiral Growth Patterns on {001} Faces of Monoclinic n-Alkanes. Calculated and Observed Morphology.* Atti Accademia Delle Scienze, **(1976)**, 119-136.

34. Frank, F. C. :*On the Kinematic Theory of Crystal Growth and Dissolution Processes, in* Growth and perfection of crystals. Doremus, R. H.,; Roberts, B. W. and Turnbull, D., eds., New York: Wiley, **(1958)**,411-419.

35. Cabrera, N.; and Vermilyea, D. A.:*The Growth of Crystals from Solution, in* Growth and perfection of crystals Doremus, R. H.,; Roberts, B. W. and Turnbull, D., eds., New York: Wiley, **(1958)**, 393-410.

36. Gilmer, G.; Ghez, R. and Cabrera, N. *Analysis of Combined Surface and Volume Diffusion Processes in Crystal Growth.* J. Cryst. Growth, **(1971)**, 8, 1, 79-93.

37. Bennema, P.; and Gilmer, G. *Kinetics of Crystal Growth, in* Crystal growth: an introduction. Hartman, P. ed., 1st ed. Amsterdam: North-Holland, **(1973)**, 263-327.

38. Chernov, A. A. *The Spiral Growth of Crystals.* Sov. Phys., **(1961)**, 4, 1, 116-148.

39. Robinson, R. A.; and Stokes, R. H.: *Electrolyte Solutions,* 2nd revised ed. New York: Dover publications, **(2002)**.

40. Sigmund, B.: *Statistical and Computational Methods in Data Analysis,*1970: North Holland, **(1970)**.

41. Madsen, H. E. L. *On the Thermonamic Formalism for Adsorbed Layer in Crystal Growth from Solution.* J. Cryst. Growth, **(1977)**, 39, 250-254.

42. Bruno, M. Personal comunication **2013**.

43. Chapon, C.; and Bonissent. A. *Morphology and Distances between Growth Boundaries of Polygonized Spiral.* J. Cryst. Growth, **(1973)**, 18, 1, 103-106.

44. Chernov,A. A.: *Modern Crystallography III,*. Vainshtein, B. K.ed., Berlin etc.: Springer, **(1981)**.

# CHAPTER 4

## NITRATINE ($NaNO_3$) MORPHOLOGY CHANGE

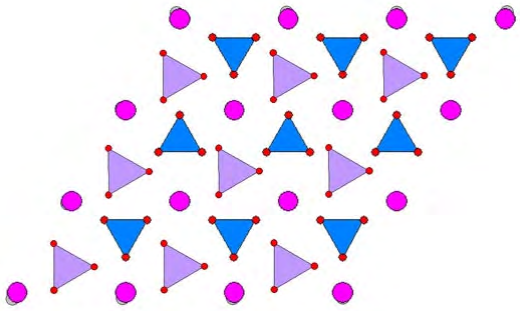

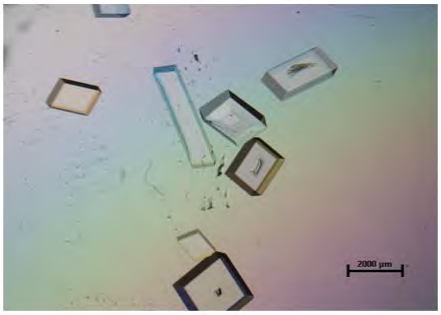


## 4.1. GENERAL INTRODUCTION

Basics of this issue are taken from Mullin's book[1] and a Chernov's book chapter[2] where the authors compiled important processes related with crystallization in presence of impurities.

It is well known that impurities are technologically very important because they are basic for many modern devices. Conductive properties of semiconductors can be modified by the quantity of foreign atoms, carbon is essential for strengthening iron and making steel, lasers need an impurity to work. Not only that, in nature impurities are also important, for example they are responsible for different colours observed in quartz and in others minerals. The importance of morphology control has been introduced in the morphology chapter (Chapter 2). Impurities can affect it as will be explained in this chapter. Certain crystal habits are disliked commercially because they give the crystalline mass a poor appearance; others make the product prone to caking, induce poor flow characteristics, or give rise to difficulties in handling or packaging of the material. For most commercial purposes a granular or prismatic habit is usually desired, but there are specific occasions when plates or needles may be wanted.[1]

Like any interfacial process, crystal growth strongly depends on active impurities present in a crystallizing system even in amounts which do not influence the properties of the bulk. On the other hand, many of these properties depend on the amount of impurities or 0-D defects in the grown crystal. Thus, the manner in which impurities are trapped by growing crystals is one of the most important characteristics of growth technology. The presence of impurities in a system can have a profound effect on the growth of the crystal. Some impurities can supress growth entirely or enhance it. Others may exert a highly selective effect, acting only on certain crystallographic faces and thus modifying the crystal habit. Some impurities can exert an influence at very low concentration, less than 1 ppm, while others need to be in fairly large amounts.[1]

Impurities are minor additives of foreign substances in the mother medium or the crystal. Thermodynamically, an impurity shifts the equilibrium between crystal and medium in accordance with the phase diagram. In fact, pure solutions are rarely encountered outside the analytical laboratory. Industrial solutions are almost invariably impure, and the presence of an impurity can have a considerable effect on the solubility characteristic of a system. If in a saturated binary system, A dissolved in B, a third component C (soluble in B) is added, four conditions can result. First, a comparatively

rare case, nothing may happen. Second, C may combine or react chemically with A forming a complex or compound, thus altering the whole nature of the system. Third, C can make the solution unsaturated with respect to A, A would be 'salted-in': more A is needed to achieve the saturation point. And fourth, C can make the solution supersaturated, thus A would be precipitated or 'salted-out'.[1]

An additive present in solution in a rather large amount (several tens of per cent) generally changes the composition, structure, and population of the complexes in solution, which in turn changes the growth rate for kinetic reasons. If the additive diminishes the solubility of the crystallizing substance, it causes an increase in the kinetic coefficient of proportionality between the growth rate and the dimensionless driving force ($\Delta\mu/kT$, where $\mu$ is the chemical potential, k is the Boltzmann constant and T the absolute temperature) for crystallization in the case of a near-linear dependence. Such dependences have been found experimentally for nitrates of alkaline metals where the kinetic coefficient increases in the series in which cation hydration decreases.[3]

The adsorption of impurities on the surface substantially changes the average binding forces operating along the surface between the particles of the surface layer. An impurity acts externally and does not incorporate into the crystal: a solid solution does not form. Therefore, it may lead to a transition from an atomically rough surface to a smooth one, and vice versa. Kinetically, the effect of impurities consists in modifying the transport processes in the bulk and on the crystallization phenomena on the surface. An impurity generally changes the structure of the liquid phase and therefore affects the diffusion coefficients, but this effect is usually small (at molar concentration of impurity $C_i << 1$). The effect of an impurity on thermal conductivity is still smaller at the usual crystallization temperatures. However, change in the structure of the liquid may also affect the association of the liquid and the structure of the near-surface layer of the solution, where the impurity concentration is increased as a result of adsorption; it may also change the diffusion resistance more substantially.

Therefore impurities exert the strongest effect on surface crystallization. This effect is again based on the adsorption of an impurity in the form of atoms, molecules, complexes, or even aggregates in different positions on the surface (kinks, steps, terraces…). The impurity concentration in different positions depends primarily on the binding energy of the impurity particle with the lattice at these sites.

If an impurity is strongly adsorbed by a kink; this kink (either step or surface) loses the opportunity for adding new particles making up the crystal. Therefore, an impurity naturally reduces the growth rate to a different extent for faces with different surface structures. A kink with an impurity particle ceases to be a growth site until the impurity is desorbed thermally or chemically, or until it is displaced (or buried) by the building blocks of the crystal.

Adsorption of impurities in steps reduces their specific edge energy, thereby increasing the chance that two-dimensional nuclei will form. In dislocation growth, this adsorption reduces the spacing between the turns of the spiral steps. Both effects also increase the growth rate. But it is not yet clear whether the moderate increase in growth rate occasionally observed upon the introduction of an impurity is due to these effects or to other factors. Nor is it unlikely that the acceleration of the growth at low impurity concentrations results from the provocation of two-dimensional nucleation by individual impurity molecules in atomically smooth areas.

To sum up, an impurity reduces the face growth rate of crystals if it is strongly adsorbed on a specific site on the surface, and this holds normally when impurity concentration is low. Foreign particles also shift the equilibrium temperature according to a ternary phase diagram sample-impurity-solvent. When impurity concentration is high enough it can assist two-dimensional nucleation or compress the step equidistance in dislocation growth. These phenomena enhance the growth rate of specific faces.

The relation between different faces determines the growth morphology of crystals, so that it is important to know how impurity affects the growth rate. In order to obtain morphology change, the growth rate behaviour of the crystal faces has to be changed. It is known that the faces that appear in the crystal are those with the slowest growth rate: the most stable ones. Thus, in order to change the morphology it is compulsory to stabilize some other faces so that they could appear in the growth morphology. In this sense epitaxial relations must be taken into account. Experience has shown that the maximum accepted mismatch between the substrate and the deposited layer must be below 15 %.[4] Furthermore, in the case of nitrates, the anion stacking should be the same.

In order to complement and compare the crystal growth of $NaNO_3$ from pure aqueous solution with that in the presence of impurities, we look for the effect of $KNO_3$ (and $LiNO_3$) on the (104) face advancement rate of $NaNO_3$ all other kinetic conditions being

equal. Both impurities have been demonstrated[5] to change $NaNO_3$ morphology by introduction of the {001} form in the growth morphology (see below).
As far as we know, nobody has studied the problem exposed above. On the contrary, the growth rate versus supersaturation dependence for $KNO_3$ in the presence of $NaNO_3$ was studied by Chernov and Sipyagin.[6] They concluded that the crystal growth rate decreases when $NaNO_3$ is present.

The study of morphology change in $NaNO_3$ is separated into four parts. First, we recall the experimental shape of $NaNO_3$ pure systems. Second, potassium ion effect in the solution is described. Thirdly, we report the lithium ion effect in the growth shape of $NaNO_3$. And finally, we describe the variation of the growth rate of $NaNO_3$ {104} form in the presence of $KNO_3$ or $LiNO_3$.
In this chapter we have addressed the question: what are the conditions for $NaNO_3$ morphology change? Our aim is to study the change of the $NaNO_3$ growth morphology by the addition of impurities. We have used mainly nitrates, but lithium carbonate appears to be the most promising additive for changing $NaNO_3$ morphology as we will see in this chapter.
Before going to the experimental section we give reasons for using $K^+$ and $Li^+$ ions in a theoretical scope taking into account epitaxial relationships. Then we explain the methodology, results and give some general conclusions at the end.

## 4.2. INTRODUCTION TO $NaNO_3$-$KNO_3$ AND $NaNO_3$-$LiNO_3$ SYSTEMS

Here we perform some calculations to predict the possibility of epitaxy formation between $NaNO_3$-$KNO_3$ and $NaNO_3$-$LiNO_3$.

Surface cell parameters must be similar between the pairs $NaNO_3$-$KNO_3$ and $NaNO_3$-$LiNO_3$ to obtain $NaNO_3$ crystal modification. It is well known that adsorption of species in a growing crystal may decrease the growth rate of a certain face and hence stabilize these faces to change the final morphology. We have already seen in chapter 2 that the surface surface energy values could be lowered by about 400 erg/cm$^2$ in order to obtain another face with respect to cleavage rhombohedron. A geometric simple approach can be made to calculate a mismatch (m) coefficient between surface cell parameters as defined in equation 1.

$$m = \frac{d_{guest} - d_{host}}{d_{host}} \qquad \textbf{Equation 1.}$$

where $d_{host}$ are the surface parameters of $NaNO_3$ and $d_{guest}$ are the surface parameters of the impurity. It should kept in mind that 'surface parameters' mean not only the parameters of the unit cell of the twu epi-crystals, this terms extend as well to any 2 D lattice cell of both crystals.

Obviously, when this coefficient is low, the adsorption in certain positions is better than when it is high. Additionally, a similar stacking of the growing crystal and impurity made the adsorption process easier.

Table 1 gives the unit cell parameters of three nitrates.

**Table 1.** Unit cell parameters of selected nitrates

| Compound | Space Group | **a** / Å | **b** / Å | **c** / Å | **Ref.** |
|---|---|---|---|---|---|
| $LiNO_3$ | $R\bar{3}c$ | 4.692 | | 15.2149 | (7) |
| II-$NaNO_3$ | $R\bar{3}c$ | 5.070 | | 16.82 | (8) |
| β-$KNO_3$ | Pmcn | 5.4119 | 9.1567 | 6.4213 | (9) |

The easiest correspondence between $NaNO_3$ and $KNO_3$ is to compare the (001) faces because in this case nitrate groups in both structures become parallel: $NaNO_3$ (001) || $KNO_3$ (001). In figure 1 we show a [001] projection for both structures. Purple

triangles are $NO_3$ groups belonging to $NaNO_3$ and blue ones are from $KNO_3$ structure, potassium atoms are pink spheres and sodium atoms are grey spheres. Here cell vectors are also shown and a scheme along [001] direction in order to highlight the different stacking sequence is drawn. It turns out that stacking sequence in $NaNO_3$ is ABABA… while for $KNO_3$ is ABCABCABC… where A is Na or K layers and B and C are $NO_3$ group layers, here we do not have taken into account the relative nitrate group orientation, only its position. Moreover, surface symmetry is different (as can be deduced by their space groups). For $KNO_3$ *m* symmetry holds whilst for $NaNO_3$ only a *3*-fold axis exists. Another drawback arises when we look at the $NO_3$ group relative orientation. In $NaNO_3$ structure, the nitrate group became tilted by 30º in respect to [100] direction whereas, in $KNO_3$ [100] direction it is parallel.

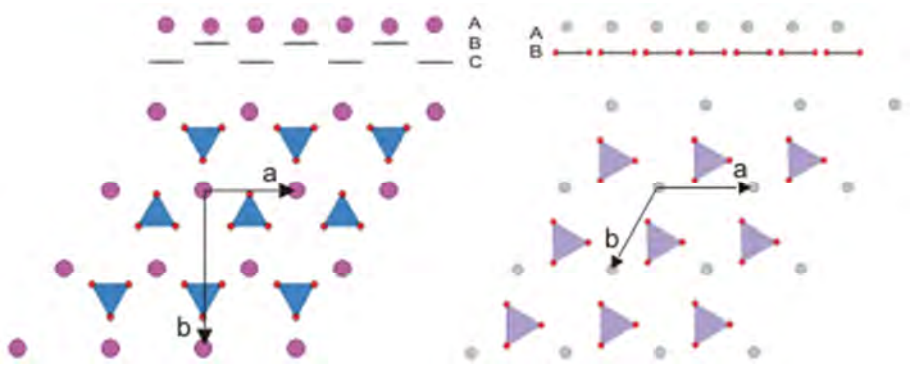


**Figure 1.** (001) face surface structure for $KNO_3$ (left) and $NaNO_3$ (right) are $NO_3$ groups, pink spheres are potassium ions and grey spheres are sodium ions.

When these surface structures are superposed we clearly observe the mismatch. In figure 2 we have superposed a sodium and potassium encircled in the image. We observe that both structures have the same hexagonal environment for the alkali ions. Instead, nitrate group 'surface' structure is totally different. First, as we stated above, the orientation is different. Secondly, in $KNO_3$ structure nitrate group has an anisotropic repetition vector length due to the difference between **a** and **b** cell parameters. And finally nitrate groups in $KNO_3$ belong to two different layers (BC stacking) while in $NaNO_3$ structure they are coplanar. The result is a non-continuity in the nitrate stacking when we go from one structure to another.

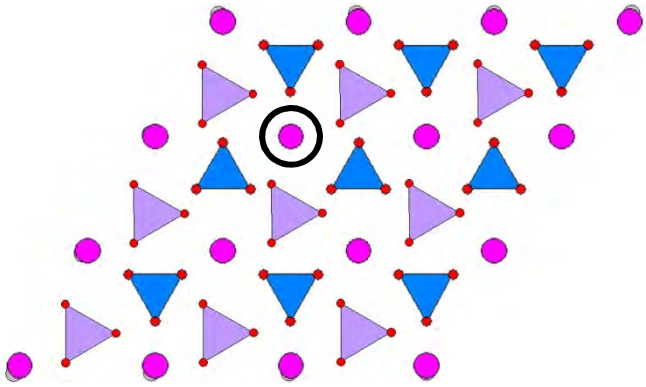

**Figure 2.** Superposition of (001) face of $NaNO_3$ and $KNO_3$.

We can calculate the mismatch in the [100] and [010] directions of $NaNO_3$ as follows:

$$\%m_a = \frac{a^K - a^{Na}}{a^{Na}} \cdot 100 = \frac{5.412 - 5.010}{5.010} \cdot 100 = 8.0\%$$

$$\%m_b = \frac{\frac{-a^K + b^K}{2} - b^{Na}}{b^{Na}} \cdot 100 = \frac{5.318 - 5.010}{5.010} \cdot 100 = 6.2\%$$

where $\mathbf{a}^{\mathbf{Na}}$, $\mathbf{a}^{\mathbf{K}}$, $\mathbf{b}^{\mathbf{Na}}$ and $\mathbf{b}^{\mathbf{K}}$ are the surface cell parameters defined in figure 1.
Calculations result in a possibility of 2D epitaxy because values are well below the proposed limit.

And what is the situation for $NaNO_3$ and $LiNO_3$? These compounds are isostructural, so stacking is the same for all directions. We can calculate a mismatch between all surfaces (with the same indices in sodium and lithium nitrate) but we will restrict the calculations to the (001) face. We show in figure 3 the superposition of the two cell projections $NaNO_3$ (001) ‖ $LiNO_3$ (001). Where orange triangles are nitrate groups belonging to $LiNO_3$ structure and small spheres represent lithium ions. The correspondence is practically perfect and the stacking sequence is equal.

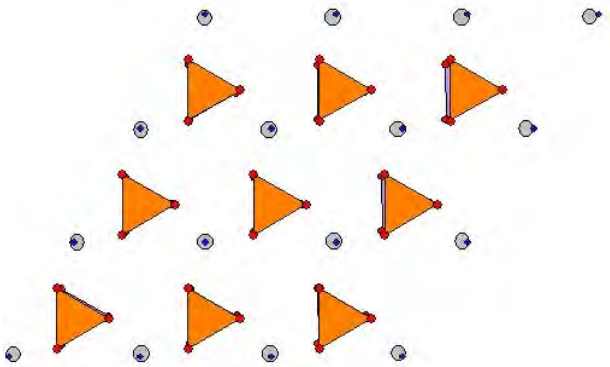

**Figure 3.** Structure projection along [001] of $LiNO_3$ and $NaNO_3$ to study the possible epitaxy.

The mismatch can be calculated easily with the formula:

$$\%M_{\{0001\}} = \frac{a^{Li} - a^{Na}}{a^{Na}} \cdot 100 = \frac{4.692 - 5.070}{5.070} \cdot 100 = -8.0\%$$

Where $\mathbf{a}^{\mathbf{Na}}$, $\mathbf{a}^{\mathbf{Li}}$ are the surface parameters of sodium and lithium nitrate.

This means that there is a real possibility of 2D epitaxy between sodium and lithium nitrate.

## 4.3. MATERIALS AND METHODS

$NaNO_3$ (analytical grade) was provided by Quality Chemicals. According to the manufacturer the major impurities are phosphorous and sulphur atoms. Its purity was checked by ionic coupled plasma (ICP) with a mass detector, and the results shows that these compounds are below the detection limit (500 ppm). However we have found 21.7 ppm of titanium and 0.22 ppm of manganese. Powder X-ray diffraction informs that the product is a single II-$NaNO_3$ phase.

In figure 4 we show electronic images of the commercial product. We can see that there are granular rounded aggregations with a monomodal grain distribution. This material tends to bind together at room temperature due to water adsorption.

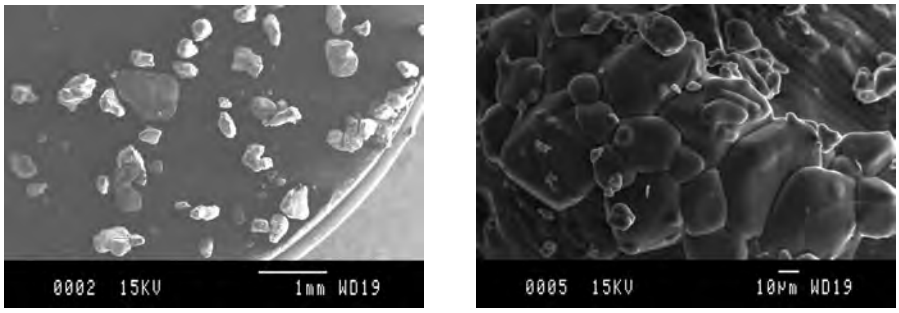


**Figure 4.** SEM images of commercial $NaNO_3$.

$KNO_3$ and $LiNO_3$ (Chemically pure) were provided by Quality Chemicals. $LiNO_3$ and $Li_2CO_3$ (purity >99%) from Acros Organic were also used.

The obtained crystals were characterized by Raman spectroscopy and scanning electron microscopy in Centres Científics i Tecnològics de la Universitat de Barcelona (CCiT-UB) used are cited here. Raman spectroscopy was carried out at room temperature with the Jobin Yvon T64000 Raman spectrometer. The liquid nitrogen cooled CCD detector was calibrated against $TiO_2$ and nominal laser power was 400 mW with a 514 nm wavelength. Five measurements of ten seconds each were performed from 24 to 1700 $cm^{-1}$. Peak position and peak intensity were measured with Origin Software. HR800 Raman microscope was used for some sample characterizations. Hitachi S-4100 field-emission and H-2300 scanning electron microscope (FE-SEM) at room temperature were used to take pictures of crystals.

As far as we know $NaNO_3$-$KNO_3$ and $NaNO_3$-$LiNO_3$ solubility curves or how these impurities affect to $NaNO_3$ crystallization are not well established. For this reason we opted to use $NaNO_3$ data as an approximation i.e. we assume that the impurity and sodium nitrate have the same behaviour.

The most reliable solubility curve (equation 2) for $NaNO_3$ is given by Xu, T.[10]

$$X_T = 0.0022 \times T - 0.1757 \qquad \textbf{Equation 2}$$

Where X is the mass fraction described by equation 3 (in this case the mass fraction is defined as the proportion of solid among the total weight, which is constant for each set of experiments) and T the absolute temperature.

$$X_T = \frac{M_{NaNO_3} + M_{XNO_3}}{M_{NaNO_3} + M_{XNO_3} + M_{H_2O}} \qquad \textbf{Equation 3}$$

In equation 3, $M_i$ is the mass of the component i. We fix the total mass of the system as $M_T$ = 25 - 30 g. depending on the experimental set. Then we calculate, with the aid of equation 3, the total amount of solids. Finally, with equations 4 - 6 we can calculate the individual masses, where X/N is the impurity/sodium atomic ratio.

$$M_{NaNO_3} = \frac{M_T \cdot X_T}{\frac{M_X}{85} \cdot \frac{X}{N} + 1} \qquad \textbf{Equation 4}$$

$$M_{XNO_3} = M_T \cdot X_T - M_{NaNO_3} \qquad \textbf{Equation 5}$$

$$M_{H_2O} = M_T - M_{NaNO_3} - M_{XNO_3} \qquad \textbf{Equation 6}$$

The supersaturation at each experiment was calculated with equation 7. Equilibrium curve ($X_{eq}$) is assumed to fit equation 2. $X_{sat}$ is the mass fraction of solids (impurity and sodium nitrate). In this case the activity coefficient was not taken into account because we are not interested in thermodynamic calculations.

$$\sigma = \frac{X_{sat} - X_{eq}}{X_{eq}}$$ **Equation 7**

For every experiment we weighted the required amount of each component with a precision of 0.1 mg. Then the solids are dissolved at room temperature. In some cases the temperature was raised to achieve complete dissolution. Finally, it was filtered with filter paper in a PP Petri capsule and sealed with Parafilm®. Dissolutions were allowed to crystallise at 293 K for 2 days in order to minimise water evaporation. After this time photographs were recorded with a magnifying glass (Nikon SM71500 connected to a SpeedXT$^{core}$3 CCD camera). Finally, we let solutions evaporate at 291 K for several months to observe if morphology changes. By using $LiNO_3$ we had problems because it is a deliquescent compound, thus we did not know how much solid and water we were weighing at each experiment. For this reason we decided to use LiOH and $Li_2CO_3$. For LiOH similar experiments were performed. Morphology change of calcite by the presence of zabuyelite ($Li_2CO_3$) has been studied from both theoretical[11] and experimental points of view.[12-14] As calcite is our model because $CaCO_3$ and $NaNO_3$ are isostructural we decided to try lithium carbonate to change sodium nitrate morphology. On the contrary, a different set of experiments were performed with $Li_2CO_3$. In this case cooling crystallization method was used, adding the required amount of $NaNO_3$ and $Li_2CO_3$. After dissolving sodium nitrate, we lowered to pH = 7 - 8 by $CO_2$ bubbling, lithium carbonate being a poor water soluble compound. Finally, solutions were placed at crystallization temperature to obtain crystals.

For crystal growth measurements we used the system built for measuring the pure $NaNO_3$ crystal growth rate (see chapter 3) but here we added different amounts of $KNO_3$ or $LiNO_3$ as impurities to determine the variation in the face advancement rate.
In this set of measurements we maintained both the equilibrium and the subcooling temperature constant while impurity content was risen, i. e. we were working with $T_{eq}$ = 292.7 K and $T_{growth}$-$T_{eq}$ = 0.3 K. It is worth remembering here, that for each measurement a new crystal seed must be used due to the change in the equilibrium temperature when an impurity is added.
When a new $KNO_3$ (or $LiNO_3$) addition was required, we worked as follows: we extracted some solution from the reservoir and then dissolved the required amount of impurity there. We heated this extracted solution in order to dissolve all the new solids

formed (salting-out effect), and finally it was returned back into the reservoir. The equilibrium temperature was rechecked and adjusted. ICP-OES were used to control the concentration of species in each step.

We would like here to recollect that our aim in this chapter is to study the crystallization of $NaNO_3$ from aqueous solutions by applying various standard methodologies, mainly crystallization at constant temperature (from supersaturated solutions) and slow evaporation. We also sought to change $NaNO_3$ shape by the addition of impurities. Finally, we study the growth rate behaviour in the presence of impurities.

## 4.4. RESULTS

We describe here the obtained morphology in pure systems, then we follow with solutions containing potassium or lithium ion. Finally, experimental growth rate of $NaNO_3$ {104} form seeds in the presence of the same ions is illustrated.

### 4.4.1. Pure $NaNO_3$.

$NaNO_3$ experimental growth morphology is always the flat {104} rhombohedron.[15, 16] When studying the surface structure by the Hartman Perdok (PBC) approach it comes out that the {104} form has by far the lowest surface energy for the athermal equilibrium form as has been calculated by Benages et al.[5] (see chapter 2).

$NaNO_3$ under controlled experimental conditions crystallizes in {104} rhombohedra. If supersaturation is high we obtain massive crystallization like that observed in industrial crystallization (figure 4). In figure 5 we show crystals obtained by solvent evaporation (left) and at constant temperature (right). In both cases the morphology is built by {104} rhombohedra form.

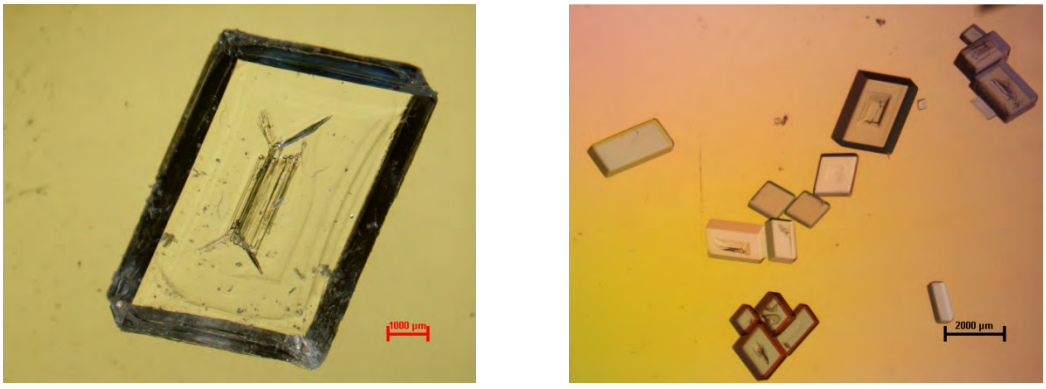


**Figure 5.** {104} $NaNO_3$ rhombohedra obtained by 8 days solvent evaporation (left) crystallization at 291 K for 2 days (right).

In this case, the crystals do not grow isotropically due to inhomogeneities in the mass transport inside the crystallizing liquid. Therefore, final results show some elongated crystals. Moreover, we obtain flat rhombohedra due to the same reason. The solutions have only ~ 1 cm height, then, the upper face has a low mass transport, and it grows more slowly and becomes more important.

In next sections we will describe the experimental results obtained by addition of impurities in the mother liquor. First, we used $KNO_3$ to obtain modified $NaNO_3$ crystals and characterized them by different methods. Second, lithium salts were used to achieve a modification in sodium nitrate.

### 4.4.2. Systems with $K^+$ ion.

We describe here the results obtained by isothermal crystallization at 293 K. We have worked at three $NaNO_3$ supersaturations corresponding to 298 K, 300 K, and 302 K equilibrium temperature. The supersaturation calculated using equation 6 is between 2.3 % and 4.2 %. On the other hand we used several Na/K molar ratios from 1000 to 25 as detailed in table 2. In this table we have marked the conditions leading to the observed modifications.

**Table 2.** Experimental conditions for obtaining modified crystals by $KNO_3$ addition.

| | T (K) | 298 | 300 | 302 |
|---|---|---|---|---|
| | σ (%) | 2,3 | 3,3 | 4,2 |
| Na/K | 25 | X | | |
| | 40 | | | |
| | 50 | | X | X |
| | 100 | | X | |
| | 200 | X | | XX |
| | 500 | | X | XX |
| | 1000 | | | XX |

From table 2 we can deduce that for obtaining modified crystals by $KNO_3$ addition the better conditions are relatively high supersaturation and low impurity content. In these conditions higher proportion of modified crystals are encountered. It is worth saying (and will be seen below) that we have not achieved modification of all crystals in any batch. In fact, only a minor concentration of modified crystal is usually observed. Only one (001) face appeared in modified crystals, which is somewhat strange. What is more, normally it is on the bottom of the growing crystal. This means that (001) face can act as the nucleation centre.

In figure 6 we show with black arrows the modified crystals obtained in different experiments. In the image on the left we observe that the two modified crystals are laying on the (001) face and that a 3-fold axis holds perpendicular to the paper. On the contrary, for the picture on the right, this is not as easy to see. In this case modifications were produced in elongated crystals; therefore, (001) face is not an equilateral triangle. Additionally, we observe that the crystal at the top of the picture has the (001) face on the upper part.

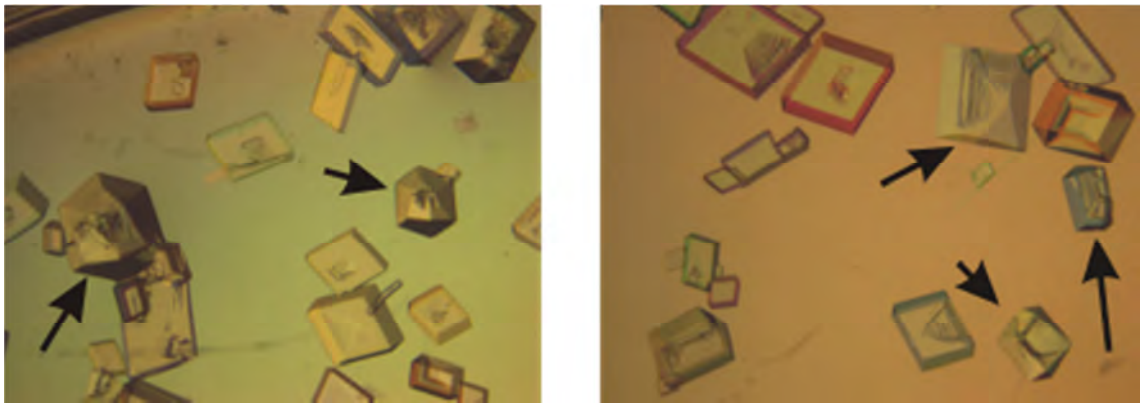

**Figure 6.** Modified $NaNO_3$ crystals obtained at $\sigma$ = 3.3 % and Na/K = 500 (left); at $\sigma$ = 4.2 % and Na/K = 500 (right).

Dissolution and evaporation experiments were also performed in this system. Several samples were allowed to evaporate slowly over the course of 8 months at 291 K. Results showed, as expected, big rhombohedra crystals. In this case growing defects such as macrosteps and curved crystals are observed. Moreover, modified crystals are detected in 4 over the 5 experiments in secondary nuclei. Examples are included in figure 7. Here, we have normally obtained the two faces belonging to the {001} form along with the {104}. Contrary to what we have seen in the isothermal crystallization, here the morphology change appears when $KNO_3$ concentration is higher: realizing that much of $NaNO_3$ is already crystallized, hence we assume to have higher Na/K ratios.

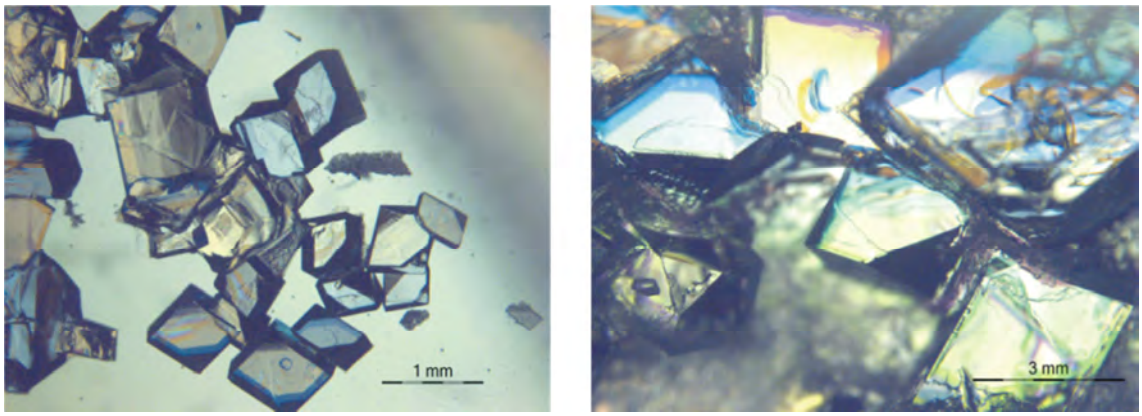


**Figure 7.** Modified $NaNO_3$ crystals obtained by water evaporation at 291 K. Left: Na/K = 10; right Na/K = 25

In figure 8 we show a SEM image where the (001) triangular face is clearly seen. Here we have marked the edges with a dotted line.

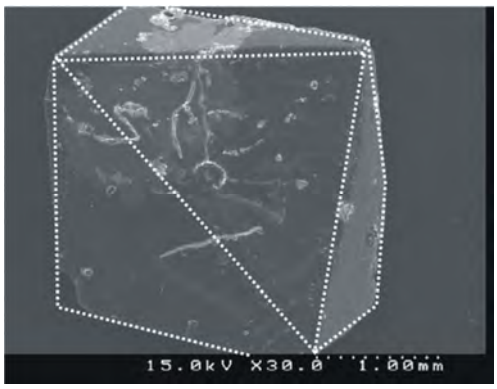


**Figure 8.** Selected modified crystal obtained by slow evaporation.

Additionally, we have selected a fully modified crystal to check if some potassium has entered into $NaNO_3$ crystal structure. The crystallization conditions were $\sigma$ = 2.3 % and Na/K = 10. According to table 2 modification does not appear under these conditions. Effectively for an isothermal crystallization at 293 K for 2 days only {104} rhombohedra has been found (see figure 9 left). Contrarily, slow evaporation over four months gives a modified crystal. It is shown in figure 9 right.

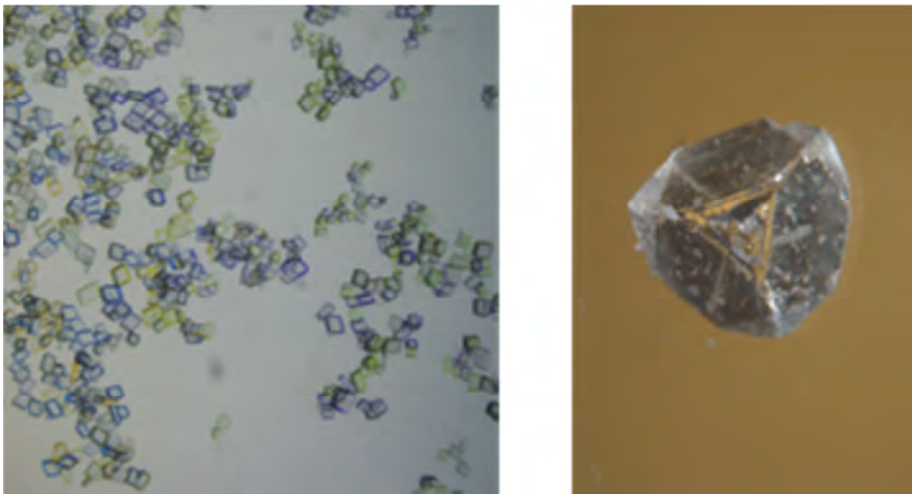

**Figure 9.** $NaNO_3$ crystallization σ = 2.3% and Na/K = 10. Left: crystallization at 293 K for two days. Right: modified crystal obtained by slow evaporation at 291 K of the same experiment after four months (0.75x).

In figure 10 we show the micro-Raman (10x) spectra of this modified crystal directly in solution (black) together with a dry {104} rhombohedron, finally, powdered $NaNO_3$ and $KNO_3$ products (macro-Raman in another equipment) are also showed. It should be noted that this modified crystal has mainly a $KNO_3$ environment as the strongest peak intensity is due to this configuration. Additionally, the line broadening can be interpreted with different possibilities: one is that the crystal has some internal stress; another is the formation of solid solution, and, finally, it can be due to the adsorbed potassium nitrate on the sodium nitrate surface. Unit cell of this crystal was determined by single crystal diffraction using 25 independent reflection spots collected by a CAD4 detector between 20.9º and 42.7º. The indexation reproduces II-$NaNO_3$ cell; therefore we confirm that $KNO_3$ is not in the structure but it is adsorbed on the surfaces.

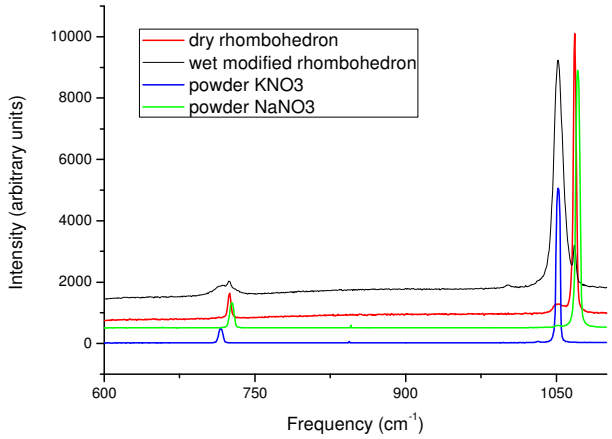


**Figure 10.** MicroRaman spectra of a wet modified rhombohedron (black), wet rhombohedron (red). Powdered sodium (green) and potassium (blue) nitrate are also presented.

### 4.4.3. Systems with $Li^+$ ion.

As we have done with $KNO_3$ impurity addition we can construct a similar table for $LiNO_3$ addition in the crystallizing batch. Therefore, we have used the same supersaturation and Na/Li ratio contents. Results are summarized in table 3. It is worth noting that with $LiNO_3$ addition, the proportion of modified crystals became larger than when $KNO_3$ was used. We arrived at ~ 10 % of modified crystals for $\sigma$ = 3.3% and Na/Li = 100. Moreover, when we experimented with $\sigma$ = 4.2 %, most of the modified crystals also presented growing defects.

**Table 3.** Experimental conditions for obtaining modified crystals by $LiNO_3$ addition.

| | T (K) | 298 | 300 | 302 |
|---|---|---|---|---|
| | σ (%) | 2,3 | 3,3 | 4,2 |
| Na/Li | 25 | X | X | X |
| | 40 | X | XX | |
| | 50 | | X | X |
| | 100 | | XXX | X |
| | 200 | X | X | X |
| | 500 | | | X |
| | 1000 | | X | X |

Lithium nitrate can change the $NaNO_3$ morphology and the {001} form appears in many experiments. In some experiments, where crystals were larger, morphology change was evident with the naked eye. Unfortunately, we did not achieve a generalised morphology change in any of our experiments.

Examining again table 3 we can deduce that the most favourable region to observe a change in the habit is at relatively high supersaturation σ = 3 - 4·% but at low lithium content, Li/Na around 100 ($LiNO_3$ < 1% of solids). In figure 11 we show two images of modified morphology; on the left we see a high amount of modification while on the right part crystals with growth defects are presented.

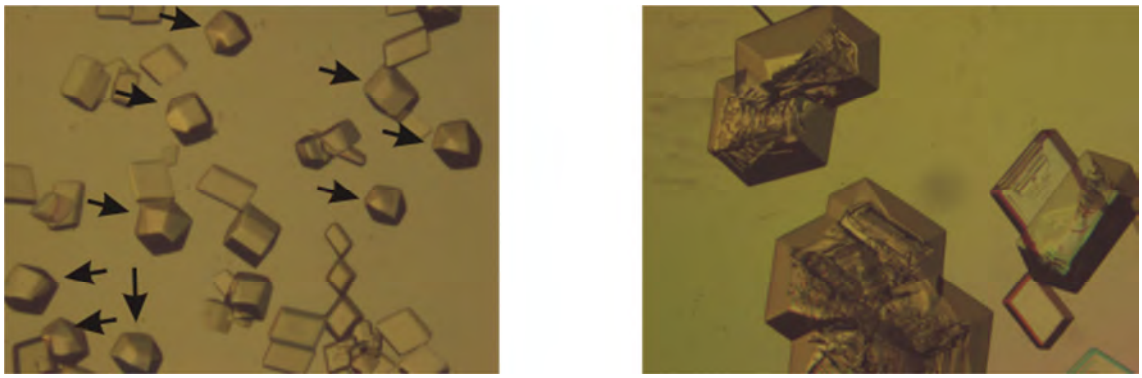

**Figure 11.** Modified $NaNO_3$ crystals by $LiNO_3$ addition. Left: σ = 3.3 % and Na/Li = 100 (2x). Right: crystals with defects at σ = 4.2 % and Na/Li = 200 (1x).

Solutions were allowed to evaporate at 291 K for two months. As in the previous case we obtained modified crystals in most experiments. Curiously, crystals with (001) face

became larger than the normal {104} form. In figure 12 we observe on the left two big modified crystals sitting on the (001) face. The image on the right is a SEM acquisition of a dried crystal oriented to look at the (001) face.

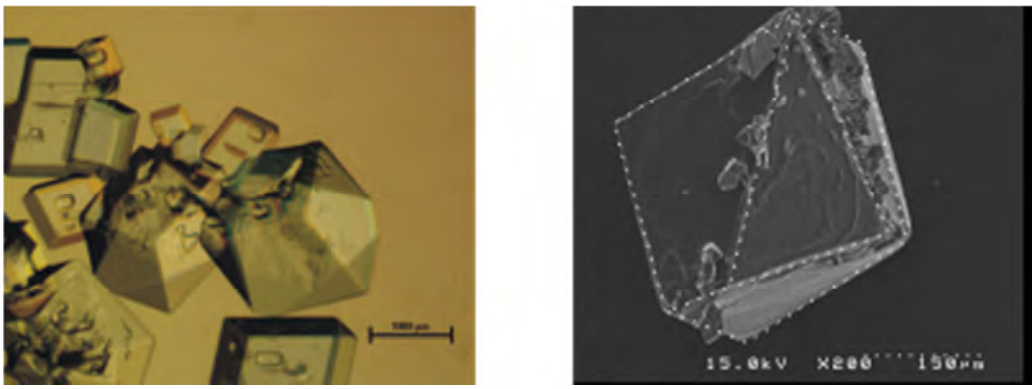


**Figure 12.** Modified crystals obtained by slow evaporation at 291 K. Left: σ = 1.4 % and Na/Li = 10; right: σ = 3.3 % and Na/Li = 100.

Continuing with lithium addition, we decided to use LiOH to detect if lithium ion is the responsible of morphology change in $NaNO_3$. In this case crystallizations were held at 291 K. Effectively, addition of LiOH also conducts to modified crystals (see figure 13). Similarly, we have found that σ = 3.3 % and Na/Li = 100 or less (ppm range) is the best region for habit modification.

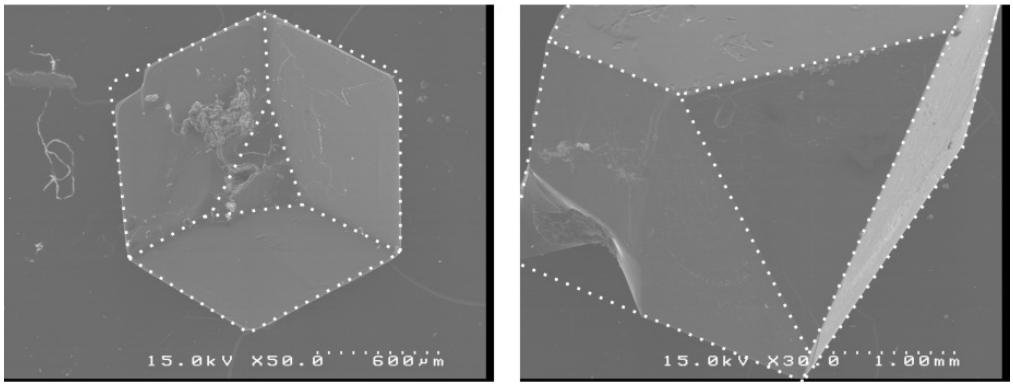


**Figure 13.** $NaNO_3$ crystals modified by LiOH addition σ = 3.3 % and Na/Li = 100 (left) and Na/Li = 500 (right).

As mentioned above, lithium carbonate (monoclinic) can modify calcium carbonate morphology (hexagonal – rhombohedral) even if they do not have the same crystal structure. Therefore, we decided to test this impurity in sodium nitrate. In this case crystallization experiments were done by cooling. Different supersaturations and Na/Li relations were used. We conclude that the best conditions to obtain modified $NaNO_3$

crystals is to prepare a $NaNO_3$ solution with σ ~ 1 % at the crystallization temperature saturated in respect to $Li_2CO_3$ at pH to 7.5 - 8.2 (adjusted by $CO_2$ bubbling). Finally, a slow cooling rate is preferred to obtain big crystals sitting on the (001) face as is shown in figure 14.


**Figure 14.** Modified crystals obtained in the presence of $Li_2CO_3$

Curiously, by crystallizing in this way a high amount of impurity is needed to change $NaNO_3$ habit. At this step we have to make a consideration. We have seen that lithium and potassium ions can modify to some extent sodium nitrate morphology but the best result was obtained using lithium carbonate addition. Consequently, we may ask: is $CO_3^{2-}$ ion responsible for morphology change? Some preliminary experiments have been made with sodium carbonate as impurity, and we have also obtained morphological modifications. But deeper experimentation is needed to prove this statement.

## 4.5. GROWTH RATE DETERMINATION

In order to determine the growth rate behaviour of the {104} form in the presence of $KNO_3$ or $LiNO_3$ impurities, we have used the device described in chapter 3. Here we have added successively different amounts of $KNO_3$ or $LiNO_3$ in the growth solution in order to change its composition. In contrast, we have maintained the equilibrium and the growth temperature ($T_{eq}$ = 292.7 K and $T_{growth}$ = 292.4 K) constant. We have determined the growth rate of the same form in two hydrodynamic conditions, face perpendicular or parallel to the flow ($R^N_{104}$ and $R^p_{104}$ respectively).

The concentration of the components are determined a posteriori by ICP-OES. For both impurities we have constructed a table to relate the growth rate with impurity concentration in the system.

### 4.5.1. $KNO_3$ addition.

In table 4 we give $NaNO_3$ and $KNO_3$ concentration determined by ICP-OES after each addition. In this table the specific growth rate for perpendicular ($R^N_{104}$ ) and parallel ($R^p_{104}$) faces in respect to the flow are also shown.

**Table 4.** Experimental values of $NaNO_3$ growth rate in the presence of $KNO_3$. Here we indicate the component concentration.

| [$NaNO_3$] (mol/l) | [$KNO_3$] (mol/l) | $R^N_{104}$ (µm/min) | $R^p_{104}$ (µm/min) |
|---|---|---|---|
| 7.801 | 0.000 | 1.310* | 1.310* |
| 7.765 | 0.013 | 0.521 | 0.871 |
| 7.663 | 0.026 | 0.698 | 0.946 |
| 7.559 | 0.069 | 0.336 | 0.756 |
| 7.404 | 0.112 | 0.038 | 0.035 |
| 7.338 | 0.196 | 0.426 | 0.258 |
| 7.278 | 0.368 | 0.298 | 0.118 |
| 7.319 | 0.449 | 0.299 | 0.220 |
| 7.385 | 0.833 | 0.219 | 0.125 |

*calculated from $NaNO_3$ pure system.

We can clearly see that $NaNO_3$ concentration decreases with the additions of $KNO_3$. This behaviour can be explained by the water added in order to have a constant equilibrium temperature for all experiments. As explained above, addition of impurity shifts the equilibrium temperature. The {104} growth rate in both perpendicular and parallel faces in respect to the flow is plotted in figure 15. We can clearly see that growth rate decays exponentially in both parallel and perpendicular measurements. For the perpendicular face, the tendency is to arrive to 0.3 µm/min whereas for parallel face 0.1 µm/min is achieved.

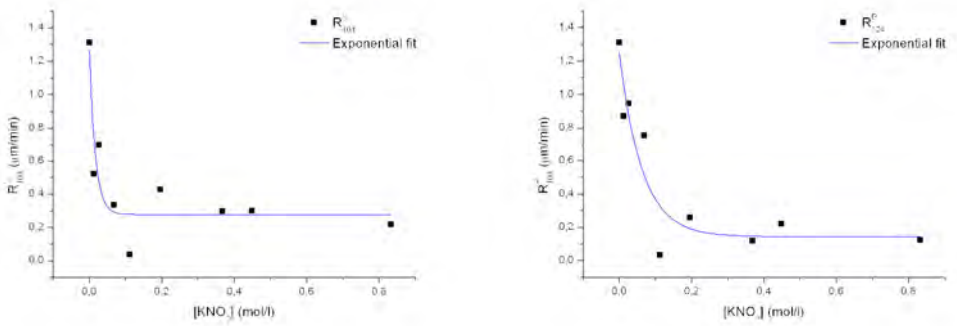


**Figure 15.** Experimental plots of $NaNO_3$ growth rate in the presence of $KNO_3$. Growth rate of perpendicular (left) and parallel face (right) to the solution flow.

### 4.5.2. $LiNO_3$ addition.

For $LiNO_3$ fewer additions have been made because the decrease in the growth rate is evident from the first addition. An asymptote is quickly reached. In this case the growth rate measured, at the asymptote, for the perpendicular and parallel faces is around 0.4 µm/min.

In table 5 we present $NaNO_3$ and $LiNO_3$ concentration determined by ICP-OES after each experiment. In this table the specific growth rate for perpendicular ($R^N_{104}$) and parallel ($R^p_{104}$) faces are also shown. From the plot of the growth rate (figure 16) we observe that the asymptotic behaviour is reached at the first $LiNO_3$ addition.

**Table 5.** Experimental values of $NaNO_3$ growth rate in the presence of $KNO_3$. Here we indicate the component concentration.

| $[NaNO_3]$ (mol/l) | $[LiNO_3]$ (mol/l) | $R^N_{104}$ (µm/min) | $R^P_{104}$ (µm/min) |
|---|---|---|---|
| 7,57 | 0 | 1,310* | 1,310* |
| 7,36 | 0.003 | 0,357 | 0,579 |
| 7,55 | 0.007 | 0,561 | 0,336 |
| 7,56 | 0.016 | 0,400 | 0,369 |
| 7,46 | 0.031 | 0,637 | 0,472 |

*calculated from $NaNO_3$ pure system

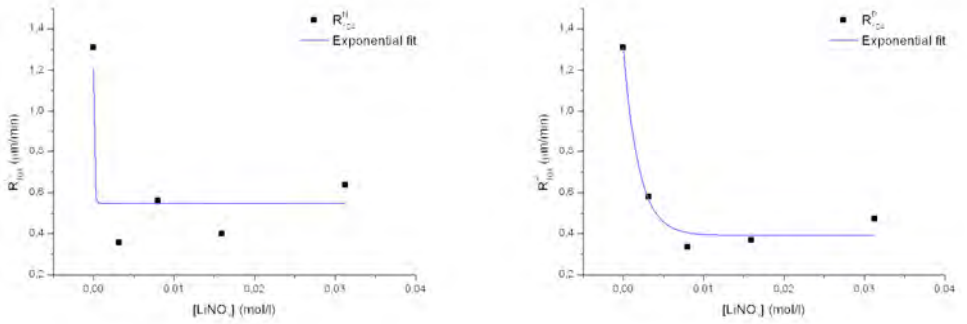


**Figure 16.** Experimental plots of $NaNO_3$ growth rate in the presence of $LiNO_3$. Growth rate of perpendicular (left) and parallel face (right) to the solution flow.

Here we observe that $LiNO_3$ is much more effective that $KNO_3$ in the lowering of $NaNO_3$ growth rate. On the contrary, by higher $KNO_3$ additions we get similar growth rates. These results are in accordance with previous sections: lithium nitrate is more effective in changing sodium nitrate morphology.

## 4.6. CONCLUSIONS

In this chapter we deal with sodium nitrate morphology modifications with addition of the following impurities: potassium and lithium nitrate, lithium hydroxide and lithium carbonate. Results show that all these compounds can induce $NaNO_3$ morphology modification. Furthermore, we have also studied the growth rate behaviour of sodium nitrate (104) faces by the addition of potassium and lithium nitrate.

Here we summarize the best condition to obtain these modifications. For isothermal crystallization with addition of potassium nitrate, lithium nitrate or lithium hydroxide the best conditions are $3 < \sigma < 4$ and atomic ratio sodium/impurity < 100.

Contrarily, for evaporation experiments it is better to use higher sodium/potassium and sodium/lithium ratios.

Additionally, we have obtained a fully modified batch by using a saturated $Li_2CO_3$ solution as an impurity and $\sigma \sim 1$ % for $NaNO_3$.

Finally, we asked if carbonate group is responsible for this change. Some more experiments have to be performed to answer the question.

On the other hand, it is clear that potassium and lithium nitrate lower the growth rate of {104} form of sodium nitrate with an exponential relationship. As {001} face also appears in some experiments its growth rate may be lowered to a higher extent to appear in the growth morphology. (001) face may become stabilized by adsorption of impurities that depress its growth rate.

## 4.7. BIBLIOGRAPHY

1. Mullin, J. W.: *Crystallization,* 2nd ed. London: Butterworths**, (1972).**

2. Chernov, A. A.: *Modern Crystallography III,*. Vainshtein, B. K.ed., Berlin: Springer, **(1981).**

3. Chernov, A. A.; and Sipyagin, V. V.: *Peculiarities in Crystal Growth from Aqueous Solutions Connected with their Structures, in* Current topics in Materials Science. Kaldis, E. ed., Amsterdam: North-Holland publishing company, **(1980)**, 279-334.

4. Herman, M. A.; Herman, M. A.; Richter, W. and Sitter, H.: *Epitaxy: Physical Principles and Technical Implementation,* Berlin, Springer**, (2004)**.

5. Benages, R.; Costa, E.; Bruno, M.; Calvet, T.; Cuevas-Diarte, M. A.; and Aquilano, D. *Experimental and Theoretical Aspects of the Growth and Equilibrium Morphology of $NaNO_3$.* Cryst. Res. Tech., **(2011)**, 1-6.

6. Sipyagin, V. V.; and Chernov, A. A. *Anomalies of Temperature Dependence of Growth-Rates of Faces of Crystals $KNO_3$, $NaNO_2$, $NaNO_3$, $NaClO_4$ and Rochelle Salt from Aqueous Solutions.* Kristallografiya, **(1972)**, 17, 5, 1003-1009.

7. Wu, X.; Fronczek F. and Butler, L. *Structure of $LiNO_3$ - Point-Charge Model and Sign of the $Li^{-7}$ Quadrupole Coupling-Constant.* Inorg. Chem., **(1994)**, 33, 7, 1363-1365.

8. Paul, G. L.; and Pryor, A. W. *Study of Sodium-Nitrate by Neutron Diffraction.* Acta Cryst. B., **(1972)**, 28, 15, 2700-2702.

9. Nimmo, J. K.; and Lucas, B. W. *A Neutron Diffraction Determination of the Crystal Structure of a-Phase Potassium Nitrate at 25ºC and 100ºC.* J. Phys. C., **(1973)**, 6, 201-211.

10. Xu, T.; and Pruess, K. *Thermophysical Properties of Sodium Nitrate and Sodium Chloride Solutions and their Effects on Fluid Flow in Unsaturated Media,* **(2001),** E. O. Lawrence Berkeley National Laboratory, Berkeley, CA (US). DOI 10.2172/790019.

11. Massaro, F. R.; Pastero, L.; Costa, E.; Sgualdino, G. and Aquilano, D. *Single and Twinned $Li_2CO_3$ Crystals (Zabuyalite) Epitaxially Grown on {0001} and {10-14} Forms of $CaCO_3$ (Calcite Crystals).* Cryst. Growth Des., **(2008)**, 8, 6, 2041-2046.

12. Pastero, L.; Costa, E.; Bruno, M.; Rubbo, M.; Sgualdino, G. and Aquilano, D. *Morphology of Calcite ($CaCO_3$) Crystals Growing from Aqueous Solutions in the Presence of $Li^+$ Ions. Surface Behaviour of the {0001} Form.* Cryst. Growth Des., **(2001)**, 4, 3, 485-490.

13. Pastero, L.; Aquilano, D.; Costa, E. and Rubbo, M. *2D Epitaxy of Lithium Carbonate Inducing Growth Mechanism Transitions on {0001}-K and {01-18}-S Forms of Calcite Crystals.* J. Cryst. Growth, **(2005)**, 275, 1-2, 1625-1630.

14. Pastero, L.; and Aquilano, D. *$CaCO_3$ (Calcite)/$Li_2CO_3$ (Zabuyelite) Anomalous Mixed Crystals. Sector Zoning and Growth Mechanisms.* Cryst. Growth Des., **(2008)**, 8, 9, 3451-3460.

15. Benages-Vilau, R.; Calvet, T.; Cuevas-Diarte, M. A. and Aquilano, D. *The Theoretical Morphology of Nitratine ($NaNO_3$).* **, (in preparation)**.

16. Benages-Vilau, R.; Calvet, T.; Cuevas-Diarte, M. A.; Rubbo, M. and Aquilano, D. *Crystal Growth of $NaNO_3$ from Pure Aqueous Solutions,* **, (submited to Crystal Growth and Design)**.

# CHAPTER 5

## $NaNO_3$-$CaCO_3$ EPITAXY

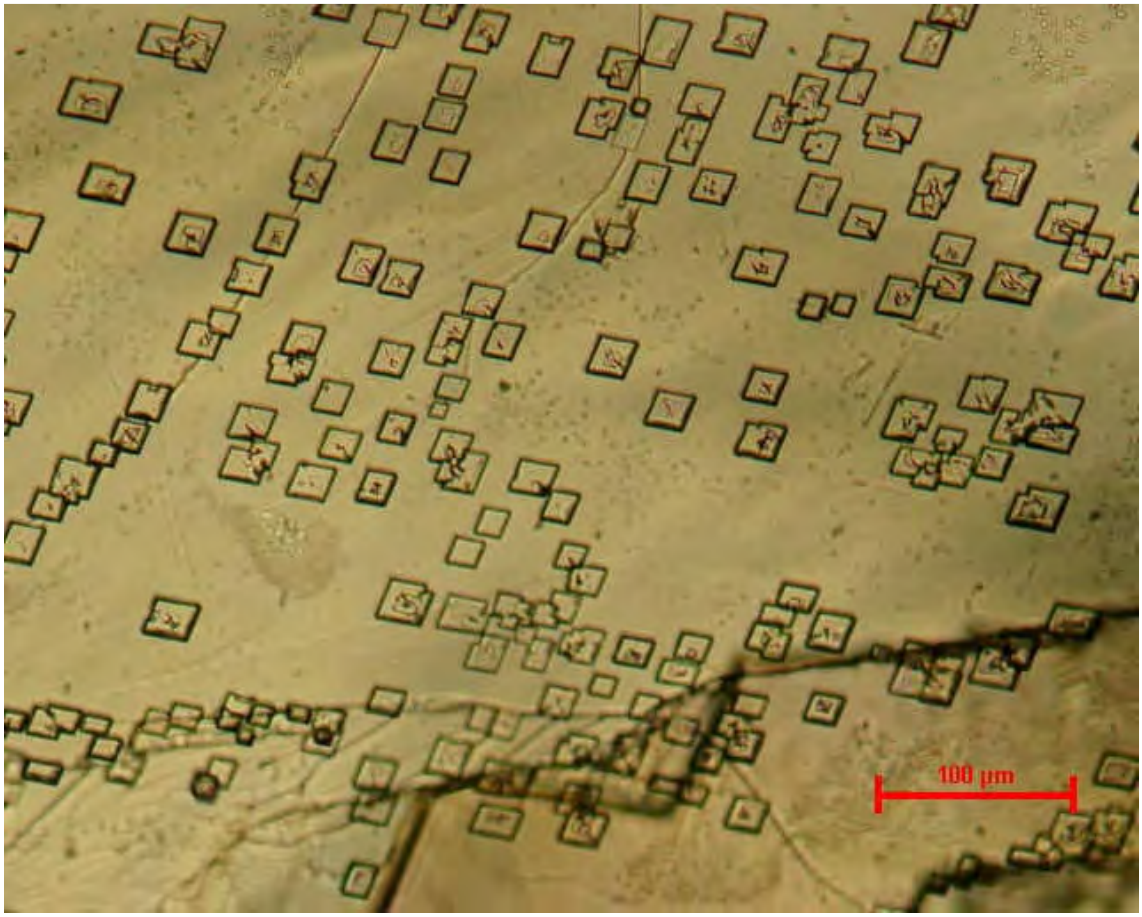

## 5.1. GENERAL INTRODUCTION

Gebhardt[1] made an excellent summary of the epitaxy phenomena, so this introduction will be mainly based on his work.

Epitaxy is a nucleation and growth relationship between two crystalline phases, which makes it possible for a crystalline phase 'g' (guest crystal) to grow in a structure dependent manner onto a given face structure 'h' (host crystal) developing, in general, an interfacial region which is chemically and structurally inhomogeneous. In principle, in a complete epitaxial reaction, there exists a two-phase system consisting of two adjacent heterochemical or isochemical epitaxial partners: host and guest. Chernov[2] defines the term epitaxy as the oriented growth of one crystal over another. In fact, Kern[3] pointed out that the only important factor for an epitaxial relationship is the difference between the crystallographic parameters of two structures.

Epitaxial deposition usually takes place under conditions strongly diverging from thermodynamic equilibrium. So the joining of the atoms into nuclei may be virtually irreversible; besides thermodynamic factors, kinetic factors play a significant role. They are manifested in the dependence, degree and nature of the process upon the host temperature, supersaturation, and the degree and nature of the host defects, including the quantity and composition of impurities adsorbed on the host surface or embedded in the guest surface layer.[2]

Stowel[4] pointed out that the orientation of a film on a suitable single crystal substrate may not only be influenced by the nucleation of the deposit but also by the subsequent growth. So we can divide the epitaxial deposits in two groups: a) orientation controlled by initial nuclei and b) growth controlled by the subsequent spreading of nuclei.

a) Epitaxial nucleation.

Epitaxial nucleation is a special case of heterogeneous nucleation: the nucleation of the guest phase on the surface of the host phase. In figure 1 different kind of host/guest relationships are schematically shown. In figure 1a host and guest crystallites are completely non-oriented. In figure 1b an orientation of texture may exist; that is, all the guest crystallites grow with the same low index (usually) stable lattice plane on the substrate surface but they are not oriented with respect to one another. In figure 1c the

guest crystallites show both texture and azimuthal orientation toward one another: this is epitaxy.

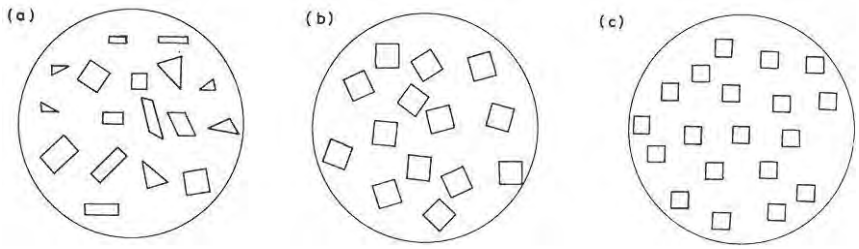


**Figure 1.** Growth of a guest (deposit) onto a host (substrate). a) Fully non-oriented; b) texture orientation: a guest plane is parallel to the host orientation; c) epitaxy: texture and azimuthal orientation.[1]

Crystallites of several epitaxial orientations may exist on the substrate surface with altogether un-oriented crystallites. The fractions of crystallites of different orientations with respect to the total number characterize the degree of epitaxy. Epitaxial overgrowth guest/host are only to be expected if the increase in chemical potential ($\Delta\mu=\mu-\mu_0$, where $\mu$ and $\mu_0$ are the chemical potential of the growing face in solid and in solution respectively) is negative and when for special crystal faces (hkl) the free interfacial energy host/guest ($\sigma_{hg}$) as a function of the azimuthal orientation shows a marked minimum caused by the atomic structure of the host surface (figure 2). It is worth remembering that the chemical potential is related to the supersaturation ($\beta$, a measure of how far from the equilibrium the system is) by the equation $\Delta\mu = k\cdot T\cdot \ln\beta$ where k is the Boltzmann constant and T the absolute temperature. The free interfacial energy host/guest ($\sigma_{hg}$) increases with the misorientation angle. This is caused by elastic tensions in the substrate/nucleus interface and by the increase of the surface energy as a result of displacements which appear by mismatchting. These variations in interfacial free energy are important when the supersaturation is low. By increasing supersaturation, the absolute value of $\sigma_{hg}$ is reduced but then the difference between the nucleation probabilities for epitaxial and non-oriented growth becomes smaller. Gebhart[1] also pointed out that epitaxy is always favoured by increasing the substrate temperature whenever the nucleation process can be described by the classical nucleation model. As Chernov indicated,[2] the host temperature effect on epitaxy is due first of all to the fact that it, together with the guest temperature, sets the supersaturation in the system, which can be understood as the relation of the activity of the substance at

the working temperature in respect to the equilibrium temperature. Secondly, and more important, it determines the mobility of condensing ad-atoms (atoms adsorbed on the host surface) on the surface (surface mobility), and also the probability of attachment of new atoms at the cluster and their detachment from it. As the temperature increases, rotations (or migration) of atomic clusters as a whole become possible, which also promotes the attainment of unified epitaxial orientation corresponding to the minimum energy.

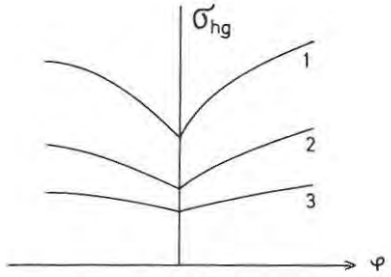


**Figure 2.** Interfacial energy host/guest ($\sigma_{hg}$) curve versus misorientation angle φ at low (1) and high (2, 3) supersaturations.[1]

Some places of the host surface seem to favour the nucleation event more than others. Along steps, for example, the roughness at atomic scale is higher than on crystal terraces and the adhesion energy $\beta_{adh}$ is, therefore, also higher. So, if one ad-atom becomes attached in this kind of places (it has more than one bond on the host), its probability to return back to the bulk solution is less than a terrace atom (with only one bond to the host), as a final result these sites are favoured. This often results in the so-called decoration of steps.

b) Epitaxy growth.

After nucleation stages, the nuclei will sooner or later start to coalesce. This agglomeration will increase as islands are formed. At a later stage, island chains join up until only channels are left. Eventually, even these will disappear and a continuous film will be obtained; the irregularities will be smoothed out by further growth.

Layers growing on another material can crystallize adopting the structure of the substrate instead of the normal structure of the layer material. As an example, Cs and Tl halides (CsCl structure) can accept NaCl structure if they grow on Na and K halides.[1]

Kern et al.[3] demonstrate that small crystals of gold (several tens of angstroms in diameter) on the (100) NaCl faces are not oriented with respect to this face in the initial stage of formation. But on annealing for several tens of minutes at ~ 100 – 150 ºC, the gold coating produces point electron diffraction patterns instead of Debye rings characteristics of the initial stage.

As Chernov pointed out,[2] from the PBC analysis it follows that the energy of the interface between two crystals is at a minimum when there is a coincidence not only between the close-packed planes of the host and guest but also between the close packed atomic rows within these planes. The fullest saturation of the surface bonds of guest and host will be achieved if the two surface structures coincide. Exact coincidence between the structure and parameters of the plane nets of different crystal is improbable but similarity between their parameters is rather common. Epitaxy occurs most often at comparatively small mismatches in lattice parameters, the general accepted mismatch is below 15 %.[5] In contrast, oriented overgrowing takes place at parameter differences as large as tens per cent. This difference can be viewed clearly in figure 1, oriented overgrowth is figure 1b and epitaxy is figure 1c.

### 5.1.1. Classification of the different epitaxial mechanisms.

This part is based on Chernov's book[2] where the three basic mechanisms of epitaxy are summarized. A graphic display of the difference is given in a Kern review and it is reproduced here in figure 3.[3]

The *Frank-van der Merve* mechanism is typical of guest-host pairs which are characterized by strong adhesion energy (β). The guest-host binding energy exceeds that between the guest atoms ($\beta > 2\sigma$). The guest atoms bound preferentially to the host, consequently a complete wetting of one or several condensate layers on the host is thermodynamically profitable even if the vapour is under-saturated. In this case we have a transition of 2D-gas to 2D-solid as indicated in figure 3. Thus, a layer by layer growth proceeds, i.e. 2D nucleation is favourable.

The *Volmer-Weber* mechanism is typical for weak adhesion energy (β) of the guest on the host crystal ($\beta < 2\sigma$). Here, the work required to form a nucleus on the substrate is larger than in the case of the *Frank-van der Merve* mechanism , and may even approach the work of homogeneous nucleation at zero adhesion energy. As is depicted in figure 3, 3D nucleation of the guest on the host is required and thus the supersaturation is higher

(compared to that of the *Frank-van der Merwe* mechanism). Accordingly, the role of inhomogeneities on the host, which lowers the nucleation barrier, is of great importance in the *Volmer-Weber* mechanism. This weak adhesion also leads to a less rigorous interrelation between the orientations of the crystalline guest and host. This fact manifests itself in the existence of several epitaxial relationships which can occur simultaneously under different deposition conditions.

The *Stranski-Krastanov* mechanism corresponds to an intermediate case between the previous mechanisms. It is characterized by the fact that the condition of good adhesion holds for the first monolayer, while the adhesion of three dimensional aggregates is weaker. Here either 2D or 3D nucleation mechanisms are manifested as is pointed in figure 3.

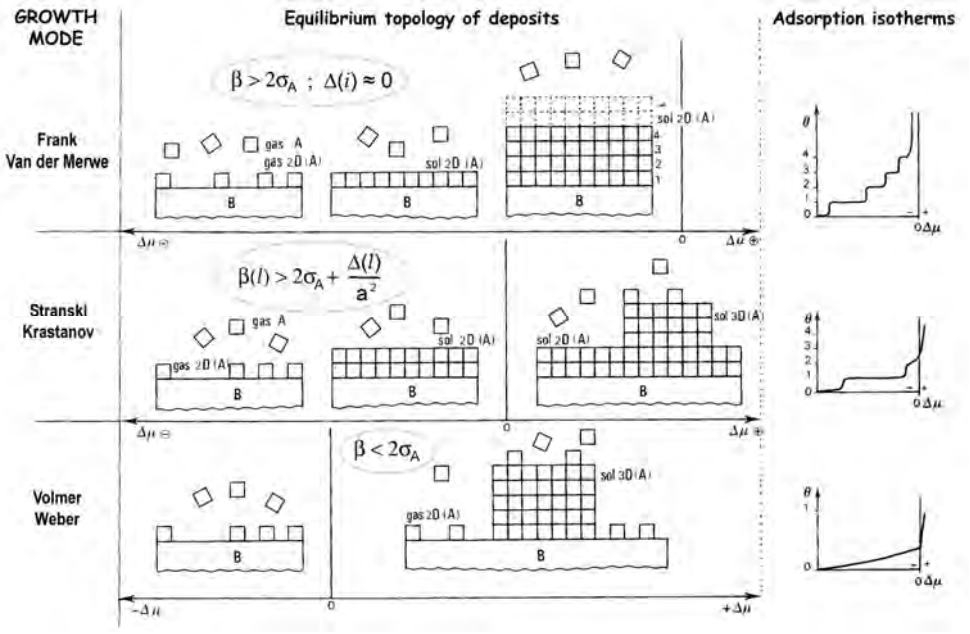


**Figure 3.** The basic mechanisms of epitaxy according to Bauer classification.[3] Here β is guest-host adhesion energy, σ is the guest binding energy, $a^2$ is the host surface cell, and Δ(l) is the host stored strain energy in the topmost layer.

Epitaxial layers are of great interest in science and industry. For example, they play an important role in natural and artificial (anti)corrosion layers, intermediate layers between metals and silicates or layers to improve chemical or abrasive properties of materials.[1] Furthermore, epitaxial layers are essential for the production of high-quality semiconductors and nanotechnology.

## 5.2. INTRODUCTION TO $NaNO_3$-$CaCO_3$ SYSTEM

Nitratine or $NaNO_3$ and calcite, a calcium carbonate ($CaCO_3$) polymorph, are a classical example for isoestructural minerals.[5] In the early 20th century, these two compounds were considered to be isomorphous by at least two authors.[6, 7] But now IUCR accepts that two compounds are isomorphous not only when they have an identical crystal structure (isostructurallity) but when they can form a continuous series of solid solutions.[8] Calcite and nitratine do not have any known solid solution, thus we consider them to be isostructural phases as others authors define these compounds.[2]

According to Déo and Finch,[9] $NaNO_3$ can easily grow epitaxially on a cleavage face of the $CaCO_3$. Indeed, this was the first recorded example of epitaxy.[10] They deposited a drop of $NaNO_3$ aqueous solution on a cleavage face of $CaCO_3$ and observed the formed crystallites in an optical microscope during their growth (figure 4, left side). In continuation, they disoriented some crystals (figure 4 middle, encircled) and found that the growth rate of disturbed and undisturbed crystals were similar (figure 4, right) indicating that the calcite substrate had little or no influence on the $NaNO_3$ growth rate.

**Figure 4.** $NaNO_3$ crystals epitaxially grown on the cleavage {104} rhombohedron of calcite. Déo and Finch[9] - Magnification 60x.

After that, only Barlow and Pope[11] made a geometrical analysis of the epitaxial relationship of $NaNO_3$-$CaCO_3$ among other pairs. On the contrary, Glikin and Plotkina[12] studied the inverse process, how calcite microcrystals slurries adhere onto a growing nitratine seed. They found that almost 40% of calcite crystals are epitaxially oriented while the rest are not oriented, joined by vertex or edges.

Both $NaNO_3$ and $CaCO_3$, considered at room temperature, have $R\bar{3}c$ space group with Z = 6. For $NaNO_3$ **a** = 5.070 Å, **c** = 16.82 Å[13] and for $CaCO_3$ **a** = 4.99 Å, **c** = 17.06 Å.[14] It means a mismatch (m) defined as:

$$m = \frac{d_{NaNO_3} - d_{CaCO_3}}{d_{CaCO_3}}$$ **equation 1**

where d represents a surface cell parameter. Therefore, the mismatch is 1.6 % in **a** and -1.4 % in **c**. These values are well below the generally accepted mismatch values for epitaxy (15 %[5]).

What is more important is the mismatch for a (104) surface cell: for the $[42\bar{1}]$ and [100] directions the mismatch is 0.25 % and 1.6 %, respectively. This is quite interesting because it permits us to discuss the effect of electric potential on the theoretical morphology of calcite and nitratine. This will be the subject of a paper.[15]

The objective of the work presented in this chapter is to observe the initial stages of $NaNO_3$ nucleation onto a fresh cleaved {104} $CaCO_3$ surface by optical microscopy, scanning electron microscopy (SEM) and atomic force microscopy (AFM).

## 5.3. MATERIALS AND METHODS

Calcite of Durango (Spain) origin was used in this work. Distilled water and ethanol were used as solvents.

Solubility measurements of nitratine ($NaNO_3$) in water-ethanol mixtures were performed as follows: a known amount of $NaNO_3$ powder (Quality Chemicals. analytical grade) was weighed (about 0.2 g) with 0.1 mg precision. Then, 1 ml of solvent was added, and the solution was stirred for enough time to assure that the maximum solubility was achieved. If any solid is found 1 ml more of solvent is added. This process is repeated until a clear solution is reached.

Calcite crystals were cleaved with a razor blade parallel to the (104) face prior to each experiment. A drop of $NaNO_3$ saturated solution was deposited onto the cleaved crystal and allowed to evaporate. Sodium nitrate crystallization was visualized with an optical or electronic microscope. Experiments with water and ethanol (EtOH, a poor solvent) as well as mixture of them (25 % $H_2O$ - 75 % EtOH) were carried out in order to find a good medium for high resolution AFM measurements in liquid and also to verify if a solvent change provoked a change in $NaNO_3$ morphology.

For ethanol solution, small pieces (about 5 x 5 x 2 mm) of freshly cleaved {104} form of calcite were placed for 30 minutes in a stirred saturated sodium nitrate etanol solution (we observed some $NaNO_3$ powder on the bottom). Then we removed the crystals and dried them at 40 ºC for 30 minutes. Characterization was made using a magnifying glass, microscope and SEM. We performed 3 kinds of surface treatments for a freshly cleaved {104} form of calcite. In the first set, we used a cleaved surface. In the second set we washed the surface for 30 minutes with deionised water. In the third set, we washed the surface for 1 minute with diluted HCl; in this case pieces of calcite were finally washed with water for 40 minutes.

Finally, with as-cleaved experiments and after having seen epitaxial growth, we immersed some calcite pieces into 99.5 % ethanol or n-pentane for three hours and dried them at 40 ºC.

Samples were analysed using a Hitachi S-4100 field-emission scanning electron microscope (FE-SEM) at room temperature. They were mounted on a slide (12 mm diameter) with a conductive adhesive (Agar Scientific) and covered with a fine carbon layer (ca. 20 nm). In-situ epitaxial growth was followed by an ESEM Quanta 200. It incorporated a Peltier to lower sample temperature and water pressure control. This

equipment permited us to evaporate water at constant temperature and pressure. Scanning electron microscopes were located in Centres Científics i Tecnològics of Universitat de Barcelona (CCiT-UB).

For an optical control we used equipment at Department de Cristal·lografia, Mineralogia i Dipòsits Minerals of the UB. Either a Nikon SMZ 1500 magnifying glass with ProgRess speed $XT^{core}$ 3 CCD camera or Nikon Eclipse LV100POL microscope with DXM 1200F digital camera were used.

AFM images were obtained with an atomic force microscope (AFM Multimode Veeco Instruments) of the Centro Nacional de Microscopia Electrónica (CNME-ICTS) at the Universidad Complutense de Madrid equipped with a ~ 14 × 14 $\mu m^2$ scanner and a fluid cell. Images were taken in contact mode while displaying the height, deflection and friction signals. Silicon nitride triangular tips with nominal force constants ranging from 0.06 to 0.58 N/m were used (Veeco DNP-S10). In order to both optimize the quality of the images and highlight different features of surface structure filters, as well as different values for the z-limit and the integral and proportional gains, were used. We worked in two different ways: a) Ex-situ growth sample, and b) In-situ growth. For shear stress determination we have used a TESP quadrangular tip model. If nothing is said all measurements in this work were made in a $NaNO_3$ saturated media. AFM images were processed with the WSxM program.[16]

## 5.4. RESULTS

First, we deal with $NaNO_3$ solubility determination in water-ethanol mixtures, and then we follow by looking at the crystallization of $NaNO_3$ over $CaCO_3$. After that, we seek out to prove if solvent change affects to $NaNO_3$ crystal morphology. Finally, we characterize the first nitratine crystals grown over calcite cleavage surface by AFM measurements.

### 5.4.1. $NaNO_3$ solubility.

The solubility of nitratine in water is very high: about 48 weight % at room temperature[17] and its temperature dependence is very elevated. These facts made AFM measurement of $NaNO_3$ crystals growing in aqueous solutions very difficult due to unwanted crystallization in the inlet/outlet tube or also inside the cell. Thus, we searched for a $NaNO_3$ poor solvent to carry out the experiments and also to find if its morphology remains the same.

$NaNO_3$ solubility at various water-ethanol solvent compositions has been determined at room temperature (Table 1). Furthermore, the solubility in 25 % $H_2O$ – 75 % EtOH as a function of temperature has been determined as well (Table 2). We thought that this composition was appropriate to work in AFM microscope but experience demonstrates that 99.5 % ethanol was the best solution.

**Table 1.** Solubility of $NaNO_3$ at room temperature for different $H_2O$-etanol solvent compositions.

| Solvent composition (% Vol) | Solubility (mg/ml) |
|---|---|
| 99.5 % EtOH | <4 |
| 25 % $H_2O$ – 75 % EtOH | 53 |
| 50 % $H_2O$ – 50 % EtOH | 117 |
| 75 % $H_2O$ – 25 % EtOH | 125 |

**Table 2.** Solubility of 25 % $H_2O$ – 75 % EtOH composition as a function of temperature.

| T (ºC) | S (mg/ml) |
|---|---|
| 23 | 60 |
| 30 | 65 |
| 35 | 75 |
| 40 | 80 |
| 45 | 80 |
| 50 | 95 |

$NaNO_3$ is poorly soluble in ethanol but increases its solubility rapidly when water is added. This behaviour is expected because water solubility is about 900 mg/ml at room temperature.

### 5.4.2. $NaNO_3$-$CaCO_3$ epitaxy in water solution.

This classical epitaxial test is made as a reference frame for the rest of the experiments. A nearly saturated sodium nitrate aqueous solution was evaporated onto a {104} calcite crystal (~ 1 cm wide). Crystallites begin to appear at the in-surrounding of the drop. Crystals of $NaNO_3$ adopt a common orientation with respect to the $CaCO_3$ substrate. Half an hour after starting the experiment oriented crystals had grown throughout the drop as is shown in Figure 5a.

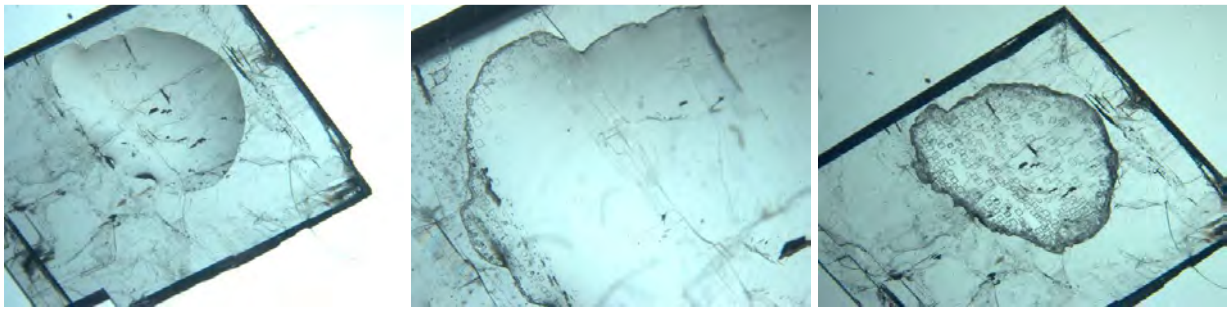

**a**

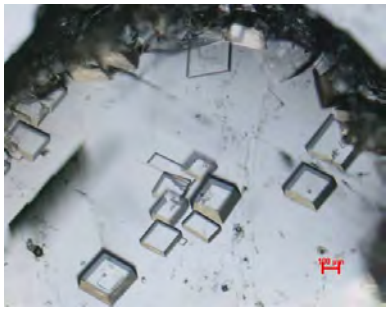

**b**

**Figure 5.** Epitaxial crystallization from an aqueous solution of $NaNO_3$ onto (104) $CaCO_3$ surface. a) Observed under a magnifying glass. b) Observed under an optical microscope (10x). Crystallization time was about 15 minutes.

In Figure 5b we observe the same results with an optical microscope (10x) using a few microliter drop. We can only see some orientations in the centre of the drop. On the border, as always occurs in this system, massive crystallization is observed. When the drop is dried three different zones can be signalled: oriented crystals in the middle of the drop, massive crystallization on the drop border and efflorescence throughout.

Only one experiment was performed in ESEM controlling water pressure and temperature. A drop of few microlitres of $NaNO_3$ saturated water solution was placed on a small piece of freshly cleaved $CaCO_3$. It was introduced into the electronic microscope chamber. Then we set a water saturated ambient condition in order to maintain the solution stable. Finally, we evaporated this drop at 5 ºC and 6 tor. Again, most of the crystals had the same orientation as can be seen in figure 6.

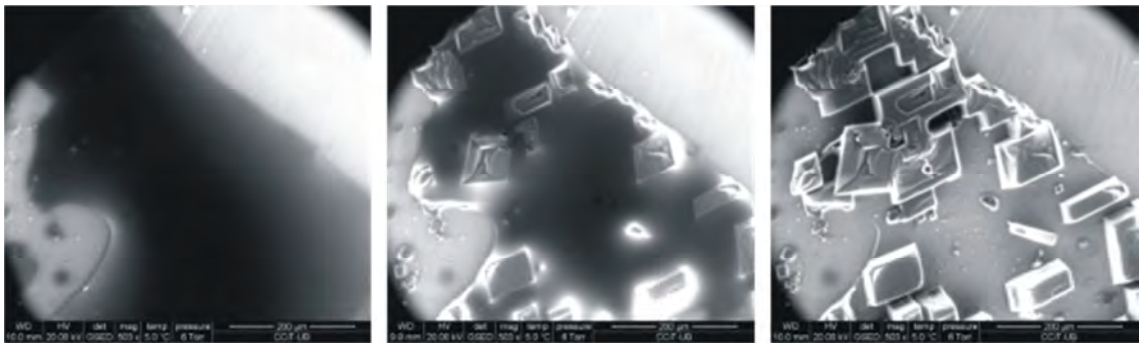

**Figure 6.** Epitaxial crystallization of a water solution of $NaNO_3$ onto (104) calcite surface in an ambient SEM. Crystallization time: few minutes.

### 5.4.3. $NaNO_3$-$CaCO_3$ epitaxy in a 25 % $H_2O$ – 75 % EtOH solvent composition.

In this section we changed the solvent to prove that epitaxy relationship still holds. In figure 7 we show the results obtained using 75 % EtOH – 25 % $H_2O$ as solvent composition. Only one experiment was performed to check the influence of the solvent. Sodium nitrate lozenge crystals have, again, the same orientation on the substrate.

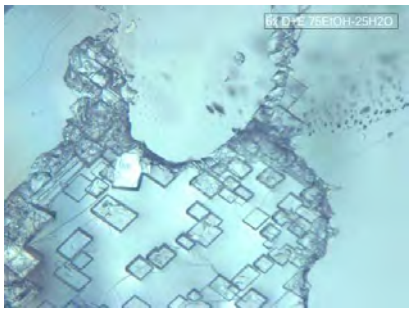

**Figure 7.** Epitaxial crystallization of a 75 % EtOH – 25 % $H_2O$ solution of $NaNO_3$ onto (104) $CaCO_3$ surface (6x). Crystallization time was about 20min.

### 5.4.4. $NaNO_3$-$CaCO_3$ epitaxy in ethanol solution.

Next, we want to know what $NaNO_3$ morphology is when we change the solvent totally. In this case, the objective is to study calcite samples into AFM, so we need to use smaller pieces. As exposed in the introduction, pieces of calcite of about 5 x 5 x 2 mm were cut so that they could be inserted into the AFM fluid cell. Prior to that, we performed 3 different surface treatments to the calcite surface. Then we studied them by optical and electron microscopy. From all experiments we point out that epitaxial crystallites are practically all independent, oriented and with similar sizes within the same experiment. This means that the nucleation events take place at the same time and the growth rate of independent crystallite is also similar.

#### 5.4.4.1. Freshly-cleaved calcite.

As was expected, also ethanol solutions are a good media to crystallize epitaxially $NaNO_3$ on a $CaCO_3$ surface. Figure 8 demonstrates that crystallites are smaller that those grown from water-ethanol solutions and that they can be washed into n-pentane (Figure 8 right) without dissolving the $NaNO_3$ crystallites. In Figure 8 (right) we can observe that many crystallites are joined together to form larger islands that change their main direction, whereas individual crystals remain with the same orientation. The direction changes may be due to imperfections on the substrate. Crystals change neither the morphology nor the relative orientation.

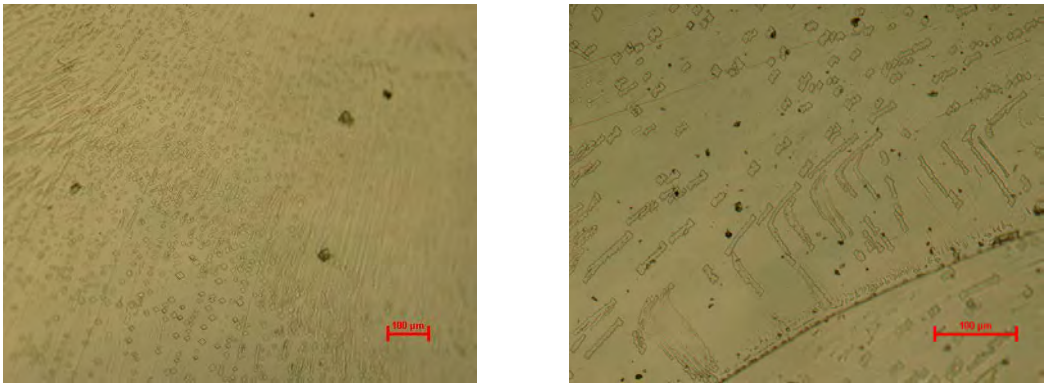

**Figure 8.** Epitaxial crystallization from an ethanol solution of $NaNO_3$ onto (104) $CaCO_3$. The right figure was taken after rinsing the calcite piece into n-pentane. Samples were in contact with a saturated ethanol solution for 30 minutes before they were dried.

### 5.4.4.2. $H_2O$ washed calcite surface.

In figure 9 we observe again a large number of $NaNO_3$ crystallites deposited onto water washed $CaCO_3$ cleavage surface.

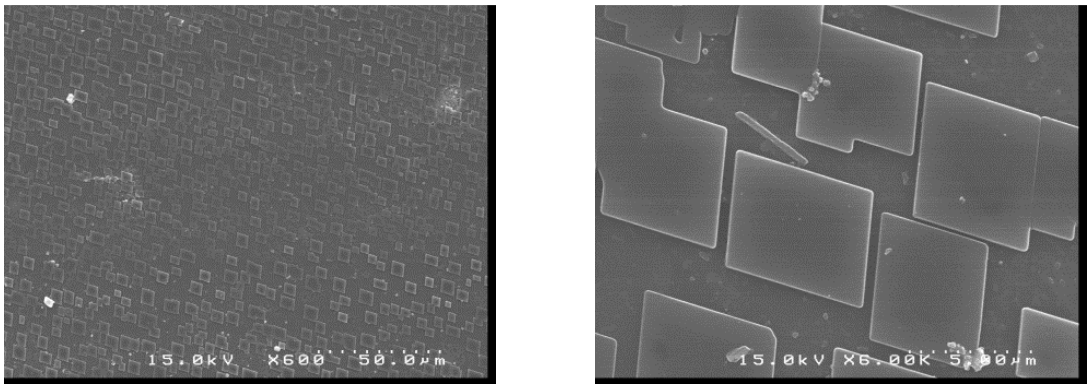


**Figure 9.** Epitaxial crystallization from an ethanol solution of $NaNO_3$ onto (104) water washed $CaCO_3$. Samples were in contact with a saturated ethanol solution for 30 minutes before they were dried.

### 5.4.4.3. HCl washed calcite surface.

When calcite surface is treated with HCl, we can observe in figure 10 that the surface has been damaged (figure 10c), but $NaNO_3$ crystallites still grew oriented.

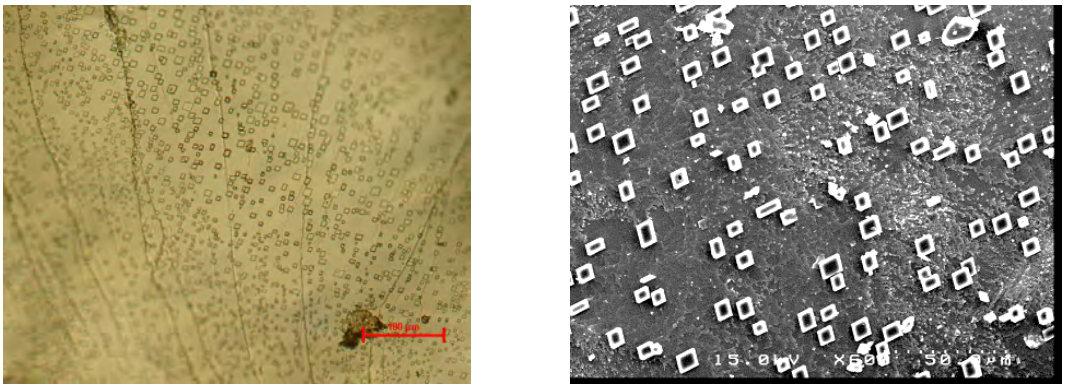

**Figure 10.** Epitaxial crystallization from an ethanol solution of $NaNO_3$ onto (104) HCl washed $CaCO_3$. The figure on the right was taken after rinsing the calcite piece in n-pentane. Samples were in contact with a saturated ethanol solution for 30 minutes before they were dried.

So we can conclude from this set of experiments that $NaNO_3$-$CaCO_3$ epitaxy occurs independently from the surface treatment.

### 5.4.5. Atomic force microscopy experiments.

After verifying that nitratine crystals are well deposited (and oriented) over calcite cleavage surface, we decided to use AFM to prove that guest and host structures are atomically aligned and to observe the first $NaNO_3$ epitaxial nuclei. We worked in two different ways: a) Ex-situ growth, and b) In-situ growth.

#### 5.4.5.1. Ex-situ growth.

Here we have used a sample of an epitaxial growth on freshly cleaved and water washed calcite. In this case calcite surface is irregular due to the water treatment. AFM measurements were made 4 months after the sodium nitrate growth.

As can be seen in the figure 11, calcite surface is rough, with a height difference of about 8 - 10 nm. The $NaNO_3$ rhombohedra growth onto $CaCO_3$ are oriented and have a height of 40 – 110 nm. (figure 12).

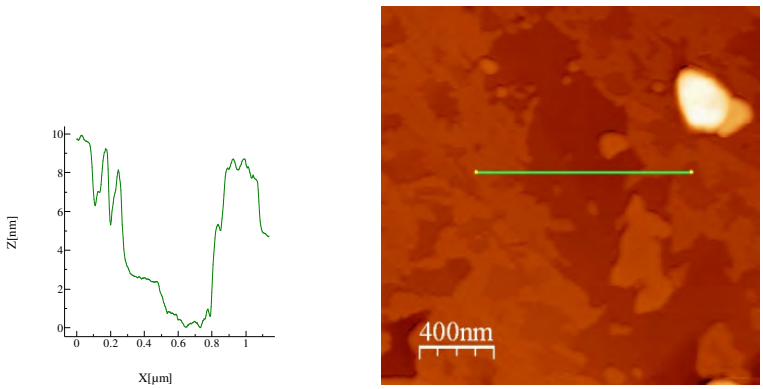


**Figure 11.** Right: $CaCO_3$ surface. Left: height measurement along the green line. Samples were in contact with saturated ethanol solution for 30 minutes.

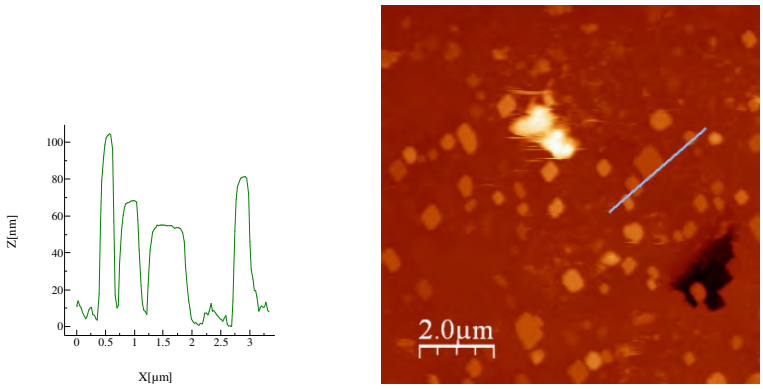


**Figure 12.** Right: $NaNO_3$ rombohedra grown over calcite surface. Left: blue line profile. $NaNO_3$ height is between 40-110 nm. Samples were in contact with saturated ethanol solution for 30 minutes.

We can observe that $NaNO_3$ is able to form a layer of ~ 25 nm (see figure 13) that is stable: the epilayer neither grows nor dissolves in the course of 17 minutes. We proved that the surface and the epilayer were different materials because friction acquisition in AFM gave different responses. From high resolution AFM measurements on the substrate and on the layer we can conclude that both surface structures are very similar so that they are practically indistinguishable within the error, as can be seen in the data of figure 13. In order to determine the surface cell parameters we filtered the best region on a given image and made a FFT so that we could measure the parameters in the reciprocal space. For the epilayer surface cell (sodium nitrate), parameters were determined from 37 images ($\mathbf{a_0} = 8.8 \pm 0.4$ Å; $\mathbf{b_0} = 5.3 \pm 0.3$ Å). For the bottom surface (calcium carbonate) only 9 images were used ($\mathbf{a_0} = 9.0 \pm 0.1$ Å; $\mathbf{b_0} = 5.2 \pm 0.3$ Å).

As an example we show two images using a self correlation filter (figure 14) of selected parts for the best high resolution acquisitions of the calcite surface and the epilayer. We can observe that both surfaces have practically the same cell vectors within the error. A nearly rectangular (or slightly oblique) cell with a bright spot inside can be drawn in both structures, but there is a drift in cell parameters when moving away from the centre to the sides. The same surface structure was observed by Rode et al.[14] on cleavage calcite and by Pina et al.[18]on cleavage surface of dolomite.

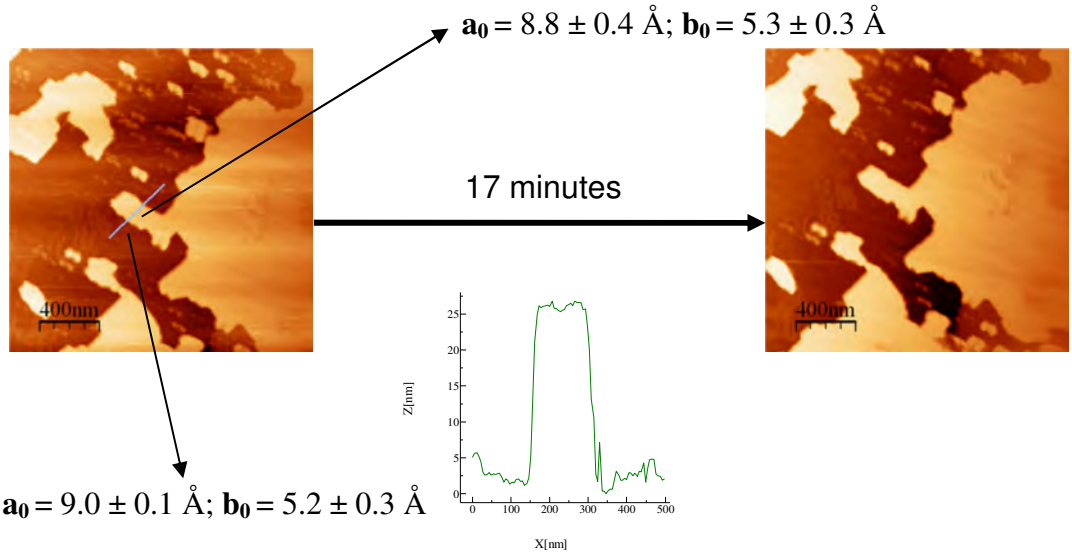


**Figure 13.** Surface images of $NaNO_3$ epitaxial growth on $CaCO_3$ surface. A layer of about 25 nm has been formed. The height along the blue line on the left is shown. The surface cells on dark (calcite) and bright (nitratine) parts determined by high resolution measurements are also given.

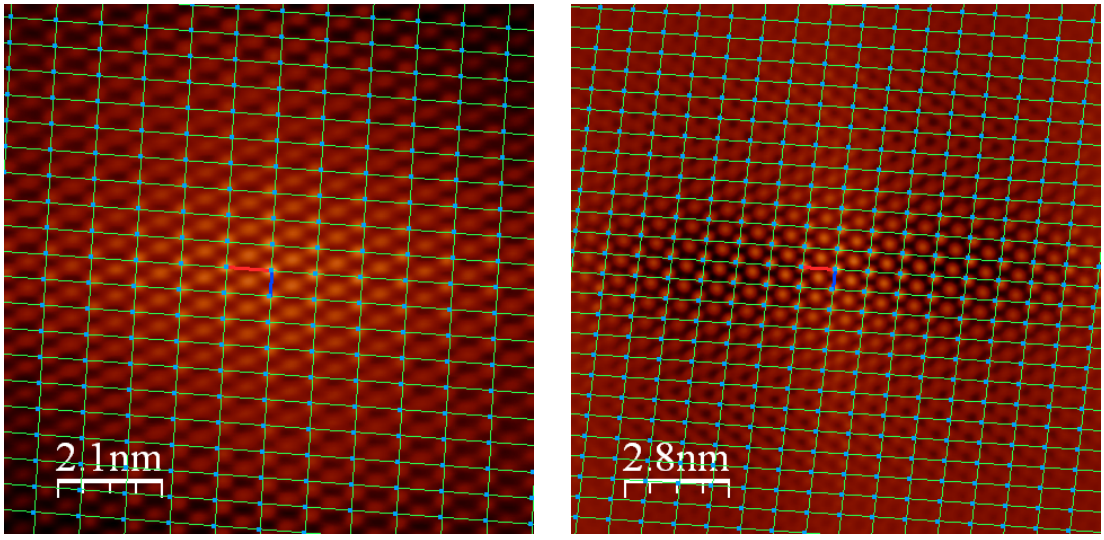


**Figure 14.** Left: the $NaNO_3$ surface cell $\mathbf{a_0}$ = 8.7 Å and $\mathbf{b_0}$ = 5,2 Å; right $CaCO_3$ $\mathbf{a_0}$ = 8,6 Å and $\mathbf{b_0}$ = 5,3 Å.

### 5.4.5.2. In-situ growth.

In this case we used a freshly cleaved surface of Durango calcite. This surface has a different aspect than the previous experience. In the previous experiments it was washed with water while in these experiments a freshly-cleaved surface is used. As can be observed in figure 15 the surface has straight steps that separate flat terraces due to the cleaving process.

The injection of $NaNO_3$ saturated ethanol solution conducts to many nucleation events of sodium nitrate onto calcite (figure 15), especially on the edges because its structure is rougher compared with the terraces, so the adhesion energy ($\beta_{adh}$) is higher.

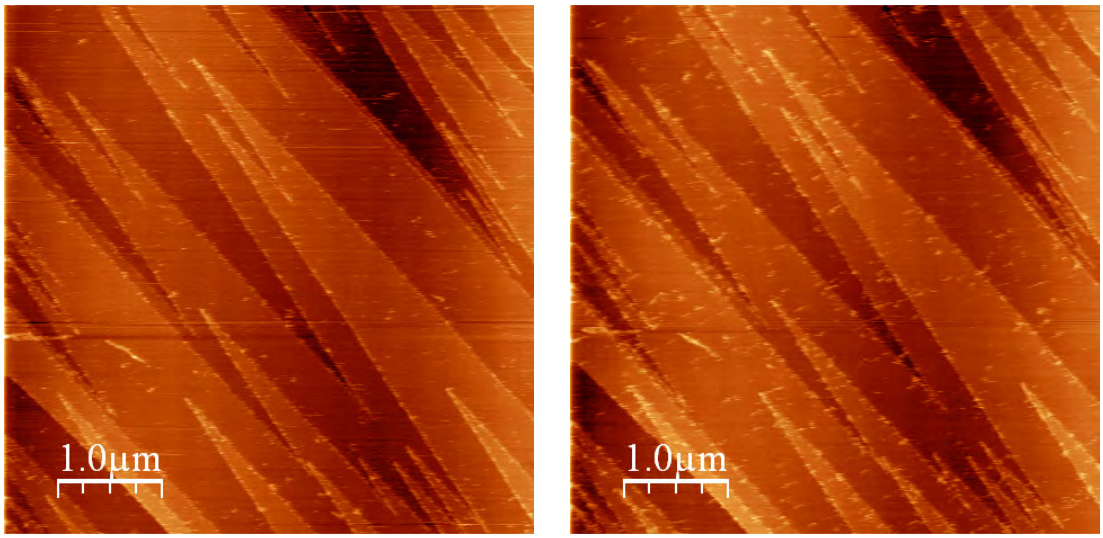


**Figure 15.** In situ crystallization of $NaNO_3$ crystallites onto $CaCO_3$ cleavage surface from a saturated ethanolic solution. Crystals are preferably nucleated onto cleavage edges. Time between images: 13 minutes.

As proof of this statement we demonstrate in figure 16 that when saturated ethanol solution is injected, surface nuclei tend to dissolve, in contrast the edge nuclei persist.

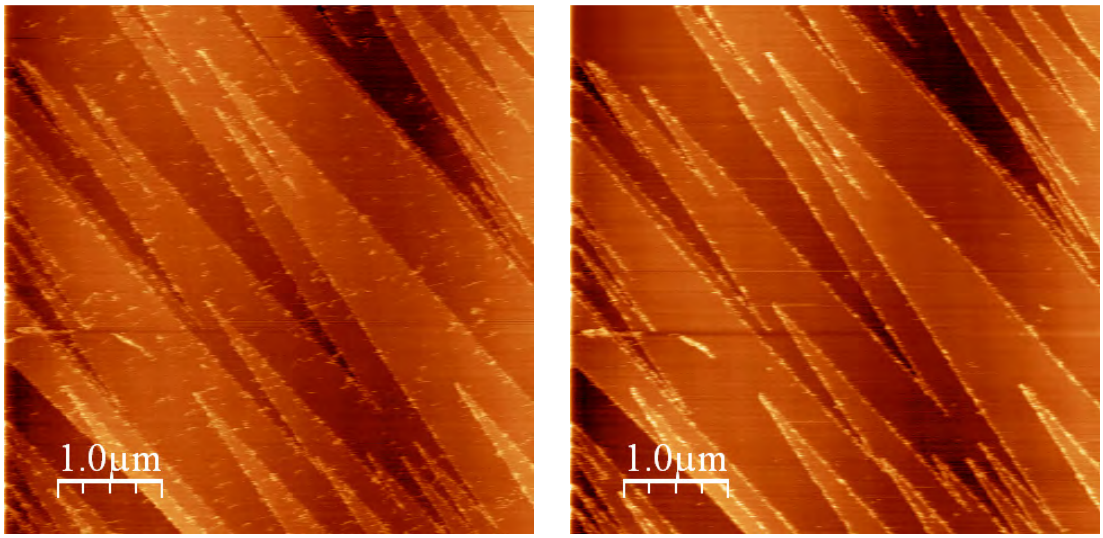


**Figure 16.** Dissolution of surface nuclei, but persistence of edge nuclei, by the injection of saturated ethanol. Time between images: 2 minutes.

The epilayer is slowly growing as can be observed in figure 17 (the time elapsed between images was ~ 17 minutes). The height of new $NaNO_3$ crystallites is about 9 Å in practically the whole image but we can measure an elementary epilayer of ~ 3 Å at some points of both images. All these mean that $NaNO_3$ is spreading over the calcite surface as well as adding new layers on its top.

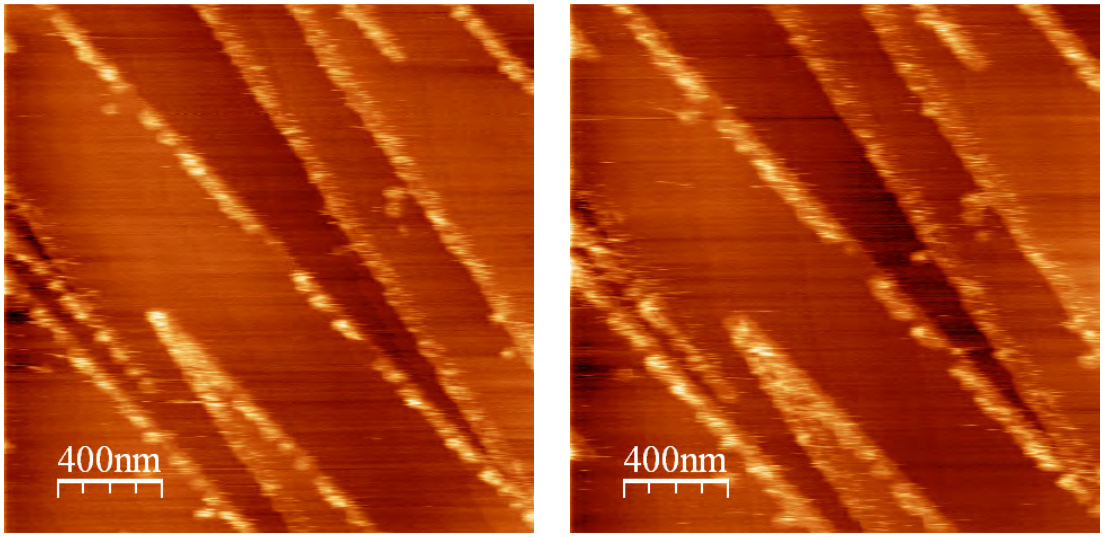


**Figure 17.** The slowly growing $NaNO_3$ crystallites on the cleavage $CaCO_3$ surface. Time between right and left images is 17 minutes.

In a different zone of the same sample we can observe single rhombohedra grown over calcite surface. In this case we have measured the height of 21 isolated crystals shown in figure 18 and we have concluded that they can be grouped into three categories: 2, 3 or 4 layers, as is indicated in Table 3.

The mean values in the three cases agree well with the proposed number of layers: n x $d_{104}$=n x 0,303 nm.

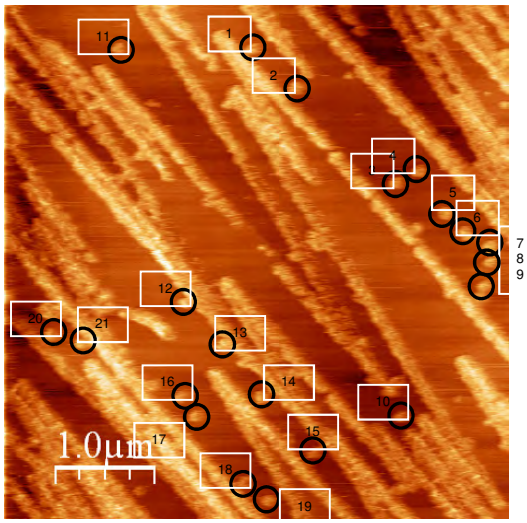


**Table 3.** Height of the islands encircled in figure 18.

| 2 layers | | 3 layers | | 4 layers | |
|---|---|---|---|---|---|
| # | height / nm | # | height / nm | # | height / nm |
| 1 | 0.752 | 2 | 0.884 | 5 | 1.101 |
| 11 | 0.786 | 3 | 1.042 | 10 | 1.112 |
| 14 | 0.685 | 4 | 0.984 | 12 | 1.287 |
| 16 | 0.541 | 6 | 0.857 | 13 | 1.351 |
| 17 | 9.769 | 7 | 1.080 | | |
| 18 | 0.582 | 8 | 1.044 | | |
| 20 | 0.598 | 9 | 0.910 | | |
| | | 15 | 0.811 | | |
| | | 19 | 0.776 | | |
| | | 21 | 1.067 | | |
| Mean value | 0.672 | Mean value | 0.946 | Mean value | 1.213 |

**Figure 18.** Single rhombohedra grown on calcite surface and their measured heights. Crystals can be divided into 3 categories according to the number of elementary layers.

When we try to obtain high resolution images of the $NaNO_3$ growth layers we observe that the tip force is higher than the shear stress needed to strip out $NaNO_3$ crystals so they disappear.

All measurements point to the same epitaxial growth mechanism, a Volmer-Weber mode: a nucleation of 3D crystals on the substrate (host) surface. The best way to prove this statement is to determine both the adhesion energy ($\beta^{adh}$) and the guest ($NaNO_3$) surface energy in order to compare them. If $\beta^{adh} < 2\sigma_{nitratine}$ then, the most probable mechanism is Volmer-Weber.[3] Unfortunately, this energy is not easy to measure.

### 5.4.5.3. Shear stress determination.

Instead of adhesion energy we can measure the shear stress required to remove $NaNO_3$ islands epitaxially grown on $CaCO_3$ (104) surface in a quite elegant way inside the AFM microscope. For doing that the applied vertical force between the AFM tip and the surfaces during scan was progressively increased until sodium nitrate islands were removed from the calcite surface. Then lateral forces related to the detachment events of $NaNO_3$ islands can be calculated from tip parameters and recorded friction signals using the following formula:[19]

$$F_L = 1.5 \cdot k_L \left(\frac{h}{L}\right) S \cdot V_L \qquad \textbf{equation 2}$$

where $k_L$ = 9.72× $10^5$ nN/μm is the torsional spring constant of the cantilever where the tip is mounted, $h$ = 19.6 μm is the height of the tip (including half of the cantilever thickness), $L$ = 125 μm is the length of the cantilever, $S$ = 35.9 nm/V is the sensitivity of the AFM photodetector and $V_L$ is half of the difference in voltage of the trace and retrace frictional signals. Rectangular cantilevers (TESP, Brucker) were used. Once the lateral forces were obtained using equation 2, shear stress for the detachment of individual sodium nitrate islands on calcite (104) can be calculated by equation 3:[20]

$$\tau = \frac{F_L}{A_C} \qquad \textbf{equation 3}$$

where $A_c$ is the contact area of the removed $NaNO_3$ island. Each image in figure 18 is taken at a progressively higher force (the voltage is indicated below each image). We can see that crystallites disappear at forces higher than 4V.

The shear stress determined is 35.3 MPa for the crystallite stripped out at 4 V (green circle in figure 19) and 23.3 MPa for the crystallite stripped out at 4.5 V (blue circle in figure 19). The shear stress measured to remove sodium nitrate crystal from calcite surface is one order of magnitude higher than that needed to remove calcite crystals from dolomite surface, which is approximately 7 MPa. This is consistent because our system has a lower mismatch than calcite - dolomite; therefore our adhesion may by higher and, hence shear stress is also higher. Furthermore, the difference on surface electrical field may also play a role.

In this chapter we have given experimental evidence that $NaNO_3$ growth mode onto $CaCO_3$ surface is a Volmer-Weber mechanism. Oriented crystals grown on calcite surface always have a lozenge shape.

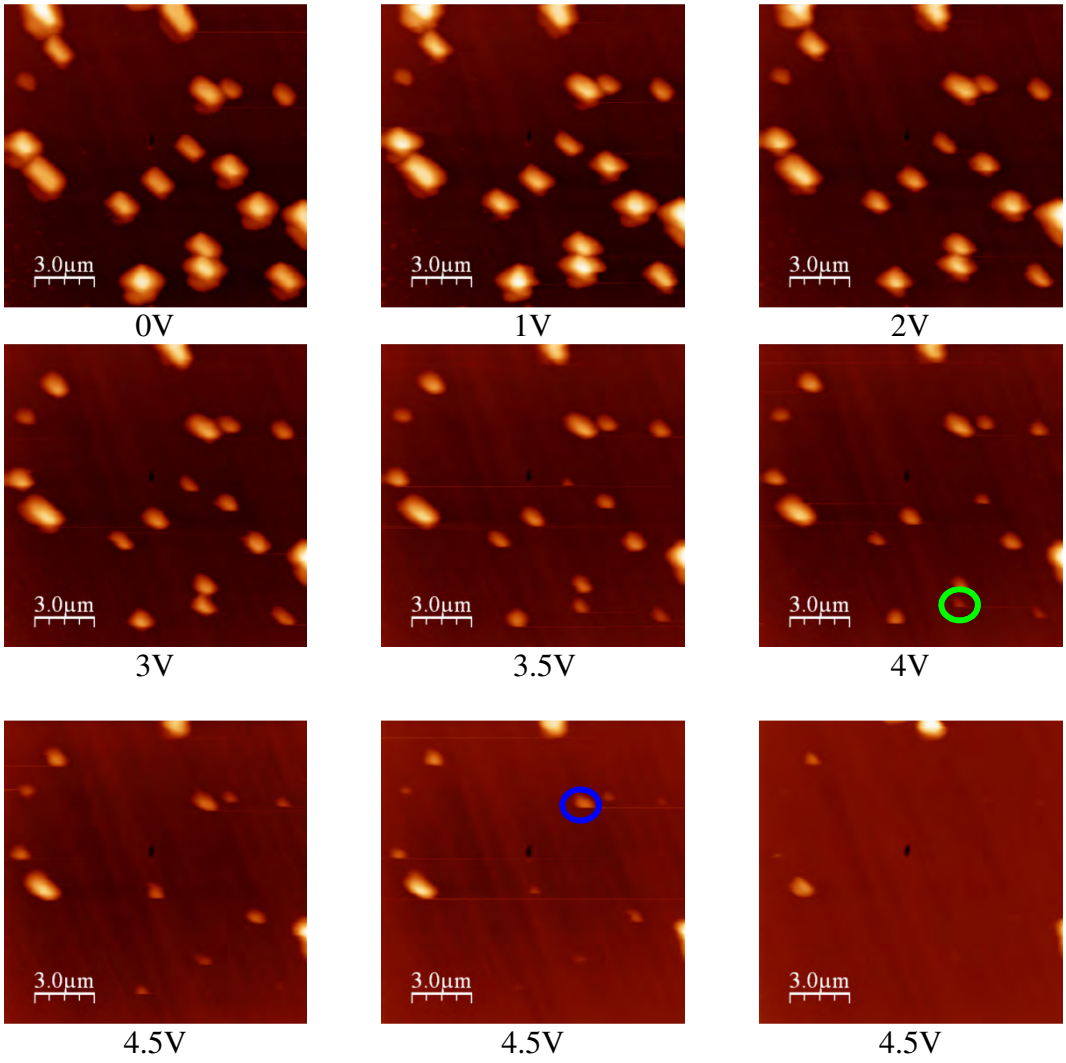


**Figure 19.** Shear stress determination sequence. The vertical tip force (set-point) in each image is indicated below each image.

## 5.5. CONCLUSIONS

Epitaxial crystallization of sodium nitrate onto freshly cleaved {104} calcite form from an aqueous as well as from an ethanol solutions have been studied. Despite the low solubility of $NaNO_3$ in ethanol (< 4 mg/ml), we were able to show how sodium nitrate crystallises in an epitaxial relationship onto (104) calcite face. $NaNO_3$ crystals growing from ethanol solutions are smaller than those grown from water or water - etanol mixtures.

The most probable epitaxial mechanism is Volmer-Weber: 3D small clusters are nucleated directly onto calcite surface and then they grow as independent islands. This means that $NaNO_3$ atoms are more strongly bound to each other than to the $CaCO_3$ substrate. The surface mismatch is 0.25 % for $[42\bar{1}]$ direction and 1.6 % for [010] direction which are the directions defining the {104} surface unit cell.

From AFM measurement we can conclude:

- Epitaxial rhombohedra height between 40 – 110 nm along with a sheet of ~ 20 nm height, (about 70 elemental layers) that covers practically the whole (104) calcite surface is observed.
- High resolution AFM images have been taken on calcite surface and $NaNO_3$ epilayer. A nearly rectangular (slightly oblique) cell with a bright spot inside can be derived from measurements in both structures, with cell parameters practically indistinguishable.
- In-situ growth of epitaxial $NaNO_3$ demonstrates that it nucleates preferably on the edges of $CaCO_3$ surface.
- New rhombohedra crystal nuclei of up to 4 elemental layers were detected. They grow slowly.
- The shear stress is estimated to be between 23 MPa and 35 MPa.

## 5.6. BIBLIOGRAPHY

1. Gebhardt, M.: *Epitaxy, in* Crystal growth: an introduction. Hartman, P. ed., 1st ed. Amsterdam: North-Holland, **(1973).**, pp. 105-142.

2. Chernov, A. A.: *Modern Crystallography III,*. Vainshtein, B. K. ed., Berlin etc.: Springer, **(1981).**

3. Kern, R.; Le Lay, G. and Metois, J. J.: *Basic Mechanisms in the Early Stages of Epitaxy, in* Current topics in material science. Kaldis, E. ed., Amsterdam: North Holland, **(1979)**, 131-419.

4. Stowell, M. J. *Roles of Deposition Parameters during Thin Film Growth.* Thin Films, **(1968)**, 1, 1.

5. Herman, M. A.; Herman, M. A.; Richter, W. and Sitter, H.: *Epitaxy: Physical Principles and Technical Implementation,* Berlin.: Springer, **(2004)**.

6. Wells, A. F.: *Structural Inorganic Chemistry,* 2nd edition ed. Oxford: Calendon Press, **(1952).**

7. Winchell, A. N.: *The Microscopic Characters of Artificial Inorganic Solid Substances of Artificial Minerals,* 2nd edition New York: John Wiley & Sons, Inc, **(1931).**

8. IUCr. *IUCr; http://reference.iucr.org/dictionary/Isomorphous_crystals,* 2012.

9. Deo, A. R.; Finch, G. I. and Gharpurey, M. K. *On the Nature of Epitaxial Crystal Growth.* Proc. R. Soc. A., **(1956)**, 236, 1204, 7-9.

10. Wakkernagel, H. Kastners Arch. Ges. Nat., **(1825)**, 5, 293.

11. Barlow, W.; and Pope, W. *On Polymorphism, with Especial Reference to Sodium Nitrate and Calcium Carbonate.* J. Chem. Soc., **(1908)**, 93, 1528-1560.

12. Glikin, A.; and Plotkina, J. *Disorientation Effects of Epitaxy at Aqueous Media.* Mat. Str., **(1999)**, 6, 2, 155-158.

13. Paul, G. L.; and Pryor, A. W. *Study of Sodium-Nitrate by Neutron Diffraction.* Acta Cryst. B, **(1972)**, 28, 15, 2700-2702.

14. Rode, S.; Oyabu, N.; Kobayashi, K.; Yamada, H. and Kuehnle, A. *True Atomic-Resolution Imaging of (10(1)$\bar{4}$) Calcite in Aqueous Solution by Frequency Modulation Atomic Force Microscopy.* Langmuir, **(2009)**, 25, 5, 2850-2853.

15. Benages-Vilau, R.; Calvet, T.; Cuevas-Diarte, M. A. and Aquilano, D. *The Theoretical Morphology of Nitratine ($NaNO_3$)***,** (in preparation).

16. Horcas, I.; Fernandez, R.; Gomez-Rodriguez, J. M.; Colchero, J.; Gomez-Herrero, J. and Baro, A. M. *WSXM: A Software for Scanning Probe Microscopy and a Tool for Nanotechnology.* Rev. Sci. Instrum., **(2007)**, 78, 1, 013705.

17. Xu, T.; and Pruess, K. *Thermophysical Properties of Sodium Nitrate and Sodium Chloride Solutions and their Effects on Fluid Flow in Unsaturated Media,* **(2001)**. E. O. Lawrence Berkeley National Laboratory, Berkeley, CA (US).

18. Pina, C. M.; Pimentel, C. and Garcia-Merino, M. *High Resolution Imaging of the Dolomite (104) Cleavage Surface by Atomic Force Microscopy.* Surf. Sci., **(2010)**, 604, 21-22, 1877-1881.

19. Luthi, R.; Meyer, E.; Haefke, H.; Howald, L.; Gutmannsbauer, W.; Guggisberg, M.; Bammerlin, M. and Guntherodt, H. J. *Nanotribology - an UHV-SFM Study on Thin-Films of C-60 and AGBR.* Surf. Sci., **(1995)**, 338, 1-3, 247-260.

20. Luthi, R.; Meyer, E.; Haefke, H.; Howald, L.; Gutmannsbauer, W. and Guntherodt, H. J. *Sled-Type Motion on the Nanometer-Scale - Determination of Dissipation and Cohesive Energies of C-60.* Science**, (1994)**, 266, 5193, 1979-1981.

# CHAPTER 6

## SOLID STATE MISCIBILITY: THE $NaNO_3$-$KNO_3$ PHASE DIAGRAM

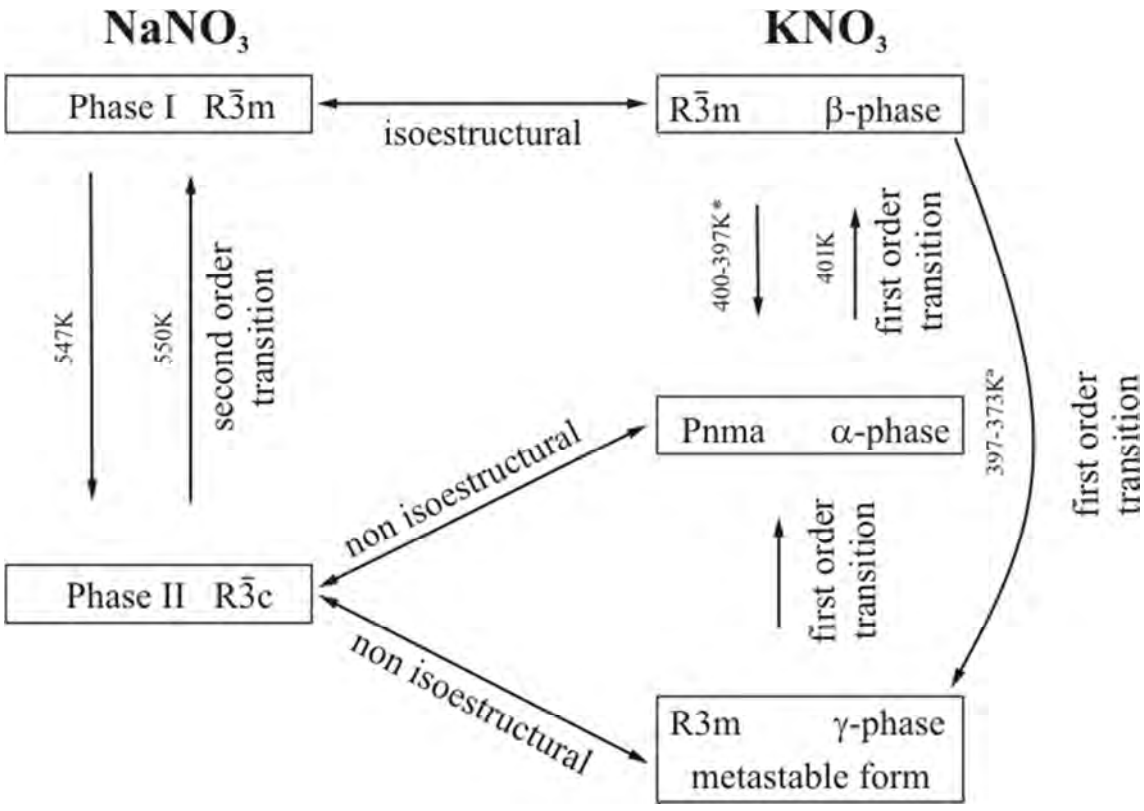

## 6.1. INTRODUCTION

Both solid state miscibility and the $NaNO_3$-$KNO_3$ phase diagram have been studied for over a century. According to Berg and Kerridge,[1] the first paper was published in 1857. In 1970 Voskresenkaya et al.[2] compiled a handbook containing 21 papers published between 1884 and 1955 relating to phase diagram determination. In these papers, two phase diagram proposals are of particular relevance: that of eutectic behaviour and the melting point minimum. In the older papers reviewed a eutectic system is proposed, followed by a continuous solid solution in more recent literature,[1] while in the most recent publications the notion of eutectic behaviour becomes prevalent again.[1, 3-5] Thus, for more than 150 years the question has remained unanswered: is the phase diagram described by eutectic behaviour or a melting point minimum? Eutectic behaviour implies a gap of miscibility, while a melting point minimum implies total solid miscibility within a certain temperature range. The process of phase diagram determination poses significant experimental difficulties and the solid state region has been only partially studied –a complete thermodynamic explanation for the whole diagram has yet to be published– which explains the lack of conclusive evidence on the topic. Various thermodynamic inconsistencies have been described in several papers from the perspective of equilibrium, which include metastable phases[6] or the influence of the first and second order transition.[7, 8] Nevertheless, pure components and mixed samples of this system have been used as a test material for a high-temperature reaction calorimeter,[9] the thermomicroscopy/DSC stage,[10] and also to test a new encapsulation technique.[4]

A strong understanding of pure compounds is vital for phase diagram determination. The study of polymorphism in alkali nitrates has received substantial attention over the years, of which an extensive summary is provided by Rao et al.[11, 12] An important consideration is the main polymorphic characteristics of $NaNO_3$ and $KNO_3$. They are described briefly in next paragraphs.

Sodium nitrate has two polymorphic forms and both are trigonal. The low temperature form (phase II-$NaNO_3$) crystallizes in the $R\bar{3}c$ space group with 6 formula units per cell. The structure consists in alternating layers of sodium ions and nitrate groups, the latter of which differ in orientation by 60º.[13] II-$NaNO_3$ has a known stability temperature range between 100 K and 550 K. The high temperature form (phase

I-$NaNO_3$) crystallizes in the $R\bar{3}m$ space group with 3 formula units per cell. Its structure is also formed by alternating layers of nitrate groups and sodium ions, but in this case nitrate ions display rotational disorder. I-$NaNO_3$ is stable until melting point (581 K).
The transition between them is a second order (order-disorder) transition[14] and some authors propose an extension of more or less 100 K**.** It is the $NO_3$ anion that changes from a static position to a rotational disorder through the transition, hence all nitrate planes become equivalent and the cell loses the **c** glide plane. Fermor and Kjekshus[15] produced a detailed report on the electric properties of $NaNO_3$ and proposed that the second order transition begins at a temperature of 433 K because the apparent energy gap changes at this temperature. Since sodium nitrate is a compound obtainable in a state of high purity, which has an extended gradual transition, it has been regarded as a particularly suitable system for testing certain theories and relations proposed for higher order transitions.[16] In this sense it has been investigated using calorimetric techniques, though these are unable to provide any structural information. X-Ray diffraction is the best technique to examine this gradual transition, as was performed for $NaNO_3$ and $CaCO_3$ by Antao et al.,[17, 18] Ballirano,[19] and Harris.[20]
At atmospheric pressure, $KNO_3$ exists in three different forms as a function of temperature.[21] During heating, a solid-solid transition takes place at 401 K, from a Pmcn (equivalent to Pnma space group) orthorhombic structure (named $\alpha$-$KNO_3$) with two unit formulas per cell, to a trigonal structure ($R\bar{3}m$, named $\beta$-$KNO_3$) with three formula units per cell. As the high temperature form has an $NO_3$ rotational disorder, this transition can also be considered order-disorder, while in contrast to $NaNO_3$, $KNO_3$ transition is a first order transition. Adiwidjaja and Pohl[22] recently reported that $\alpha$-$KNO_3$ is better described as a superstructure with the $Cmc2_1$ space group (which is a subgroup of the Pmcn space group generally accepted in literature). Upon cooling, the $\beta$-$KNO_3$ phase transforms into another trigonal phase (R3m, named $\gamma$-$KNO_3$) somewhere between 397 K and 373 K, before reverting back to $\alpha$-$KNO_3$. However, Asadov et al.[23] claimed that the $\alpha$-$KNO_3 \rightarrow \beta$-$KNO_3$ transition is reversible when working in a temperature range between 400 K and 397 K. Moreover, Fermor and Kjekshus[24] claimed to have found another phase at temperatures below 213 K but unfortunately could not determinate the space group. As a function of pressure, potassium nitrate has seven polymorphic forms.[25]

In α-$KNO_3$, the stacking sequence is ABCABC…, where A is a K layer and B and C are $NO_3$ layers. Obviously in order to maintain electroneutrality, the number of $NO_3$ groups in each layer is half that of K ions in each layer. In contrast for β-$KNO_3$ the stacking of $NO_3$ and K layers is similar to that of I-$NaNO_3$.[26]

Finally, in the γ-$KNO_3$ phase the stacking is similar to that of the β-$KNO_3$ phase, but in this case the $NO_3$ groups are not located half way between the K layers, and are not coplanar i.e. the four atoms in $NO_3$ do not lie in the same plane. This explains the dipole moment and ferroelectricity displayed by this phase, justifying why it has been studied in so much detail. When crystals are cooled from temperatures above 453 K, γ-$KNO_3$ always appears, but it does not appear when crystals are heated from the α-phase.[27] Nimmo and Lucas[21] found that the γ-$KNO_3$ phase could be cooled to room temperature and remain stable for approximately 30 minutes. Indeed, the stability of the γ-$KNO_3$ phase depends on the preparation, particle size, thermal history, impurities in the sample,[28] and the cooling rate.[29] Additionally hydrostatic stress may be responsible for the extended γ-$KNO_3$ phase stability in small particles.[30] Some attempts to stabilize γ-phase at room temperature have been reported in the literature. [30-34] Fermor and Kjekshus[35] highlight that when $KNO_3$ is heated at 473 K it recrystallizes, increasing the complexity of the γ-$KNO_3$→α-$KNO_3$ transition on cooling.

Knowing the polymorphism of both $NaNO_3$ and $KNO_3$ could they be considered as isomorphous? Two requirements are necessary, but not sufficient, for a solid solution formation between two compounds, A and B. Firstly, their space group must be the same and secondly, the atomic radii difference should be less than 10 – 15 %.[36] Within the 6 possible combinations for the structure of the $NaNO_3$-$KNO_3$ system there is only one that fits the first rule of having the same space group; β-$KNO_3$ (**a** = 5.425(1) Å, **c** = 9.836(4) Å at 424 K[26]) and I-$NaNO_3$ (**a** = 5.0889(5) Å, **c** = 8.868(3) Å at 563 K[14]) have the same $R\bar{3}m$ space group. Despite Na and K atomic radii difference is approximately 26 %, we can find a total solid state miscibility in another system. This is provided by the NaCl-KCl system at high temperatures.[37] As Oonk[38] has demonstrated with a series of alkali halides phase diagrams, the substitution of Na by K and vice versa also depends on the anion volume. Therefore, a complete series of solid solutions at high temperatures in the $NaNO_3$-$KNO_3$ system is possible. Whether a γ-$KNO_3$ based solid solution can be formed remains to be answered, and to do so, the

problem of the space group must be addressed. Stromme[39] reported that the structure of γ-$KNO_3$ is not substantially different to that of β-$KNO_3$ and some years later Nimmo and Lucas[21] stated that γ-$KNO_3$ is a simple modification of β-$KNO_3$. Consequently one might expect a degree of miscibility between I-$NaNO_3$ and γ-$KNO_3$. Furthermore, the introduction of sodium into the γ-$KNO_3$ structure can, in certain ways, stabilize this hypothetical γ-$KNO_3$ solid solution type. There are some evidences of its metastability in the literature. Working with $Na_{0.05}K_{0.95}NO_3$, Shimada and Aoki[28] established that the γ-phase is observed at 293 K for approximately 6.5 hours. Additionally, Baryshnikov[34] stated that for the $Na_{0.10}K_{0.90}NO_3$ composition the γ-$KNO_3$ → α-$KNO_3$ is completed well below room temperature. Xu and Chen[40] pointed out that a period of 2 days was required to detect the α-$KNO_3$ phase for a $Na_{0.8}K_{0.2}NO_3$. In a recent study, Ping et al.[5] demonstrated the differences in second heating solid-solid transition as a function of the previous cooling rate i.e. the amount of solid that overtook γ-$KNO_3$ → α-$KNO_3$ varied with time.

As mentioned earlier, the literature available on determining the phase diagram of $NaNO_3$-$KNO_3$ is vast. From all the papers reviewed, the preferred technique is thermal analysis (DSC when it becomes available)[4, 6, 7, 41-46]. For the phase diagram determination some authors used the second heating run data[4, 6, 42, 43] as it was consistent with a third heating run, as evidence that the system has arrived at equilibrium. Nevertheless metastable γ-$KNO_3$ plays a fundamental role in the diagram because it is always formed upon cooling,[21, 47-49] but the transition from γ-$KNO_3$ to α-$KNO_3$ depends on many factors as we have already highlighted. It is possible, that researchers were actually measuring γ-$KNO_3$ solid solution type. As anyone checked crystal data before thermal analyses were carried out we can assume that these experiences were out of equilibrium. Before the process of thermal analysis was developed, some authors carried out chemical analyses of the solid and the liquid fractions in the mushy zone in order to determine solidus and liquidus lines, respectively.[50-53] Kofler[54] published a microthermal analysis and stated that it was very difficult to differentiate between the two components.

Only four researchers have studied solid state using XRD to address the problem discussed here. Kramer and Wilson[41] found rhombohedral $NaNO_3$ and orthorhombic $KNO_3$ patterns when quenching from both above and below the liquidus line i.e.

immiscibility at room temperature. They suggested that 'high temperature X-ray diffraction is necessary to observe the solid solution. One year later Kamimoto[42] worked with the equimolar composition using XRD at 473 K. It was reported that he found a different XRD pattern and, in his opinion, a solid solution was consequently formed. Nonetheless he only gave stick patterns, which are difficult to interpret in this case. He also observed the presence of γ-$KNO_3$ upon cooling and although he did not recognize it as such, but he pointed out that the sample was not in a thermodynamically stable state. Abe et al.[44] only observed immiscibility at room temperature. Furthermore, in their recent study[46], Zhang et al. measured XRD of an equimolar mixture at 473 K and found a mixture of β-$KNO_3$ and I-$NaNO_3$ patterns. Additionally, Xu and Chen[40] argued that XRD would give a structure with a level of symmetry that is higher than that measured by spectroscopic techniques in disordered systems.

In some papers, a calculated phase diagram was proposed. Results show that both options, eutectic[4, 46] or a minimum melting point[8, 45], can be justified. Dessureault et al.[8] carried out a review of more than 30 papers in 1990 and carried out a statistical analysis of the thermodynamic data presented within the papers. They also constructed a thermodynamic model for the entire diagram, predicting a melting point minimum.

Another technique widely used in recent years is the Raman spectroscopy and all researchers[1, 3, 40, 55] that used it concluded that the $NaNO_3$-$KNO_3$ phase diagram shows eutectic behaviour.

Mechanical characterization was also used in this system[56] and Eweka tried to address the problem with electrical measurements throughout the melting process[57, 58].

The aim of the present chapter is to univocally determine the $NaNO_3$-$KNO_3$ equilibrium phase diagram and to demonstrate whether a complete solid state miscibility at high temperature (only compatible with a melting point minimum) is possible – a question that has remained unanswered for over 150 years.

Our group boasts extensive experience in polymorphism[59-62] and phase diagram determination[63, 64] and our publications show the importance of using complementary techniques to effectively establish the stability regions within a binary system.

It is clear that the $NaNO_3$-$KNO_3$ system presents real experimental difficulties due to metastability and transition kinetics. Taking this into account our proposal is to solve the unanswered questions surrounding this binary system.

## 6.2. MATERIALS AND METHODS

Samples of $NaNO_3$ and $KNO_3$ with a high purity (99 % or higher) were purchased from Quality Chemicals. The purity of these nitrates was checked with ICP-OES, revealing the major impurities in $NaNO_3$ and $KNO_3$, to be K and Na, respectively. Further purification was therefore not carried out. Water content in pure compounds was checked by thermogravimetry (being less than 0. 3 %).

Samples of 1 gram of selected compositions (in total there were 17 different samples, including pure compounds) were weighed in the correct molar proportions with an accuracy of 1 milligram. They were melted and quenched in liquid nitrogen, then ground and stored at room temperature.

Thermal analyses were performed with a Perkin Elmer DSC-7. Samples were sealed in 50 μL 2 bars aluminium pans, and a scan rate of 10 K/min was used. With the exception of several samples only two independent runs were carried out for each sample. The DSC-7 was calibrated against indium and n-decane standards. From the DSC curves the characteristic temperatures were determined by the shape factor method[65] and enthalpy effects were evaluated by integration of the DSC signals.

Powder diffraction data was recorded with a Panalytical X'pert Pro diffractometer at room temperature with Bragg-Brentano geometry (θ - 2θ). The pattern was acquired over a period of 39 minutes within a range 4º to 100º (2θ) using Cu $K_{\alpha 1}$ radiation (λ = 1.5405 Å). Samples were mounted on a flat automatic sample charger. A spin rotation of 2 rev/min was selected to minimize sample orientation. The diffractometer was equipped with a hybrid monochromator and an X'Celerator Detector. Temperature dependent X-ray diffraction was recorded with the same geometry for all compositions using an Anton Paar HTK-1200N Oven. Acquisition temperatures were set at 301-323-373-393-403-413-473-493-523-553-563-573-583-593 K for a period of 2 h at each temperature. Stabilization time at each temperature was 5 min except at 393 K, which was 15 min. Additionally, the heating rate of 10 K/min and the maximum temperature depended on the sample melting point.

For selected compositions, in order to achieve equilibrium at high temperatures, annealing at various temperatures was carried out for up to 7 days in the FURCAP

device from INEL, which enables capillary samples to be heated from room temperature to 623 K. A powder pattern was collected after every two hours of exposure. In this case diffraction patterns were recorded in a horizontally mounted 120º and 25 cm of radius curved position sensitive detector INEL CPS-120 in transmission geometry. The detector was used in its 4,096 channels resolution mode. Samples were placed in 0.5 mm. diameter glass Lindemann capillaries. Cu $K\alpha_1$ radiation was selected by means of a Ge (111) primary flat monochromator. A parabolic multiplayer mirror 'OSMIC Gutman optics # 13B-413' was placed between the tube and the monochromator. $Na_2Ca_3Al_2F_{14}$ (NAC) was used as an external standard to calibrate the detector and convert the channels to $2\theta$ values. The data was linearized to a constant step size of 0.029º in $2\theta$ by means of a cubic spline function. Calibration and linearization were performed with the PEAKOC application from DIFFRACTINEL software.
The Materials Studio software was used for cell parameter determination in some powder patterns[(66)], while peak intensity and peak wideness were determined using the WinplotR software.

Raman spectroscopy was carried out at room temperature with the Jobin Yvon T64000 Raman spectrometer. The liquid nitrogen cooled CCD detector was calibrated against $TiO_2$ and nominal laser power was 400 mW with a 514 nm wavelength. Five measurements of ten seconds each were performed from 24 to 1700 $cm^{-1}$. Peak position and peak intensity were measured with Origin Software.

For hot stage microscopic measurements, a Linkam THMSG-600 stage mounted to a Nikon Eclipse 50iPol Microscope was used. The sample was placed on a 7 mm quartz cover slip, and encased within a pure silver lid so that it was heated from all sides, ensuring a uniform temperature. An LNP liquid nitrogen cooling system and a TMS94 temperature controller were used. Images were captured with a digital camera. In order to visualize phase transition and the solidus line (on heating runs) a thin film was required. To obtain this the sample was placed on a glass cover slip, heated above its melting point and then covered with another glass cover slip to obtain the thin film. The system was left for approximately 1 minute in the liquid state and was then finally cooled to room temperature at 100 K/min.

## 6.3. RESULTS

Nitrates are highly corrosive salts –demonstrated by the Ellingham diagrams[67]– therefore the capsule selection in the DSC analyses is an important procedure. Decomposition products (mainly $NO_2$)[68-71] can react with aluminium, gold and platinum, particularly at high temperatures or during periods of prolonged exposure. For example, Roger and Janz[43] used platinum capsules for a thermal analysis. Carling[72] experimented with aluminium and gold sealed capsules below 800 K and Iwadate et al.[73] tested specific heat below 700 K with Au and Al open pans. Furthermore, at 700 K Marangonni effect has been described in the literature[43], i.e. liquid movement to achieve surface equilibrium. We carried out a number of experiments to determine the most effective configuration, which was 2 bar aluminium capsules with a sample weight of between 4.4 and 4.8 mg and a heating rate of 10 K/min and the upper temperature was approximately 10 K higher than the liquidus line for each composition. Some experiments were performed with aluminium capsules with holes.

The experimental section has been divided into three parts to explain the proposed phase diagram. Firstly, the thermal analyses are described to assess phase transition boundaries and to compare our findings with information gathered from the literature review. Secondly, we sought to determine the solid state miscibility and lastly, we propose a thermodynamic model.

The DSC analyses were performed to determine the stability limits of the different forms, the temperatures of solid-solid transition, the solidus and liquidus curves and the enthalpies concerned.

### 6.3.1. Solid-liquid equilibrium.

DSC measurements were reproducible in temperature and enthalpy values. This chapter was not focused on calorimetric data but on determining melting behaviour and in doing so provide an accurate thermodynamic assessment of the $NaNO_3$ and $KNO_3$ phase diagram. Thus Table 1 only shows typical values from the results of the DCS analyses. When observing $T_{solidus}$ a eutectic phase diagram seemed the most likely solution due to the line flatness throughout the compositions. However, as was pointed out by Kramer and Wilson,[41] the DSC melting signal is not characteristic of eutectic systems. Therefore nothing can be concluded using only DSC results. Enthalpy

measurements can be approximated with a quadratic equation; the minimum lies at a composition 82 % $KNO_3$ while the maximum excess enthalpy is approximately 2000 J/mol.

**Table 1.** Results for temperatures and enthalpies of phase transitions for the $NaNO_3$-$KNO_3$ system.

| | Solid-solid transition | | | | | Solid-liquid transition | | | |
|---|---|---|---|---|---|---|---|---|---|
| Composition (%mol $KNO_3$) | $T_{\alpha\rightarrow\beta}$ (K) | $T_{end\ (II\rightarrow I)}$ (K) | $T_{eutectoid}$ (K) | $T_{(end\ eutectoid)}$ (K) | $\Delta H_{s-s}$ (J/mol) | $T_{melting}$ (K) | $T_{solidus}$ (K) | $T_{liquidus}$ (K) | $\Delta H_{s-l}$ (J/mol) |
| 0 | | 544 | | | | 581 | | | 15435 |
| 10 | | | 394 | 398 | 410 | | 494 | 567 | 13433 |
| 20 | | | 395 | 397 | 930 | | 494 | 545 | 12561 |
| 30 | | | 394 | 395 | 1699 | | 495 | 535 | 10926 |
| 40 | | | 392 | 402 | 2180 | | 494 | 503 | 10223 |
| 50 | | | 396 | 399 | 2616 | | 492 | 492 | 10009 |
| 60 | | | 390 | 398 | 3192 | | 495 | 505 | 9473 |
| 70 | | | 389 | 398 | 3743 | | 495 | 530 | 9954 |
| 80 | | | 390 | 400 | 4105 | | 494 | 554 | 9233 |
| 90 | | | 391 | 399 | 4634 | | 495 | 586 | 10308 |
| 100 | 404 | | | | 5164 | 610 | | | 9498 |

### 6.3.2. Solid-solid equilibrium.

Several DSC cycles were carried out in each sample. Compositions (with a 10 % gap) were cycled 2 times (using aluminium capsules with holes). In the first heating run we observed a solid-solid transition for all compositions at approximately 393 K, which can be assigned to the $\alpha$-$KNO_3$ → $\beta$-$KNO_3$ transition type. For the second heating run the solid-solid transition was only observed in certain compositions, which may have some relation to the $\gamma$-$KNO_3$ phase influence. To ascertain whether this was the case, some samples were re-cycled with a time gap between either weeks or months to test the solid-solid transition evolution. As expected, significant differences were observed. Baryshnikov demonstrated that while in the first run, II-$NaNO_3$ and $\beta$-$KNO_3$ coexist, in the second heating run only the $\gamma$-$KNO_3$ solid solution type seems to be present,[34] which is consistent with the results of our DSC stability experiments. Thus we can conclude here that only the first heating run started from stable phases at room

temperature, for which data is shown in Table 1. Furthermore, the second order transition was only observed for high sodium nitrate content. This transition and the melting signal were overlapped in some compositions.

X-ray diffraction analyses were carried out at room temperature to assess crystal phases. Diffractograms were indexed as α-$KNO_3$ and II-$NaNO_3$, except for the extreme compositions (1 % $KNO_3$ and 99 % $KNO_3$) in which only pure components are observed. In this case X-ray diffraction revealed somewhat wider and less defined peaks. Minor component peak intensities for these compositions, if any, may be very close to the detection limit of XRD so they cannot be resolved from background. Furthermore, for compositions from 1$KNO_3$ to 20$KNO_3$ a weak reflection at 27.10º was visible, which can be assigned to the γ-$KNO_3$ phase. According to Westhphal,[30, 74] γ-$KNO_3$ → α-$KNO_3$ can be considered as a cooperative phase transition, which explains that when the mass fraction is small this transition is slower because each γ-$KNO_3$ particle have to nucleate its own path for phase transition. Therefore, part of the γ-$KNO_3$ phase can be retained as the result of a kinetic effect.

The narrow miscibility range at room temperature was confirmed by macro Raman measurements of 19 samples, including pure compounds. Figure 1 shows the most important band positions and intensities (N-O stretching mode $\nu_1$ at 1068 $cm^{-1}$ and at 1049 $cm^{-1}$ for $NaNO_3$ and $KNO_3$, respectively).[75] Intensity values are almost linear with composition, and the position of bands does not change within experimental error. If sodium and potassium nitrate are miscible at room temperature their range must be below 1 % (of the other components), which is echoed by Hissink[51] who stated that miscibility at room temperature was about 0.5 %.

According to miscibility rules previously described, $NaNO_3$ and $KNO_3$ cannot form a solid solution at low temperature because they have different crystal structures, different space groups, different cell parameters, and their cation volume difference is too high. Nevertheless, some authors report solubility as high as 10 % $KNO_3$ in $NaNO_3$.[8]

The results of the DSC analyses revealed a solid-solid transition throughout the phase diagram at an almost constant temperature of 393 K. It was therefore likely that a eutectoid invariant was present, which was confirmed by the results of the powder X-ray diffraction and macro Raman analyses. The eutectoid can be interpreted as the influence of the first order transition of the $KNO_3$ in the mixed samples. When a

composition versus enthalpy plot for the solid-solid transition is represented, a linear relationship is observed, indicating that the heat process is only dependent upon the quantity of $KNO_3$ in the mixed sample.

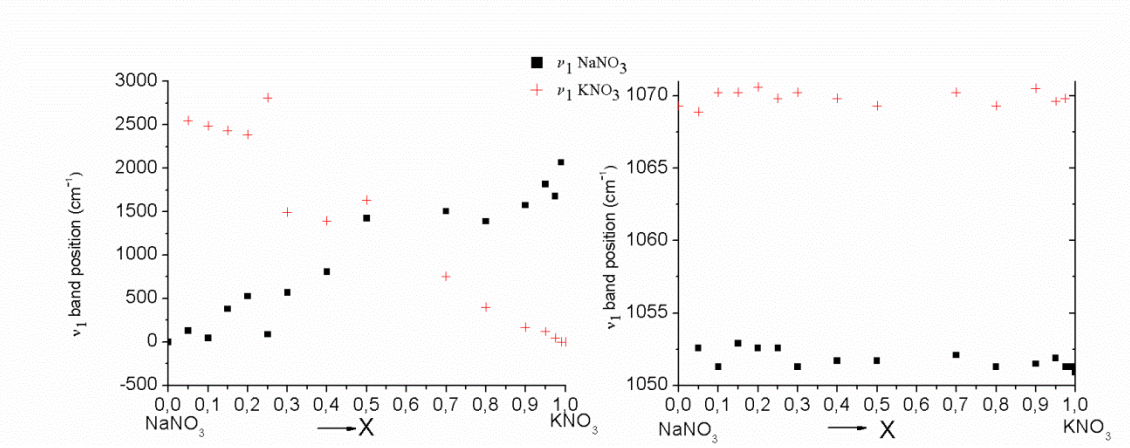


**Figure 1.** Stretching ($\nu_1$) Raman band intensities (left) and position (right) for $NaNO_3$ (black squares) and $KNO_3$ (red crosses).

Although this binary system has been studied for a long time, very few researchers have crystallographically characterized mixed samples. From those who used X-ray diffraction at high temperatures, a contradiction is observed even when working with the same composition and temperature (equimolar composition at 473 K). While Kamimoto[42] found a different diffraction pattern and thus confirmed the existence of a solid solution, Zhang[46] showed the coexistence of β-$KNO_3$ and I-$NaNO_3$ patterns, confirming the existence of eutectic behaviour. Our X-ray diffraction results from 301 K to liquid are shown in Figure 2 for the equimolar composition. Here we observe that from room temperature to 373 K, α-$KNO_3$ and II-$NaNO_3$ phases coexist. At 393 K a phase change takes place, confirming the existence of a eutectoid invariant in accordance with the DSC data. Following this, between 393 K and 473 K those peaks that can be assigned to the β-$KNO_3$ solid solution are not well developed (some are marked with an arrow). This is a general trend throughout the phase diagram indicating that the system is out of equilibrium. Therefore, annealing for selected compositions was performed at different temperatures and times in order to reach the equilibrium state. Finally, it is important to indicate the discovery of a completely developed new phase at 483 K, meaning that our results are consistent with those of Kamimoto.[42] In fact II-$NaNO_3$ diffraction peaks disappeared at 473 K but the sample had not completed

the transition to a unique phase. If we compare diffraction at 473 K and 483 K we observe that only some peaks (encircled in Figure 2) persist while others disappear. Consequently, careful X-ray diffraction has to be performed to discern between a melting point minimum and a eutectic phase diagram.

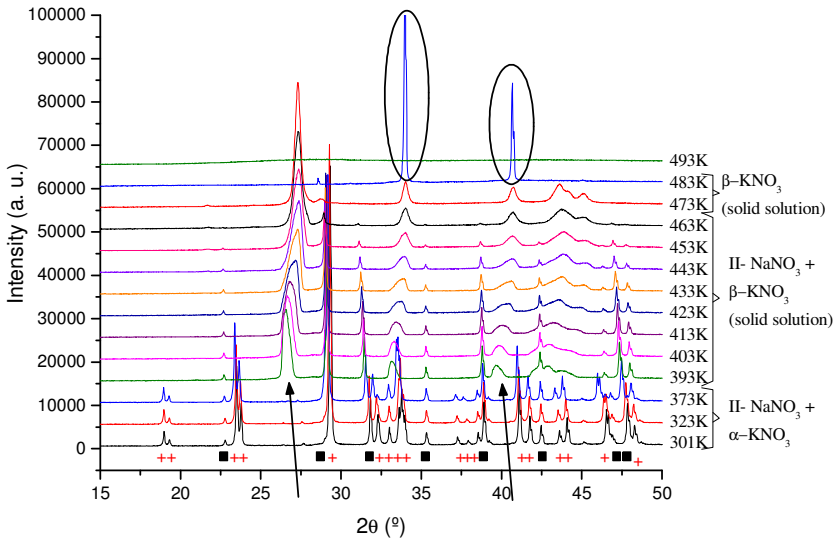


**Figure 2.** Powder X-ray diffraction as a function of temperature for the equimolar composition. Between temperatures of 301K and 373 K, II-$NaNO_3$ (black squares) and α-$KNO_3$ (red crosses) coexist. At 393 K new peaks appear: arrows point to the α-$KNO_3$ → β-$KNO_3$ transition. Encircled peaks indicate the new phase, which appears at 483 K.

The compositions selected were $5KNO_3$, $20KNO_3$, $40KNO_3$, $50KNO_3$, $70KNO_3$ and $90KNO_3$. The annealing temperatures used were 403, 433, 453 and 483 K, and the annealing time was set for up to 168 hours (7 days). The equilibrium is achieved when no further change in the XRD pattern is observed i.e. when peak wideness and intensity are constant. This process can be followed through integral breath evolution. The results for one reflection of β-solid solution type and another of I-$NaNO_3$ solid solution type as a function of time for $20KNO_3$ at 483 K are shown in Figure 3. This demonstrates the importance of annealing time in achieving equilibrium. It can be seen that the integral breath for both reflections decreases and then reaches an almost constant value after approximately 80 hours of annealing. The same results were obtained for intensity. Although the aim of this research was not to calculate the grain size or the sample strain with these measurements, we estimate that they are likely to be highly strained and/or very small size immediately after transition takes place.

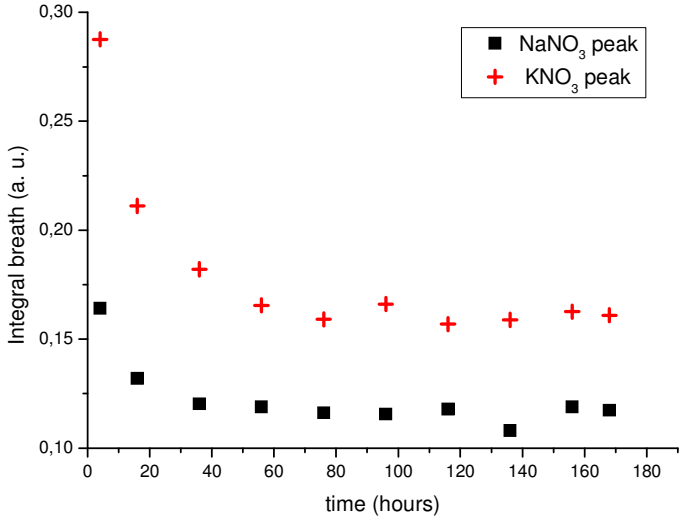


**Figure 3.** Integral breath of diffraction peaks as a function of annealing time for $20KNO_3$ at 483 K. Figure shows II-$NaNO_3$ (black squares) and α-$KNO_3$ (red crosses).

The next section of results relates to that of isothermal measurements for different compositions at the temperatures studied: 403, 433, 453 and 483 K. All the samples (except pure components) were kept for 48 h at the relevant temperature.

As Figure 4a shows, although the equilibrium state was not achieved after being kept for 48h at a temperature of 403 K, a β-$KNO_3$ pattern type was observed and the reflections were displaced to values higher than 2θ, indicating a smaller cell size which would be the result of the introduction of sodium cations into the structure. Thus a new phase appeared (as stated above), which was named β-solid solution because it has the same space group as β-$KNO_3$, $R\bar{3}m$. In contrast, the II-$NaNO_3$ pattern hardly changed, meaning that a significant amount of potassium did not enter the $R\bar{3}c$ structure of $NaNO_3$.

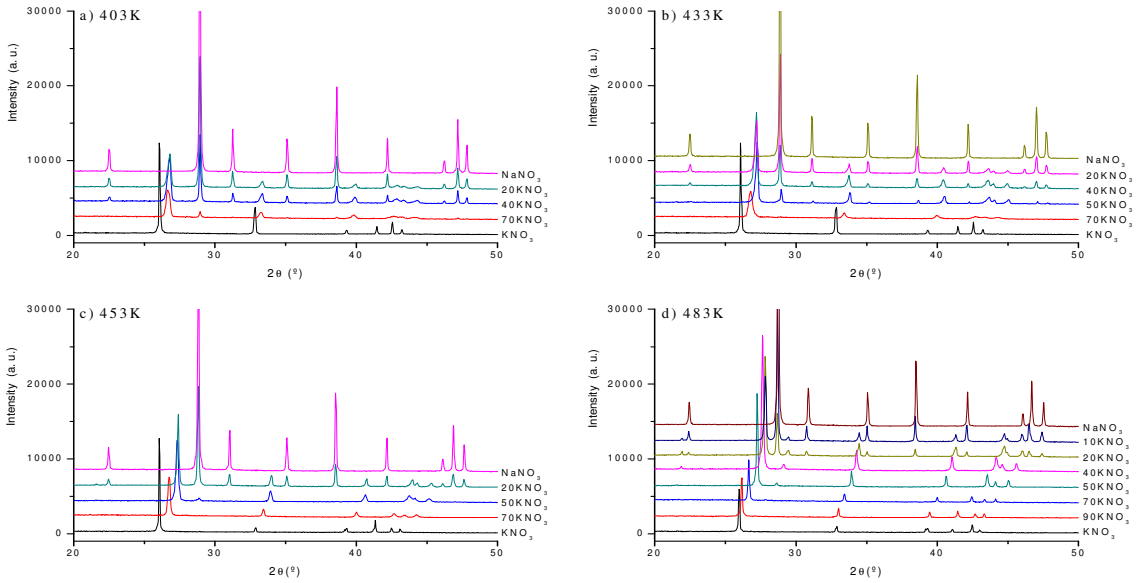


**Figure 4.** X-ray powder patterns as a function of the composition after 48 hours of annealing at: a) 403 K; b) 433 K; c) 453 K and d) 483 K.

At 433K, for $70KNO_3$ composition, only β-solid solution structure appeared (Figure 4b). However, it was not completely formed because the diffraction peaks were still relatively wide. For the remaining compositions analyzed, the coexistence of β-solid solution and the II-$NaNO_3$ patterns were observed with a constant angle of 2θ, typical of an immiscibility zone.

When the equimolar composition was annealed at a temperature of 453 K (Figure 4c), the II-$NaNO_3$ pattern type almost disappeared with only a minor II-$NaNO_3$ 104 reflection remaining. This indicates an increasing presence of the β-solid solution as it incorporates more sodium into its structure. Moreover, for the $20KNO_3$ diffraction pattern, reflections due to II-$NaNO_3$ were slightly displaced to lower angle values (i.e. a larger unit cell) indicating that some potassium was incorporated into its structure. Furthermore, a weak reflection at 21.6º is present, which can be indexed as (101) for the new $R\bar{3}m$ phase.

At a temperature of 483 K (Figure 4d), the β-solid solution with the $R\bar{3}m$ space group was indexed in the region from pure potassium nitrate to a composition of $40KNO_3$. For higher sodium concentrations a mixture between the β-solid solution and the II-$NaNO_3$ solid solution was observed. The diffraction lines of the $R\bar{3}c$ (II-$NaNO_3$) phase are

displaced to lower angles, indicating a higher unit cell compatible with the introduction of potassium into its structure, as explained above. Second order transition is only defined when the II-$NaNO_3$ solid solution type to I-$NaNO_3$ solid solution type (which is structurally equivalent to the β-solid solution) takes place. Therefore, although the II-$NaNO_3$ solid solution type must exist, we were unable to isolate it even by performing similar ageing experiments for the $5KNO_3$ composition.

When a single solid solution is achieved at 483 K, its space group and cell parameters were determined with Materials Studio software.[66] Taking at least 8 reflections of apparently well separated peaks, the X-CELL indexing program[76] found the potential solutions of cell parameters and space groups. Those that best correspond to the experimental X-ray diffraction pattern were finally obtained using a Pawley profile-fitting procedure[77] available in the Powder Indexing module of Materials Studio. For $40KNO_3$, $50KNO_3$, $70KNO_3$ and $90KNO_3$ a solution with $R\bar{3}m$ symmetry was obtained. In all cases the agreement between experimental and simulated pattern expressed by the weighted R-factor (Rwp) was below 7%. Figure 5 shows the cell parameters (**a** and **c**) for these compositions together with pure $KNO_3$ and pure $NaNO_3$ (in this case the **c** parameter is halved). As shown, Vegard's law is obeyed until $40KNO_3$ i.e. in all single phase regions.

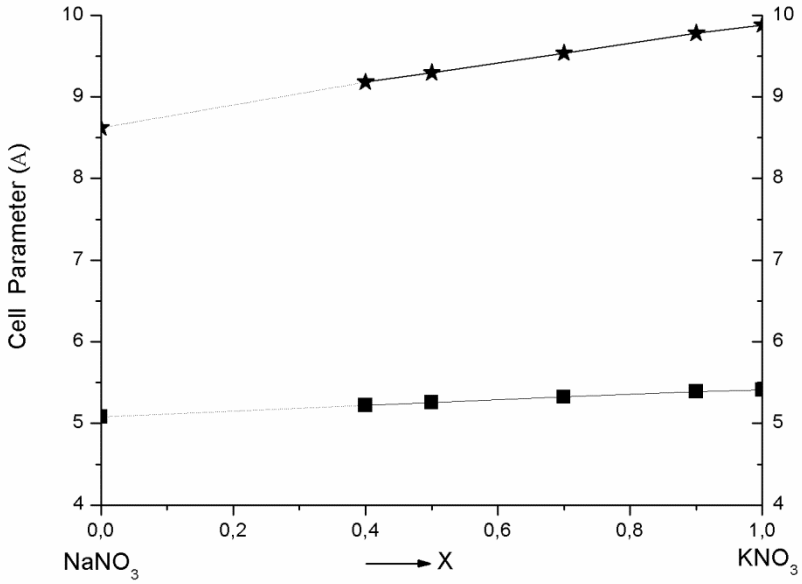


**Figure 5.** The evolution of cell parameters as a function of composition at 483 K. **a** square marks, **c** stars.

When annealing is performed at 493 K for 20$KNO_3$, composition peaks of II-$NaNO_3$ solid solution tend to disappear. Nevertheless 48 h was not enough time for completing the transition. Thus a single phase is also present in this composition but at higher temperatures.

An experimentally coherent phase diagram was developed using all experimental results and is shown in Figure 6. Below eutectoid we propose that the solubility of Na in α-$KNO_3$ is slightly higher than K in the II-$NaNO_3$ structure when they are kept at the same temperature. Both the II-$NaNO_3$ solid solution type and α-$KNO_3$ solid solution type have a narrow gap of existence with a maximum solubility at 393 K (eutectoid invariant) and 483 K, respectively. Above the eutectoid invariant we observed a very asymmetric immiscibility gap and a large domain of β-$KNO_3$ solid solution type, which is present throughout compositions for certain temperature ranges. The second order transition ends at the top of this immiscibility gap. Finally, solid-liquid biphasic equilibrium with a flat minimum at 495 K was observed.

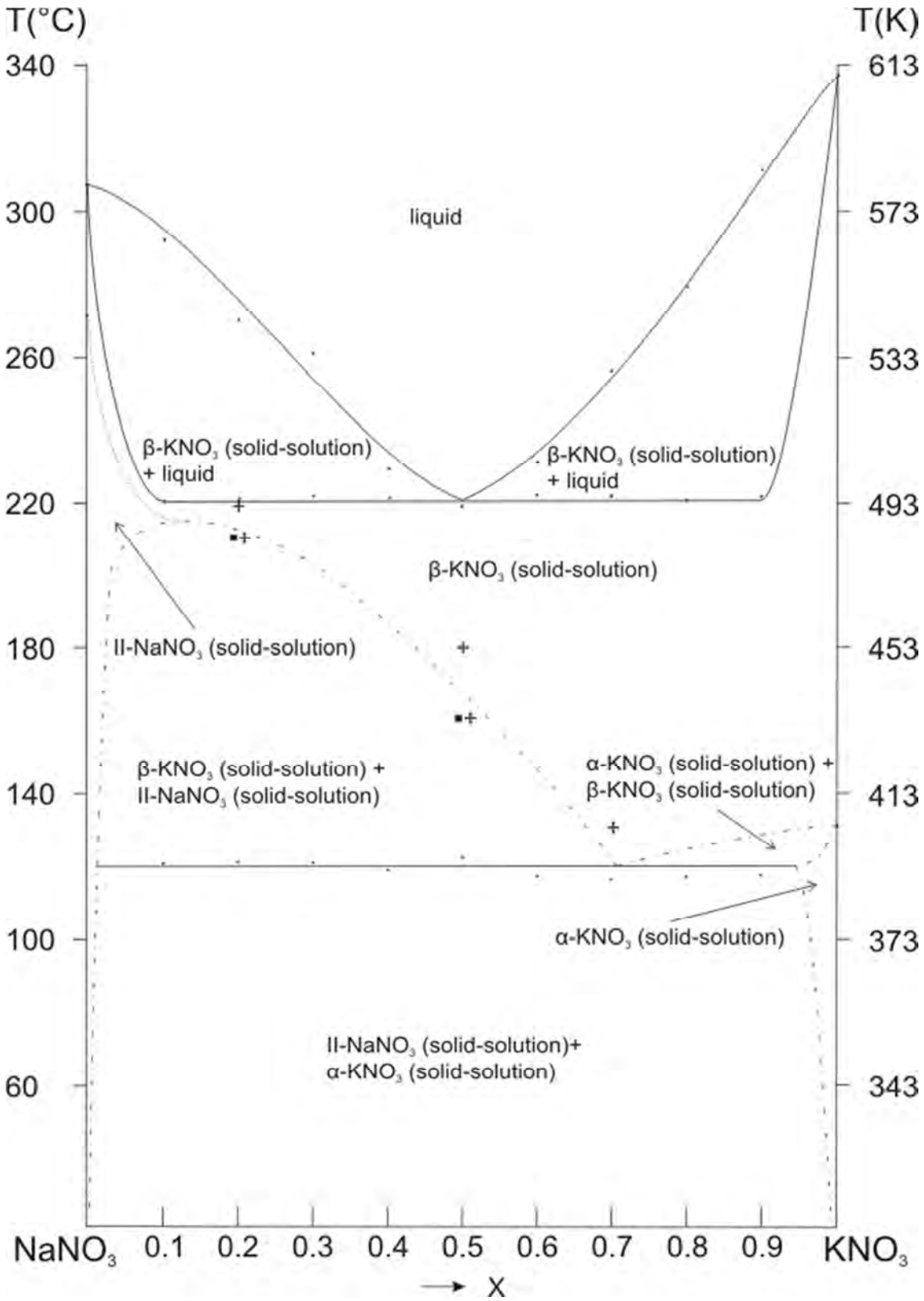


**Figure 6.** $NaNO_3$-$KNO_3$ phase diagram. Points: experimental DSC temperatures; stars: β-$KNO_3$ solid solution type; squares: II-$NaNO_3$ solid solution type. Experimental XRD points are only depicted in the vicinity of the solvus line.

Greiss et al.[6] proposed two solutions. The first one is derived from the DSC cooling data and the second from the DSC heating data. In our opinion neither of them accurately describes the equilibrium state. In the first proposition, γ-$KNO_3$ is included because cooling runs were used, and in the second proposition it is also included because they worked with the second heating runs and γ-$KNO_3$ is formed during cooling. Although they highlighted that discrepancies in the literature were caused by equilibrium achievement difficulties, no efforts were made to address the discrepancies. Furthermore, consistent with our observations, they proposed that the eutectoid reaction is kinetically hindered. However, they proposed an $R\bar{3}m$ solid solution at high temperature based on a previous study by Tamman and Ruppelt,[50] but rejected the existence of an $R\bar{3}c$ $NaNO_3$ solid solution type. In contrast, we have demonstrated the existence of both an $R\bar{3}m$ solid solution and $R\bar{3}c$ $NaNO_3$ solid solution type at high temperatures by means of temperature dependent X-ray diffraction.
The DSC analyses performed by Zamali and Jemal[7] revealed a eutectoid at 380 K, which is consistent with our invariant at 393 K. For the solid-liquid equilibrium they proposed a minimum at a temperature of 494 K for an equimolecular composition. Nevertheless, in our opinion, they mixed first and second order transition.

Using Raman spectroscopy as a function of temperature, Xu and Chen[40, 55] tested the phase diagram described by Greis et al.[6] and discovered three slightly different solid solutions at high temperatures: II-$NaNO_3$ solid solution type, β-$KNO_3$ solid solution type, and a new disordered state. They concluded that solid-liquid equilibrium with a minimum, as proposed by Greis et al., was inconsistent with their spectroscopic measurements. Thus a limited solid solution was preferred. Inconsistencies arise in the paper by Xu and Chen. They proposed that for intermediate compositions ($Na_{0.33}K_{0.67}NO_3$) pure components are formed upon cooling, whereas for terminal compositions they achieve solid solutions with the same heat treatment. This fact is only compatible with a high influence of transition kinetics and in this case the equilibrium state was not achieved. We have shown the existence of an $R\bar{3}m$ solid solution above 433 K for a similar composition ($Na_{0.30}K_{0.70}NO_3$), which is closely related to $KNO_3$ (Figure 4b). Its formation kinetics is quite slow and more than 48 h are required to reach the equilibrium state.
Using confocal Raman spectroscopy, Berg and Kerridge[1] recently demonstrated a eutectic microstructure of conglomerate type at room temperature; however, they did

not take into account the eutectoid invariant, thus it corresponds to a eutectoid microstructure, which is generally accepted. While heating an equimolar sample, they observed how the $\nu_1$ stretching mode of both $NaNO_3$ and $KNO_3$ were becoming progressively closer together but never became a single symmetric band. Unfortunately they did not take into account slow transition kinetics (homogenization time).

In hot stage microscopy only first order solid-solid transitions could be studied, i.e. those related to $KNO_3$. The $\alpha$-$\beta$ transition on heating and the $\beta$-$\gamma$ transition on cooling were not destructive. In contrast, the $\gamma$-$\alpha$ transition is totally destructive causing crystals to break into smaller pieces. Furthermore, since $\gamma$-phase is metastable at room temperature the transition time changes in different experiments and different compositions, as was described in the Introduction section. When temperature is above the eutectoid temperature (see below) all crystal phase boundaries move fast and tend to grow to achieve the minimum free energy in accordance with Tamman and Ruppelt work.[50]

As a summary, high temperature $\beta$ solid solution ($R\bar{3}m$) exists below the solidus line in all compositions and thus, melting behaviour is a minimum rather than a eutectic invariant. As expected, Na has a higher solubility in $KNO_3$ than K in $NaNO_3$. Nevertheless, $R\bar{3}c$ sodium nitrate based solid solution type is formed at approximately 453 K, slightly below the second order transition line in a narrow composition range. However, this was not observed directly. From our observation, it is likely that a demixing zone exists between the eutectoid invariant and the minimum solid-liquid domain. Below the eutectoid invariant reciprocal miscibility is very limited.

## 6.4. THERMODYNAMIC ASSESSMENT

Figure 7 is the phase diagram of the $NaNO_3$-$KNO_3$ system such as it follows from the experimental observations, and interpretation, by Tamman and Ruppelt.[50] This diagram is supported by the outcome of the resent investigation. At the $NaNO_3$ side, the diagram is incomplete an in particular the authors ignore the $NaNO_3$'s (second order) transition.

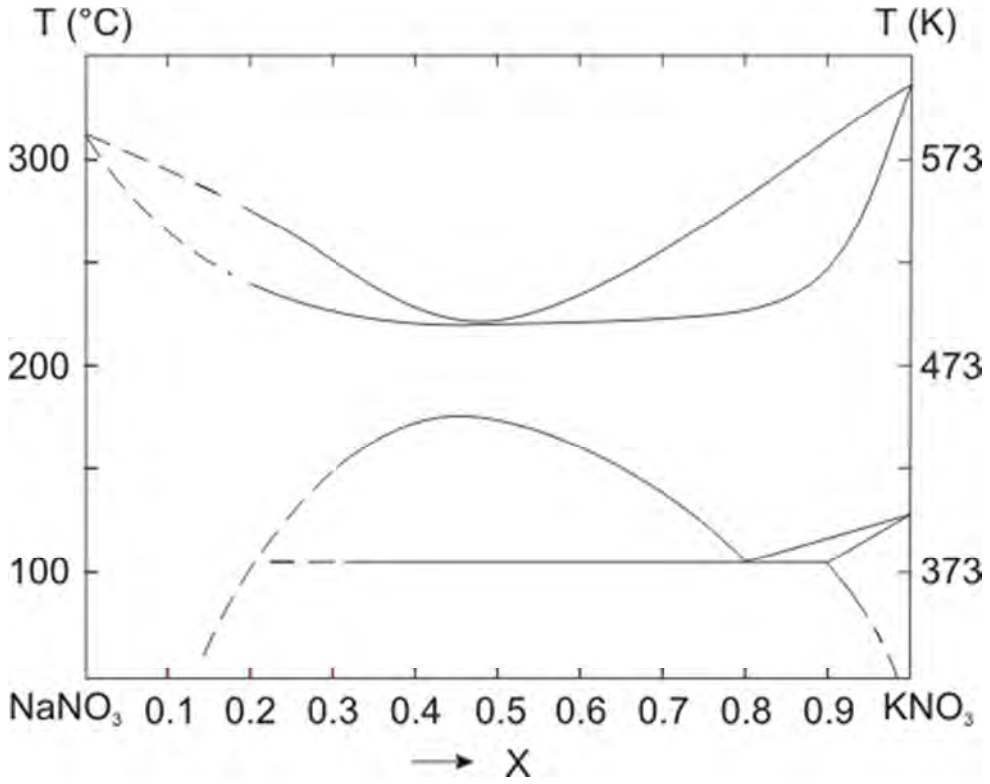


**Figure 7.** The $NaNO_3$-$KNO_3$ phase diagram as determined by Tamman and Ruppelt.[50]

The diagram, as it is, is evidence of complete subsolidus miscibility: the solid liquid equilibrium does not interferewith the miscibility gap. The minimum of the solid-liquid loop is about 494 K and at equimolar compositions. The critical point of (solid-state) mixing, the top of the miscibility gap, is at about 440K and between 40 - 50 mole % $KNO_3$.

The aim of the treatment presented in the following text is two-fold. On the one hand it aims yo explore to which extent the underlying system complies with the general characteristics found for mixed crystals. On the other hand it aims to assess to which extent the phase diagram, figure 7, is consistent with the thermochemical data that are available for the sustem itself.

To start with, and as regards the characteristics of mixed crystals, recent research has shown that their thermodynamic mixing properties are (surprisingly) well accounted by the ABθ model for the excess Gibss energy, see Oonk and references therein.[38]
In terms of the ABθ model the molar excess Gibbs energy, as a function of temperature and mole fraction of tne second component (here $KNO_3$) is given by the following expression:

$$G^E(T,X)=A\,X\,(1-X)\left(1-\frac{T}{\theta}\right)\left[1+B\,(1-2X)\right] \qquad \textbf{equation 1}$$

Where A, B, and θ are system – dependent parameters. The parameter A (in $J \cdot mol^{-1}$) represents the magnitude of the excess function; θ (in K) the function's dependence on temperature; and B (dimensionless) the asymmetry of the function. The form in X between the square brackets has the advantage tha the excess function of the equimolar mixture does not contain the parameter B.

The fact that $G^E$ is linear in temperature implies that the excess enthalpy does not change with temperature:

$$H^E(T,X) \rightarrow H^E(X) = A\,X\,(1-X)\left(1-\frac{T}{\theta}\right)\left[1+B\,(1-2X)\right] \qquad \textbf{equation 2}$$

Another characteristic of the ABθ model is the fact that the mole fraction of the critical point of mixing ($X_c$) is the solution of the quadratic equation:

$$(18B)X^2-(2+18B)X+(1+3B)=0 \qquad \textbf{equation 3}$$

Next the critical temperature of mixing ($T_c$) is obtained on the substitution of $X_c$'s value in:

$$T(X_c) = \frac{[2A+GAB(1-2X_c)]X_c(1-X_c)}{R+(1/\theta)[2A+GAB(1-2X_c)]X_c(1-X_c)} \qquad \textbf{equation 4}$$

And intriguing aspect of mixed crystals is the existence of an empirical relationship between the value of the model parameter θ and the melting temperature ($T_m$) of the equimolar mixture:

$$\frac{\log\left(\theta/K\right)}{\log\left(T_m/K\right)} = 1.10 \pm 0.05 \qquad \textbf{equation 5}$$

At this place we may observe that the melting point of the equimolar mixture together with the coordinates of the critical point of mixing are capable of giving a first impression of the values of the system - depentdent parameters A, B, and θ.
For the system at hand we have: $T_m$ = 494 K; $T_c$ = 448 K; and $X_c$ between 0.4 and 0.5. The last of these values goes well with B = 0.1, for which $X_c$ = 0.43. An opening to the value of θ is offered by equation 5: θ = 920 K; for $T_m$ = 494 K. The value of parameter A follows from equation 4 with $T_c$ = 448 K; B = 0.1; θ = 920 K; $X_c$ = 0.43; and the value of 8.314472 J · $mol^{-1}$ · $K^{-1}$ constant R: the result is A = 14250 J · $mol^{-1}$.
In the last part of our analysis we concentrate on the change from the solid to the liquid of the equimolar mixture in terms of thermochemistry. The key thermochemical quantities are the change in enthalpy and the change in Gibbs energy.
The change in enthalpy is the enthalpy of melting, whose value is 9370 J · $mol^{-1}$, as given by Rogers and Janz.[43] and confirmed by our measurements.:

$$\Delta H\ (X=0.5;T=494\ K)=9370\ J \cdot mol^{-1} \qquad \textbf{equation 7}$$

At the minimum of the solid – liquid loop the coexisting solid and liquid phases have equal Gibbs energies. Accordingly,

$$\Delta G\ (X=0.5;T=494\ K)=G\ (liquid)-G\ (solid)=0 \qquad \textbf{equation 8}$$

The two quantities ΔH and ΔG have an ideal part and an excess part:

$$\Delta H\ (0.5;494\ K) = 0.5\ \Delta H_A^*(494K) + 0.5\ \Delta H_B^*(494K) + \Delta H^E\ (0.5;\ 494K) \qquad \textbf{equation 8}$$

$$\Delta G\ (0.5;494\ K) = 0.5\ \Delta G_A^*(494K) + 0.5\ \Delta G_B^*(494K) + \Delta G^E\ (0.5;\ 494K) \qquad \textbf{equation 9}$$

In equations 8 and 9 the subscript A is for $NaNO_3$ and the subscript B is for $KNO_3$. As a result, in order to assess the numerical value of $\Delta H^E$, and $\Delta G^E$, one has to know the numerical values of the pure component properties $\Delta H^*_A$, $\Delta H^*_B$, $\Delta G^*_A$, and $\Delta G^*_B$.

**Table 2.** Pure component data at T = 494 K for A = $NaNO_3$ and B = $KNO_3$, expressed in $J \cdot mol^{-1}$, and derived from the Barin's thermochemical tables.[81]

| | $\Delta H^*_A$ | $\Delta H^*_B$ | $\Delta G^*_A$ | $\Delta G^*_B$ |
|---|---|---|---|---|
| Liquid | 41264 | -528521 | 3616 | -565381 |
| Solid | 22627 | -531228 | 26856 | -567338 |
| Liquid - Solid | 18637 | 2707 | 9295 | 1057 |

The pure copmponent data in table 2 are in integer numbers, such as they are obtained by the calculation. The data for the solid state are found by interpolation; those for the (undercooled) liquid state by the extrapolation from the melting temperatures. From the numerical values of table 2 and through equations 8 and 9 we have:

$$\Delta H^E(0.5;494\ K) = -4596\ J \cdot mol^{-1} \qquad \textbf{equation 10}$$

$$\Delta G^E(0.5;494\ K) = -2282\ J \cdot mol^{-1} \qquad \textbf{equation 11}$$

The last step of the evaluation of the equimolar excess properties of the mixed crystalline solid statet is shown in table 3:

**Table 3.** Equimolar excess enthalpies and excess Gibbs energies at T = 494 K in $J \cdot mol^{-1}$

| | Excess enthalpy | Excess Gibbs energy |
|---|---|---|
| Liquid | -525 | -350 |
| Liquid – Solid | -4596 | -3382 |
| Solid | 4071 | 1932 |

In table 3, the data for the liquid state are based on experimental heat of mixing data published by Kleppa.[9] the latter were subjected to the empirical relationships found for binary liquid mixtures of common-ion alkali halides.[82, 83]

Through equations 1 and 2, the solid state data in table 3 give rise to A = 16284 J · $mol^{-1}$ and θ = 940 K. Along with B = 0.1, the computed A and θ yields 485 K for the critical temperature of mixing, which is 9 K below the mímum of the solid – liquid loop.

**Table 4.** Survey of the outcome of the analysis; numbers between parentheses are the imput data.

| | A (J · $mol^{-1}$) | B | Θ (K) | $T_c$ (K) |
|---|---|---|---|---|
| Figure 7 + equations | 14250 | 0.1 | 920 | (448) |
| Thermochemical data | 16284 | (0.1) | 940 | 485 |

All this analysis conducts to conclude that the reliable part of the phase diagram and the available thermochemical data constitute a coherent whole. Furthermore, the results of the analysis are not in conflict with the experimental evidence for (complete) subsolidus miscibility. Finally the phase diagram of the system $NaNO_3$-$KNO_3$ and its thermodynamic mixing properties are fully in line with the general characteristics found for the systmes of mixed crystal.

## 6.5. DISCUSSION

The $NaNO_3$-$KNO_3$ phase diagram has been studied for more than 150 years. As outlined in this chapter it is easy to understand the difficulties in developing an accurate unique phase diagram. While some studies demonstrated the presence of solid-liquid equilibrium with a minimum, others justify a eutectic invariant. It is, in fact, not surprising because the system is complex and certain experimental precautions must be considered. Both metastability and solid-solid transition kinetics are always present. Furthermore, the existence of a second order transition in $NaNO_3$ causes difficulties in the system.

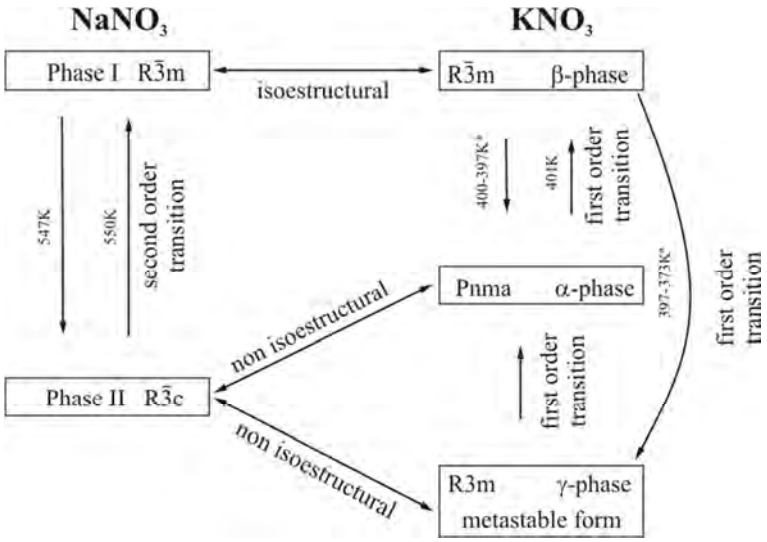


**Figure 8.** $NaNO_3$ and $KNO_3$ polymorphic and isostructural relationships. * β-$KNO_3$ to α-$KNO_3$ is reversible only when working in the temperature range of 400 - 397 K. [a] The β-$KNO_3$ to γ-$KNO_3$ transition temperature depends on many factors. See Introduction for more information.

Figure 8 shows, as much as possible, the polymorphic behaviour of $NaNO_3$ and $KNO_3$. It is important to consider that a necessary but not sufficient condition to achieve total miscibility in solid state is that components crystallize in the same spatial group. At room temperature, phase II $NaNO_3$ crystallizes in the $R\bar{3}c$ spatial group and α-$KNO_3$ phase crystallizes in the Pnma group. Total miscibility at room temperature is impossible. Our experimental and theoretical results show that the miscibility at room temperature in this binary system is reduced. However, the situation is more complicated because if $KNO_3$ is melted, then the γ-$KNO_3$ phase is formed during cooling and coexistence of II-$NaNO_3$ and γ-$KNO_3$ becomes possible. Nevertheless, in this case total miscibility is also impossible (γ-$KNO_3$ crystallize in R3m group). In

conclusion, an immiscibility gap is theoretically expected and experimentally confirmed at room temperature for this binary system.

At higher temperatures (401 K) Pnma α-$KNO_3$ transforms into an $R\bar{3}m$ β-$KNO_3$ by a first order transition. Thermodynamically, a two phase domain with α-$KNO_3$ and β-$KNO_3$ is required. Effectively, our experimental and theoretical results show us this two solid phase domain. The first order transition conduces to a eutectoid invariant at 393 K, and to a high temperature miscibility domain, thus solid-liquid equilibrium is present. Equilibrium between two solid solutions, one rich in II-$NaNO_3$ and the other rich in β-$KNO_3$, exists.

For sodium nitrate, a second order transition from the II-$NaNO_3$ phase to the I-$NaNO_3$ phase is present. The $R\bar{3}m$ I-$NaNO_3$ phase is isostructural with the high temperature $R\bar{3}m$ β-$KNO_3$. Second order transitions are not always considered in the literature for phase diagram determination, however, in this case the order-disorder transition is crucial for the isomorphic relationships analysis between $NaNO_3$ and $KNO_3$. For this transition type only the final temperature can be determined by a DSC analysis.
The existence of the second order transition at high temperatures in sodium nitrate has some implications for miscibility behaviour. It was not possible for us to follow this second order transition by DSC because it overlaps with the melting peak. Nevertheless, as far as we know there are few reports in the literature that have considered these implications using DSC or other techniques. For example Klement[78] was able to follow the transition until 10% of $KNO_3$ with DSC, while Ping et al.[5] were able to follow it until 50% of $KNO_3$. However, they assigned two transitions for the equimolar composition, which has no thermodynamic significance.

For mixed samples X-ray diffraction helps us to determine the stability limits of ordered and disordered phases. Indeed, a better way to study such transitions is by means of X-ray diffraction as a function of the temperature, as Harris,[20] Ballirano[19] and Antao[17] did for $NaNO_3$ and as Antao[18] investigated for the related mineral calcite. The disappearance of 113 and 211 Bragg reflections during heating allowed us to ensure the end of the $R\bar{3}C \rightarrow R\bar{3}m$ second order transition. Accordingly, it is interesting to define second order transition only when the change from $R\bar{3}c$ to $R\bar{3}m$ takes place i.e. when

the $R\bar{3}c$ $NaNO_3$ solid solution type is formed at high temperatures (by K ion incorporation).

The question that has remained unanswered for over 150 years is: does the solvus intersect with the solidus? To solve this question, experimental precautions regarding metastability must be taken into account. To achieve equilibrium at a high temperature, a minimum of 48 hours is required (depending on composition and temperature). Without this annealing period, a metastable mixture of different phases is observed. A solid solution (named in this study as β-$KNO_3$ solid solution) between isostructural $R\bar{3}m$ I-$NaNO_3$ and $R\bar{3}m$ β-$KNO_3$ exists. In some compositions it is only present within a narrow temperature range just below the solidus line. At this stage we can confirm that I-$NaNO_3$ and β-$KNO_3$ are isomorphous, that the binary system between $NaNO_3$ and $KNO_3$ is a system with high temperature total miscibility, and that the solid-liquid equilibrium is a two phase domain with a minimum.

At the atomic level $R\bar{3}m$ I-$NaNO_3$ and $R\bar{3}m$ β-$KNO_3$ are essentially the same. Static and dynamic disorder has been proposed for β-$KNO_3$, see Nimmo and Lucas[21] and references therein for more information. They proposed that $NO_3^-$ is not planar and thus a structural difference between I-$NaNO_3$ and β-$KNO_3$ is possible (although they have the same space group). In contrast, Stromme[39, 79, 80] made a least square refinement of both $R\bar{3}m$ structures, I-$NaNO_3$ (at 563 K) and β-$KNO_3$ (at 425 K) and arrived at the same solution: disorder at high temperature can be modelized in the same manner. Slight differences in the structures are accepted and thus, interchanging between Na and K is possible particularly at high temperatures. Therefore isomorphism between $R\bar{3}m$ I-$NaNO_3$ and $R\bar{3}m$ β-$KNO_3$ does exist.

## 6.6. CONCLUSIONS

The $NaNO_3$-$KNO_3$ phase diagram can be described as a eutectoid invariant at 393 K, with an extended immiscibility zone below this invariant. We found that a narrow biphasic domain (α-$KNO_3$ solid solution and β-$KNO_3$ solid solution) is induced by the first order transition in $KNO_3$. We also found that above the eutectoid invariant (II-$NaNO_3$ (solid solution) + α-$KNO_3$ (solid solution) → β-(solid solution)) there is an asymmetric immiscibility gap (II-$NaNO_3$ (solid solution) + β-$KNO_3$ (solid solution) → β-$KNO_3$ (solid solution)), and that the $NaNO_3$ second order transition ends in the uppermost point of the immiscibility gap. A narrow $NaNO_3$ $R\bar{3}c$ solid solution domain exists. Finally, we also describe the diagram as having minimum solid-liquid equilibrium and that at high temperatures, a solid solution is observed.

Our research has revealed that slow transition kinetics for the formation of high temperature solid solutions can explain the conflicting arguments that exist in the literature as to whether the diagram is eutectic or melting point minimum.

I-$NaNO_3$ and β-$KNO_3$ are only isomorphous at high temperatures because they are isostructural, chemically analogous and can form a solid solution in all compositions.

The results of the thermodynamic analysis are not in conflict with the experimental evidence for (complete) subsolidus miscibility.

The phase diagram of $NaNO_3$-$KNO_3$ and the thermodynamic mixing properties of the system are fully in line with the general characteristics found for systems of mixed crystals.

## 6.7. BIBLIOGRAPHY

1. Berg, R. W.; and Kerridge, D. H. *The $NaNO_3$ -$KNO_3$ System: The Position of the Solidus and Sub-Solidus.* Dalton Trans., **(2004)**, 2224-2229.

2. Voskresenskaya, N. K.; Evseeva, N. N.; Berul, S. I. and Vereshchetina,I. P.: *Handbook of Solid-Liquid Equilibria in Systems of Anhydrous Inorganic Salts,*. Voskresenskaya, N. K. ed., 1st ed. Jerusalem: Keter Press**, (1970).**

3. Berg, R. W.; and Kerridge, D. H. *Raman Mapping in the Elucidation of Solid Salt Eutectic and Near Eutectic Structures.* J. Raman Spec., **(2002)**, 33, 165-172.

4. Benes, O.; Konings, R.; Wurzer, S.; Sierig, M. and Dockendorf, A. *A DSC Study of the $NaNO_3$-$KNO_3$ System using an Innovative Encapsulation Technique.* Thermochim. Acta, **(2010)**, 509, 1-2, 62-66.

5. Ping, W.; Harrowell, P. B., N. and Angell, C. A. *Composition Dependence of the Solid State Transitions in $NaNO_3$/$KNO_3$ Mixtures.* Thermochim. Acta, **(2009)**, 486, 27-31.

6. Greis, O.; Bahamadan, K. M. and Uwais, B. M. *the Phase Diagram of the System $NaNO_3$-$KNO_3$ Studied by Differential Scanning Calorimetry.* Thermochim. Acta, **(1985)**, 86, 343-350.

7. Zamali, H.; and Jemal, M. *Diagrammes De Phases Des Systemes Binaires $KNO_3$-$CsNO_3$ Et $KNO_3$-$NaNO_3$.* J. Thermal Anal., **(1994)**, 41, 1091.1099.

8. Dessureault, Y.; Sangster, J. and Pelton, A. D. *Evaluation Critique Des Donées Thermodynamiques et des Diagrammes de Phases des Systèmes AOH-AX, $ANO_3$-AX, $ANO_3$-$BNO_3$, AOX, BOX où A, B= Li, Na, K et X=Cl, F, $NO_3$, OH.* J. Chim. Phys., **(1990)**, 87, 407-453.

9. Kleppa, O. J. *A New Twin High-Temperature Reaction Calorimeter. the Heats of Mixing in Liquid Sodium-Potasium Nitrates.* J. Phys. Chem., **(1960)**, 64, 1937-1940.

10. Wiedemann, H. G.; and Bayer, G. *Application of Simultaneous thermomicroscopy/DSC to the Study of Phase Diagrams.* J. Thermal Anal., **(1985)**, 30, 1273-1281.

11. Rao, C. N. R.; Prakash, B. and Natarajan, M. *Crystal Structure Transformations in Inorganic Nitrites, Nitrates, and Carbonates.* National Standard Reference Data System - National Bureau of Standards, **(1975)**.

12. Rao, K. J.; and Rao, N. R. *Crystal Structure Tranformation of Alkali Sulphates, Nitrates and Related Substances: Thermal Hysteresis in Reversible Transformations.* J. Mat. Sci., **(1966)**, 1, 238-248.

13. Paul, G. L.; and Pryor, A. W. *Study of Sodium-Nitrate by Neutron Diffraction.* Acta Cryst. B, **(1972)**, 28, 15, 2700-2702.

14. Gonschorek, G.; Weitzel, H.; Miehe, G. and Schmahl, W. *the Crystal Structure of $NaNO_3$ at 100K, 120K, and 563K.* Zeits. Krist., **(2000)**, 215, 752-756.

15. Fermor, J. H.; and Kjekshus, A. *On the Electrical Properties of $NaNO_3$.* Acta Chem. Scand., **(1968)**, 22, 5, 1628-1636.

16. Parsonage, N. G.; and Staveley, L. A. K.: *Disorder in Crystals,*Oxford: Calerendon Press, **(1978).**

17. Antao, S. M.; Hassan, I.; Mulder, W. H.;and Lee, P. L., *The R3c -> R3m Transition in Nitratine, $NaNO_3$, and Implications for Calcite, $CaCO_3$.* Phys. Chem. Min., **(2008),** 35,10. 545-557.

18. Antao, S. M.; Hassan, I.; Mulder, W. H.; Lee, P. L. and Toby, B. H. *In Situ of the R-3c -->R-3m Orientational Disorder in Calcite.* Phys. Chem. Min., **(2009)**, 36, 159-169.

19. Ballirano, P. *Laboratory Parallel-Beam Transmission X-Ray Powder Diffraction Investigation of the Thermal Behavior of Nitratine $NaNO_3$: Spontaneous Strain and Structure Evolution.* Phys. Chem. Min., **(2011)**, 38, 7, 531-541.

20. Harris, M. J. *A New Explanation for the Unusual Critical Behaviour of Calcite and Sodium Nitrate, $NaNO_3$.* Am. Miner., **(1999)**, 84, 1632-1640.

21. Nimmo, J. K.; and Lucas, B. W. *the Crystal Structures of g- and b-$KNO_3$ and the $\alpha$->$\gamma$->$\beta$ Phase Transformations.* Acta Cryst. B, **(1976)**, B-32, 1968-1971.

22. Adiwidjaja, G.; and Pohl, D. *Superstructure of a-Phase Potassium Nitrate.* Acta Cryst. C., **(2003)**, 59, i139-i140.

23. Asadov, Y. G.; Nasirov, V. I. and Jarailova, G. A. *Morphology of Crystal Growth at Polymorphic Transformations in $KNO_3$, $AgNO_3$ and $NH_4NO_3$ Single Crystals.* J. Cryst. Growth, **(1972)**, 15, 45-50.

24. Fermor, J. H.; and Kjekshus, A. *A Phase Transition in $KNO_3$ at Low Temperatures.* Acta Chem. Scand., **(1968)**, 22, 836-842.

25. Adams, D. M., Hatton, P. D.; Heath, A. E.; and Russell, D. R. *X-Ray Diffration Measurements on Potassium Nitrate Under High Pressure using Synchrotron Radiation.* J. Phys. C., **(1988)**, 21, 3. 505-515.

26. Nimmo, J. K.; and Lucas, B. W. *A Neutron Diffraction Determination of the Crystal Structure of a-Phase Potassium Nitrate at 25ºC and 100ºC.* J. Phys. C., **(1973)**, 6, 201-211.

27. Chen, A.; and Chernow, F. *Nature of Ferroelectricity in $KNO_3$.* Phys. Rev., **(1967)**, 154, 2, 493-505.

28. Shimada, S.; and Aoki, T. *Stabilization of the Ferroelectric G-Phase by Doping with $Na^+$, Determined by the Acoustic Emision Method.* Chem. Let., **(1996)**, 393-394.

29. Christensen, A. N.; Norby, P.; Hanson, J. C. and Shimada, S. *Phase Transition of $KNO_3$ Monitored by Sincrotón X-Ray Powder Diffraction.* App. Cryst., **(1996)**, 29, 265-269.

30. Westphal, M. J. *Particle Size and Cooperative Behaviour Effects on $KNO_3$ Phase Transitions.* J. App. Phys., **(1993)**, 74, 10, 6107-6114.

31. Khana, R. K.; Lingscheid, J. and Decius, J. C. *Infrared Absorption Spectra of Potassium Nitrate in Phases I, II and III.* Spectrochim. Acta, **(1964)**, 20, 1109-1116.

32. Shimada, S.; Katsuda, Y. and Inagaki, M. *Phase Transition of Potassium Nitrate Monitored by Acoustic Emission Technique and the Healing Effect on the Gamma-Alpha. Transition.* J. Phys. Chem., **(1993)**, 97, 34, 8803-8807.

33. Poprawski, R.; Rysiakiewicz-Pasek, E.; Sieradzki, A.; Ciżman, A. and Polańska, J. *Ferroelectric Phase Transitions in $KNO_3$ Embedded into Porous Glasses.* J. Non Cryst. Solids, **(2007)**, 353, 47-51, 4457-4461.

34. Baryshnikov, S. V.; Charnaya, E. V.; Milinkiy, A. Y.; Stukova, E. V.; Tien, C. and Michel, D. *Phase Transition in $K_{1-x}Na_xNO_3$ Embedded into Molecular Sieves.* J. Phys., **(2009)**, 21, 325902.

35. Fermor, J. H.; and Kjekshus, A. *On the Electrical Properties of $KNO_3$.* Acta Chem. Scand., **(1967)**, 21, 5, 1265-1276.

36. Vainshtein, B. K.; Fridkin, V. M. and Indenbom, V. L.: *Structure of Crystals,* 2ed. Berlin; Springer-Verlag, **(1995).**

37. Barret, W. T.; and Wallace, W. E. *Studies of NaCl-KCl Solid Solutions. I. Heats of Formation, Lattice Spacings, Densities, Schottky Defects and Mutual Solubilities.* J. Amer. Chem. Soc., **(1954)**, 76, 366-369.

38. Oonk, H. A. J. *Solid-State Solubility and its Limits. the Alkali Halide Case.* P. App. Chem., **(2001)**, 73, 5, 807-823.

39. Stromme, K. O. *On the Crystal Structure of Potassium Nitrate in the High Temperature Phases I and III.* Acta Chem. Scand., **(1969)**, 23, 1625-1636.

40. Xu, K.; and Chen, Y. *Raman Spectroscopic Studies of Mixed Crystals of $NaNO_3$-$KNO_3$ Quenched from Different Temperatures: Evidence for Limited Solid Solutions in the System.* J. Raman Spectros., **(1999)**, 30, 6. 441-448.

41. Kramer, C. M.; and Wilson, C. J. *The Phase Diagram of $NaNO_3$-$KNO_3$.* Thermochim. Acta, **(1980)**, 42, 253-264.

42. Kamimoto, M. *Thermodynamic Properties of 50 Mole% $NaNO_3$-$50KNO_3$ ($HTS_2$).* Thermochim. Acta, **(1981)**, 49, 319-331.

43. Rogers, D. J.; and Janz, G. J. *Melting-Crystallization and Premelting Properties $NaNO_3$-$NaNO_3$. Enthalpies and Heat Capacities.* J. Chem.Eng. Data, **(1982)**, 27, 424-428.

44. Abe, O.; Utsunomiya, T. and Hoshino, Y. *The Thermal Stability of Binary Alcali Metal Nitrates.* Thermochim. Acta, **(1984)**, 78, 251-260.

45. Zamali, H.; Jriri, R.; Rogez, J.; Jemal, M. and Mathieu, J. C. *Mixing Properties in the Continuous Solid Solution of the System $KNO_3$-$NaNO_3$.* Thermochim. Acta, **(1994)**, 233, 1, 1-11.

46. Zhang, X.; Tian, J.; Xu, K. and Gao, Y. *Thermodinamic Evaluation of Phase Equilibria in $NaNO_3$-$KNO_3$ Systems.* J. Phase Eq., **(2003)**, 24, 5, 441-446.

47. Harmealin, M. *Relation of Quantitative Differential Thermal Analysis to Study on Polymorphism of Potassium Nitrate at Atmospheric Pressure.* J Therm Anal., **(1972)**, 4, 4, 403.

48. Kracek, F. *The Polymorphism of Potassium Nitrate.* J. Phy. Chem., **(1930)**, 34. 225.

49. . Muntasell, J.; Navarro, J. and Cesari, E. *A Study of the Polymorphism of Potassium Nitrate Starting from Room Temperature and at Atmospheric Pressure.* Thermochim. Acta, **(1985)**, 83, 2, 173-179.

50. Tammann, V. G.; and Ruppelt, A. *Die Entmischung Lückenloser Mischkristallreihen.* Z. Anor. Allg. Chem., **(1931)**, 197, 1, 65-89.

51. Hissink, D. J. *On the Formation and Conversion of Mixed Crystals from Sodium Nitrate and Potassium Nitrate and from Sodium Nitrate with Silver Nitrate.* Z. Phys. Chem., **(1900)**, 32, 3, 537-563.

52. Madgin, W. M.; and Briscoe, H. V. A. *The Melting Point (Solidus) Curve for Mixtures of Potassium Nitrate and Sodium Nitrate.* J. Chem. Soc., **(1923)**, 123, 2914-2916.

53. Briscoe, H. V. A.; and Madgin, W. M. *The Freezing Point Curve for Mixtures of Potassium Nitrate and Sodium Nitrate.* J. Chem. Soc., **(1923)**, 123, 1608-1618.

54. Kofler, V. A. *Über Periodische Umlagerungen Beim Kristallisieren Und Scgmelzen Von Mischkristallen.* Z. Elektro., **(1955)**, 59, 10, 939-941.

55. Xu, K.; and Chen, Y. *Temperature-Dependent Raman Spectra of Mixed Crystals of $NaNO_3$-$KNO_3$: Evidence for Limited Solid Solution.* J. Raman Spectros., **(1999)**, 30, 173-179.

56. Laybourn, K.; and Madgin, W. M. *On the Measurement of Mechanical Properties of Binary Inorganic Salt Mixtures.* J. Chem. Soc., **(1932)**, 28, 857-866.

57. Eweka, E. I.; and Kerridge, D. H. *Non-Ideal Change of Electrical Conductivity on Solidification and Remelting of Salt Eutectics: 1. Oxyanion-Based Systems.* Sol. St. Ionics, **(2006)**, 177, 15-16, 1245-1250.

58. Eweka, I. E.; and Kerridge, D. H. *Changes in Electrical Conductivity of Salt Eutectic through the Melting Point.* Phys. Let. A, **(1993)**, 174, 441-442.

59. Moreno, E.; Cordobilla, R.; Calvet, T.; Cuevas-Diarte, M. A.; Gbbode, G.; Negrier, P.; Mondieig, D. and Oonk, H. A. J. *Polymorphism of Even Saturated Carboxilic Acid from n-Decanoic to n-Eicosanoic Acid.* New J. Chem., **(2007)**, 31, 947-957.

60. Gbbode, G.; Negrier, P.; Mondieig, D.; Moreno, E.; Calvet, T. and Cuevas-Diarte, M. A. *Polymorphism and Solid-State Miscibility in the Pentadecanoic Acid-Heptadecanoic Acid Binary System.* Chem. Phys. Lip., **(2008)**, 154, 68-77.

61. Metivaud, V.; Lefevre, A.; Ventolà, L.; Negrier, P.; Moreno, E.; Calvet, T. and Cuevas-Diarte, M. A. *Hexadecane ($C_{16}H_{34}$) 1-Hexadecanol ($C_{16}H_{33}OH$) Binary System: Crystal Structures of the Components and Experimental Phase Diagram. Application to Thermal Protection of Liquids.* Chem. Mat., **(2005)**, 17, 12, 3302.

62. Ventolà, L.; Calvet, T.; Cuevas-Diarte, M. A.; Oonk, H. A. J. and Mondieig, D. *Solid-Solid and Solid-Liquid Equilibria in the n-Alkanols Family: $C_{18}H_{37}OH$-$C_{20}H_{41}OH$ System.* Phys. Chem. Chem. Phys., **(2004)**, 6, 13, 3726.

63. Ventolà, L.; Metivaud, V.; Bayés, L.; Benages, R.; Cuevas.Diarte, M. A.; Calvet, T. and Mondieig, D. *The Binary System Tetradecanedioic Acid- Hexadecanedioic Acid: Polymorphism of the Components and Experimental Phase Diagram.* Helv. Chim. Acta., **(2006)**, 89, 2027-2039.

64. Ventolà, L.; Bayés, L.; Benages, R.; Novegil-Anleo, F. A.; Cuevas.Diarte, M. A.; Calvet, T. and Mondieig, D. *Decanedioic Acid ($C_{10}H_{18}O_4$)/Dodecanedioic Acid ($C_{12}H_{22}O_4$) System: Polymorphism of the Components and Experimental Phase Diagram.* Helv. Chim. Acta,**,** **(2008)**, 91, 1286-1298.

65. Courchinoux, R.; Chanh, N. B.; Haget, Y.; Calvet, T.; Estop, E. and Cuevas-Diarte, M. A. *Du Signal Aux Phénomènes: Una Approche Pratique r L'Établissement Des Diagrammes De Phases Par Analyse Thermique.* J. Chim. Phys., **(1989)**, 86, 3, 561-593.

66. *Materials Studio Modeling 4.2. Information Available at http://accelrys.com/products/materials-Studio.*

67. Bartlett, H. E.; and Johnson, K. E. *Electrolytic Reduction and Ellingham Diagrams for Oxy-Anions Systems.* Can. J. Chem., **(1966)**, 44, 18, 2119-2129.

68. Freeman, E. S. *The Kinetics of the Thermal Decomposition of Sodium Nitrate and of the Reaction between Sodium Nitrite and Oxygen.* J. Phys. Chem., **(1956)**, 60, 1487-1493.

69. Freeman, E. S. *The Kinetics of the Thermal Descomposition of Potassium Nitrate and of the Reaction between Potassium Nitrite and Oxygen.***,** J Am. Chem. Soc., **(1957)**, 79, 4, 838-842

70. Alexander, J., J.; and Hindin, S. G. *Phase Relations in Heat Transfer Salt Systems.* Ind. Eng. Chem., **(1947)**, 39, 8, 1044-1049.

71. Bartholomew, R. F. *A Study of the Equilibrium $KNO_3(l)$ <-->$KNO_2(l)$ + $1/2O_2(g)$ Over the Temperature Range 550-750ºC.* J. Phys. Chem., **(1966)**, 70, 3442-3446.

72. Carling, R. W. *Heat Capacities of $NaNO_3$ and $KNO_3$ from 350 to 800 K.* Thermochim. Acta, **(1983)**, 60, 265-275.

73. Iwadate, Y.; Okada, I. and Kawamura, K. *Density and Heat Capacity of Molten $NaNO_2$-$KNO_3$ Mixtures.* J. Chem. Eng. Data, **(1982)**, 27, 288-290.

74. Westphal, M. J. *Cooperative Behavior during Ferroelectric Transition in $KNO_3$ Powder.* J. App. Phys., **(1993)**, 74, 5, 3131-3136.

75. Nakamoto, K. *Inorganic Compounds, in* Infrared and Raman Spectra of Inorganic and Coordination Compounds.4th ed. New York: Wiley, **(1986).**

76. Neumann, M. *X-Cell: A Novel Indexing Algorithm for Routine Tasks and Difficult Cases.* J. Appl. Crystallogr., **(2003)**, 36, 356-365.

77. Pawley, G. S. *Unit-Cell Refinement from Powder Diffraction Scans.* J. Appl. Crystallogr., **(1981)**, 14, 357-361.

78. Klement, W. J. *Variation of l Transition Temperature in $NaNO_3$-Base Binary Alloys with $AgNO_3$, $KNO_3$, and $NaNO_2$,* J. Inorg. Nuc. Chem., **(1974)**, 36, 8, 1916-1918.

79. Stromme, K. O. *The Crystal Structure of Sodium Nitrate in the High Temperature Phase.* Acta Chem. Scand., **(1969)**, 23, 1616-1624..

80. Stromme, K. O. *On the Crystal Structure of Potassium Nitrate in the High Temperature Phases I and III.* Acta Chem. Scand., **(1969)**, 23, 1625-1636.

81. Barin, I. *Thermochemical Data of Pure substances.* VCH Verlagsgesellschaft, Weinhein. Germany, **(1989)**.

82. Oonk, H. A. J.; Bouwstra, J. A.; van Ekeren, P. J. *Binary Common-anion Alkali Halides Mixtures. Correlation of the Thermochemical and Phase Diagram Data.* Calphad, **(1986)**¸10, 137-161.

83. van der Kemp, W. J. M.; Blok, J. G.; van Genderen, A. C. G.; van Ekeren, P. J.; Oonk, H. A. J. *Binary Common-ion Alkali Halide Mixture; a Uniform Description of the Liquid and Solid State*. Thermochim. Acta **(1992)**, 196, 301-315.